NANO STUDIES

2

2010

NANO STUDIES

2

2010

Nano Studies, 2 (2010)

UDG [53 + 54 + 620.22] (051.2)
N – 21

Nano Studies is a biannual scientific journal published in Georgia.

Nano Studies' topics of interest include Nanocscience and related problems of Physics, Chemistry and Materials Science.

Nano Studies publish following categories of scientific articles: research papers, communications, reviews and discussions.

Nano Studies publish scientific articles in English and also in Georgian and in Russian.

English summaries of all the articles of **Nano Studies** are referred in **Georgian Abstracts Journal** and their full-texts are free-accessible in **Tech Inform** (Georgia's Central Institute for Seintific and Technical Information) database:
www.tech.org.ge
www.tech.caucasus.net

E-mail: chkharti2003@yahoo.com
Phone: 31 45 93
Mobile: 8 99 34 07 36

Articles included in present volume are published by financial support of the GNSF (Georgia National Science Foundation), Grant GNSN/ST 08/4-411. Any idea in these publications is possessed by the authors and may not represent the opinion of the Georgia National Science Foundation itself.

Publishing House **"UNIVERSAL"**

19, I. Chavchavadze Ave., 0179, Tbilisi,Georgią : 22 36 09, 8(99) 17 22 30
E-mail: universal@internet.ge

ISSN 1987 – 8826

CONTENTS

Spin transport properties of manganese doped nanostructured magnetic semiconductors
P.J. Kervalishvili **5-14**

Geometries of boron nitride multi-walled nanotubes and multi-shelled fullerenes – in Russian
L. Chkhartishvili, T. Berberashvili **15-21**

Titan carbide based nano-crystalline solid solutions: Production and compacting – in Russian
A.A. Gachechiladze, A.G. Mikeladze, D.L. Gabunia, B.G. Margiev, R.V. Chedia, T.A. Tsuladze, R.K. Zekalashvili, O.A. Tsagareishvili **23-29**

Some issues of precious linear measurements in nanometric region – in Russian
A.G. Danelyan, V.A. Danelyan, R.R. Kankia, S.A. Mkrtychyan, S.V. Shotashvili, D.I. Gharibashvili, I.R. Lomidze **31-44**

Nanometrology: Topicality and problems – in Russian
A.G. Danelyan, R.R. Kankia, C.A. Mkrtychyan, D.I. Gharibashvili, I.R. Lomidze **45-52**

UV–Vis and FT–IR spectra of ultraviolet irradiated collagen in the presence of antioxidant ascorbic acid
N.O. Metreveli, K.K. Jariashvili, L.O. Namicheishvili, D.V. Svintradze, E.N. Chikvaidze, A. Sionkowska, J. Skopinska..... **53-64**

Microbial synthesis of metal and semiconductor nanoparticles
N. Tsibakhashvili **65-70**

Carbon nanosystems – in Georgian
A.P. Bibilashvili **71-83**

Heat capacity of the 3D and 2D systems according to interatomic chemical bonding
Z. Gogua, G. Kantidze **85-94**

Doping of thulium, praseodymium and neodymium sulfides thin films – in Georgian
K.D. Davitadze, T.A. Minashvili, G.N. Iluridze..... **95-97**

Stimulated phenomena in glass doped with CdSe quantum dots
G. Dekanozishvili, D. Driaev, T. Kalabegishvili, V. Kvatchadze **99-102**

Proposals for formation of a nanotechnology center in Georgia – in Russian
R.I. Chikovani **103-118**

On elaboration of optoelectronic elements exploiting properties of nanosilicon formed in "silicon-on-sapphire"-structure – in Russian
R.E. Kazarov, R.I. Chikovani, D.I. Garibashvili,
G.I. Goderdzishvili, T.I. Khachidze **119-121**

Photoelectric parameters determination for AlGaAs heterostructure-based photo-cells by a conctacless method – in Georgian
A.B. Guchmazov, G.N. Iluridze, T.A. Minashvili,
G.V. Rtveliashvili, M.S. Taktakishvili **123-125**

Competitive nanotechnologies for nanoelectronics, piezoengineering, photocatalysis and composites particularly using electroless deposition
T.N. Khoperia, T.I. Zedginidze **127-138**

Boron nitride nanostructures: Molecules, sheets, tubes, fullerenes (An overview)
L. Chkhartishvili **139-174**

Preparation of iron oxide nanoparticles by laser ablation method – in Russian
V.G. Kvachadze, T.I. Pavliashvili,
G.G. Abramishvili, T.L. Kalabegishvili,
V.M. Gabunia **175-177**

Synthesis of silver nanoparticles using bacteria
N. Tsibakhashvili, T. Kalabegishvili, V. Gabunia,
E. Gintury, N. Kuchava, N. Bagdavadze, D. Pataraya,
M. Gurielidzse, D. Gvarjaladze, L. Lomidze **179-182**

On relative stability of single-walled boron nitride nanotubes
L. Chkhartishvili, I. Murusidze **183-212**

Summaries **213-216**

SPIN TRANSPORT PROPERTIES OF MANGANESE DOPED NANOSTRUCTURED MAGNETIC SEMICONDUCTORS

P.J. Kervalishvili

Georgian Technical University
PaataKervalishvili@gtu.ge

Accepted January 27, 2010

The preparation of multilayer nanostructures of GaSb / Mn is proposed to be implemented by the methods of MOS hydrate epitaxy and laser epitaxy with usage of laser doping during the layer growing. Analysis of quality and chemical composition was performed with usage of atomic force microscopy, by measurements of photo-electric spectrums and luminescence, by methods of the scanning Auger microscopy, and also with usage of X-ray diffraction experiments.

For the deposition of GaSb and Mn layers the pulsed Q-switched IAG-LASER at the wave length of 1064 nm was used. Plates of non-doped single crystal of GaSb and polycrystalline Mn purity 99.8 % were served as targets [1–3]. The special rotary holder was designed and manufactured to get discrete alloys (DA) with various thicknesses of separated GaSb and Mn layers and at various relations between them allowing to volatilize targets in series, subjecting their to the action of chosen amount of the laser pulses. The target was fixed on the rotary holder in such a way that the normal to its surface forms an angle relatively to the normal of the holder basis. Thus, the track of the laser transpiration on a target circumscribed a circle, and the laser torch which is flying apart along the normal to its surface, made the circular motions analogous to the precession of the rotary gyroscope. By matching the geometrical sizes of the evaporation area it was possible to gain layers with the minimal dispersion on thickness. Estimates have shown that on surface the size 20×20 mm^2 the straggling on thickness did not exceed 5 %. Test experiments on deposition of "thick" layers (suitable for measuring the thickness by means of the interference microscope) allowed defining the effective thickness of a layer for one volatilizing pulse. Thus, the thicknesses of separate layers in periodic structure could be determined with the split-hair accuracy. The plates of semi-insulating GaAs with the orientation (100) are served as substrates. The temperature of a deposition varied over the range (200 – 440) ºC. This method had been brought up discrete alloys with effective thickness of layers of manganese from 0.2 up to 2.0 nm and thickness of layers GaSb from 0.7 up to 10 nm. The number of periods in structures changed from 10 up to 50.

Testing of the obtained structures has shown strong dependence of their properties from the temperature of growing. At the temperatures of growth around (400 – 450) °C any of structures did not manifest an appreciable ferromagnetism in the Hall effect measurements at temperatures from room down to 77 K. The holes concentration in layers made in this case is ~ 10^{19} cm^{-3}, the Hall mobility is (20 – 30) cm^2 / V · s. Annealing of structures with parameters the close to 6 – 7 (A4) pulses of radiation of the ruby laser with the power of (10^5 – 10^6 W / cm^2 gave appreciable decrease of the hole mobility up to (6 – 9) cm^2 / V · s and considerable increment of their concentration (more than on the order of magnitude). Thus, the Hall effect versus magnetic field curve became anomalous (without a loop) at room temperature and it has shown hysteresis only at 77 K.

Other pattern was observed in structures, which have been grown at 20 ºC. Typical results of the Hall measurements, obtained in this case, are presented in Table 1.

Table 1. Results of the Hall effect measurements for GaSb / Mn multilayers.

# #	d_{Mn}, nm	d_{GaSb}, nm	Measurings Hall effect (HE), presence of a hysteresis	Number of periods
6–7 (A4)	1.9	8.1	AHE at 300 K a loop at 77 K	16
6–7 (B1)	0.95	9.2	AHE at 300 K, a loop at 77 K	16
8–6	0.5	0.95	AHE with a loop at 300 and 77 K	30
6–7 (B2)	0.5	3.8	Ordinary HE	16
6–7 (A1)	0.25	1.2	AHE at 300 and 77 K, loops are not present	16
7–10	0.25	2.6	AHE at 300 and 77 K, loops are not present	46
6–7 (B3)	0.25	4.0	Ordinary HE	16

We have investigated the corresponding literature and patent sources related preparation of pure metallic Mn. We have found that small amount of pure Mn used as doping material should be prepared by electrolyze of the water solution of $MnSO_4$ by addition of $(NH_4)_2SO_4$ on Pb (anode) and Ti (cathode) electrodes followed by the thermal treatment and crystallization in vacuum chamber. Approbation of the given method has been already conducted [4].

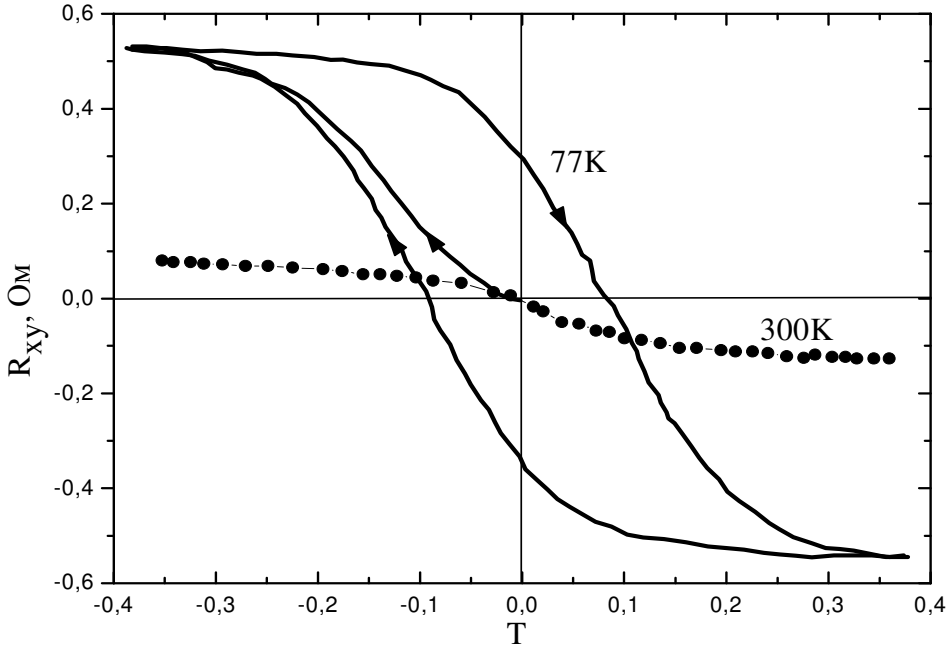

Fig. 1. Magnetic field dependences of Hall resistance for the sample 6–7 (A4).

Examinations of structures performed by the method of the X-ray diffraction have shown that in structures with the period $d \geq 10$ nm is detected the periodicity with parameters close to incorporated in the technology of their growth. The depth of manganese penetration in adjacent

GaSb layers was near 4 nm. Thus, it is possible to assume that are implemented requirements of the almost complete intermixing of Mn and GaSb in discrete alloys with $d < 10\,\text{nm}$, and the behavior of the Hall effect in those samples is similar to its behavior in homogeneously doped GaMnSb layers. In structures 6–7 (A4) and 6–7 (B1) the complete intermixing Mn does not take place, and the field dependence of the Hall effect shown in Fig. 1 for the sample 6–7 (A4), corresponds to discrete alloy [5–7].

Novel very exiting properties of semiconductors are determined by impurities and their disordered distribution. At the same time the last theoretical and experimental achievements have shown that disorders in semiconductors should be controlled – should have the necessary regulations. So it is a very important to know relatively well the properties of materials such as GaSb applicable for spin transport organization in diluted semiconductors.

For design the technology of periodic layer GaSb / Mn structure getting, the structural and magneto-transport properties of thin GaMnSb films with increased content of Mn, up to 10 at. %, grown by use the laser dispersion in vacuum have been studied. The structures have shown that the GaMnSb layers, regardless to the Ga replacing by the Mn-acceptors, also contain ferromagnetic MnSb nanoclusters and shallow acceptor defects controlled by the growth temperature. The Hall effect measurements and magnetoresistance effect study have been performed at magnetic fields up to 20 T and temperatures (4 – 300 K).

In order to determine the characteristic scale of magneto-electrical non-uniformities in ferromagnetic semiconductors the technique based on investigating mesoscopic fluctuations of the Hall voltage (or the transverse resistance R_{xy}) in varying magnetic field is proposed. That technique is founded on the analysis of the magnetic field dependency of the even (over the magnetic field) component $R_a(H) = (R_{xy}^{+} + R_{xy}^{-})/2$ of the transverse resistance and comparing that with the magnetic field dependency $R_{xx}(H)$ of the longitudinal resistance (R_{xy}^{+}, R_{xy}^{-} are transverse resistances referring to the positive and the negative directions of the magnetic field). The scale of magneto-electrical non-uniformities was shown to be connected with $R_a(H)$ and $R_{xx}(H)$ by the relation: $\Delta l_{me} \approx l_p R_a(0)/R_{xx}(0)[R_a(H)R_{xx}(0)/R_a(0)R_{xx}(H) - 1]$, where l_p is the distance between the potential probes at the lateral sample facets.

In order to reveal of concentration and ionization energy of thin acceptor centers of undoped p-GaSb we performed the measurement of temperature dependence of Hall coefficient in the temperature range (13 – 100) K. At the typical temperature dependence of Hall coefficient for investigated samples of undoped p-GaSb maximum of the curve is connecting with transfer from band-conductivity to hopping when the current carriers haven't enough energy for transition from impurity levels to conduction band, and current is determined by the hopping of charge carriers directly without activation.

Values of the acceptors and donors concentration as well as the ionization energy were evaluated from the analysis of experimental curves and solution of electro-neutrality equation by method of the least squares for two levels model with estimation of compensation. Selection of parameters was performed by using computers which was made searching much easy.

Fig. 2 shows photoluminescence (PL) spectra for some structures with variation of Mn quantity in δ-doped layers. It was demonstrated that the intensity of the (1.20 – 1.25) eV peak, related with the transition from the first electron level to the heavy hole level in QW, shows decrease monotonically with the increase of Mn quantity in δ<Mn>-doped layer. The best parameters of structures (the Curie temperature is less than 40 K; decrease of the QW PL is no more than one order of magnitude comparing with structures without the Mn-doping) were achieved at the Mn quantity no more than 0.25 ml.

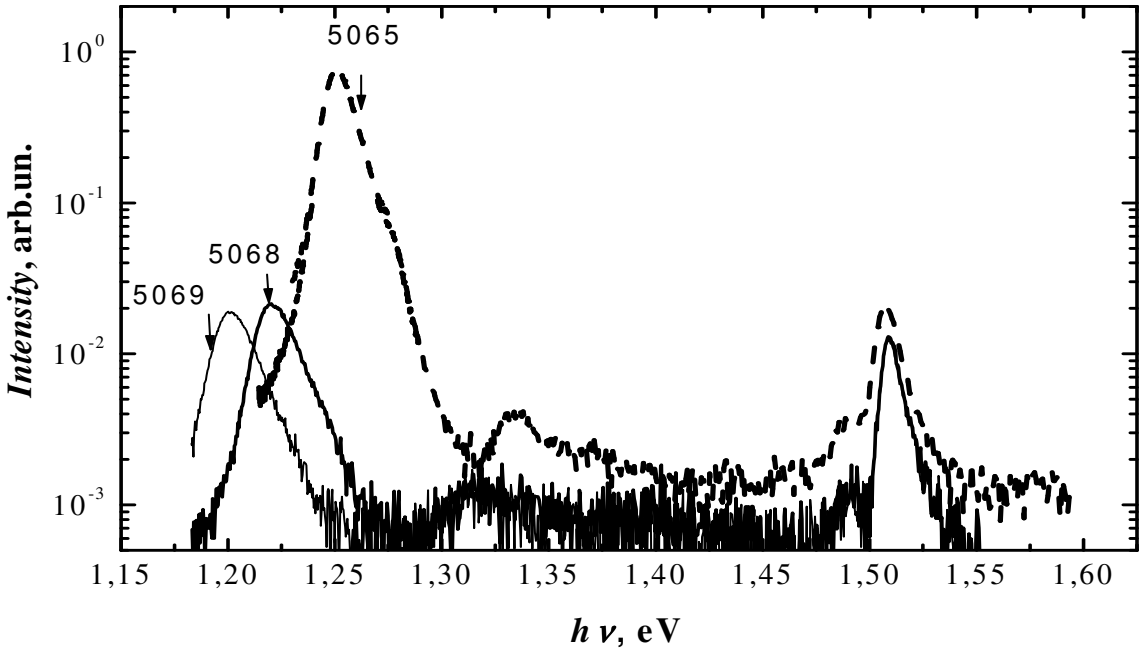

Fig. 2. Photoluminescence spectra of the structures at 77 K.

The study of the obtained structure was carried out using the microscope DSM – 960 (Carl Zeiss, Germany). SEM pictures had been produced by integrated signal of the secondary and reflected electron beams regime (initial accelerating voltage $E_0 = 20\,\text{keV}$). SEM pictures are shown that: at the crystal surface (substrate) as well as on the surface of deposited layer are observed effects of charge and voltage contrasts. They are connected with the surface contaminations of thin film (Fig. 3).

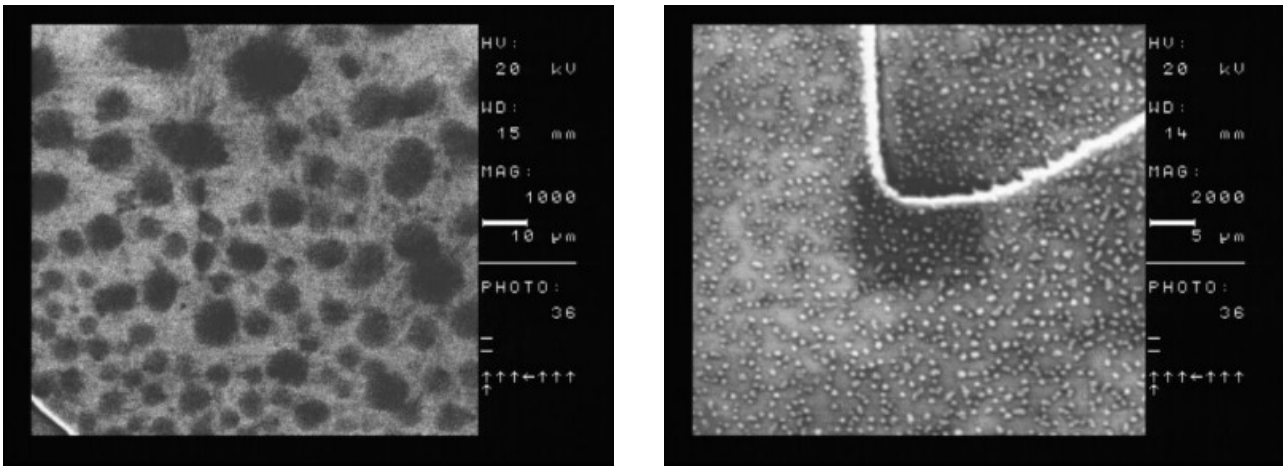

a **b**

Fig. 3. SEM pictures of the prepared sample's surfaces: (a) and (b).

Vacuum cryostat for the conductance, the Hall effect, and the structure magneto-conductance and mesoscopic property study has been developed, manufactured and managed. The cryostat is developed as a prefix for usual nitrogen storage, and posses: the sample management in-between the electromagnet poles (magnetic field is up to 1.5 T); the sample temperature setting by variation of the nitrogen gas flow and temperature of the nitrogen vapor in the range from 80 to 500 K.

The cryostat is managed with the precise thermo-sensor and resistive elements (evaporator and heater) for variation and setting the nitrogen gas flow and temperature. The cryostat has been tested at laboratory conditions. The sample temperature variation and setting validity in the range of (80 – 500) K have been improved. Precision regulator for the cryostat temperature regime management also has been developed.

Experimental system for study the extraordinary and planar Hall effect, magneto-transport, and mesoscopic fluctuations has been developed. The system provides a high sensitivity for the Hall-effect voltage, ~ 1 μV, and the resistance variation, $\delta R/R \sim 10^{-5}$, for the sample resistance up to 10^{10} Ohm. The precision is caused by adoption of digital filtration method success to experiments.

Novel very exiting properties of semiconductors are determined by impurities and their disordered distribution. At the same time the last theoretical and experimental achievements have shown that disorders in semiconductors should be controlled – should have the necessary regulations. So it is a very important to know relatively well the properties of materials such as GaSb applicable for spin transport organization in diluted semiconductors [8].

In order to reveal of concentration and ionization energy of thin acceptor centers of undoped p-GaSb we performed the measurement of temperature dependence of Hall coefficient in the temperature range (13 – 100) K.

Values of the acceptors and donors concentration as well as the ionization energy were evaluated from the analysis of experimental curves and solution of electro-neutrality equation by method of the least squares for two levels model with estimation of compensation. Selection of parameters was performed by using computers which was made searching much easy.

Determination of equation is given the value for activation energy $E_1 = 0.013\,\text{eV}$, acceptors $N_{a1} = 4.2 \cdot 10^{15}$ and donors $N_d = 3.6 \cdot 10^{15}\,\text{cm}^{-3}$ concentrations. Therefore the compensation degree of shallow acceptor level $K = N_d / N_{a1} = 0.86$. Obviously because of strong compensation the found value of shallow acceptor level activation energy $E_1 = E_0 + \varepsilon_3$, where E_0 is the energy of isolated acceptor, and ε_3 is the activation energy of hopping conductivity. On the basis of energy activation and carriers concentration values it is possible to determine the Bohr radius and the average distance between impurities.

Table 2. Main parameters of some samples studied.

N_{a1}, cm^{-3}	N_{a2}, cm^{-3}	N_d, cm^{-3}	K	E_1,eV	E_2,eV	a_L, Å	$N^{1/3}a$
$4.2 \cdot 10^{15}$	$6.0 \cdot 10^{16}$	$3.6 \cdot 10^{15}$	0.86	0.013	0.034	75	0.12

In case of big difference among masses asymptotic character of the wave functions in a long distances determines by the light holes, and because of it $a = a_L = \hbar / \sqrt{2m_L E}$, where $\hbar$ is the Plank's constant, $m_L = 0.052 m_0$ is the effective mass of the light hole. Table 2 shows some parameters of investigated samples. It is evident from these data that $N^{1/3}a << 1$. That means that

the average distance between impurities is considerably higher than the magnitude of the wave function, which is obligatory condition of the weak doping [9].

At the Fig. 4 there is shown the typical dependence of specific resistance from back temperature for undoped p-GaSb in temperature range of (3 – 77) K. At the Curve it is possible to underline two areas: I – in temperature range (3 – 10) K, which is relevant to hopping conductivity, and II – in temperature range (15 – 77) K, which is connecting with band-conductivity and ionization of energy levels $E_1 = 0.013$ and $E_2 = 0.034$ eV.

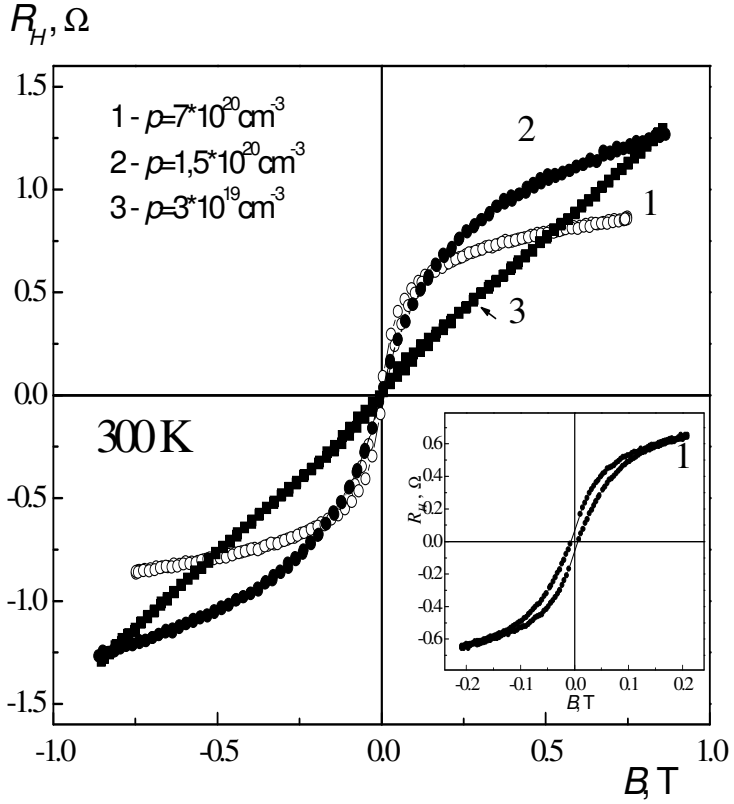

Fig. 4. Magnetic field dependences of Hall resistance for three GaMnSb samples with different hole concentration at room temperature: 1 – $p = 5 \cdot 10^{20}$, 2 – $1.5 \cdot 10^{20}$, 3 – $3 \cdot 10^{19}$ cm^{-3}. Curve numbers correspond to sample numbers.

Area I is possible to be described with the formula $\rho = \rho_3 \exp(\varepsilon_3 / kT)$, and by the curve inclination to determine activation energy of hopping conductivity ε_3. These values of ε_3 for investigate samples equal to 3.6 MeV, which is in good connection with activation energy calculated by theoretical formula for a strong compensation.

From Fig. 4 it is obvious that dependence $\ln\rho$ of $1/T$ in low temperatures case is linear which demonstrate existence of hopping conductivity with activation energy of constant. In condition of liner part of dependence extrapolation $\ln\rho = f(1/T)$ into infinity high temperature area $(1/T = 0)$, e.g. finding the crossing point of that line with coordinates, when $\rho = \rho_3 \exp(\varepsilon_3 / kT)$ it is possible to find out experimental value of $\ln\rho_3$. In Fig. 5 this point corresponds to 7.5 Ohm · cm. The value of ρ_3 exponentially depends on the impurity concentration and the Bohr orbital parameters – $\rho_3 = \rho_{03} \exp(1.73 / N^{1/3} a)$, where $\rho_{03} = 10^{-3}$ Ohm · cm and depends on the degree of the impurity concentration and distribution of the energy states. When $a = 75$ a=75 Å in above mentioned equation, for the impurity concentration we get that $N_{a1} = 4.2 \cdot 10^{15}$ cm^{-3}. As seen that value is equal to concentration value from electro-neutrality equation.

Taking into account non-ohmic character of conductivity in very small fields we studied also the influence of electrical field on the hopping conductivity in undoped p-GaSb. It was very interesting to investigate the area of very low fields, where the hopping conductivity was observed in the area of the Ohm's law. Propagation of the ohmic region is determined by crystal parameters characterizing mechanism of the hopping conductivity. High value of the resistivity of measured samples ($R > 10^9$ Ohm) created the problems during the measuring procedures. But method of measurement offered in our works, which provides complete excluding of the contact resistivity and is much more crimpstable, gave possibility to carry out experiments in the mV range fields.

At the $\ln\sigma = f(E)$ at 4.2 K in area of weak fields the ohmic conductivity takes place $\ln\sigma = const$, we have the parabolic region transferring to exponential dependence from electrical field $\ln\sigma \sim E$, and with mechanism of conductivity corresponding to $\ln\sigma \sim \sqrt{E}$ then. In case of strong electrical fields dependence $\sigma(E)$ becomes weaker, and the preleakage region starts.

When temperature decreased deviation from Ohm's law as well as transition from exponential dependence to $\ln\sigma \sim \sqrt{E}$ became in more weak fields and the inclination of exponential part of the curve is increasing.

In obtained dual phase ferromagnetic GaMnSb films, regardless to the case of previously studied single phase GaMnSb systems (Curie temperatures not exceeding 30 K), the anomalous Hall effect (AHE) and the AHE hysteresis character at temperatures up to 300 K, as stronger as more the hole concentration, has been observed. The unusual properties of GaMnSb films have been interpreted as interaction of magnetic nanoclusters in a semiconductor matrix, where the matrix has huge concentration of free holes and magnetic ions. The interaction seems to be caused by the potential Shottky barriers at the cluster / semiconductor interface sensitive to the holes concentration in the semiconductor matrix [10].

It is established, that in quantum-sized GaAs / $In_xGa_{1-x}As$ / GaAs-structures with δ-doped Mn layer in GaAs placed on optimum (≈ 3 nm) distance from the quantum well, the mobility of two-dimensional charge carriers in the quantum well reaches ≈ 2000 $cm^2 / V \cdot s$ that is more than order of value higher than the carrier mobility in the relevant 2D ferromagnetic structures. At that these structures in temperature dependences of conductivity show obvious ferromagnetic transition at temperatures about 30 K. It was revealed that the anomalous Hall effect takes place in quantum wells with the activation character of conductivity, but only in the limited interval of temperatures above and below the Curie temperature, whereas it is practically absent in quantum wells with the "quasi-metallic" conductivity. Inefficiency of the AHE usage to study magnetic ordering in semiconductor systems with high mobility of the current carriers has been shown. Obtained peculiarities in behavior of resistance, magnetoresistance and Hall effect are explained in terms of interaction of holes with magnetic ions of Mn taking into account fluctuations of their potential, transfer of holes across the percolation level of and the hopping conductivity.

Maximum at the obtained curve is connected with transfer from band-conductivity to hopping when the current carriers haven't enough energy for transition from impurity levels to conduction band, and current determines by the hopping of charge carriers directly without activation.

Theoretical approaches developed during the last decade present invaluable tools for studying the microscopic origins of ferromagnetism and predicting electronic, magnetic and structural ground state properties of magnetic semiconductors. It is necessary to underline that the local density approximation combined with disorder averaging coherent potential approximation is very useful for studying diluted magnetic semiconductors [11].

Models of the virtual crystal approximation have been used to study the influence of the impurity disorder on transport and magnetic properties of magnetic semiconductors. The Boltzmann equation with Born approximation for scattering rates provides the estimate of anisotropic magnetoresistance effect up to 12 %. The key for understanding kinetic and magnetic anisotropy effects is a strong spin–orbit coupling in the semiconductor valence band. The most striking feature in off-diagonal conductivity coefficients, in (GaMn)As is the large anomalous Hall effect (AHE),

which occurs due to the spin–orbit interaction. In metals, standard assumption is that AHE arises due to spin–orbit coupling component in the interaction between band quasi-particles and crystal defects, which can lead to the so called skew scattering with the Hall resistivity contribution proportional to the diagonal resistivity [12]. For diluted magnetic semiconductors, AHE is based on the spin–orbit coupling in the Hamiltonian of the ideal crystal and implies the finite Hall conductivity even without the disorder. More detailed studies of the disorder will combine Kondo description of the spin interactions as well as relevant Monte Carlo techniques applied to both metallic and insulating conditions. The model problem concerning the formation of a ferromagnetic cluster (magnetic polaron) consisting of the free electron bound to a non-magnetic donor impurity in an antiferromagnetic matrix was analyzed. The analysis was performed in the framework of two- and three-dimensional Kondo-lattice models in the double exchange limit. The bound electron forms a ferromagnetic core of the size on the order of the electron localization length.

The studies of the structure of magnetic polarons (nanoscale ferromagnetic droplets) in magnetic semiconductors were performed with a special emphasis to frustrated lattices (square lattice with nearest-neighbor and diagonal interactions and the triangular lattice) characteristic for layered heterostructures. Magnetic polaron can produce rather extended spin distortions of the antiferromagnetic background around its ferromagnetic core. In a wide range of distances r from the core these distortions decay as $1/r^4$ for cubic lattice and as $1/r^2$ for square lattice. On triangular lattice, spin distortions decay slower (as $1/r$) because of strong geometrical frustration of the lattice. The characteristic size of this 'coat' decreases for stronger next-nearest neighbor interaction or with increase of magnetic anisotropy.

It was found that there also exists a solution corresponding to rather long-range extended spin distortions of the antiferromagnetic background around the ferromagnetic core. The frustrations lead to a slower decay of these distortions in comparison to magnetic polarons for the lattices without the frustrations. For doped anisotropic antiferromagnets, it was shown that the most favorable shape of a magnetic polaron corresponds to an ellipse in the two dimensional case and to an ellipsoid in the three dimensional case.

Such a magnetic polaron state can be favorable in energy in comparison to usually considered one (saturated core without extended distortions) [13].

The situation with the indirect interactions of different kinds of charge carriers giving rise to an inhomogeneous charge distribution was analyzed. The analysis was based on the two-band Hubbard model in the limit of strong on-site Coulomb repulsion. It was shown that such a system has a tendency to phase separation into the regions with different charge densities and exists even in the absence of magnetic or any other ordering, if the ratio of the bandwidths is large enough. Analytical results have been obtained in the framework of the generalized mean-field theory for diluted semiconductors with RKKY interaction. That theory accounts for the non-equivalency of different lattice sites by introducing the distribution function of local effective magnetic fields for non-regular (random) systems with magnetic interaction. The procedure is described that permits to deduce the analytical expression for that function. Space distribution of magnetization there is describing by nonlinear integrate equation. Its solution determines the radial distribution of magnetization, which is not only inhomogeneous but also significantly non-monotonous. The concrete appearance of this distribution is depending of wire's radius, longitude of interaction, and concentration of magnetic impurities and free carriers as well.

For analysis of the possibilities of charge carriers' inhomogeneous distribution in highly correlated electronic systems with two types of conductivity the two bands Hubbard model was used with special emphasis on situation familiar for cooperate superconductors. Exfoliation on phases responding to charge density is characterizing of such kind systems because of redistribution of charge carriers among energy bands. This mechanism doesn't include any magnetic interactions on interstitial Coulomb's repulsion. Hybridization of energy bands is followed to establishment of pick of density of electron states, and Fermi level of one of phases is situated near by of that pick.

Appeared redistribution of charge density might influences on dependence of critical temperature T_c of superconductivity transition from doping level.

In the framework of two-dimensional Ising model the mechanisms of inhomogeneous cluster states formation with competitive interaction between nearest diagonal neighbors were investigated. The model was observed by different methods including precise diagonalization for small clusters, method of transfer-matrix, and modeling by Monte Carlo method for big size lattices. The full phase diagram prepared by these computations includes besides ordinary antiferromagnetic Ising and Stripe phases, the glass type phase, which is characterizing by complicate interclusteral interactions [14].

Conditions of establishing the ferromagnetic state and its parameters in quasi-two-dimensional semiconductor systems with magnetic impurities coupled via RKKY interaction have been studied, and two new important factors have been included in the consideration: allowing for the spatial disarray of interacting magnetic impurities, and the temperature dependence of the carrier degeneracy [15]. Both factors complicate transition of the system into ferromagnetic state: disorder of the impurities arrangement reduces the Curie temperature (as compared to the regular system) while lifting the degeneracy of carriers makes the Curie temperature finite even in the extreme case of the infinitely strong interaction. Besides, the concentration dependence of the transition temperature is non-monotone and there is the threshold of the interaction strength to drive the system into ferromagnetic state.

ACKNOWLEDGMENTS

Let me express my great appreciation to colleagues from: Georgian Technical University, Professors – D. Aladashvili, E. Kutelia, T. Dadiani; Russian Research Center “Kurchatov Institute”, Professors – S. Yakimov, E. Meilikhov, B. Aronzon, A. Lagutin; Nizhnij Novgorod University Physics-Technology Institute, Doctors – V. Podolskij, E. Dimidov, and many others who in the framework of the ISTC granted project G 1335 performed unusual experimental and theoretical works for spinelectronics development.

REFERENCES

1. P. Kervalishvili. In: European Nano Systems’06. Paris, 145 (2006).
2. M.A. Chuev, I.A. Subbotin, E.M. Pashaev, V.V. Kvardakov, I.A. Lihachyov, A.E. Golovanov, P.G. Medvedev, V.V. Podolskij, V.P. Lesnikov. In: Mat. XI Int. Symp. “The Nanophysics and Nanoelectronics – 2007”. Nizhnij Novgorod: IPM RAS, 247 (2007).
3. B.N. Zvonkov, F.Z. Guilmutdinov, O.V. Vikhrova, Yu.A. Danilov, Yu.N. Drozdov. In: Proc. Int. Sci. Conf. “75 Years for Udmurtiya High School”. Izhevsk, **2** (Nat. Sci.), 52 (2007).
4. P. Kervalishvili, A. Lagutin. Microelectr. J., **39**, 1060 (2008).
5. O.V. Vikhrova, Yu.A. Danilov, Yu.N. Drozdov, B.N. Zvonkov, F. Iikawa, M.J.S.P. Brasil. Surface: X-Ray, Synchrot. & Neutr. Investig., **2**, 9 (2007).
6. V.V. Rylkov, B.A. Aronzon, A.B. Granovskij. In: Coll. Papers XX Int. School-Seminar “New magnetic materials of microelectronics”. Moscow, 523 (2006).
7. B.A. Aronzon, V.A. Kulbachinskij, P.V. Gurin, A.B. Davydov, V.V. Rylkov, A.B. Granovskij, O.V. Vikhrova, Yu.A. Danilov, B.N. Zvonkov, Y. Horikoshi, K. Onomitsu. JETP Lett., **85**, 27 (2007).
8. P. Kervalishvili. Rev. Adv. Mat. Sci., **14**, 14 (2007).

9. B.A. Aronzon. In: XVI Ural Int. Winter School on Physics of Semiconductors (Program and Theses of Reports). Ekaterinburg, 77 (2006).
10. N. Nikolaev, M.E. Dokukin, V.V. Rylkov, A.V. Sitnikov. Radioengin. Electr., **52**, 1 (2007).
11. S.L. Ogarkov, M.Yu. Kagan, A.O. Sboychakov, A.L. Rakhmanov, K.I. Kugel. Phys. Rev. B, **74**, 014436 (2006).
12. E.Z. Meilikhov. Phys. Rev. B, **75**, 045204 (2007).
13. P.J. Kervalishvili. In: 6th Japanese–Mediterranean Workshop on Applied Electromagnetic Engineering for Magnetic, Superconducting and Nanomaterials. Bucharest: Politechnica University of Bucharest, **45**, 15 (2009).
14. A. O'Hare, F.V. Kusmartsev, K.I. Kugel, M.S. Laad. Phys. Rev. B, **76**, 064528 (2007).
15. E.Z. Meilikhov, R.M. Farzetdinova. Phys. Rev. B, **74**, 125204 (2006).

ГЕОМЕТРИИ МНОГОСТЕННЫХ НАНОТРУБОК И МНОГООБОЛОЧНЫХ ФУЛЛЕРЕНОВ НИТРИДА БОРА

Л. Чхартишвили, Т. Берберашвили

Грузинский технический университет
chkharti2003@yahoo.com

Принята 28 января 2010 года

1. ВВЕДЕНИЕ

Нанотрубный и фуллеренный нитриды бора BN считаются весьма перспективными материаламы с точки зрения их применений во многих областях техники. Эти возможности, а также о способы получения подобных наносистем, нами были уже описаны во вводных частях работ [1] и [2], соответственно. Здесь же отметим лишь две недавные работы. Во-первых, оказалось [3], что под воздействиием концентрированной световой энергии порошки мелкозернистого слоистого кристалла нитрида бора в потоке азота можно превратить в химически чистую и структурно-совершенную наноструктуру, включающую и многостенные нанотрубки. Во-вторых, методом конденсации из пара в герметизированной камере без катализатора в значительных объемах были выращены длинные одно- и многостенные нанотрубки нитрида бора малого радиуса [4], из которых удалось получить пряжу нити макроскопических размеров (~ 1 cm в длину).

Наносистемы нитрида бора, как правило, представляют собой структуры, составленные из атомных слоев, в которых межслоевые расстояния близки к наблюдаемым в слойстых кристаллах гексагонального h-BN, ромбоэдрического r-BN и турбостратного t-BN нитридов бора. Но порядок их упаковки отчасти оказывается отличным. Если для уединенных нанотрубки или фуллерена относительную стабильность можно оценить с помощью расчетов молярных энергий связывания (см., например, [5]), то в случае многослойных наноструктур решение аналогичной задачи требует, чтобы наряду с энергетическим был учтен и геометрический фактор.

Целью настоящей работы является построение последовательности слоев в многостенных нантрубках и многоболочных фуллеренах нитрида бора по заданным значениям их внутренних или внешних радиусов. При этом мы будем основываться на ранее предложенные геометрические модели регулярных нанотрубок и регулярных фуллеренов нитрида бора [1,2,6].

2. АССОЦИАЦИИ УЕДИНЕННЫХ НАНОТРУБОК В МНОГОСТЕННЫХ НАНОТРУБКАХ

Согласно модели одностенной регулярной нанотрубки нитрида бора [1,6], (1) все атомные узлы лежат на одной и той же круговой цилиндрической поверхности; (2) атомы бора B и атомы азота N поочередно занимают вершины правильных шестиугольников, плоскости которых изломаны вдоль параллельных цилиндрической оси сторон и / или диагоналей; (3) длины всех B–N связей (вне зависимости от их ориентации относительно оси) равны.

Из перечисленных условий, которые с приемлемой точностью удовлетворяются реальными нанотрубками нитрида бора, вытекает, что регулярными следует считать лишь нехиральные нанотрубки – зигзагная $(n,0)$ и кресловидная (n,n), где индекс n принимает натуральные значения: $n = 1,2,3,\ldots$. Анализ состава элементарных ячеек одномерных кристал-

лов нехиральных нанотрубок обоих типов ведет к химической формуле $B_{2n}N_{2n}$. В этих структурах плоскости 6-членных атомных колец оказываются изломанными соответственно вдоль B–N связей и диагоналов, соединяющих разноименные атомные узлы, и диагоналов, соединяющих одноименные атомные узлы. Что же касается хиральной нанотрубки (*n*,*m*), где дополнительный индекс m при фиксированной величине n может принимать значения $m = 0,1,2,...,n$, то ее получение из плоского гексагонального «листа» нитрида бора его сворачиванием в цилиндр невозможно, по крайней мере, без искажений валентных углов.

Для радиусов регулярных, т.е. зигзагных и кресловидных, нанотрубок нитрида бора, $r_{(n,0)}$ и $r_{(n,n)}$, ранее были получены формулы

$$\frac{r_{(n,0)}}{d_{(n,0)}} = \frac{\sqrt{3}}{4\sin\dfrac{\pi}{2n}}, \tag{1}$$

$$\frac{r_{(n,n)}}{d_{(n,n)}} = \frac{\sqrt{5+4\cos\dfrac{\pi}{2n}}}{4\sin\dfrac{\pi}{2n}}, \tag{2}$$

в которых $d_{(n,0)}$ и $d_{(n,n)}$ соответственно являются длинами B–N связей в зигзагной и кресловидной нанотрубках.

Известно, что радиус хиральной нанотрубки $r_{(n,m)}$ всегда лежит между радиусами нехиральных нанотрубок с тем же индексом n: $r_{(n,0)} \le r_{(n,m)} \le r_{(n,n)}$. При этом величина $r_{(n,m)}$ монотонно возрастает с увеличением индекса m. Принимая во внимание данные обстоятельства, по формулам (1) и (2) можно построить интерполяционную формулу, определяющую радиус хиральной нанотрубки:

$$\frac{r_{(n,m)}}{d_{(n,m)}} \approx \frac{\sqrt{3+\dfrac{2m}{n}\left(1+\cos\dfrac{\pi}{2n}\right)}}{4\sin\dfrac{\pi}{2n}}, \tag{3}$$

где $d_{(n,m)}$ – длина B–N связей в хиральной нантрубке (*n*,*m*). Этот параметр и в рамках предложенного обобщения модели регулярной нанотрубки предполагается независимой от ориентации связи относительно оси цилиндрической трубки. Таким образом все хиральные искажения мы относим за счет отклонений атомных шестиугольников от правильной формы. Легко можно убедиться в том, что подстановками $m = 0$ и $m = n$ интерполяционная формула (3) точно переходит в формулы (1) и (2), соответствующие зигзагным и кресловидным нанотрубкам.

Выращиваемые на практике нанотрубки BN, за редкими исключениями, большие – характеризуются высокими значениями индекса n. По этой причине целесообразно отдельно представить асимптотики формул (1–3) при $n >> 1$:

$$\frac{r_{(n,0)}}{d_{(n,0)}} \approx \frac{\sqrt{3}\,n}{2\pi}, \tag{4}$$

$$\frac{r_{(n,n)}}{d_{(n,n)}} \approx \frac{3n}{2\pi}, \tag{5}$$

$$\frac{r_{(n,m)}}{d_{(n,m)}} \approx \frac{\sqrt{3n(n+2m)}}{2\pi}, \tag{6}$$

Поскольку длины B–N связей в реальных нанотрубках нитрида бора слабо зависят от индексов, то на основании выражений (4) и (5) приходим к заключению, что при больших n радиусы нехиральных нанотрубок обоих типов должны возрастать приблизительно линейно, образовывая две арифметические прогрессии.

Что же касается асимптотической форме (6) предложенного выше выражения для радиусов хиралных нанотрубок, она также приводит к интересным выводам. Во-первых, большие ($n >> 1$) хиральные нанотрубки с относительно невысокими значениями индекса m (подразумевается, что $2m/n << 1$) должны быть по своим радиусам практически неразличимыми друг от друга и от соответствующей зигзагной нанотрубки (n,0). Во-вторых, с хорошей точностью должны совпадать радиусы и тех хиральных нанотрубок, для которых совпадают произведения целых чисел $n(n+2m)$, образуемые их индексами. Таким образом, среди возможных нанотрубок BN при $n >> 1$ имеется ряд групп отдельных образцов с различными хиральностьями, но почти с одинаковыми радиусами.

Данный результат анализа геометрий нанотрубок нитрида бора приводит к мысли, что в длинных нанотрубках, тем более в изогнутых и / или разветвленных, вполне возможно чередование различных нанотрубок приближенно равных радиусов, соединенных с помощью переходных дефектных областей больших или меньших размеров. Отметим, что подобная картина действительно характерна для продуктов ряда технологических процессов роста нанотрубок нитрида бора.

Таблица 1. Радиусы одностенных нанотрубок нитрида бора, Å.

(n,m)	$r_{(n,m)}$	(n,m)	$r_{(n,m)}$	(n,m)	$r_{(n,m)}$	(n,m)	$r_{(n,m)}$	(n,m)	$r_{(n,m)}$
(1,0)	0.6260	(5,3)	2.9779	(7,5)	4.3625	(11,3)	5.4618	(14,2)	6.3368
(1,1)	0.8082	(6,2)	3.1083	(10,1)	4.3807	(9,6)	5.4908	(11,6)	6.3493
(2,0)	0.8853	(7,1)	3.1840	(11,0)	4.3987	(12,2)	5.5340	(15,1)	6.3743
(2,1)	1.1893	(8,0)	3.2088	(8,4)	4.5234	(8,8)	5.5340	(16,0)	6.3867
(3,0)	1.2520	(5,4)	3.2335	(7,6)	4.6103	(13,1)	5.5769	(10,8)	6.4363
(2,2)	1.4301	(6,3)	3.4011	(9,3)	4.6446	(14,0)	5.5911	(12,5)	6.4854
(3,1)	1.5872	(5,5)	3.4704	(10,2)	4.7293	(10,5)	5.6477	(13,4)	6.5947
(4,0)	1.6358	(7,2)	3.5159	(11,1)	4.7794	(9,7)	5.7452	(11,7)	6.6187
(3,2)	1.8630	(8,1)	3.5830	(12,0)	4.7960	(11,4)	5.7728	(14,3)	6.6785
(4,1)	1.9865	(9,0)	3.6050	(8,5)	4.7961	(12,3)	5.8683	(10,9)	6.6785
(5,0)	2.0258	(6,4)	3.6706	(7,7)	4.8455	(10,6)	5.9222	(15,2)	6.7377
(3,3)	2.1038	(7,3)	3.8190	(9,4)	4.9428	(13,2)	5.9356	(16,1)	6.7729
(4,2)	2.2839	(8,2)	3.9216	(10,3)	5.0540	(14,1)	5.9756	(12,6)	6.7729
(5,1)	2.3859	(6,5)	3.9216	(8,6)	5.0540	(15,0)	5.9889	(17,0)	6.7846
(6,0)	2.4187	(9,1)	3.9818	(11,2)	5.1320	(9,8)	5.9889	(11,8)	6.8776
(4,3)	2.5468	(10,0)	4.0017	(12,1)	5.1782	(11,5)	6.0679	(13,5)	6.9007
(5,2)	2.6981	(7,4)	4.0998	(13,0)	5.1935	(12,4)	6.1846	(10,10)	6,9122
(6,1)	2.7849	(6,6)	4.1575	(9,5)	5.2240	(10,7)	6.1846	(14,14)	7.0035
(4,4)	2.7850	(8,3)	4.2332	(8,7)	5.2995	(9,9)	6.2230	(12,7)	7.0487
(7,0)	2.8133	(9,2)	4.3260	(10,4)	5.3591	(13,3)	6.2738	(15,3)	7.0824

Полагая, что длины B–N связей в любой нанотрубке близки к измеренному значению 1.4457 Å [7] длины внутрислоевых связей в реальном слойстом кристалле гексагонального

нитрида бора h-BN, нами по формуле (3) были рассчитаны радиусы всевозможных одностенных нанотрубок BN с индексом n в интервале от 1 до 75 включительно. Часть результатов (для 100 наиболее малых нанотрубок) представлены в Таблице 1, где эти нанотрубки расположены в порядке возрастания радиуса. Отсюда действительно становится очевидным наличие ряда групп образцов с почти одинаковыми радиусами.

Таблица 2. Структуры многостенных нанотрубок нитрида бора и относительные отклонения межстенных расстояний от межслоевых – в слойстом кристалле.

(1,0)	@ 0.76 %	(9,1)	@ 0.05 %	(14,5)	@ 0.09 %	(23,4)	@ 0.44 %	(28,8)	@ 0.31 %	(31,15)
(1,1)	@ 0.56 %	(6,6)	@ 1.52 %	(17,2)	@ 1.09 %	(22,6)	@ 0.13 %	(22,18)	@ 0.12 %	(36,9)
(2,0)	@ 0.52 %	(8,3)	@ 0.19 %	(18,1)	@ 0.14 %	(22,6)	@ 0.13 %	(22,18)	@ 0.12 %	(36,9)
(2,1)	@ 0.11 %	(8,4)	@ 0.10 %	(17,3)	@ 0.06 %	(22,7)	@ 0.09 %	(31,6)	@ 0.23 %	(31,17)
(3,0)	@ 0.83 %	(7,6)	@ 0.84 %	(19,1)	@ 0.41 %	(23,6)	@ 0.44 %	(26,13)	@ 0.45 %	(34,13)
(2,2)	@ 0.56 %	(11,1)	@ 0.80 %	(16,5)	@ 0.19 %	(18,14)	@ 0.16 %	(30,8)	@ 0.14 %	(28,23)

Далее, основываясь на эти значения были построены многостенные, а именно, 6-стенные, нанотрубки, в которых в качестве внутренней стенки служили 6 самых маленьких нанотрубок, а разности радиусов соседных нанотрубок, т.е. межстенные расстояния, чуть превосходили экспериментальное значение 3.3306 Å [7] межслоевых расстояний в слойстом кристалле h-BN. Структуры этих нанотрубок представлены в Таблице 2 совместно с относительными отклонениями предсказываемых расстояний между соседными стенами многостенной нанотрубки нитрида бора от межслоевого расстояния в трехмерных кристаллах этого же вещества. Из-за многовариантности значений радиусов уединенных нанотрубок указанные отклонения в большинстве случаев очень малы. Остающийся расхождения в многостенных нанотрубках должны компенсироваться сплющиванием соседных нанотрубок во взаимоперпедикулярных направлениях и / или взаимным отклонением осей соседных нанотрубок. Благодаря указанным эффектам определенные части соседных нанотрубок окажутся на равновесное расстояние, которое благоприятствует образованию межслоевой связи.

3. АССОЦИАЦИИ УЕДИНЕННЫХ ФУЛЛЕРЕНОВ В МНОГООБОЛОЧНЫХ ФУЛЛЕРЕНАХ

Понятие однооболочного регулярного фуллерена нитрида бора было предложено в работах [2,6]. Согласно соответствующей модели, (1) все атомные узлы располагаются на одной и той же сферической поверхности; (2) структура содержит равные количества атомов B и N; (3) координационное число любого узла равно 3; (4) все атомные кольца являются правильными многоугольниками с четными числом вершин (теперь уже необязательно только шестиугольниками), которых поочередно занимают атомы B и N. Подобное определение ведет к химической формуле регулярного фуллерена $B_{2n(n+1)}N_{2n(n+1)}$, где $n = 1,2,3,...$ – его индекс, и к равенству длин всех B–N связей в нем.

Удается построение схемы аналитического вывода зависимости радиуса фуллерена $r_{(n)}$ от длины B–N связей $d_{(n)}$ и индекса n. В частности, когда указанный индекс совпадает с целой степенью 2, $n = 2^0, 2^1, 2^2, ...$ (т.е. для фуллеренов B_4N_4, $B_{12}N_{12}$, $B_{24}N_{24}$ и т.д.), соседние «меридианные» атомные плоскости в «северном» и «южном» полушариях сливаются друг с другом в «экваторяльной» плоскости, что позволяет получить явное выражения для радиуса фуллерена:

$$\frac{r_{(n)}^2}{d_{(n)}^2} = \frac{1}{\sin^2 \pi/2n}\left(\frac{3}{4} + \frac{\cos \pi/2n}{\sqrt{2}}\right). \tag{7}$$

Как и в случае регулярных нанотрубок, при большом индексе, $n >> 1$, радиус регулярного фуллерена нитрида бора оказывается приближенно пропорциональной индексу:

$$\frac{r_{(n)}}{d_{(n)}} \approx \frac{\sqrt{3+2\sqrt{2}}\, n}{\pi}. \tag{8}$$

Простота формы этого выражения позволяет предположить, что асимптотика, полученная для дискретных значений индекса ($n = 2^0, 2^1, 2^2, ...$), окажется верной и в общем случае. Следовательно, радиусы больших регулярных фуллеренов нитрида бора с хорошей точностью должны образовывать арифметическую прогрессию.

Таблица 3. Радиусы однооболочных фуллеренов нитрида бора, Å.

(n)	$r_{(n)}$	(n)	$r_{(n)}$	(n)	$r_{(n)}$	(n)	$r_{(n)}$	(n)	$r_{(n)}$
(1)	1.2520	(11)	12.2320	(21)	23.3364	(31)	34.4442	(41)	45.5530
(2)	2.2859	(12)	13.3421	(22)	24.4471	(32)	35.5551	(42)	46.6639
(3)	3.3749	(13)	14.4522	(23)	25.5578	(33)	36.6659	(43)	47.7748
(4)	4.4752	(14)	15.5625	(24)	26.6686	(34)	37.7768	(44)	48.8857
(5)	5.5798	(15)	16.6729	(25)	27.7793	(35)	38.8877	(45)	49.9966
(6)	6.6866	(16)	17.7834	(26)	28.8901	(36)	39.9985	(46)	51.1075
(7)	7.7946	(17)	18.8939	(27)	30.0009	(37)	41.1094	(47)	52.2184
(8)	8.9034	(18)	20.0045	(28)	31.1117	(38)	42.2203	(48)	53.3294
(9)	10.0126	(19)	21.1151	(29)	32.2225	(39)	43.3312	(49)	54.4403
(10)	11.1222	(20)	22.2257	(30)	33.3334	(40)	44.4421	(50)	55.5512

Интерполируя формулу (7) таким образом, чтобы она охватывала все допустимые значения n, в том числе и малые, намы были расчитаны радиусы всевозможных (т.е. не только регулярных) фуллеренов нитрида бора вплоть до индекса $n = 50$. При этом, как и в случае нанотрубок, предполагалось, что длина B–N связей практически не зависит от индекса и приближенно совпадает с длиной внутрислоевых связей 1.4457 Å в слойстых кристаллах этого вещества. Результаты представлены в Таблице 3, где фуллерены перечислены в порядке возрастания размеров. Разумеется, из-за единственности индекса n этот порядок совпадает с его ростом.

Затем из них мы построили многооболочные, а именно 7-оболочные, фуллерены нитрида бора, в которых в качестве внутренней оболочки служили 7 самых малых регулярных фуллеренов, а разности радиусов соседных фуллеренов, т.е. межоболочные расстояния, чуть превосходили экспериментальное значение 3.3306 Å межслоевых расстояний в слойстых кристаллах BN. Эти малые расхождения могут быть скомпенсированы сплющиванем фуллеренов во взаимоперпендикулярных направлениях и / или взаимным отклоненем их полярных осей. Предсказанные таком образом структуры показаны в Таблице 4.

Таблица 4. Структуры многооболочных феллеренов нитрида бора и относительные отклонения межоболочных расстояний от межслоевых – в слоийстом кристалле.

(1)	@ 29.94 %	(5)	@ 33.09 %	(9)	@ 33.30 %	(13)	@ 0.02 %	(16)	@ 0.03 %	(19)	@ 0.04 %	(22)
(2)	@ 32.13 %	(6)	@ 33.18 %	(10)	@ 33.32 %	(14)	@ 0.02 %	(17)	@ 0.04 %	(20)	@ 0.05 %	(23)
(3)	@ 32.70 %	(7)	@ 33.23 %	(11)	@ 33.34 %	(15)	@ 0.03 %	(18)	@ 0.04 %	(21)	@ 0.05 %	(24)
(4)	@ 32.96 %	(8)	@ 33.27 %	(12)	@ 0.01 %	(15)	@ 0.03 %	(18)	@ 0.04 %	(21)	@ 0.05 %	(24)
(5)	@ 33.09 %	(9)	@ 33.30 %	(13)	@ 0.01 %	(16)	@ 0.03 %	(19)	@ 0.04 %	(22)	@ 0.05 %	(25)
(6)	@ 33.18 %	(10)	@ 33.32 %	(14)	@ 0.02 %	(17)	@ 0.04 %	(20)	@ 0.05 %	(23)	@ 0.05 %	(26)
(7)	@ 33.23 %	(11)	@ 33.34 %	(15)	@ 0.03 %	(18)	@ 0.04 %	(21)	@ 0.05 %	(24)	@ 0.05 %	(27)

Как видно из этой таблицы при больших n обнаруживаются определенные тенденции: разность индексов регулярных фуллеренов, образующих соседние оболочки, всегда составляет 3, а относительные отклонения разностей радиусов от ожидаемого межслоевого расстояния чрезвычайно малы. Объяснение заключается в том, что при $n >> 1$ эти разности составляют $r_{(n+3)} - r_{(n)} \approx 3\sqrt{3+2\sqrt{2}}\, d_{(n)} / \pi$. Откуда подстановкой вместо $d_{(n)}$ величины 1.4457 Å получим $r_{(n+3)} - r_{(n)} \approx 3.3329$ Å, что очень мало отличается от 3.3306 Å. Подобное, на

первый взгляд, неожиданное совпадение кажется неслучайным. Может быть, в выведенной формуле радиуса регулярного фуллерена нитрида бора проявляется некоторое общее соотношение между внутри- и межслоевыми параметрами a и c всех слоистых структур нитрида бора $c/a = 2\sqrt{3(3+2\sqrt{2})}/\pi \approx 2.6621$. Для сравнения заметим, что экспериментальное значение этого же отношения в реальных кристаллах равно 2.6602.

4. ЗАКЛЮЧЕНИЕ

Подытоживая полученные результаты, в первую очередь следует отметить возможность довольно точного представления пространственных структур слойстых наносистем нитрида в рамках простых геометрических моделей. Анализ моделей регулярных одностенных цилиндрических нанотрубок и регулярных однооболочных сферических фуллеренов нитрида бора, построенных из атомных колец в форме плоских или изломанных по сторонам и диагоналам правильных многоугольников с четным числом вершин, позволяет введение интерполяционных формул, которые аналитически определяют радиусы отдельных стенок или оболочек, как функций индексов наносистем и длины внутрислоевых связей. С одной стороны, исключительное многообразие значений радиусов больших хиральных нанорубок, а с другой стороны, чрезвычайная близость к равновесному межслоевому расстоянию разностей радиусов пар больших фуллеренов с отличающимися на 3 индексами, наглядно объясняют легкость образования многослойных наносистем нитрида бора.

БЛАГОДАРНОСТЬ

Авторы благодарны Национальному научному фонду Грузии (ННФГ) за поддержку работы через проект GNSF/ST08/4-411.

ССЫЛКИ

1. Л.С. Чхартишвили Л.С. В сб.: Доклады Харьковской нанотехнологической ассамблеи – 2006. Т. 2: Тонкие пленки в оптике и наноэлектронике. Харьков: ННЦ «ХФТИ» – ИПП «Контраст», 367 (2006).
2. Л.С. Чхартишвили. В сб.: Доклады Харьковской нанотехнологической ассамблеи – 2008. Т. 2: Наночастицы и наноструктурные функциональные покрытия. Объемные наноматериалы. Харьков: ННЦ «ХФТИ», 23 (2008).
3. L.L. Sartinska, A.A. Frolov, A.Yu. Koval', N.A. Danilenko, I.I. Timofeeva, B.M. Rud'. Mat. Chem. Phys., **109**, 20 (2008).
4. M.W. Smith, K.C. Jordan, Ch. Park, J.-W. Kim, P.T. Lillehei, R. Crooks, J.S. Harrison. Nanotechnol., **20**, 505604 (2009).
5. Л.С. Чхартишвили. Наноструктур. материаловед., **1**, 33 (2009).
6. L. Chkhartishvili. J. Phys.: Conf. Ser., **176**, 012014 (2009).
7. Ю.Б. Кузьма, Н.Ф. Чабан. Двойные и тройные системы, содержащие бор: Справочник. Москва: Металлургия (1990).

НАНОКРИСТАЛЛИЧЕСКИЕ ТВЕРДЫЕ СПЛАВЫ НА ОСНОВЕ КАРБИДА ТИТАНА: ПОЛУЧЕНИЕ И КОМПАКТИРОВАНИЕ

А.А. Гачечиладзе [1], А.Г. Микеладзе [1], Д.Л. Габуния [1], Б.Г. Маргиев [1], Р.В. Чедия [2], Т.А. Цуладзе [1], Р.К. Зекалашвили [1], О.А. Цагарейшвили [1]

[1] Институт металлургии и материаловедения им. Ф. Тавадзе
archilgachechiladze@gmail.ru
[2] Институт физической и органической химии им. П. Меликишвили
Chedia@yahoo.com

Принята 29 января 2010 года

Твердые сплавы на основе карбидов вольфрама и титана, полученные традиционными технологическими методами являются объектами широкого промышленного использования [1–6]. Они успешно применяются в машиностроении, ракетостроении, самолетостроении, в атомной энергетике. Поэтому повышение эксплуатационных параметров твердосплавных изделий является важной задачей материаловедения. Однако резервы дальнейшего повышения свойств твердых сплавов традиционными способами практически исчерпали себя. Реальным путем улучшения их служебных характеристик является создание нанокристаллических систем, в которых размер частиц не превышают 50 nm. Свойства таких материалов качественно отличаются от свойств тех же материалов в крупнокристаллическом состоянии.

В этой связи создание твердых сплавов с нанокристаллической структурой является весьма важной задачей. Нанокристаллическая структура дает возможность существенно повысить износостойкие, абразивные и жаростойкие свойства твердых сплавов при сохранении их ударной вязкости и удовлетворительной пластичности.

В настоящее время существует несколько способов получения нанокристаллических систем. Распространенным методом является механический помол шихты в высокоэнергетических аттриторах (т.н. механохимическая активация). Недостатком этого способа является: малая производительность, загрязнение шихты кислородом и материалом аттритора и увеличение контакта абразивных составляющих.

Сравнительно хорошие результаты были получены способом химического синтезирования водных растворов солей вольфрама и кобальта [7]. Карбидизация высушенных смесей производилась в контроллируемой атмосфере CO / CO_2, CO / Ar или CO / H_2. Однако этот способ не приемлем к титановой шихте из-за высокого сродства титана и кислорода. Водные растворы способствуют появлению Ti – O связей и последующий пиролиз в восстановительной среде всегда заканчивается образованием TiO_2.

Лазерные и плазменные методы производства нанокристаллических материалов энергоемкие, дорогостоящие и малопроизводительные. Поэтому применение этих методов оправдано лишь в специфических условиях.

Методы получения нанокристаллического карбида титана описаны в американских патентах US 3812239 и US 4662215. По первому из них карбидообразование происходит при взаимодействии паров галогенида титана и углеводорода. Процесс протекает в реакторе с температурной зоной (150 – 200) °C при поддержке вспомогательного газа. Согласно второго, карбид титана образуется после пиролиза продукта, полученного при взаимодействии органотитаната и полимера. В обоих методах трудности возникнают при введении в состав реагентов дополнительных соединений для получения твердых сплавов на базе карбида титана. Аморфные титанокарбидные материалы получают также после пиролиза тетрабензола

титана $Ti(CH_2PH)_4$. Однако эти материалы содержат значительное количество свободного углерода, что отрицательно влияет на качество карбида титана и твердых сплавов на его основе.

Представляло интерес разработка нанокристаллических композиционных сплавов нового типа со структурными особенностями, где металл переходит в керамику с непрерывным изменением структуры, морфологии и свойств, что предотвращает возникновение внутренних напряжений и тем самым создаются условия сочетания жаропрочных, жаростойких, износостойких свойств керамики с пластичностью вязкостью металла. Это позволит увеличить рабочий ресурс изделий и температурный интервал эксплуатации. Появится возможность создания нового поколения этих материалов.

С учетом указанных обстоятельств была предпринята попытка разработать метод получения нанокристаллических порошков карбида титана с цементирующим металломсвязкой и технологию их компактирования для получения образцов и изделий, пригодных для исследования служебных характеристик и конкретного применения.

В настоящей работе приводится результаты исследовании по получению твердых сплавов на основе карбида титана методом химического синтезирования с использованием в качестве реагентов гидридных соединений титана, карбидообразующих и цементирующих компонентов. В качестве цементирующего металла выбран никель, так как известно, что в ряду металлов Fe, Co, Ni, никель в большей степени смачивает карбид титана [8,9].

С целью определения возможности образования различных фаз, температурных и концентрационных границ их существования был проведен термодинамический анализ тройной системы (Ti – C) – Ni (10 %).

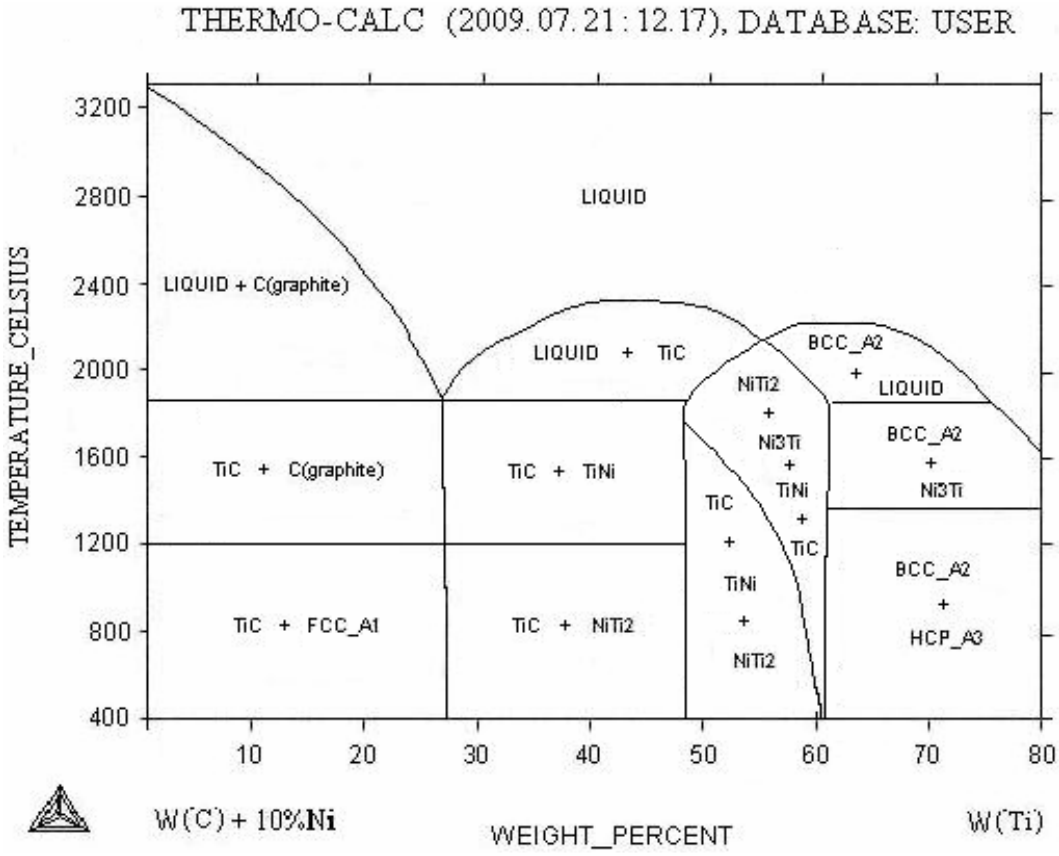

Рис. 1. Расчетная равновесная диаграмма системы (Ti – C) – Ni (10 %).

Для расчета энергии образования сплавов и фаз в указанной системе была использована база данных программы Thermo-Calc. Расчетная равновесия диаграмма системы (Ti – C) – Ni (10 %) представлена на рис. 1.

Из возможных соединении, образованных в указанной системе, следует отметить существования TiC и TiNi в широком концентрационном интервале, (28 – 48) wt. %.

Карбид титана получали при температуре (850 – 950) °C с использованием таких карбидообразующих реагентов как сажа, графит, пар органических соединении а также смесь паров CO, H_2, CH_4. Для синтеза использовали титан и гидрид титана. Титан получали нагревом гидрида титана при температуре 800 °C. Использование гидрида титана для получения TiC перспективно, т.к. при карбидизации он регенерирует необходимый для карбидизации порошок активного титана и водород.

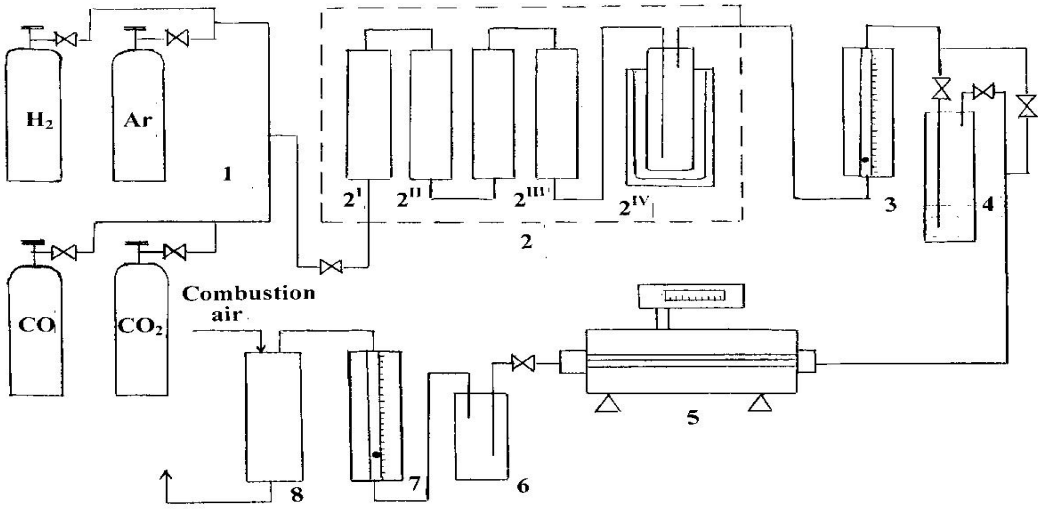

Рис. 2. Принципиальная схема установки для получения карбида титана. 1 – необходимые для синтеза газы; 2 – система очистки газов: 2^I – Al_2O_3; 2^{II} – катализатор Cu – Cr, 2^{III} – цеолит; 2^{IV} – охладительная система; 3 – расходомер; 4 – жидкостный клапан; 5 – печь для карбидизации с терморегулятором; 6 – улавливатель жидких и газообразных продуктов; 7 – реометр; 8 – печь для сжигания выделенных газов.

Карбид титана получали в лабораторной установке, принципиальная схема которой представлена на рис.2.

Порошок активного титана (в отличии от порошка, полученного традиционным методом) при низких температурах легко взаимодействует с карбидообразуемыми реагентами. Протекающий при этом процесс можно изобразить схематически:

$TiH_2 \rightarrow Ti^* + H_2$ (Ti^* – активный),

$Ti^* + C \rightarrow TiC$.

В полученном карбиде титана для использования в качестве связки никеля необходимо продолжение вышеуказанного процесса следующим образом:

$$NiCl_2 \cdot 6H_2O \rightarrow NiCl_2 \xrightarrow{H_2(C)} Ni + HCl + H_2O,$$

$TiC + Ni \rightarrow (TiC – Ni)$.

Выделенная HCl вызывает частичное хлорирование титана и активацию его поверхности. Содержание Ni в сплаве изменяется в пределах (6 – 20) wt. %. Хлорирования титана можно избежать применением никельсодержащих соединении, таких как оксид, карбонат, ацетат, формиат и др.

Для получения сплава TiC + Ni (10 %) были использованы гидрид титана, хлорид никеля и сажа в таких количествах, что в молярное соотношение соответствующих компонентов в шихте было Ti : C : Ni = 1 : 1 : 0.1. Для обеспечения равномерного распределения компонентов шихту перемешивали в течении 1 h. Перемешанную шихту клали в корундовый тигель в форме лодочки, которую помещали в трубчатую печь. Для удаления воздуха трубку продували потоком аргона в течении 30 min. Затем температуру печи повышали до температуры карбидизации, 850 °C, выдерживали в течении 1 h и охлаждали до комнатной температуры в потоке аргона.

Полученные продукт представляет собой агломерированный порошок черного цвета с насыпной плотностью (0.45 – 0.48) g / cm^3. Фазовый состав сплавов, синтезированных при температурах 850 и 950 °C представлен на рис. 3.

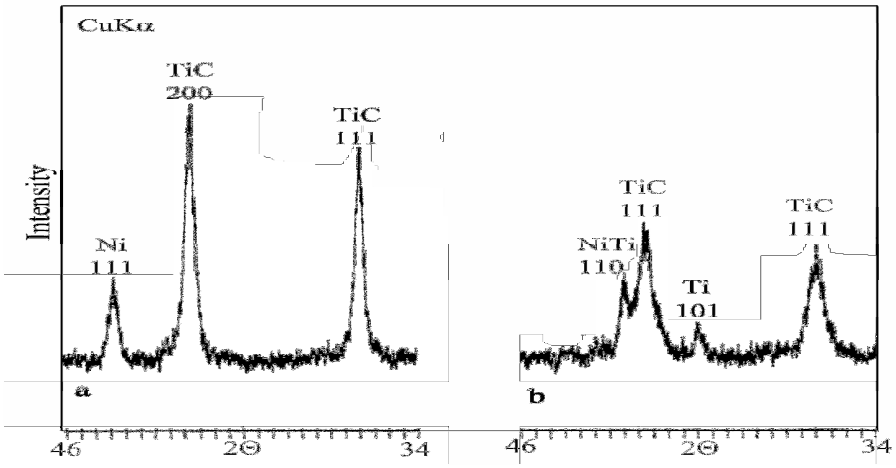

Рис. 3. Дифрактограммы сплавов TiC + Ni, синтезированных при 950 (а) и 850 °C (б).

На дифрактограмме образца, синтезированного при 850 °C (рис. 3б) наблюдаются максимумы, характерные для TiC, а также фазы свободного титана и NiTi. Последняя не наблюдается в образце, синтезированного при 950 °C (рис. 3а). Следует отметить, что увеличение времени карбидизации от 1 до 3 h , дает возможность уже при 850 °C получить сплав TiC + Ni без NiTi и свободного титана.

Наблюдаемый на дифрактограмме максимум NiTi указывает на неравновесное состояние, обусловленное технологией получения соединения. Низкая интенсивность наблюдаемого максимума TiC и его уширение указывает на высокую дисперсность фазы. Таким образом можно заключить, что получено соединение карбида титана, где функцию связывающих компонентов выполняют Ti и NiTi.

Полученный материал находится в неравновесном состоянии. Поэтому повышение температуры термической обработки вызывает его структурную стабилизацию. В частности – рост размера зерна с одной стороны и с другой стороны распад нестабильного соединения NiTi на составляющие компоненты. При этом, никель остается в свободном состоянии, а находящийся в системе свободный титан взаимодействует с остаточным углеродом, образуя TiC (рис. 3а).

Таким образом, полученные результаты показывают, что термическая обработка при 850 °C достаточна для получения высокодисперсного композиционного порошка на основе карбида титана.

Однако, получение нанокристаллического композиционного порошка TiC + Ni (10 %) – эта часть решения проблемы получения образцов и изделий на основе TiC. Не менее важная задача – осуществить консолидацию полученного материала, не ухудшая его нанокристаллическое состояние и связанное с этим преимущества. Использование

традиционных методов компактирования в этом случае не приемлемо, т.к. они приводят к росту размера зерна и повышению остаточной пористости.

Нетрадиционные методы быстрой консолидации дают возможность уменьшить время воздействия высоких температур, что обусловливает ограничения роста размеров зерен и соответственно – высокую плотность компактированных материалов.

Среди известных методов быстрого компактирования для консолидации нанокристаллического порошка на основе TiC был выбран метод искрового плазменного синтеза (ИПС) [10]. При реализации ИПС импульсный ток, проходящий через частицы предварительно компактированного при низких давлениях порошка образует высокоэнергетический плазменный разряд на границе раздела частиц. Для ИПС характерно: кумулятивное воздействие давления и электрического тока на процесс компактирования порошка и фазообразования; уменьшение скорости роста частиц, обеспечивающееся быстрым объемным нагревом, что дает возможность снизить скорости роста частиц. Таким образом ИПС обеспечивает быстрое проведение процесса компактирования и охлаждения.

Для компактирования нанокристаллических материалов была создана установка, общий вид которой представлена на рис. 4.

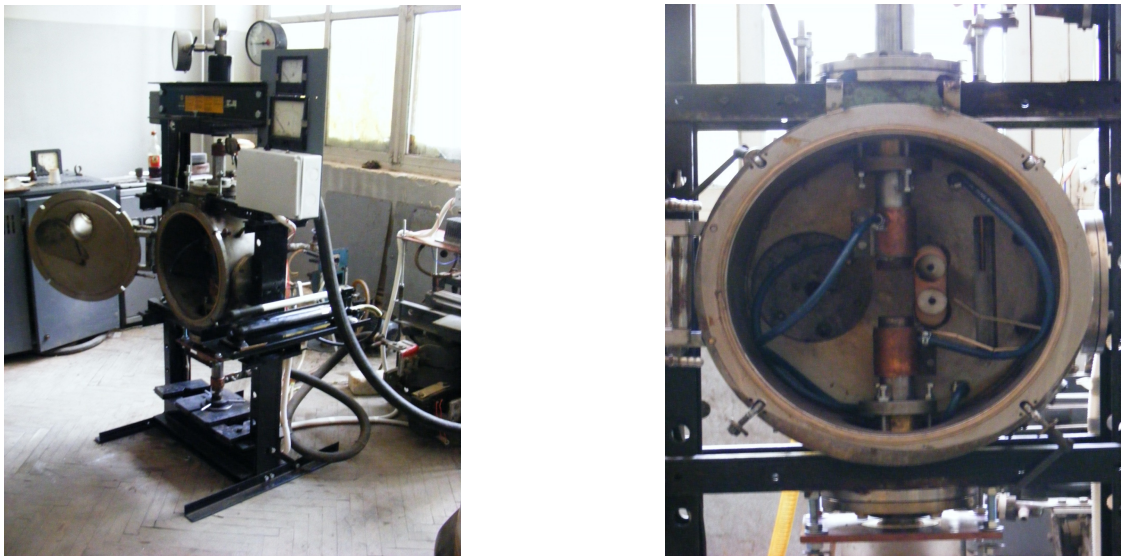

а **б**

Рис. 4. Установка искрового плазменного синтеза.
а – общий вид; б – камера для компактирования материалов.

Установка позволяет проводить компактирование нанокристаллических материалов как в вакууме, так и в инертной атмосфере. Рабочее давление создается гидравлической системой, а максимальная нагрузка на образец составляет 25000 kgf. Основным узлом нагревательной системы является понижающий трансформатор, управляемый электронным блоком. Нагревательная система позволяет пропускать в компактированном объеме переменный ток до 4000 А. Для пуансонов используются графит марки КМ 54 – 15. Это позволяет получать рабочее давление до 100 MPa. Регистрация параметров компактирования (давление, проходящий через образец ток, сопротивление образца, температура, перемещение пуансонов) производится с помощью компютерного блока.

Процесс компактирования TiC + Ni (10 %) проводится в два этапа. На первом этапе стартовый нагрев образца и активирование процесса компактирования производится пропусканием тока до 500 А при напряжением 10 V и начальном давлении не более 5 MPa. На втором этапе используется переменный ток, сила которого возрастает от 500 до 2000 А, а давление на образец увеличивается от 5 до 20 MPa. Продолжительность полного цикла компактирования составляет (3 – 4) min.

Перемещение температурного фронта от поверхности пуансона к центру образца и скорость его перемещения определяется теплопроводностью компактированного материала. При компактировании сплава TiC + Ni (10 %) температурный градиент от центра до его поверхности не превышал 100 °C.

Для предварительного прессования образцов из TiC + Ni (10 %) использовали одноразовые втулки (рис. 5). Втулки готовили из смеси порошка корунда и парафина (3 wt. %). При (70 – 80) °C смесь размягчается и под давлением в (2 – 4) atm заполняет пресс-форму (рис. 6).

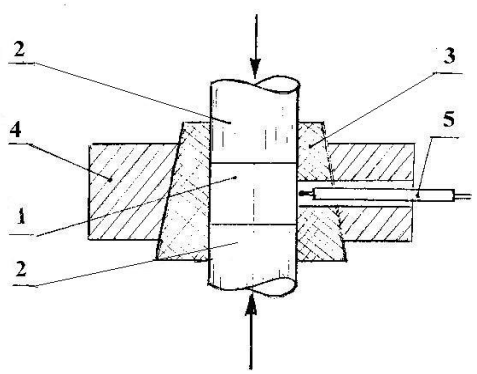

Рис. 5. Схема консолидации металлокерамических образцов. 1 – образец; 2 – графитовый пуансон; 3 – корундовая матрица; 4 – стальные кольца; 5 – термопара.

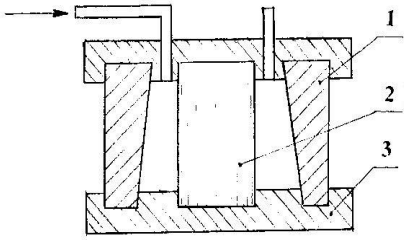

Рис. 6. Форма для подготовки цилиндрических образцов. 1 – алюминиевый корпус; 2 – стержень; 3 – подставка.

После охлаждения для удаления парафина втулка помещается в нагретую до (300 – 400) °C в печь. Окончательная термическая обработка втулки проводится при температуре 1400 °C в течении 3 h.

В результате компактирования получали образцы из TiC + Ni (10 %) двух типов – цилиндрические (диаметром 16, длиной (3 – 10) mm) и призматические ($4 \times 4 \times 20$ mm^3). Цилиндрические образцы предназначены для определения триботехнических характеристик, а призматические – для исследования механических свойств.

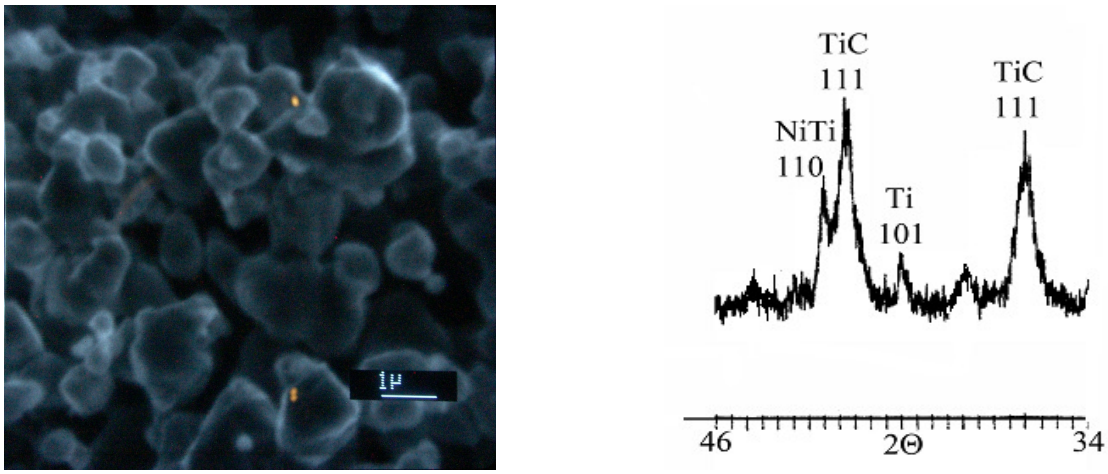

а **б**

Рис. 7. Растрово-электрономикроскопическое (РЭМ) изображение поверхности (а) и дифрактограмма (б) компактированного образца из TiC + Ni (10 %).

Растрово-электрономикроскопическое (РЭМ) изображение поверхности и дифрактограмма компактированного образца TiC + Ni (10 %) представлены на рис. 7.

Размер частиц, оцененый по степени уширения максимумов на дифрактограмме составляет 100 nm. С учетов этих результатов можно предположить, что наблюдаемый на РЭМ снимке зерна представляют агломераты более мелких частиц. Плотность образцов составляла 4.63 g / cm^3, предел прочности – 24 MPa; пористость – 6 %; твердость – HRA = 93.8 kgf / cm^2.

Таким образом, разработан технологический процесс компактирования твердосплавных материалов из нанокристаллических композиционных порошков карбида титана, сохраняющий в образцах и изделиях нанокристаллическую структуру.

Твердые сплавы на основе карбида титана, полученные разработанной технологией могут быть применены для изготовления жаропрочных, износостойких изделий, сопел реактивных двигателей, двигателей внутреннего сгорания, бронежилетов и других объектов специального назначения. Изучение эксплуатационных свойств образцов и изделии, полученных из разработанного материала является предметом дальнейшего исследования.

Работа выполнена в рамках проекта № 481 GNSF (Грузия) .

ССЫЛКИ

1. Г.В. Самсонов, Г.П. Упадхая, В.С. Нешпор. Физическое материаловедение карбидов. Киев: Наукова думка (1974).
2. О.С. Кипарисов, Ю.В. Левинский, А.П. Петров. Карбид титана: Получение, свойства, применение. Москва: Металлургия (1987).
3. W.S. Williams. Materials, **38**, 78 (1997).
4. K.S. Suslick, G.J. Price. Ann. Rev. Mat. Sci., **99**, 295 (1999).
5. S.C. Tjong, H Chen. Mat. Sci. Eng. B, **45**, 1 (2004).
6. M.A. Meyers, A. Mishra, D.J. Benson. Prog. Mat. Sci., **51**, 427 (2006).
7. L.E. Mc Candlish, B.H. Kear, B.-K. Kim. US Patent # 5230729 (1993).
8. L. Ramqvist. Int. J. Powd. Metall., **1**, 2 (1965).
9. В.И. Третьяков. Основы металловедения и технологии производства спеченных твердых сплавов. Москва: Металлургия (1976).
10. А.И. Райченко. Основы процесса спекания порошков пропусканием электрического тока. Москва: Металлургия (1987).

НЕКОТОРЫЕ ВОПРОСЫ ПРЕЦИЗИОННЫХ ЛИНЕЙНЫХ ИЗМЕРЕНИЙ В НАНОМЕТРОВОМ ДИАПАЗОНЕ

А.Г. Данелян [1], В.А. Данелян [1], Р.Р. Канкия [1], С.А. Мкртычян [1], С.В. Шоташвили [1], Д.И. Гарибашвили [2], И.Р. Ломидзе [3]

[1] Институт метрологии Национального агентства Грузии по стандартизации, техническому регулированию и метрологии
adanelyan@mal.ru
[2] Институт физики им. Э. Андроникашвили
devigar@mail.ru
[3] Грузинский университет им. Андрея Первозванного Патриаршества Грузии
lomiltsu@gmail.com

Принята 29 января 2010 года

Возникновенние и начальный этап развития нанотехнологий дали стимул для становления нового направления метрологии – нанометрологии. Основные задачи нанометрологии – это все аспекты метрологического обеспечения единства измерений в нанотехнологиях. Метрологическое обеспечение включает в себя высокоточные методы и средства измерений (эталоны, эталонные установки, стандартные образцы состава, физических свойств и др.) для передачи размеров единиц физических величин от Первичных эталонов этих единиц в нанодиапазон.

Нанотехнологии оперируют с объектами нанометровой протяжённости, а также с процессами, протекающими в объёмах, хотя бы один из размеров которых относится к нанодиапазону. В ряде случаев при таких наноразмерах (соизмеримых, например, с длиной волны де Бройля, длиной свободного пробега электронов и др.) могут проявиться специфичные эффекты (например, связанные с туннелированием электронов и др.), характер которых отличается от подобных процессов, описываемых известными законами макрофизики. Исследования этих явлений, эффектов, свойств, которыми занимается нанонаука, углубляют наши знания, дают возможность и основание пересмотреть наши взгляды на законы физики, на изменения физико-химических свойств веществ. Если вещество находится не в виде макротела, а в состоянии в виде отдельных наночастиц, и т.д., создают базис для развития нанометрологии.

Но перейдём к прецизионным линейным измерениям в нанодиапазоне. Для этого целесообразно привести следующую пространную выдержку из [1]: «Из самого определения нанотехнологии, оперирующей с объектами нанометровой протяжённости, естественным образом следует первоочередная задача измерений геометрических параметров объекта, что, в свою очередь, обусловливает необходимость обеспечения единства линейных измерений в нанометровом диапазоне. Но этим обстоятельством роль нанометрологии линейных измерений не исчерпывается. Она присутствует в неявном виде в подавляющем большинстве методов и средств обеспечения единства измерений физико-химических параметров и свойств объектов нанотехнологий, таких, как механические, оптические, электрические, магнитные, акустические и т.д. Часто необходимо осуществлять прецизионное пространственное позиционирование зонда измерительного устройства в место требуемого съёма измерительной информации. При этом диапазон линейного сканирования по каждой коор-

динате может простираться от единиц нанометра до сотен или более микрометров, а требуемая точность выставления координаты – составлять десятые доли нанометра.

Почему в нанометрологии столь большое внимание уделяют проблеме реализации линейной шкалы в нанометровом и прилегающем к нему диапазонах? Во-первых, потому, что решение первоочередной задачи метрологии в нанотехнологиях – обеспечение единства измерений геометрических параметров нанообъекта – опирается на метрологию линейных измерений. Во-вторых, ... измерения механических, электрических, магнитных, оптических и многих других параметров и свойств объектов нанотехнологии связаны с необходимостью позиционирования зонда измерительного устройства в заданное место с наивысшей точностью [2].

Обеспечение единства измерений физико-химических параметров и свойств объекта измерения требует привязки соответствующего средства измерений к эталону, воспроизводящему единицу данной физической величины (например, проводимости – к эталонному сопротивлению), а в нанотехнологиях в большинстве случаев – *ещё и обязательной привязки к базисному эталону длины* (*для «точного попадания в цель»*)».

Позволим себе напомнить современное принятое определение единицы длины – метра и ситуацию с практической реализацией этой единицы Первичным эталоном единицы длины. Напомним также, что в настоящее время эталонные измерения в области линейных измерений основаны на лазерной интерферометрии перемещений [3]. При этом постараемся пояснить насколько, на наш взгляд, воспроизведение единицы длины методами лазерной интерферометрии (ЛИ) соответствует определению единицы длины и насколько оно удовлетворяет требованиям нанометрологии. Для этого ниже приведён анализ некоторых известных нам и, на наш взгляд, наиболее прецизионных методов линейных измерений в нанотехнологиях.

Не вдаваясь в историю развития лазерной интерферометрии перемещений (ЛИП), которая применялась и применяется для прецизионных линейных измерений начиная с 70-ых годов, отметим, что развитие науки, техники и технологий в течение последних 40 лет постоянно требовало повышения точности измерений длин и перемещений. Отвечая этой необходимости, методы ЛИП постоянно совершенствовались. Наиболее наглядно это отразилось, в первую очередь, на Первичном эталоне единице длины, назначение которого – воспроизведение единицы длины – метра – и передача её размера с предельно достижимой точностью. Так, ещё в 1980 году для воспроизведения единицы длины в качестве эталонной использовалась длина волны излучения $\lambda_{\mathrm{Kr}} = 6057.80211 \cdot 10^{-10}$ m, соответствующего переходу $5d_5 \rightarrow 2p_{10}$ между уровнями атомов ^{86}Kr, и использование применяемой эталонной интерференционной установки обеспечивало воспроизведение метра с погрешностью порядка 20 nm. В то время такая погрешность объяснялась нестабильностью частоты оптического излучения ^{86}Kr, который не являлся лазерным источником, а единица длины – метр – определялась, как расстояние, на котором укладывалось 1650763.7300 длин волн в вакууме. Создание современных высокостабилизированных по частоте лазеров (оптических стандартов частоты) и их использование в качестве источников в лазерных интерферометрах перемещений позволило существенно повысить точность измерений длин и линейных перемещений. В настоящее время максимальная точность воспроизведения единицы длины Первичным эталоном метра (методами лазерной интерферометрии) определяется неопределённостью порядка 0.02 nm [3].

Как уже отмечалось, в основу современных прецизионных линейных измерений положены методы ЛИП. Ориентировка на ЛИП основывается на двух положениях. Во-первых, после выдающихся экспериментов группы К. Ивенсона по уточнению значения скорости света, завершённых в 1972 году в Национальном Бюро Стандартов (США) [4], с 1983 года принято, что **скорость света в вакууме** c **постоянна в любой инерциальной системе и её значение, как фундаментальной физической константы, принято абсолютным (без погрешности) и равным 299792458 m / s.** Во вторых, в последнем десятилетии разработаны

высокоточные (с точностью до 15 знака!) методы прямых измерений частоты ν оптического излучения стабилизированных лазеров (с нестабильностью частоты порядка $10^{-14} - 10^{-15}$). Это даёт возможность из выражения $c = \lambda\nu$ вычислить значение длины волны λ (в вакууме) излучения высокостабилизированного лазера (например, He – Ne – I_2-лазера, стабилизированного по линии насыщенного поглощения в молекулярном йоде) тоже с точностью до 15 знака. А дальше вступает в силу соображение, что эта длина волны лазера является материальным носителем единицы длины и должна позволить передать размер единицы длины от эталона метра вплоть до нанометра интерферометрически. Естественно, предполагается, что это должно осуществиться методами лазерной интерферометрии (ЛИ), которые уже четыре десятилетия успешно применяются в передаче размера единицы длины диапазона сравнительно больших длин от 50 m до 1 mm, удовлетворяя практическим требованиям точности прецизионных линейных измерений в этом диапазоне. Развитие нанотехнологий потребовало передачу размера единицы длины и в нанодиапазон, поскольку уже оказались востребованными измерения линейных размеров, которые меньше (а всё чаще, и намного меньше) длины волны. Но, как отмечается в работе [3], минимальная погрешность, неизбежно возникающая при передаче установленными методами размера единицы длины вниз – в нанодиапазон, определяется величиной 100 nm. Это уже совсем не удовлетворяет требованиям нанотехнологий. Специфика нанодиапазона требует принципиально новых подходов к этим методам измерений. Один из них – это усовершенствование возможностей одного из перспективных направлений лазерной интерферометрии перемещений – лазерной интерферометрии-фазометрии (ЛИФ) [5].

Возникает вопрос, какие причины определяют ситуацию, когда значение длины волны стабилизированного лазера может быть известно с точностью до 15 знака, а Первичный эталон метра, реализующий принцип воспроизведения пространственного интервала размером в 1 m на основе ЛИ (используя длину волны этого лазера) «обеспечивает воспроизведение единицы длины (метра) с относительным среднеквадратическим отклонением (неопределённостью) $2 \cdot 10^{-11}$?» [3]. Разница на целых 4 порядка! В чём причина? Наверное, дело не только в неточности измерения и учёта значения показателя преломления окружающей среды, а также в неточности учёта других внешних факторов. Представляется, что это вызвано ограниченными возможностями методов ЛИ (в том числе и ЛИФ).

Обратим внимание на то, что из определения единицы длины – метра, принятого в 1983 году на 17-ой Генеральной Конференции по мерам и весам (ГКМВ), не следует, что длина волны стабилизированного лазера должна быть мерой для воспроизведения единицы длины. Принятое в 1983 году определение единицы длины является фундаментальным определением единицы этой физической величины, согласно которому за единицу длины – **МЕТР** – принято **расстояние, которое проходит электромагнитная волна в вакууме за промежуток времени, равный 1 / 299792458 секунды**. Определение базируется на установленном и неизменном значении скорости света c в вакууме. Напомним, что значение $c = 299792458$ m / s принято абсолютным (без погрешности). Учитывая фундаментальность этой величины, более простого и универсального определения единицы длины, как через скорость электромагнитной волны и времени её прохождения, предложить уже невозможно. Однако, при попытке практически реализовать это определение, возникает вопрос, как зарегистрировать плоскую волну в одной и другой пространственных точках и по этим пространственным событиям отметить интервал времени (равный 3.335640951948 ns) между ними. При этом, погрешность измерения этого интервала времени не должна превышать $10^{-19} - 10^{-20}$ s, чтобы ошибка, возникающая при реализации единицы длины, была соизмерима с лучшими известными методами воспроизведения единицы длины (например, с использованием лазерных интерферометров перемещений). Сложности измерения таких коротких интервалов времени с указанной точностью привели к тому, что с 1983 года практической реализации этого (прямого) определения единицы длины так и не существует. Поэтому, как выход из положения, на 17-ой ГКМВ было рекомендовано использовать

интерференционные методы для воспроизведения единицы длины и были рекомендованы эталонные частоты (длины волн) нескольких стабилизированных лазеров (стандартов оптических частот), регламентированные новым определением метра.

Обратим внимание, что понятия «реализация единицы» и «воспроизведение единицы» в некоторых случаях трактуются нечётко. По этой причине иногда возникает путаница в терминологии. Поэтому позволим себе напомнить, как эти понятия определены в Отчёте четвёртого проекта Международного бюро мер и весов (МБМВ) для правительств стран Метрической конвенции [6]. В разделе 3.2 отчета, где описываются методы, которые используют национальные метрологические институты (НМИ) при разработке своих национальных эталонов измерений, говорится:

«НМИ имеет возможность выбора методов, необходимых при разработке каждого из своих национальных эталонов измерений...

1. В соответствии с первым из методов, НМИ включается в работы по физической реализации единицы, исходя из её определения, тем самым по созданию первичного эталона, который будет служить в качестве национального эталона. Это – наиболее фундаментальный подход, и он имеет большое значение, т.к. физическая реализация обеспечивает прочную связь между определением единицы и её физическим воплощением, как эталона. Однако, это наиболее трудный и дорогой подход.

2. Второй метод годится только для ограниченного числа физических величин. Он также предусматривает создание первичного эталона, который будет служить национальным эталоном, но в этом случае не с помощью реализации единицы, исходя из её определения, а с помощью создания высоко-воспроизводимого эталона, значение которого было согласовано через МБМВ *с помощью международного договора*. Эта процедура скорее относится к «воспроизведению» единицы, нежели к её «реализации». Примерами служат использование рекомендованных частотно-стабилизированных лазеров для создания эталона метра, эффекта Джозефсона – для вольта, и квантового эффекта Холла – для ома...».

Приведённый фрагмент из [6] подтверждает, что до последнего времени не было реальных предложений по физической реализации единицы длины, исходя из её определения.

С середины 70-ых годов единица длины воспроизводится с помощью лазерных интерферометров перемещений (ЛИП) [7]. С 1983 года в этих ЛИП в качестве источника эталонной длины волны применяются стабилизированные по частоте лазеры нескольких типов, рекомендованный перечень которых с развитием лазерной техники уточняется. Каждый из ЛИП представляет собой систему измерения разности фаз оптических сигналов (плоских электромагнитных волн), распространяющихся в опорном и сигнальном каналах интерферометра. Т.е., в ЛИП измеряется, насколько сдвинуты друг относительно друга во времени (по фазе) электромагнитные колебания (оптические колебания), распространяющиеся в каналах (плечах) интерферометра. Эти колебания, прошедшие каналы интерферометра, суммируются на выходе интерферометра, в результате чего происходит интерференция этих световых пучков и возникает интерференционная картина в виде чередующихся светлых и тёмных полос. На выходе ЛИП суммарный сигнал поступает на фотодетектор. По изменениям интенсивности интерференционной картины (возникающих при перемещении отражателя в измерительном канале), образованной совмещёнными сигналами из опорного и сигнального каналов интерферометра, может быть получена информация об изменениях разности фаз сигналов, «вызванных различного рода процессами в фазовом объекте в каналах ЛИП. Они могут быть обусловлены изменениями в излучении или исследуемом объекте, которые вследствие частотной, пространственной или поляризационной дисперсии приводят к вариациям разности фаз» [5]. Отметим, что фазовые измерения относятся к методам обработки сигналов во временной области. С успехами последних двадцати лет в области радиоспектроскопии высокой разрешающей способности более высокие точности можно ожидать при обработке сигналов в частотной области.

В работе [8], анализируя вопросы измерений геометрических величин в нанотехнологиях, в частности говорится: «Интерферометры первого поколения, использовали одночастотные лазеры и имели диапазон измерения преимущественно 3...10 м, а скорость перемещения отражателя не превышала 10 м / мин [7]. Однако, при использовании одночастотных лазеров главной проблемой является зависимость точности измерений интерферометров от интенсивности излучения лазеров и высокая чувствительность к колебаниям интерференционного фона. Также недостатком таких интерферометров является потеря информации при смене направления движения объектов.

Значительно упростить оптическую схему интерферометра и перейти к обработке сигнала в частотной области спектра позволило создание двухчастотного лазера. Интерферометры, разработанные по такой схеме, расширили диапазон измерений до 60 м при скоростном пределе в 18 м / мин и более.

Поскольку указанные интерферометры имеют расширенные функции в части измерения углов поворота, показателей преломления вещества, измерений по нескольким координатам и пр., особые требования предъявляются к мощности лазерного излучения и разностной частоте. Кроме того, должна обеспечиваться высокая стабильность оптической частоты в течение всего срока службы лазеров».

Рассуждая о применении одночастотных или двухчастотных лазеров в лазерных интерферометрах перемещений и говоря об интерферометрах Майкельсона, как наиболее распространённых системах для прецизионных линейных измерений в нанотехнологиях, в работе [9] отмечается, что «для техники улучшений возможностей интерферометров Майкельсона высокого разрешения известны две фундаментальные системы детектирования: 1-ая – это лазерные интерферометры с двухчастотными лазерами и гетеродинные системы детектирования (смешивание частот); 2-ая – это лазерные интерферометры с одночастотными лазерами и амплитудная область интерференционных измерений».

В большинстве из современных прецизионных систем ЛИП для измерений наноперемещений используются гетеродинные методы на основе или двухчастотных лазеров, или на одночастотном лазере, но с применением методов сдвига частоты лазера (например, акустооптических методов), и использования этих двух оптических частот.

Анализ ограничений точности прецизионных линейных измерений, основанных на гетеродинном варианте ЛИП, проведён в работе [10], в которой вопросы влияния шумов в интерферометре на точность измерения не рассматриваются. Однако анализируются ограничения, связанные с неопределённостью (погрешностью) значения показателя преломления n в плечах интерферометра, неопределённостью вычисленного значения длины волны лазерного источника, применённого в интерферометре (по измерениям частоты излучения этого лазера, сравнением с частотой эталонного лазера, которая, в свою очередь, была измерена в сравнении с цезиевым эталоном радиочастоты), ошибки в значении числа подсчитанных импульсов (с учётом дробной части интерференционной полосы) при перемещении подвижного отражателя интерферометра. В этой работе описана созданная и исследованная авторами наноизмерительная машина на базе конструкции оригинального интерферометра (на двухчастотном лазере и с использованием свойств поляризованного лазерного излучения). В этой машине используются одновременно три интерферометра (однолучевой, двухлучевой и трёхлучевой) измеряющие перемещения по трём направлениям. Это позволяет осуществлять позиционирование по трём взаимноперепендикулярным осям (x, y, z). При этом указанные три интерферометра позволяют учитывать и корректировать угловые девиации каждого из трёх перемещаемых плоских зеркал. В машине была достигнута разрешающая способность измерений порядка 0.1 nm и неопределённость измерений порядка 3 nm.

Вопросы шумов довольно глубоко рассмотрены в работе [5], в которой описан оригинальный лазерный гетеродинный интерферометр-фазометр с акустооптическим преобразованием оптической частоты (сдвига оптической частоты излучения лазера). Представляется, что наиболее «узким местом» в схемах ЛИП является фотодетектор, который практи-

чески является фазовым детектором. В [5] рассмотрены случаи небольшой мощности сигнала, поступающего на фотодетектор, когда основные источники шума сосредоточены в самом фотодетекторе. Поэтому для увеличения чувствительности желательно увеличить поступающую на фотодетектор мощность, но с увеличением мощности растёт и дробовой шум, обусловленный распределением числа фотонов в опорном и сигнальном пучках ЛИП. Из анализа в [5] делается вывод, что наиболее точными и чувствительными при измерении фазовых сдвигов в оптике являются модуляционно-компенсационный метод и метод переноса частоты (оптическое гетеродинирование), что позволяет перенести фазовые соотношения между измеряемыми оптическими колебаниями в радиодиапазон, где измерения разности фаз можно произвести с существенно более высокой точностью, чем в оптическом диапазоне. При этом учитываются флуктуации оптических длин пути, вызываемые самыми разнообразными причинами. Из анализа, проведённого в [5], «следует, что с учётом большого класса шумов, используя лазерные интерферометры, можно измерять фазовые сдвиги на уровне 10^{-3} градуса на длине волны $\lambda = 0.6328$ мкм, что эквивалентно линейному смещению 0.1 нм». Со своей стороны отметим, что указанный уровень точности 10^{-3} градуса в настоящее время является предельно достигнутым в диапазоне частот от 500 Hz до 100 kHz. В диапазоне частот выше 1 MHz (в который реально переносятся фазовые измерения из оптического диапазона) наивысшие точности определяются значением 10^{-2} градуса. Со всем этим анализом, приведённым в [5], безусловно следует согласиться. Хотя представляется, что к источникам неопределённостей, которые необходимо учитывать при анализе точностей в ЛИП (или ЛИФ), следует отнести ещё один ограничивающий и существенный момент, не отмеченный в литературе.

Свою негативную роль может сыграть амплитудно-фазовая характеристика (АФХ) фотоэлектрического преобразователя (фотоприёмника), т.е. зависимость изменений фазы выходного сигнала при изменении интенсивности излучения (интерференционной картины) поступающего на фотоприёмник (ФП). Известно, что в качестве фотодетекторов в современных ФП в схемах ЛИП применяются в основном фотодиоды (лавинные фотодиоды, p-i-n фотодиоды и др.). Эквивалентная схема фотоприёмника представляет собой определённую RC-схему (в зависимости от схемы включения фотодиода), в которой помимо входного сопротивления фотодиода в качестве элементов схемы фигурируют и ёмкость перехода детектора и другие паразитные ёмкости схемы (см., например, [11] – раздел 5.10), неизбежно присутствующие в конкретном устройстве и которые практически невозможно точно определить или измерить. Такая RC-схема имеет фазо-частотную характеристику, определяемую реактивными элементами, входящими в схему. Но эта характеристика строится при постоянном уровне сигнала, поступающего на вход схемы. Если же какой-либо элемент схемы изменяет свои параметры в зависимости от уровня входного сигнала, то соответственно будет изменяться и фазовая характеристика схемы. При изменении интенсивности поступающего на фотодиоды излучения все они изменяют своё входное сопротивление (причем в довольно широких пределах). Это изменение входного сопротивления, имеющего обычно значение порядка $(10^5 - 10^7)$ Ohm, в сочетании даже с небольшими паразитными ёмкостями входной части ФП, может вызвать довольно существенные сдвиги фазовой характеристики ФП, которые невозможно точно учитывать, что может привести к весьма существенной амплитудно-фазовой погрешности, вносимой ФП. Эту АФХ следует как-то учитывать при измерениях перемещений (при изменениях длины измерительного плеча ЛИП), которые в пределах одной длины волны лазерного излучения (а это происходит в нанодиапазоне) производятся по измерению изменений интенсивности суммарной (интерференционной) картины, поступающей на ФП. Поэтому, для уменьшения влияния этой погрешности может возникнуть соблазн стабилизировать уровень (интенсивность) оптического сигнала, поступающего на ФП. В то же время, стабилизация интенсивности излучения, поступающего на ФП, противоречит методам лазерной интерферометрии переме-

щений. Напомним, что измерение перемещений (с использованием ЛИП) основано на поиске местоположения, соответствующего на изменяющейся интерференционной картине (*в динамике процесса измерений*) экстремально минимальной или максимальной интенсивности, поступающей на ФП. Нахождение этих положений в динамике процесса перемещения отражателя в сигнальном канале интерферометра очень сложная и трудоёмкая задача и, как показала практика, до настоящего времени не позволило достичь неопределённости измерений перемещений меньшей, чем 0.02 nm, даже в лучших системах лазерных интерферометров перемещений (например, применённых в аппаратуре Первичного эталона метра).

Недавно появились сообщения о достижении пикометровой разрешающей способности, но нолько в схеме интерферометра-деформографа, предназначенного для геофизических измерений [12], не применимого в нанотехнологиях без модернизации. В этом интерферометре дополнительно было применено проецирование интерференционной картины (близкое по своему техническому решению к принципу работы баллистического гальванометра или шлейфового осциллографа) для получения увеличенного изображения интерференционной картины. При этом была создана оригинальная аналоговая следящая система регистрации сдвига интерферограммы. В этой системе применялся специальный оптический дискриминатор интерферограммы (используется зеркальная прозрачно-отражающая решетка из 28 штрихов) и измерялся сдвиг интерференционной картины относительно этой решётки. Такой приём позволил получить увеличенное изображение интерференционной картины, фрагмент которой поступает на ФП. В результате была существенно увеличена разрешающая способность интерферометра. В работе [12] разрешающая способность достигла рекордного значения – 1 pm. Такая система нашла применение в геофизическом мониторинге. Окажется ли возможным применить такого типа систему (при таких масштабах проецирования и увеличения размеров интерференционной картины) для линейных измерений в нанодиапазоне, в нанотехнологиях – неизвестно. В то же время измерительная система с такой разрешающей способностью была бы очень желательна для нанотехнологий.

В рассмотренных вариантах ЛИП для прецизионных измерений длин и линейных перемещений в нанометровом диапазоне разрешающая способность измерений в лучшем случае составляла 0.1 nm. В то же время, как указано в работе [2], в маршрутной карте, которую разработали в США для нужд полупроводниковой промышленности, для некоторых технологических процессов уже требуются линейные измерения с разрешающей способностью порядка (0.001 – 0.002) nm. Описанные выше системы интерферометров этим требованиям пока не удовлетворяют. В ряде источников (например, [1,3,5]) ставится вопрос об актуальности и поиске новых методов линейных измерений в нанодиапазоне для решения этой проблемы. Отметим, что уже появились первые предложения по применению частотных методов для линейных измерений в нанодиапазоне. Но при анализе этих предложений оказалось, что это не частотные методы измерений, а методы стабилизации частоты лазерного источника оптического излучения, на котором работает интерферометр перемещений.

Так, в работе [9] (выполненной в институте научных приборов, в Чехии, г. Брно), наименование которой «Частотный метод измерений суб-нанометровых измерений расстояний с применением оптического резонатора и перестраиваемого полупроводникового лазера», рассмаривается устройство на базе интерферометра, в котором источником оптического излучения является стабилизированный по частоте лазер. В качестве источника излучения авторы создали лазер с «растянутым» резонатором, в который встроен перестраиваемый полупроводниковый лазер, непрерывное излучение которого пропускается через перестраиваемый резонатор интерферометра Фабри–Перо (ИФП). Этот резонатор практически является оптическим узкополосным фильтром, пропускающим при перестройке полупроводникового лазера излучение только тех оптических частот, которые имеют резонанс в резонаторе ИФП. А это происходит тогда, когда выполняется соотношение $(2L/c)(\omega_0 - \omega_e) = K\pi$, где ($L$ – длина резонатора, ω_e – резонансная частота ИФП, ω_0 –

частота вводимого в ИФП лазерного излучения. Интенсивность прошедшего через резонатор света будет максимальной при резонансной настройке $(\omega_0 - \omega_e)$ и уменьшится при изменении длины резонатора. Авторы создали замкнутую следящую систему автоматической подстройки частоты такого лазера с цифровой коррекцией частоты (с введением для этой цели дополнительной низкочастотной модуляции мощности лазера). Выходная частота излучения ИФП сравнивалась с частотой стабилизированного по частоте He – Ne – I_2-лазера. По частоте биений этих излучений подстраивалась частота полупроводникового лазера и резонатора ИФП. Не вдаваясь в подробности этой системы, отметим, что фактически в [9] исследовался не частотный метод измерения длин или линейных перемещений, а оригинальная система дифференциального интерферометра для измерения линейных перемещений со схемой стабилизации (и, практически, подстройки и фильтрации) частоты лазерного источника. Отметим, что в данной *системе интерферометра* была достигнута разрешающая способность линейных измерений порядка 0.05 nm при измерении перемещений до 400 nm.

Несколько другой вариант предложен в работе [13]. В ней также предлагается применить интерферометр Фабри–Перо (ИФП) для стабилизации частоты лазера, который может быть применён в качестве источника образцовой длины волны в интерферометре для линейных измерений. В отличие от [9], в данной работе предлагается пропускать через ИФП не непрерывное лазерное излучение, а лазерные импульсы, точнее излучение импульсного лазера с синхронизацией мод (ЛСМ). При этом анализируется прохождение через резонатор ИФП импульсных сигналов, которые имеют сложный спектр (в зависимости от длительности импульса). Анализировалась функция пропускания резонатора ИФП при импульсной форме когерентного света и изменение временных характеристик прошедших через ИФП импульсов. На основаниии этого анализа сделан вывод, что, чтобы ИФП представлял собой оптический фильтр (что необходимо для его привязки к стабильному лазерному излучению), его база должна быть такой, чтобы время Θ двойного прохождения базы ИФП импульсом света было меньше длительности падающего импульса τ, т.е. $\Theta < \tau$, где $\Theta = 2L/c$. Это накладывает определённые требования на базу эталона длины, который может быть создан на основе предложенной в [13] системы. «Так, при фемтосекундной длительности входящих импульсов интервал межу зеркалами интерферометра – 0.15 – 15 мкм, пикосекундной – $1.5 \cdot (10^2 - 10^4)$ мкм или 0.015 – 1.5 см, наносекундной – $1.5 \cdot (10^5 - 10^7)$ мкм или 15 – 1500 см» [13]. Исходя из этого, предлагается применить импульсный ЛСМ наносекундной длительности. При таких условиях длина резонатора ИФП позволяет параллельно его оси дополнительно поместить активную среду He – Ne-лазера, чтобы получить источник непрерывного стабильного оптического излучения, перестраиваемый в небольшом частотном интервале. Они предлагают таким образом стабилизировать длину резонатора ИФП, привязав её к водородному мазеру. Такая стабильная длина резонатора ИФП должна обеспечить стабильность и монохроматичность излучения He – Ne-лазера, встроенного (помещённого) в резонатор ИФП. При этом ИФП становится узкополосным оптическим фильтром. Это излучение предлагается использовать в качестве образцового по частоте источника для лазерного интерферометра, на базе которого будет построен эталон метра. Т.е. и в этой работе рассмстривается интерферометр со стабилизированным по частоте непрерывным лазерным излучением. «В итоге погрешность базы эталона метра составит 10^{-10}. Это означает неопределённость расстояния между зеркалами (1 м) около 0.1 нм. Для реализации такой точности измерения длины необходимо использовать современные технологии изготовления зеркал интерферометра. Здесь отметим, что применение лазерного излучения позволяет значительно снизить требования к отражающим свойствам зеркал ИФП. Так, предельная неопределённость положения плоскости отражения света для стандартных размеров луча He – Ne-лазера (диаметр около 1 мм) оценивается значенем $10^{-13} - 10^{-15}$ м, что на несколько порядков увеличивает резерв точности определения длин с помощью лазерной интерферометрии» [13].

Нам представляется, что заслуживают внимания предложения по созданию прецизионного измерителя длин и линейных наноперемещений не только на интерференционных методах, а на альтернативных вариантах, например, на частотных или время-частотных измерениях, которые позволили бы практически реализовать определение единицы длины хотя бы в нанодиапазоне. Ниже представлены наши предложения по созданию метода и общей структурной схемы для измерений длин и линейных наноперемещений и практической реализации определения единицы длины, основанных на время-частотных измерениях [14]. При этом можно решить две основные задачи:

- фиксацию фазы плоской электромагнитной волны в заданных точках пространства;
- прецизионное измерение интервала времени, в течение которого электромагнитная волна проходит между указанными точками пространства.

Принятое в 1983 г. определение единицы длины основано на абсолютном и неизменном значении скорости света в вакууме. Оно, по-существу, отражает положение теории относительности А. Эйнштейна о единстве пространства и времени. Исходя из этого, предлагаем для создания указанного метода и схемы использовать оптическую задержку (ОЗ), что обеспечивает ряд преимуществ.

Предложенное нами устройство должно содержать систему на основе замкнутой, регулируемой ОЗ, в которую поступает непрерывное когерентное оптическое излучение, например, от внешнего лазера. Также необходимо использовать эффект прерывания света светом [15]. В данной полностью оптической системе непрерывное излучение лазера, попадающее в контур ОЗ, прерывается световым излучением, прошедшим этот контур. Такая система должна формировать прямоугольные импульсы света – генерировать оптический меандр. При этом длительность каждого импульса равна длительности паузы между соседними импульсами и определяется оптической длиной контура задержки и скоростью распространения в ней света. Необходимо скомпенсировать потери света при прохождении этого контура.

Условная схема генератора оптического меандра (ГОМ) приведена на рис. 1.

Ниже показано, что изменения длины контура задержки (или интервала времени прохождения светом замкнутого контура задержки) можно измерять по частоте повторения импульсов, генерируемых в такой системе. Таким образом, частота связывает длину и время задержки и ее можно сличать с частотами сигналов эталона частоты.

ГОМ формирует импульсы света длительностью $T_i = L/c$ и с паузой между соседними импульсами $T_p = L/c$ где L – оптическая длина контура ОЗ (рис. 2). Другими словами, в описанной системе генерируется оптический меандр, временные характеристики которого однозначно определяются размерами замкнутого контура ОЗ:

$$f = 1/2T_i = c/2L. \qquad (1)$$

Выражение (1) связывает длительность генерируемого импульса света T_i частоту f повторения этих импульсов и расстояние L, которое проходит плоская электромагнитная волна в рабочем плече ГОМ. Далее будем учитывать, что оптическая длина L и геометрическая l связаны соотношением $L = nl$, где n – коэффициент преломления среды.

Если призма 5 (см. рис. 1) жестко соединена с микроскопом (или зондом), положения которого определяют начальную и конечную точки воспроизводимого (или измеряемого) пространственного интервала, а также изменения интервала времени, проходимого светом, то эту систему можно применять для измерений длины (структурная схема представлена на рис. 3).

При изменении положения призмы 5 воспроизводимую (или измеряемую) длину Δl определяют по изменению частоты импульсов, генерируемых ГОМ. С использованием (1) легко показать, что искомое значение Δl (расстояние между двумя положениями призмы 5

при наведении микроскопа 6 на точки, ограничивающие измеряемый объект 7) вычисляют по формуле

$$\Delta l = \frac{c}{4n}(T_2 - T_1) = \frac{c}{4n}\left(\frac{1}{f_2} - \frac{1}{f_1}\right) = \frac{c(f_1 - f_2)}{4\,n\,f_1 f_2}, \qquad (2)$$

а интервал времени Δt, в течение которого свет проходит между этими точками, – по формуле

$$\Delta t = \frac{T_2 - T_1}{4n} = \frac{1}{4n}\left(\frac{1}{f_2} - \frac{1}{f_1}\right) = \frac{f_1 - f_2}{4\,n\,f_1 f_2},$$

где T_1, T_2 – периоды повторения импульсов, генерируемых ГОМ, соответствующие начальному и конечному положениям призмы 5; f_1, f_2 – значения частот этих импульсов.

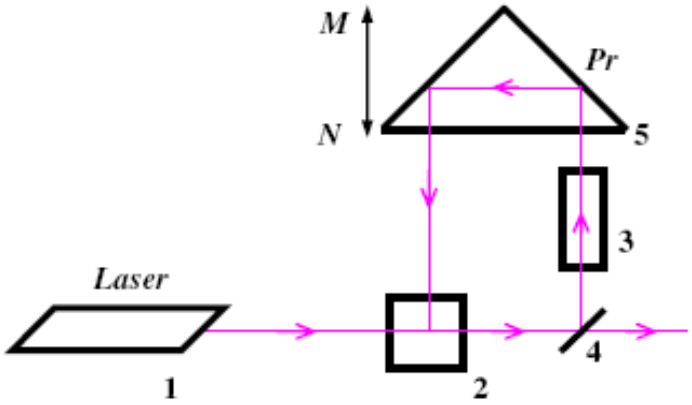

Рис. 1.

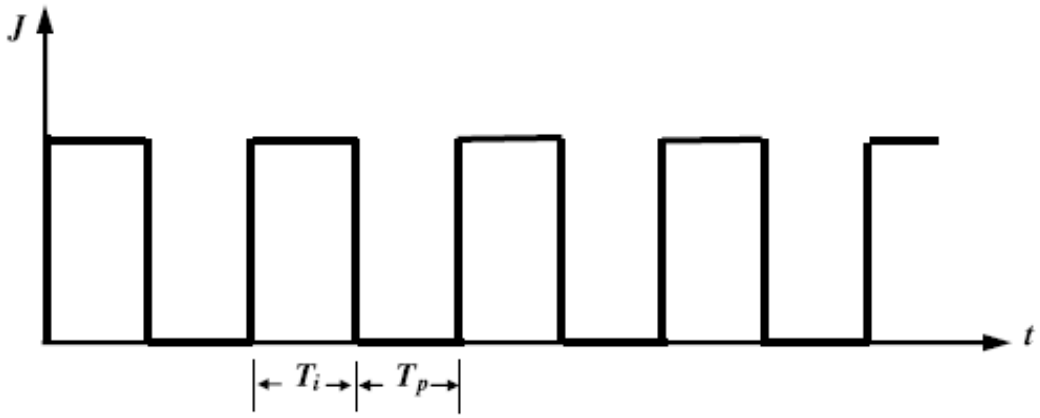

Рис. 2.

При измерениях длины объекта в процессе наведения микроскопа 6 на начальную точку измеряемого объекта 7 путем регулировки оптической длины дополнительной задержки 9 целесообразно выбрать частоту f_1 импульсов ГОМ, равную одной из стандартных частот, принятых в эталонных измерениях времени и частоты, например 5 MHz. Для этого регулируют длину задержки 9 до совпадения в системе сличений частот значений частот импульсов ГОМ и стандарта частоты. При наведении микроскопа 6 на вторую точку измеряемого объекта изменяют частоту сигналов синтезатора частот (синхронизируемого со

стандартом) до совпадения с ней частоты f_2 импульсов ГОМ. Заметим, что для сличений этих частот можно применять прецизионные частотные или фазо-частотные компараторы, эксплуатируемые в комплексах эталонов частоты в метрологических лабораториях времени и частоты.

Для оценки возможностей описанного метода были использованы данные компаратора VCH – 314 («Время-Ч», Россия, www.vremya-ch.com), который предназначен для прецизионного сравнения частоты и фазы сигналов стандартов частоты и времени. Он содержит два идентичных измерительных канала и благодаря корреляционной обработке обеспечивает предельно малую погрешность измерения и расчет нестабильности частоты каждого отдельного сигнала. Входные сигналы – синусоидальные 5, 10, 100 MHz; (0.6 – 1.2) V на нагрузке 50 Ohm. Предел измерения относительной разности частот $\Delta f / f = \pm 1 \cdot 10^{-6}$. Диапазон значения времени измерения $t = 1...10^5$ s. Погрешности измерения (вносимая нестабильность частоты в зависимости от режима работы и разности частот) представлены в таблице 1.

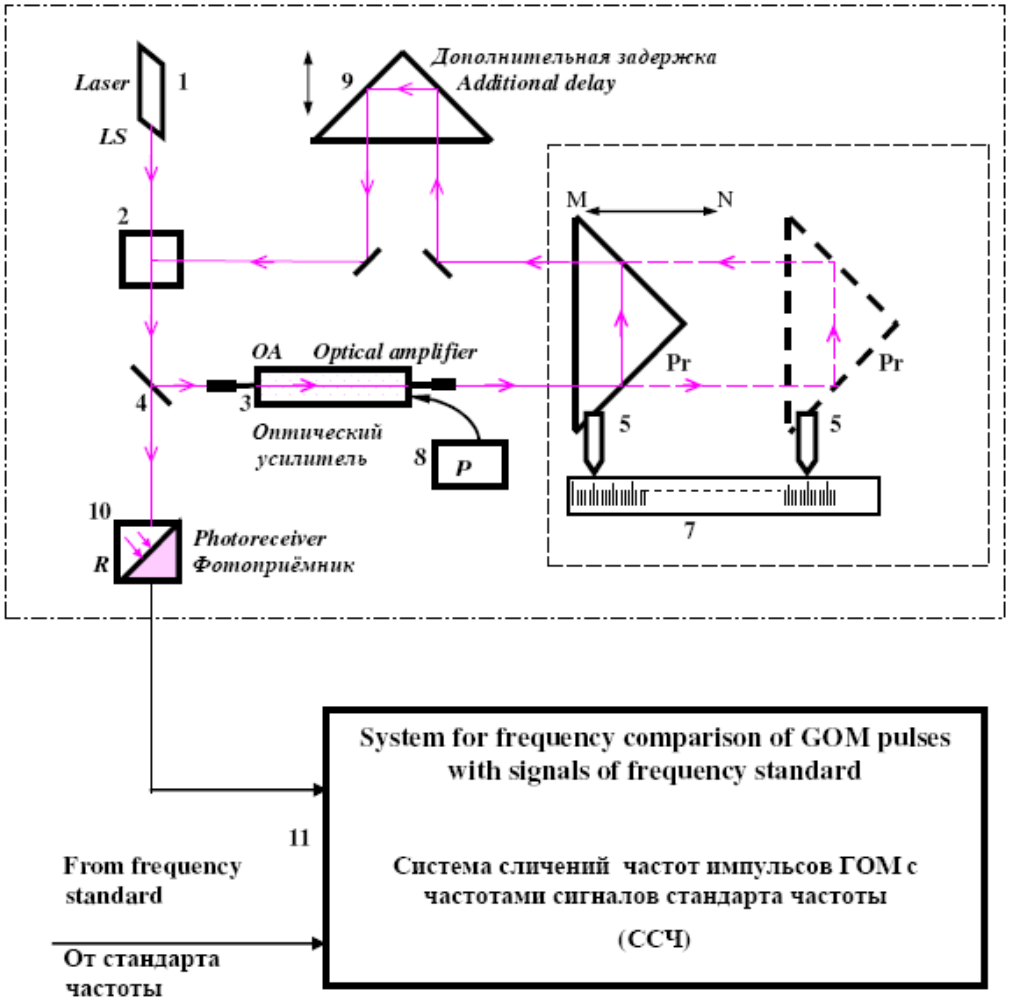

Рис. 3.

Таблица 1. Погрешности измерения частотного компаратора VCH – 314.

Время измерения, s	Основная погрешность ($\Delta f / f = 0$, полоса пропускания 3 Hz), менее		Дополнительная погрешность ($\Delta f / f$), менее
	Одноканальный режим	Двухканальный режим	
1	$8 \cdot 10^{-14}$	$2 \cdot 10^{-14}$	$2 \cdot 10^{-3}$
10	$1 \cdot 10^{-14}$	$3 \cdot 10^{-15}$	–
100	$1.5 \cdot 10^{-15}$	$1.5 \cdot 10^{-15}$	–
1000	$5 \cdot 10^{-16}$	$5 \cdot 10^{-16}$	–

Полагаем, что предложенный метод воспроизведения и измерения длин и линейных перемещений может оказаться особенно эффективным для нанометрового диапазона. Расчетная оценка частот импульсов ГОМ с использованием (2) для Δl (при измерениях в вакууме, $n = 1$), полученная для случаев перемещений призмы 5 (см. рис. 3) на задаваемые значения Δl (при увеличении длины контура задержки ГОМ), лежащие в нанометровом диапазоне, приведена в таблице 2, из которой следует, что если за начальную точку при перемещениях призмы 5 выбрать положение, при котором частота $f_1 = 5\,\text{MHz}$, то перемещения этой призмы в диапазоне (0 – 3) μm вызовут изменения частоты импульсов ГОМ в пределах, когда относительная разность частот $\Delta f / f$ не превышает $\pm 1 \cdot 10^{-6}$. При этом можно считать, что разрешающая способность измерения частоты (с учетом характеристик VCH – 314 в двухканальном режиме) составляет $\Delta f_p = 5 \cdot 10^6 \times 2 \cdot 10^{-14}\,\text{Hz} = = 10^{-7}\,\text{Hz}$. При подстановке значений $f_1 = 5\,\text{MHz}$, $f_2 \approx 5\,\text{MHz}$, в выражение (2) для изменения частоты импульсов ГОМ на $\Delta f_p = 10^{-7}\,\text{Hz}$ получим разрешающую способность измерения длины $\Delta l_p = 3 \cdot 10^{-13}\,\text{m} = 0.0003\,\text{nm}$.

Заметим, что по изменениям частоты импульсов ГОМ $\Delta f = f_1 - f_2$ можно измерять изменения длины контура задержки Δl. В пределах от 0 до 2 μm зависимость $\Delta l = F(\Delta f)$ очень близка к линейной и для упрощенного расчета можно воспользоваться выражением $\Delta l = 2.997925 \cdot 10^{-6} \Delta f$, где длина выражается в метрах, а частота – в герцах.

Таблица 2. Расчетные значения изменений частоты импульсов ГОМ при заданных значениях перемещения призмы.

Δl , nm	Δf , Hz	Примечания
0.0003	0.0000001000	Разрешающая способность, VCH – 314 при времени измерения 1 s
0.0005	0.0000001668	–
0.002	0.0000006671	–
0.003	0.0000010006	–
0.02	0.0000066713	Предельная (достигнутая) разрешающая способность при воспроизведении единицы длины – МЕТРА – методами лазерной интерферометрии
0.1	0.0000333564	По принятой оценке соответствует размерам атомов
1.0	0.0003335642	–
2.0	0.0006671283	–
5.0	0.0016678202	–
15	0.0050034624	–
20	0.0066712819	–
35	0.0116744645	Размеры уровней технологических узлов маршрутной карты ITRS (для производства компонентов наноэлектроники) [2], для которых должна быть обеспечена разрешающая способность менее (0.003 – 0.002) nm
50	0.0166782047	
70	0.0233494936	
100	0.0333564192	
130	0.0433633332	–
200	0.0667128181	–
500	0.1667820420	–
1000	0.3335641729	–
2000	0.6671282014	–
3000	1.0043983523	–

Из таблицы 2 можно сделать вывод, что указанные в [2] проблемы точности измерений размеров уровней технологических узлов маршрутной карты ITRS (35, 50, 70 и 100 nm с точностью порядка 0.002 nm) для производства компонентов наноэлектроники решаются при реализации описанного метода.

В заключение отметим, что частотный метод измерения длин может облегчить решение задач прослеживаемости измерений, важность которых указана в [1,2]. Прослеживаемость измерений, проводимых в нанометровой области, обеспечивает их точность и воспроизводимость. При этом частота стандарта частоты (как и эталонные интервалы времени) может быть передана через каналы связи. Предложенный метод позволяет поддерживать одноступенчатую связь с первичным стандартом частоты любых удаленных средств измерений и систем.

Описанный метод задания (или измерения) изменения длины Δl контура задержки ГОМ дает возможность по двум частотам (при известном значении скорости света c) с наивысшей точностью задавать (или измерять) изменение периода повторения генерируемых импульсов ГОМ. Это изменение периода, в свою очередь, равняется половине времени прохождения светом расстояния, равного задаваемой (измеряемой) длине, выраженной в метрах, согласно определению Метра, принятому в 1983 г. 17-ой Генеральной конференцией по мерам и весам.

ССЫЛКИ

1. П.А. Тодуа. Измер. техн., **5**, 5 (2008).
2. M.T. Postek. Proc. SPIE, **4608**, 84 (2002).
3. Ю.А. Новиков, А.В. Раков, П.А. Тодуа. Тр. Инст. общей физики им. А.М. Прохорова РАН, **62**, 3 (2006).
4. K.M. Evenson, J.S. Wells, F.R. Petersen, B.L. Danielson, G.W. Day, R.L. Barger, J.L. Hall. Phys. Rev. Lett., **29**, 1346 (1972).
5. С.А. Дарзнек, Ж. Желкобаев, В.В. Календин, Ю.А. Новиков Тр. Инст. общей физики им. А.М. Прохорова РАН, **62**, 14 (2006).
6. National and International Needs Relating to Metrology: International Collaborations and the Role of the BIPM – A report prepared by the CIPM for the governments of the Member States of the Convention of the Metre (Ed. BIPM). Sèvres: Intergov. Org. Metre, 71 (1998).
7. В.П. Коронкевич, В.С. Соболев, Ю.Н. Дубнищев. Лазерная интерферометрия. Новосибирск: Наука (1983).
8. Е.Г. Чуляева, А.А. Кондрахин, М.Ю. Керносов, С.А. Складчиков. Мир измерений, **1**, 11 (2008).
9. O. Cip, J. Lazar, F. Petru. Frequency Method of Sub-Nanometer Distance Measurement Using the Optical Resonator and Tunable Semiconductor Laser: http://www.ursi.org/Proceedings/ProcGA02/papers/p1309.pdf.
10. G. Jaeger. In: Proc. XIX IMEKO World Cong. Fund. & Appl. Metrology. Lisbon, 1915 (2009).
11. Fundamentals of Optical Fiber Communications (Ed. M.K. Barnoski). New York – San Francisco – London: Academic Press (1976).
12. М.Н. Дубров, В.А. Алёшин. Журнал радиоэлектроники, **10** (2000): http://jre.cplire.ru/mac/oct00/4/text.html; а также M.N. Dubrov, V.A. Alyoshin. Журнал радиоэлектроники, **5** (2004): http://jre.cplire.ru/alt/may04/1/text.html.
13. Б.С. Могильницкий, А.С. Толстиков, В.Я. Черепанов. Измер. техн., **8**, 9 (2004).
14. А.Г. Данелян, Д.И. Гарибашвили, Р.Р. Канкия, С.А. Мкртычян, С.В. Шоташвили. Измер. техн., **11**, 17 (2009).
15. Х. Гиббс. Оптическая бистабильность. Управление светом с помощью света. англ. Москва: Мир (1988).

НАНОМЕТРОЛОГИЯ: АКТУАЛЬНОСТЬ И ПРОБЛЕМЫ

А.Г. Данелян [1], Р.Р. Канкия [1], С.А. Мкртычян [1], Д.И. Гарибашвили [2], И.Р. Ломидзе [3]

[1] Институт метрологии Национального агентства Грузии по стандартам, техническому регулированию и метрологии
adanelyan@mal.ru
[2] Институт физики им. Э. Андроникашвили
devigar@mail.ru
[3] Грузинский университет им. Андрея Первозванного Патриаршества Грузии
lomiltsu@gmail.com

Принята 29 января 2010 года

Мы живём в период, когда человечество переживает очередную и, возможно, самую масштабную научно-техническую революцию – нанотехнологическую революцию, начавшуюся в конце XX века. Все ведущие страны своевременно оценили перспективы этого витка научно-технического прогресса, увидев в его развитии порой поистине фантастические возможности для человечества. Эти возможности наглядно описаны и систематизированы по разным областям применения в популярной книге пионеров нанотехнологий М. Ратнера и Д. Ратнера [1]. По их оценке, к 2015 году нанотехнология может стать сферой с оборотом в триллион долларов. Поэтому не удивительны те огромные суммы, которые вкладывают сейчас правительства ведущих стран, и многие частные компании и фирмы, в нанонауку и в нанотехнологии (чтобы не упустить свои позиции в этой области). Например, в 2000 г. в США была принята обширная долгосрочная Национальная нанотехнологическая инициатива, подписанная Президентом США Б. Клинтоном, и рассчитанная на двадцать лет (см., например, http://www.nano.gov/html/res/nni2.pdf). Такого же типа программа – A Future Society Built by Nanotechnology (n-pan 21) – была принята в 2001 году и в Японии (http://sciencelinks.jp/j-east/article/200220/000020022002A0759436.php), в которой намечены основные национальные приоритеты в этой области: информационные технологии, биология, энергетика, экология и материаловедение. Был принят и специальный девиз: «создание общества гармонии с природой». Подобные национальные программы по нанотехнологиям были приняты и в других передовых странах. Известно, что в нанотехнологиях пока наибольшее финансирование вкладывается в разные направления наноэлектроники [2].

Специфика нанодиапазона требует для развития нанонауки и нанотехнологий довольно внушительных материальных затрат. Очевидно, этим можно объяснить, что в Грузии, при существующем сегодняшнем состоянии экономики и политической ситуации, не было соответствующих возможностей для активных работ в этой области. Тем не менее, факт появления настоящего сборника говорит о высоком научном потенциале учёных Грузии, которые хоть с какой-то задержкой (по сравнению с другими странами) и в таких экстремально сложных для научного творчества условиях, не располагая требуемыми современными оборудованием и материалами (компонентами), смогли заявить о своих возможностях внести свой вклад в нанонауку и нанотехнологии. При этом хотелось бы надеяться, что все требования, предъявляемые к нанонауке и нанотехнологиям, будут учтены в исследованиях, работах по нанотехнологиям и в нашей стране.

Особо следует отметить роль метрологии в развитии нанотехнологии. Если разработчики Грузии своими исследованиями намерены включиться в международное сотрудничество, нужно активно развить метрологические работы. Ведь результаты выполненных в Грузии

исследований могут быть проанализированы или воспроизведены в других странах (и это было бы очень желательно). При этом должно быть соблюдено единство измерений, чтобы измерения, выполненные в Грузии и в других странах (или даже в пределах Грузии, но в разных лабораториях) были сделаны в одних единицах, размеры этих единиц были одинаковыми и были привязаны к одному Первичному эталону (ПЭ) единицы измерения, чтобы существовало доверие к оценке неопределённости измерений, выполненных в Грузии. Заметим, что в настоящее время во всём мире перешли от привычной в прошлые годы оценки погрешности измерений к оценке неопределённости измерений, которая охватывает учёт ряда дополнтельных факторов, которые не учитывались раньше. Важным является вопрос о прослеживаемости измерений, т.е. документально подтверждённой связи применяемого средства измерения с Первичным эталоном соответствующей единицы физической величины посредством сличений эталонов единиц величин, калибровки средств измерений. По прослеживаемости оценивают качество измерений, т.е. насколько точность выполненных измерений или точность применяемых средств измерений отличается от точности единицы измерения, воспроизводимой эталоном этой единицы (т.е. насколько близко к точности эталона производятся измерения) и многое другое в современной метрологии.

Метрология – это наука об измерениях, методах и средствах обеспечения их единства и способах достижения требуемой точности [3]. Когда речь идёт о метрологии для задач нанодиапазона, понимаются измерения объектов, процессов, явлений, которые находятся или протекают в предельном масштабе – молекулярном (или атомном). Уже почти 10 лет введён термин – нанометрология. Нанотехнология оперирует с характерными размерами от сотен нанометров до десятых долей нанометра (расстояние между атомами в твердом теле). Такие малые размеры измеряемых объектов при переходе к нанотехнологиям выдвинули перед наукой ряд новых специфических задач. Здесь особенно актуален тезис «если нельзя правильно измерить, то невозможно создать». Этот тезис перекликается с известными рассуждениями в конце XIX века великого английского физика Вильяма Томсона (Сэра Лорда Кельвина), который конечно не мог знать и думать о нанотехнологиях: «В физической науке первым и наиболее важным шагом в направлении исследования любого объекта является нахождение принципов количественного расчёта и практических методов для измерения некоторых свойств, связанных с ним. Я часто говорю, когда Вы можете измерить что-то, о чём говорите, и выразить количественно, Вы знаете кое-что об этом; если же не можете измерить его, если не можете это выразить количественно, Ваши знания ограничены и неудовлетворительны. Однако, началом знаний может стать, если сможете хотя бы выдвинуть предложения, мысли, как реально поставить эти исследования».

В работе [4] подчёркивается, что «все страны, вступившие на путь освоения нанотехнологий, прекрасно представляют себе необходимость опережающего формирования метрологии в этой бурно развивающейся области знания, поскольку именно уровень точности и достоверности измерений способен либо стимулировать прогресс соответствующих отраслей экономической жизни общества, либо служить сдерживающим фактором».

«Причина, по которой нанотехнологии поднялись на поверхность в наше время, заключается в том, что возникли инструменты, позволяющие видеть, измерять и манипулировать веществом на наноскопическом уровне. Они всё ещё грубые, и технологии их получения неоптимальные, но ситуация быстро меняется». Этим в работе [1] подтверждается, что возникновение и развитие нанонауки и нанотехнологий было бы невозможным без визуализации нанообъектов и без создания соответствующих методов и техники измерений. Устройства визуализации исследуемых нанообъектов и средства измерений представляют собой инструменты для измерения наноструктур. Отметим, что развитые в прошлом веке методы оптической микроскопии не позволяли наблюдение наноскопических объектов из-за дифракционных ограничений.

Одними из первых инструментов, которые способствовали началу и бурному развитию нанотехнологической революции, стали сканирующие зонды, основанные на идее, впервые разработанной в 1980 г. под руководством Г. Биннинга в лаборатории IBM в Цюрихе. Самыми распространёнными сканирующими зондами стали сканирующие зондовые микроскопы (СЗМ). Первым из них был разработан сканирующий туннельный микроскоп (СТМ). За его открытие и создание Г. Биннинг и Г. Рорер в 1986 г. были удостоены Нобелевской премии. Позже были разработаны и нашли широкое применение и другие типы СЗМ: атомно-силовые микроскопы (АСМ), магнитно-силовые микроскопы (МСМ) и некоторые другие. В последнее время появляются сообщения о новых типах зондовых оптических микроскопов ближнего поля, применяемых для нанотехнологий. Образное описание идеи работы сканирующих зондов приведено в [1]. «По сути, данная идея проста: если провести пальцем по поверхности, легко отличить бархат от стали, или дерево от смолы. Различные материалы с различной силой воздействуют на палец, когда им проводят по различным поверхностям. В данных экспериментах палец действует, как структура изменения силы. Им легче провести по атласной простыне, чем по нагретой смоле, поскольку нагретая смола оказывает более сильное сопротивление пальцу. Данная идея положена в основу сканирующего микроскопа, одного из распространённых сканирующих зондов. При измерении с помощью сканирующего зонда, зонд скользит по поверхности так же, как это делают пальцы. Зонд имеет наноскопический размер...». В туннельном микроскопе (СТМ) измеряется величина электрического тока, протекающего между сканирующим зондом и поверхностью. В зависимости от того, как проводятся измерения, микроскоп можно использовать для измерения локальной геометрии (насколько поверхность локально выступает вперёд), либо для измерения локальных характеристик электропроводности. В АСМ электроника используется для измерения силы, вводимой кончиком зонда (кантилевера) при его движении вдоль поверхности. Это точно те же измерения, что проводятся скользящими пальцами, только сведённые до наноскопических масштабов. В МСМ зонд, сканирующий поверхность, является магнитным. Он позволяет почувствовать на поверхности локальную магнитную структуру. Зонд МСМ работает подобно считывающей головке жесткого диска компьютера – «винчестера» или магнитофона.

«Чтобы изображение любого сканирующего инструмента подать человеку, часто используется компьютерное представление. Это позволяет улучшить необработанные данные, которые будут выглядеть так же хорошо, как прозрачное рентгеновское изображение багажа в аэропорту... Сканирующий наноскопический зонд, скользящий по поверхности, используется для изучения наноскопическх структур через измерение сил, токов, магнитного сопротивления, химической чистоты или других специфических свойств... Сканирующие микроскопы позволили впервые увидеть вещи размером с атома. Это было необходимо для измерения и понимания наноразмерных структур» [1].

Отметим, что до сих пор шла речь о методах визуализации измеряемых нанообъектов. Создание сканирующих зондов, сканирующих зондовых микроскопов позволило получить лишь качественную визуальную информацию о технологических процессах и научных исследованиях в нанометровом диапазоне. Измерения были относительными, без привязки к существующим шкалам единиц физических величин. Развитие нанонауки, нанотехнологий потребовало и количественных оценок. Эти оценки позволяют обеспечить получение с требуемой точностью измерительную информацию о заданных эксплуатационных показателях или результатах измерения и контроля нанообъектов. Это необходимо и для обеспечения единства измерений в нанодиапазоне. Для того, чтобы возможно было проводить измерения, необходимо связать с применяемым зондом (микроскопом) средство измерений, шкала которого прокалибрована в единицах измеряемой величины. Например, если проводятся измерения линейных наноразмеров, то в качестве таких средств измерений наибольшее распространение получили лазерные интерферометры перемещений, в которых материальным носите-

лем единицы длины является длина волны излучения высокостабилизированного лазера. Длина волны этого лазера, прокалиброванная на соответствующем эталоне единицы длины, позволяет перенести размер единицы длины – метра – в нанодиапазон. Но это происходит с определённой погрешностью. При этом необходимо отметить следующее. В конце XX века метрологическое обеспечение измерения длин и перемещений менее 1 m осуществлялось только в диапазоне 1 μm – 1 m. Этому соответствовала принятая многоступенчатая передача размера единицы длины от ПЭ метра к измеряемому объекту. Такую схему передачи во многих публикациях по метрологии представляют в виде пирамиды, в основании которой располагается вся совокупность рабочих средств измерений. В вершине располагается Первичный эталон (в данном случае Первичный эталон единицы длины). «На промежуточных уровнях (на различных сечениях, параллельных основанию призмы) расположены эталоны 1-го, 2-го, 3-го разрядов. Каждый из них обладает некоторыми свойствами как эталонов верхнего, так и нижнего уровня, что позволяет передать размер единицы между уровнями. Такое большое количество уровней понижает точность измерений от 0.02 нм для Первичного эталона до 100 нм на измеряемом объекте, что не позволяет производить измерения менее 1 мкм» [6]. Но такая точность сегодня уже совершенно недостаточна для измерений в нанотехнологиях. Например, в работе [2] приведена информация о маршрутной карте, разработанной согласно Программе развития микроэлектроники США для полупроводниковой промышленности. Согласно этой карте ещё в 2002 году для некоторых технологических операций уже требовалось измерять размеры порядка 100 nm с разрешающей способностью порядка 0.004 nm. Но тогда решение этой задачи было проблематичным. А согласно этой маршрутной карте на ближайшие годы планировалось достичь измерений критических размеров узлов микросхем порядка (30 – 50) nm с разрешающей способностью порядка 0.002 nm. Лазерная интерферометрия, применяемая в этих технологических процессах, по многим причинам до настоящего времени не позволила решить эти проблемы с требуемой точностью. Требовался и требуется новый подход. Отметим, что авторами настоящей работы предложен новый частотно-временной метод измерения длин и линейных перемещений, альтернативный методам лазерной интерферометрии [7,8]. По предварительной оценке, метод должен позволить достичь разрешающей способности измерений лучше, чем 0.001 nm. При этом возможна одноступенчатая передача размера единицы длины от ПЭ к рабочим средствам измерений. Т.е. возможна организация одноступенчатой прослеживаемости линейных измерений (без потерь точности на промежуточных этапах). И ряд ещё других преимуществ. Однако, это всё требует экспериментальной проверки.

Сказанное выше относилось к линейным измерениям. Но проблемы, связанные с передачей размеров единиц любых физических величин от Первичных эталонов единиц этих физических величин в нанодиапазон (и при этом с возможно минимальными потерями точности) относятся ко всем видам измерений, которые проводятся в нанодиапазоне. Для каждого вида измерений существуют свои проблемы с передачей размера единицы с минимальными потерями точности. Однако, при измерениях некоторых физических величин в нанодиапазоне проблемы не ограничиваются только точностью передачи размера единицы в нанодиапазон. Проявляется особая специфика, связанная с наноразмерами (часто намного меньшими, чем длина волны). Понять эту специфику и некоторые проблемы метрологии для нанодиапазона можно из приведённой ниже выдержки из работы [8]:

«Как известно, в метрологии рассматривают связь между физическими величинами и принципами построения системы единиц измерения. В свою очередь, физическая величина трактуется как свойство физических объектов, качественно общее для многих объектов, но количественно индвидуальное для каждого объекта. Особенность построения метрологии истинных нанообъектов ($L = 1...100$ нм), т.е. нанометрологии, состоит в том, что при уменьшении размеров массивного тела до нанометровых, его физико-химические свойства постепенно (или скачкообразно) меняются, и при этом формируется новая фаза вещества, отлич-

ная от исходной (объёмного твердого тела). Наночастицы, в которых характерный размер становится соизмеримым с какой либо физической величиной размерности длины (длина волны Де Бройля, свободного пробега электронов проводимости, глубины скин-слоя), будут проявлять свойства, отличные от свойств частиц больших размеров. Например, в металлах происходит изменение характера межатомной связи от металлической до ковалентной с переходом кластера (кластер – группа близко расположенных, тесно связанных друг с другом атомов, молекул, ионов, ультрадисперсных частиц. – *прим*. *авт*.) металла в неметаллическое состояние при уменьшении его размера до 2-3 нм. Наблюдаются также явления локализации электронов и флуктуации проводимости, приводящие к отсутствию самоусредняемости в системе наночастиц. В системе наночастиц возникает каталитическая активность, отсутствующая в объёмных материалах, флуктуации формы наночастиц. Изменение физических характеристик нанокластеров также определяется соотношением атомов в объёме и на поверхности кластера, свойства которых существенно отличаются.

В силу этого нанометрология должна развиваться в двух направлениях. Первое заключается в повышении точности существующих методов измерения характеристик макроскопических объектов до наномасштаба и, главным образом, связано с совершенствованием технологии; второе – в разработке новых методов измерения характеристик наноразмерных объектов в области, где начинают проявляться особые свойства вещества, не присущие макроскопическим объектам.

Поскольку объективной количественной оценкой физической величины является её единица, т.е. шкала физической величины, в случае нанообъектов трудно однозначно определить такую шкалу. Кроме проблемы создания единиц физических величин в нанометрологии существует также проблема выбора методов и средств измерений, методов определения точности и обеспечения единства измерений. Так, известно, что добавки наночастиц в некоторые материалы, даже при незначительных концентрациях могут приводить к существенному изменению макроскопических свойств таких материалов (например, упрочняющие нанодобавки в бетоны, или антисептическое действие частиц серебра, имплантированных в ткани перевязочные материалы). Однако не всегда существующие аналитические методы позволяют регистрировать малые концентрации наночастиц (числовую плотность частиц), что затрудняет сертификацию такой продукции. С другой стороны, переход микроэлектронной промышленности на изготовление микросхем с проектными нормами 45 нм предъявляет новые требования к чистым комнатам, что связано с разработкой методов детектирования и методик анализа дисперсного состава частиц атмосферы с размерами в несколько десятков нанометров, а также создание эталонов наночастиц.

Для исследований и создания наноструктурированных покрытий, тонких плёнок и малых элементов начинает применяться наноиндентирование, т.е. измерение твердости материалов на уровне наномасштабов. Однако, несмотря на выпуск приборов для этой цели, в настоящее время их метрологическое обеспечение отсутствует. Возникают задачи разработки эталонов твердости на наноуровне, стандартов на размеры наноинденторов, методик расчётов твердости, и, возможно, пересмотра самого определения твердости применительно к наноразмерным масштабам ...».

В связи с бурным развитием нанонауки и нанотехнологий в некоторых источниках (например, [9,10]) уже ставится вопрос о необходимости общего пересмотра определений единиц измерений с учётом открытых и открываемых исследователями квантовых явлений, которые характеризуются фундаментальными константами. Напомним, что к таким эффектам и явлениям можно отнести, например, стационарный и нестационарный эффекты Джозефсона, квантовый эффект Холла, явление «кулоновской блокады» и эффект одноэлектронного туннелирования – «кулоновской лестницы» и др. Уже известны предложения по созданию на основе эффекта одноэлектронного туннелирования одноэлектронных транзисторов [11]. В работе [10] предлагается, например, на базе нестационарного эффекта Джо-

зефсона, квантового эффекта Холла и эффекта одноэлектронного тунелирования создать квантовый электрический стандарт («метрологическую триаду»), связывающий измеряемые величины – напряжение V, силу тока I и частоту ν с указанными квантовыми явлениями и физическими константами. Все эти успехи нанонауки стимулируют создание новых материалов, которые могут позволить создание элементов наноэлектроники, работающих не только при криогенных, но и комнатных температурах. Например, в 2004 году россйкими учёными А. Геймом и К. Новоселовым, работающими сейчас в Манчестерском университете, создан материал графен [12] – углеродная пленка толщиной в один атом. Графен можно представить себе как двумерный «срез» кристаллической гексагональной решетки графита. Предварительные исследования показали, что графен самый прочный материал. Этим учёным удалось вырезать (выделять) из графена площадки размером до 10 nm, на которых были созданы одноэлектронные транзисторы. Оказалось, что графен проводит электроны намного лучше, чем кремний. Кроме того, графен обладает очень хорошей теплопроводностью. Оказалось, что транзисторы на ооснове графена могут работать в терагерцовой частотной области. Все эти свойства предсказывают графену очень большую перспективу в создании сверхбыстродействующих и малогабаритных квантовых компьютеров будущего. Тем более, что эта же группа ведёт активные работы по созданию графеновых одноэлектронных транзисторов с размерами порядка 1 nm. Сказанное приводится для того, чтобы показать, какие стоят перед нанометрологией сложные проблемы измерений в случае таких специфичных экспериментов и технологий в нанонауке, тесно связанных с квантовыми эффектами, проблемы метрологического обеспечения этих экспериментов и технологий, проблемы методов и техники измерений физико-химических характеристик новых материалов при экстремально малых наноразмерах. Возможно даже создание новых систем единиц измерений, учитывающих и эффекты нанодиапазона, и законы классической физики.

Особо следует сказать о возможном влиянии нанообъектов, наночастиц (физико-химические свойства которых могут существенно отличаться от свойств этих веществ в макротеле) на здоровье, на окружающую среду. Вопросы безопасности выдвигаются на первый план. И в этом случае вопросы метрологии, вопросы точных измерений физико-химических характеристик нанообъектов становятся особенно важными при дальнейшем развитии нанотехнологий. В работе [9], в которой особое внимание уделяется важности метрологии для решений проблем безопасности для нанотехнологий, говорится: «В Европейском союзе в рамках 7-ой рамочной программы финансируются проекты по таким направлениям, как оборудование и методы для нанотехнологии; координация разработок в области нанометрологии; оценка рисков производства и использования наночастиц для здоровья и окружающей среды; разработка базы данных по вопросам влияния наночастиц на здоровье, безопасность и окружающую среду; методы измерения параметров наноструктурированных материалов».

Во всех передовых странах предпринимаются организационные меры по предупреждению возможных рисков, связанных с развитием нанотехнологий. Так, в Германии исследования и анализ влияния нанотехнологий проводятся в рамках Федерального агентства по образованию и исследованиям при тесном сотрудничестве с Федеральным агентством по охране окружающей среды, Федеральным институтом безопасности жизнедеятельности и здоровья, Федеральным институтом оценки рисков при финансировании, Федеральным министерством образования и исследований. В США система стандартизации нанотехнологий в рамках государственной целевой программы Национальная нанотехнологическая инициатива поддерживается двадцатью департаментами и агнетствами, включая Национальный Институт стандартов и технологий (NIST), Управление по контролю за продуктами и лекарствами (FDA), Комиссию по безопасности потребительских товаров (CPSC) и Управление по охране окружающей среды (EPA). Аналогично и в других странах. Т.е. уделяется особое внимание контролю (направленному на обеспечение безопасности для здоровья и

экологии) за нанотехнологической продукцией, разработке и созданию стандартов, согласно требованиям которых следует осуществлять этот контроль. Но в основе всех этих стандартов лежит метрология.

Отметим, что Международная организация по стандартизации (ISO) в 2005 году создала новый технический Комитет ISO / TC 229 «Нанотехнологии». Первоочередные задачи этого комитета в стандартизации в области нанотехнологий определены на первом заседании ISO / TC 229 (в ноябре 2005 года в Лондоне) в следующих направлениях: термины и определения, метрология и методы испытаний и измерений, стандартные образцы состава и свойств, моделирование процессов, медицина и безопасность, воздействие на окружающую среду. Решение этих первоочередных задач должно дать мощный импульс развитию нанотехнологий и их практическим применениям и внедрениям в различных отраслях. При этом были определены страны, ответственные за руководство указанными выше направлениями. Так Британский институт стандартизации ведёт общий секретариат; Япония – страна, ответственная за подкомитет ISO / TC 229 / WG2 по метрологии, методам измерений и испытаний; Канада – за подкомитет ISO / TC 229 / WG1 по терминам и определениям; США – за подкомитет ISO / TC 229 / WG3 – по здоровью, безопасности, окружающей среде.

В заключение хотелось бы ещё раз отметить ту огромную заинтересованность в развитии нанонауки и нанотехнологий, которую сейчас проявляют во всех развитых странах, подчеркнуть, что стержневым направлением развития нанонауки и нанотехнологий является метрология (в особенности, её новое направление – нанометрология), об актуальности и проблемах которой говорилось выше. Поскольку учёные Грузии нашли возможность заявить о своих исследованиях в области нанотехнологий, крайне необходимо, чтобы в руководстве Грузии (и на правительственном уровне и в руководстве научными програмами Грузии) было бы понимание актуальности и необходимости развития метрологии (и, конечно, нанометрологии) для работ в области нанотехнологий в нашей стране, чтобы для этого была бы существенная организационная и финансовая поддержка со стороны государства, что необходимо создать систему своих национальных эталонных средств и стандартов для работ и исследований в нанотехнологиях. А для того, чтобы учёные Грузии могли бы гармонично влиться своими работами в международное сотрудничество в области нанотехнологий, необходимо в этих работах учесть требования, которые выдвигает указанный технический Комитет ISO / TC 229 к работам в области нанотехнологий, к стандартам в этой области. Необходимо также, чтобы со своей стороны и наши исследователи понимали бы роль измерений в их работах и сотрудничали с учёными-метрологами Национального института метрологии для создания новых методов измерений, специфичных для их области, чтобы эти измерения были сделаны в установленных в системе SI единицах измерений, чтобы размеры этих единиц воспроизводились от существующих эталонов единиц измерений, а результаты измерений были получены с учётом требований и возможностей современной метрологии.

ССЫЛКИ

1. М. Ратнер, Д. Ратнер. Нанотехнология: Простое объяснение очередной гениальной идеи. Москва: Изд. дом «Вильямс» (2004).
2. M.T. Postek. Proc. SPIE, **4608**, 84 (2002).
3. М.Ф. Юдин, М.Н. Селиванов, О.Ф. Тищенко, А.И. Скороходов. Основные термины в области метрологии. Словарь-справочник (Ред. Ю.В. Тарбеев). Москва: Изд. стандартов (1989).
4. П.А. Тодуа. Мир измерений, **1**, 4 (2008).
5. Ю.А. Новиков, П.А. Тодуа. Мир измерений, **8**, 4 (2005).

6. Ю.А. Новиков, А.В. Раков, П.А. Тодуа. Тр. Инст. общей физики им. А.М. Прохорова РАН, **62**, 3 (2006).
7. А.Г. Данелян, Д.И. Гарибашвили, Р.Р. Канкия, С.А. Мкртычян, С.В. Шоташвили. Измер. техника, **11**, 17 2009).
8. В.И. Троян, М.А. Пушкин, В.Н. Тронин, В.Д. Борман, П.А. Красовский. Измер. техника, **8**, 45 (2008).
9. J. Flowers. Science, **306**, 1324 (2004).
10. А.А. Щука. Наноэлектроника. Москва: Физматкнига (2007).
11. A.K. Geim. Science, **324**, 1530 (2009).
12. С.В. Морозов, К.С. Новоселов, А.К. Гейм, УФН, **178**, 776 (2008).

UV–VIS AND FT–IR SPECTRA OF ULTRAVIOLET IRRADIATED COLLAGEN IN THE PRESENCE OF ANTIOXIDANT ASCORBIC ACID

N.O. Metreveli [1], K.K. Jariashvili [1], L.O. Namicheishvili [2], D.V. Svintradze [2], E.N. Chikvaidze [2], A. Sionkowska [3], J. Skopinska [3]

[1] Ilia State University
nunumetreveli@yahoo.com
[2] I. Javakhishvili Tbilisi State University
[3] Nicolaus Copernicus University

Accepted January 30, 2010

1. INTRODUCTION

Collagen is one of the main components of skin and connective tissue [1,2], which consist of tree polypeptide α-chains wound together in a rod-like helical structure. Each molecule is 300 nm in length and 1.5 nm in diameter with a molecular weight of 300,000. The sequence of amino acid residues in the chains is very specific: glycine is every third residue in repeating sequence; Gly – X – Y and proline and hydroxyproline imino acids are X and Y, respectively, with a high probability. The molecular structure is stabilized by a net of intra- and inter-chain hydrogen bonds between – NH group of glycine and carbonyl group C = O of residues from another polypeptide chain or by hydrogen bridges with water molecules [3–5]. Collagen is the primary target of external factors such as ultraviolet (UV) radiation, which induces various physical, chemical and physical-chemical processes in living organisms. Deleterious UV light absorption is responsible for skin tanning and has been implicated as a causative factor in many kinds of skin cancer. Therefore, the study of UV radiation on a collagen molecule – to illustrate the structural changes in radiated macromolecules, to discover the possible damages after radiation and to search the effective means against the damages – attracts a special interest [6–9].

Many studies have considered the effect of UV radiation on collagen. It has been shown that the solution of collagen, after radiation, loses the ability to form natural fibrils [10]. The fluorescence observed after UV radiation is due to the presence of phenylalanine and tyrosine in this protein [11,12]. Photocrosslinking [13,14] and photodegradation [8,15] of collagen may also occur during exposure to UV radiation.

This paper is a collaboration of Georgian and Polish groups, financially supported by a NATO CLG grant. Both groups have considerable experience studying the effect of UV radiation on collagen. It has been shown that UV radiation changes the thermal helix-coil transitions of collagen samples [16,17]. In addition, the relative viscosity and fluorescence of collagen decreased, whereas the absorption / scattering of collagen solution increased during the radiation of the sample [18].

The Electron Spin Resonance (ESR) method shows that after UV radiation, the generation of primary free radicals (hydrogen atoms and acetic acid radicals) takes place in the water surrounding the acid soluble collagen. The free radicals destabilize proteins, causing the appearance of the secondary free radicals on proline and glycine residues [19,20]. Some molecular compounds, such as melanin, β-carotene and ascorbic acid, have been revealed as photo-stabilizers against photochemical changes in collagen using various techniques [18,19,21–23].

Using UV–Vis and FT–IR spectroscopy, we demonstrate that ascorbic acid, one of the effective antioxidants, acts as a photo-protective system against UV radiation.

2. MATERIALS AND METHODS

Rat tail tendon collagen was selected for investigation. Rat tails were obtained from Poznan University of Medical Sciences (Poland). Each of animals (rats) was before used in another biomedical research according the agreement done by Bioethical Commission working at Medical University in Poznan.

After washing in distilled water the tendons were dissolved in 0.04 M acetic solution [24]. Samples for investigations were prepared as in the form of solutions, as in the form of films, 0.015 mm thick. The films were dried at 35 °C and preserved at room temperature and humidity equal to 60 %.

The samples (films and solutions) of pure collagen (0.9 mg / ml) and collagen containing ascorbic acid (with concentrations of 0.0015, 0.003 and 0.006 mg / ml) were irradiated under air at room temperature using a mercury lamp, Philips TUV – 30, which emits light of mainly 254 nm wavelength. The intensity of radiation during 1 h exposition was 16 J / cm^2. The intensity of the incident light was measured using an IL 1400 A Radiometer (International Light, USA). Irradiation experiments were carried out in a quartz cuvette at a distance of 3 cm from the light source.

The UV–Vis absorption spectra of the collagen solution, before and immediately after irradiation were recorded with Shimadzu Spectrophotometer (model UV – 1601 PC). Data collection and plotting were accomplished by the UVPC program and the computer data station supplied by the manufacturer.

The infrared spectra of films, before and immediately after irradiation, were recorded using spectrophotometer Mattson Genesis II (USA). Spectra were recorded by absorption mode at 4 cm^{-1} interval and 16-times scanning.

3. RESULTS

3.1. UV–Vis absorption spectra

Fig. 1 shows the UV–Vis spectra of pure collagen solution before and immediately after irradiation. Due to the aromatic residues (tyrosine and phenylalanine) absorption in the range of (250 – 300) nm with a maximum at 275 nm takes place for each spectrum. This is consistent with the results obtained in prior studies [16,18]. The authors offer the following explanation: under UV irradiation, the turbidity of the solution increases due to the radiation causing changes in the structure of the collagen molecule (helix-coil transition). After 1 and 2 h irradiation, the maximum of absorption / scattering is almost the same. This fact shows that after 1 h of irradiation, collagen molecules completely change their conformational state.

Fig. 2 shows the UV–Vis spectra of non-irradiated and irradiated collagen solution in the presence of ascorbic acid, with a concentration of 0.0015 mg / ml. The conformation changes in the collagen – ascorbic acid system during irradiation occur much more slowly than in pure collagen.

In the collagen – ascorbic acid system, the difference between the maxima of absorption ($\Delta A = A - A_0$) slightly decreases (Fig. 3, curve with circles) with the increasing dose of radiation. This is in contrast to ΔA of pure collagen (curve with squares).

When the concentration of ascorbic acid was higher (0.003 mg / ml), the sample had no distinctly separate absorption with maximum at 275 nm before irradiation (Fig. 4). Under UV radiation, the absorption at (250 – 300) nm takes place again, although the process connected to the conformational changes of collagen is impeded.

Increasing the concentration of ascorbic acid (0.006 mg / ml) curves only after 45 min of irradiation have typical peak of absorption (Fig. 5) and the above mentioned process is further slowed.

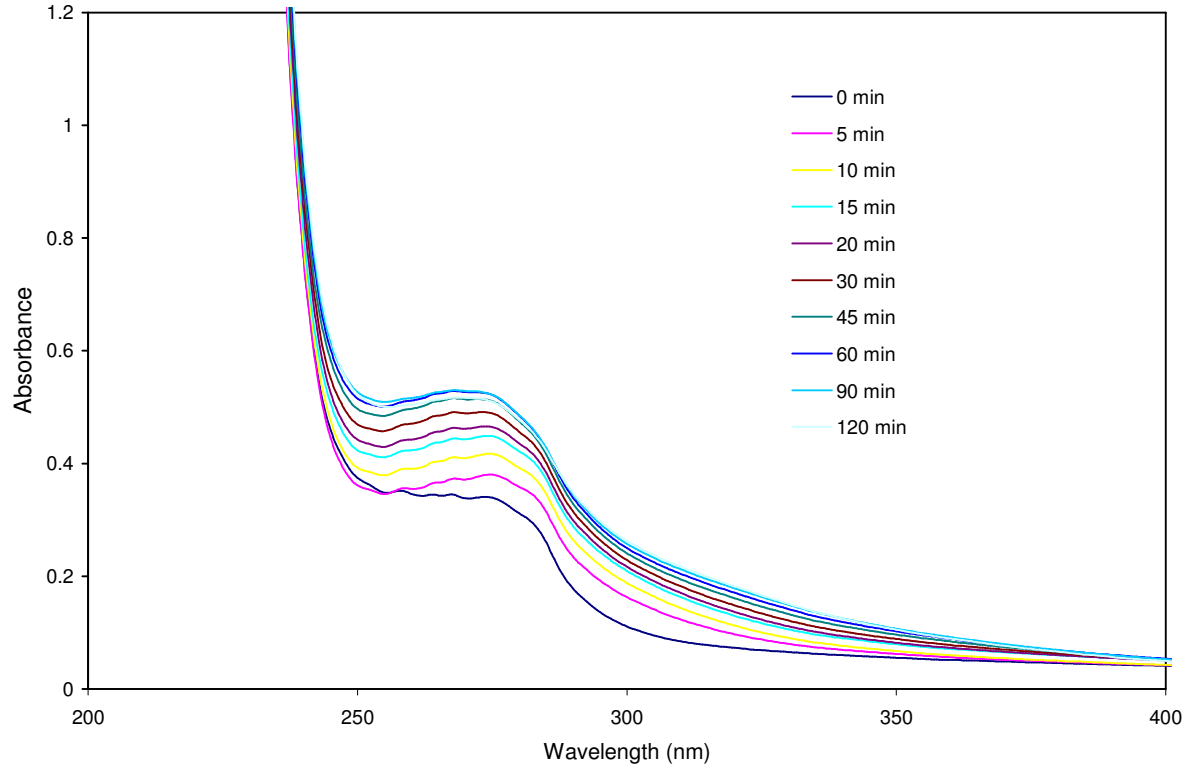

Fig. 1. UV−Vis spectra of pure collagen solution before and after increasing dose of radiation (numbers indicate the times of irradiation in min).

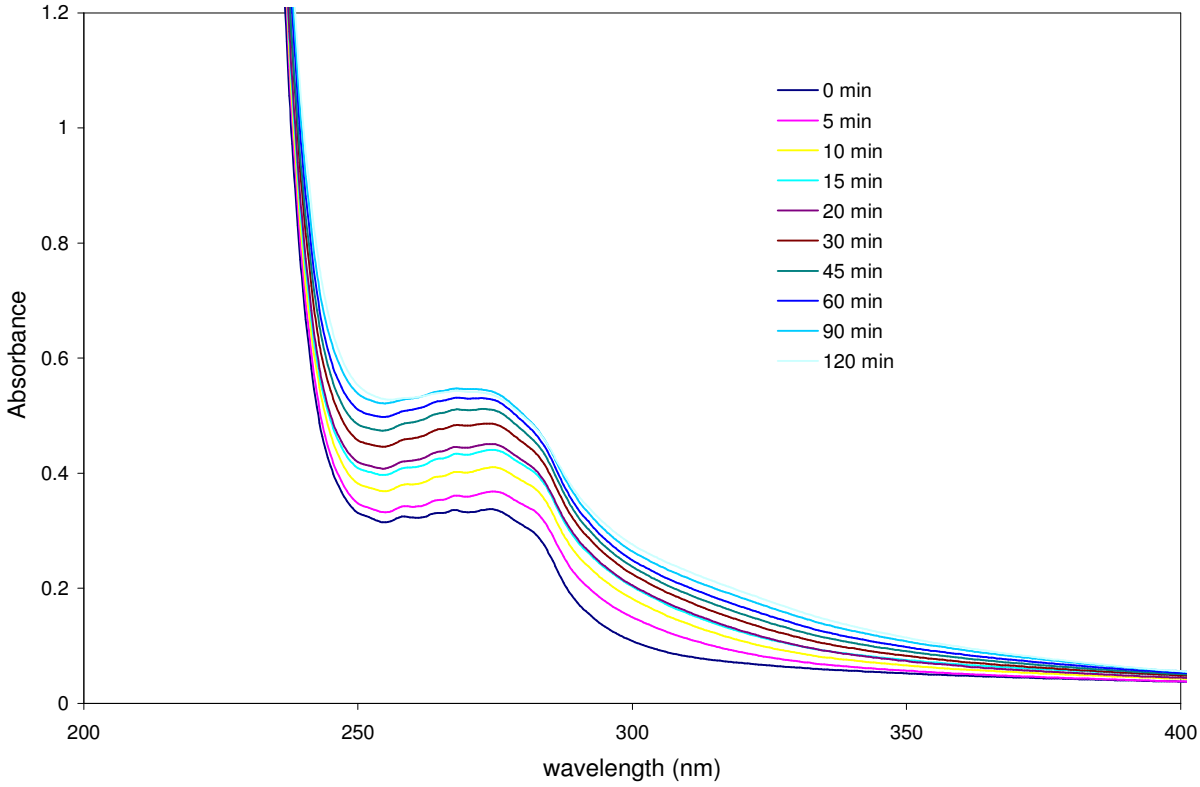

Fig. 2. UV−Vis spectra of collagen solution in the presence of ascorbic acid (0.0015 mg / ml) before and after increasing dose of radiation (numbers indicate the times of irradiation in min).

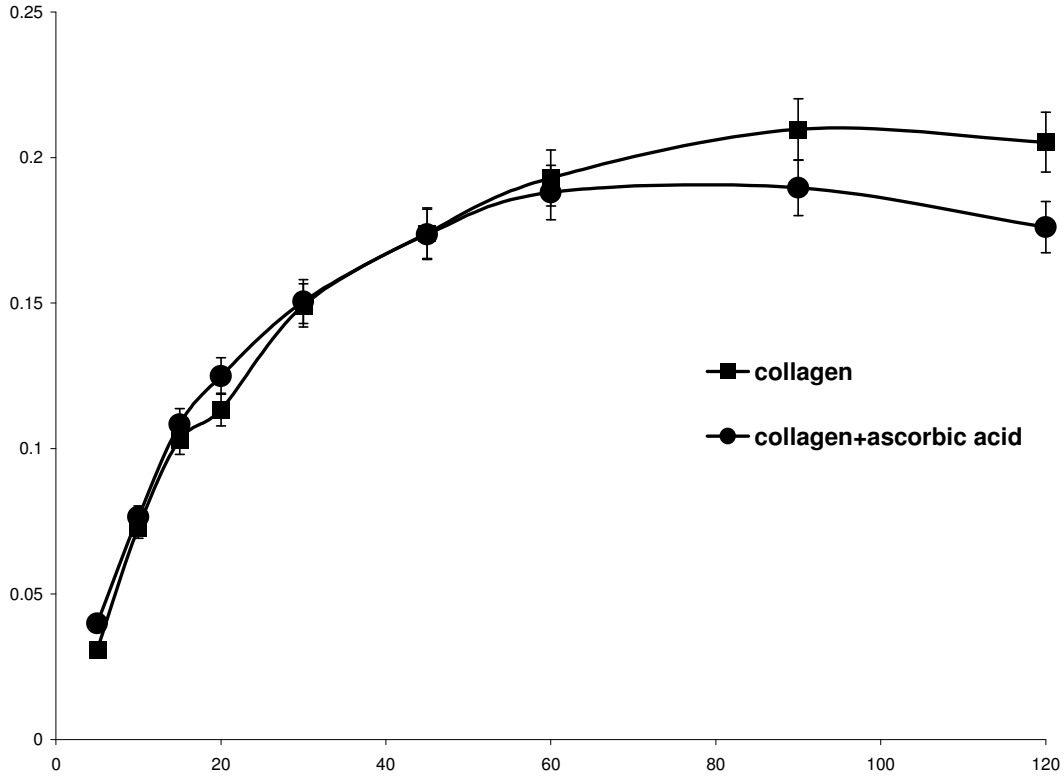

Fig. 3. Dependence of the difference (ΔA) due to the absorbance of radiation at 275 nm of collagen (curve with squares) and collagen with ascorbic acid (curve with circles) on the time of radiation in min (A – absorbance for irradiated sample, A_0 – absorbance for non-irradiated sample).

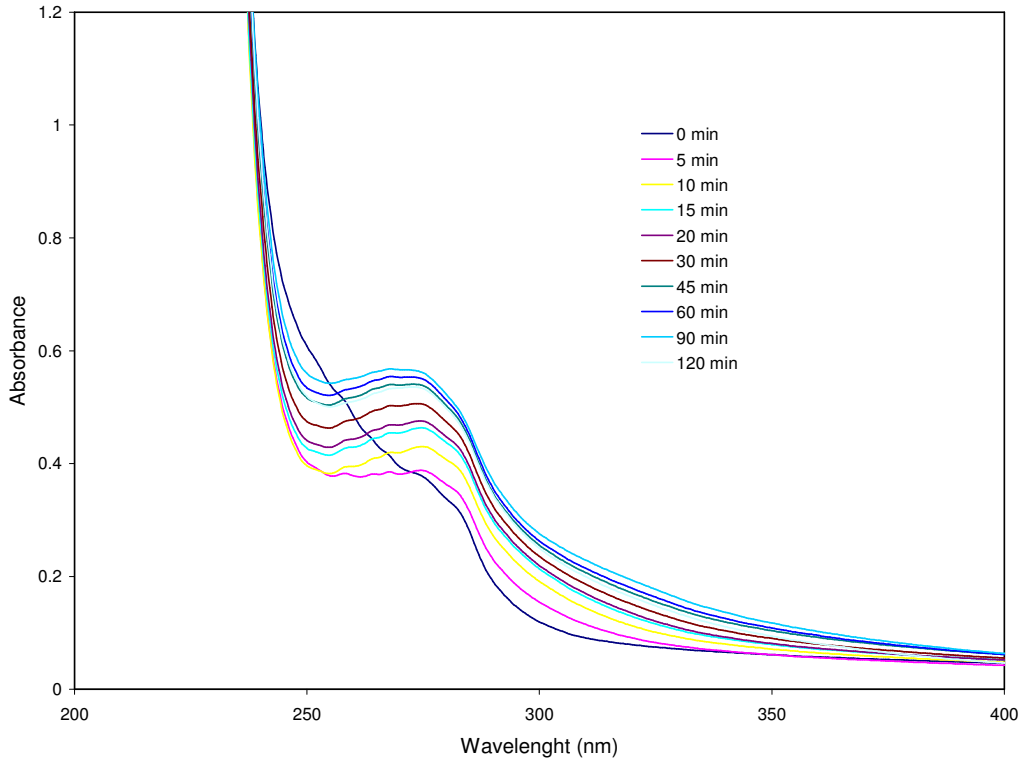

Fig. 4. UV–Vis spectra of collagen solution in the presence of ascorbic acid (0.003 mg / ml) before and after increasing dose of radiation (numbers indicate the times of irradiation in min).

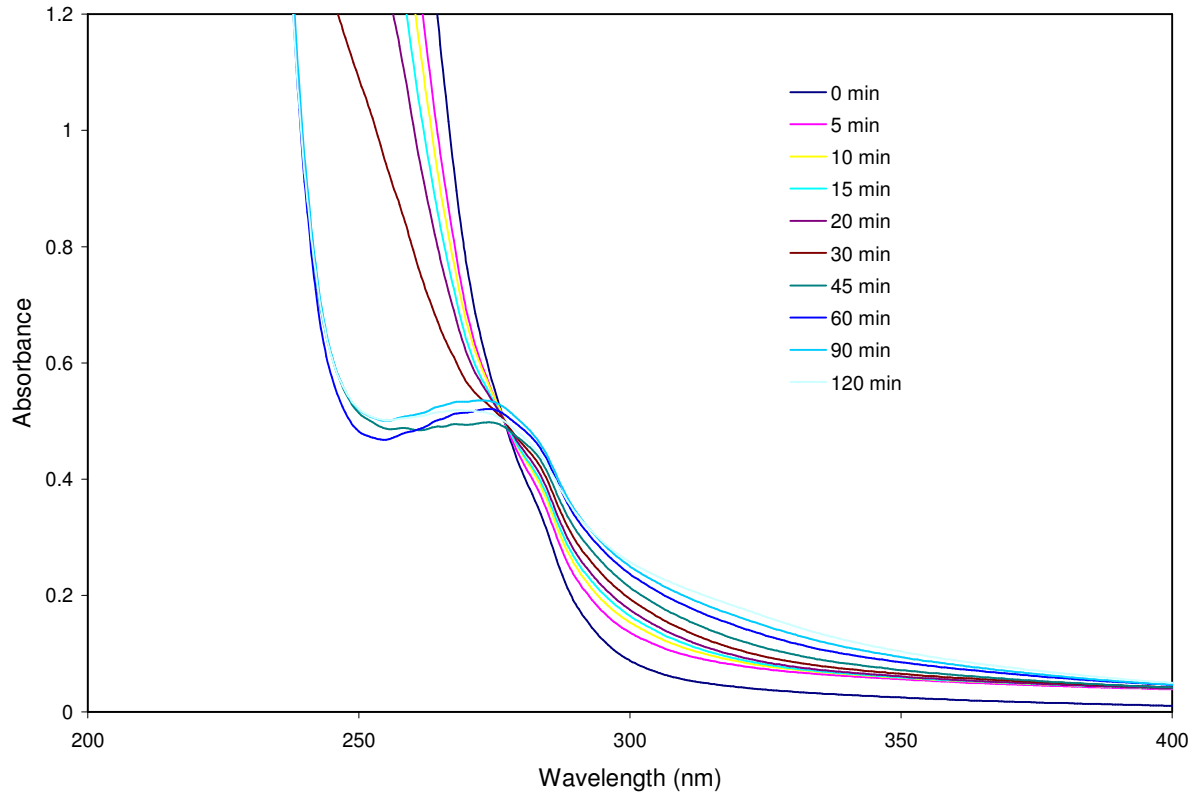

Fig. 5. UV–Vis spectra of collagen solution in the presence of ascorbic acid (0.006 mg / ml) before and after increasing dose of radiation (numbers indicate the times of radiation in min).

3.2. FT–IR spectra

Fig. 6 shows IR spectra of pure collagen films before and after UV radiation. Each spectrum represents the complex of many of the overlapping vibrational bands. Though it is not difficult to separate spectral regions of the amide A, B, I and II bands appearing at the frequencies of 3330, 3082, 1658 and 1558 cm^{-1}, respectively, and amide A and B are shifted to lower frequencies for irradiated samples.

The broad band at 3330 cm^{-1}, amide A, is due to the NH-stretching vibration. It is also due to the OH component, which confirms the active participation of water in the collagen molecule. This band is distinct from other proteins (their amide A is observed at comparatively lower frequency (3300 cm^{-1}), and it is more stable due to the unchangeable distance of N · · · O, even when the α-chains are disordered. The higher the dose of UV radiation, the lower the intensity of absorption and the more narrow the band. There is a noticeable width of amide A band in the range of (3400 – 3600) cm^{-1}, which sharply narrows during irradiation.

The amide B band is observed at around (3050 – 3180) cm^{-1}, with a maximum at 3082 cm^{-1}. This band also shifts to a lower wavenumber and becomes less in intensity.

The amide I band appears in the range of (1600 – 1700) cm^{-1} with a maximum near 1658 cm^{-1}. It is produced mainly by the peptide bond C = O stretching vibration, with intensity slightly decreasing under UV radiation. This band is used for secondary-structure analysis of the polypeptide [25]. Under UV radiation, the dose does not change the position of the band.

The amide II band with a maximum at 1558 cm^{-1} is connected with CNH groups, the intensity of which also decreases under UV radiation. Band position is not shifted to a lower frequency.

The data at the frequencies of the amide bands of pure collagen before and after 8 h UV radiation is shown in the table on Fig. 6.

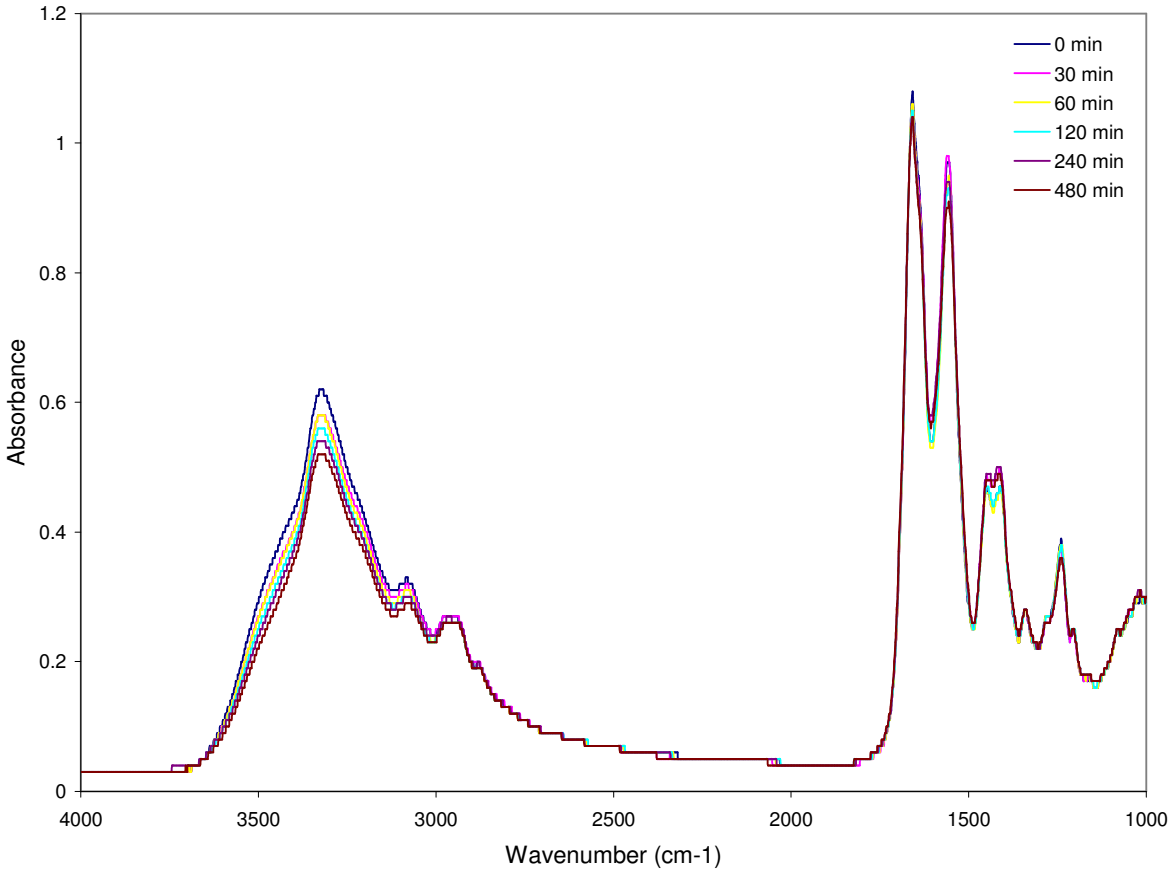

Band	Frequencies of amide bands (cm^{-1})		Change in frequency $\Delta\nu$ (cm^{-1})
	Time of UV irradiation (h)		
	0	8	
Amide A	3330	3326	4
Amide B	3082	3078	4
Amide I	1658	1658	0
Amide II	1558	1558	0

Fig. 6. FT–IR spectra of pure collagen before (0 min) and after (30, 60, 120, 240 and 480 min) radiation.

Figs. 7 and 8 show the IR spectra of collagen films in the presence of ascorbic acid with different concentrations of and 0.003 mg / ml, respectively. Under UV radiation, the intensities of amide bands in both samples decrease as compared to non-irradiated ones, though not as sharply as it occurs in pure collagen. The amide A and B are shifted to a lower frequency at both concentrations of ascorbic acid, though far weaker than in case of pure collagen (changes in frequencies $\Delta\nu$ are less than those for pure collagen). The amide I and II bands do not change their positions (Tables on Figs. 7 and 8).

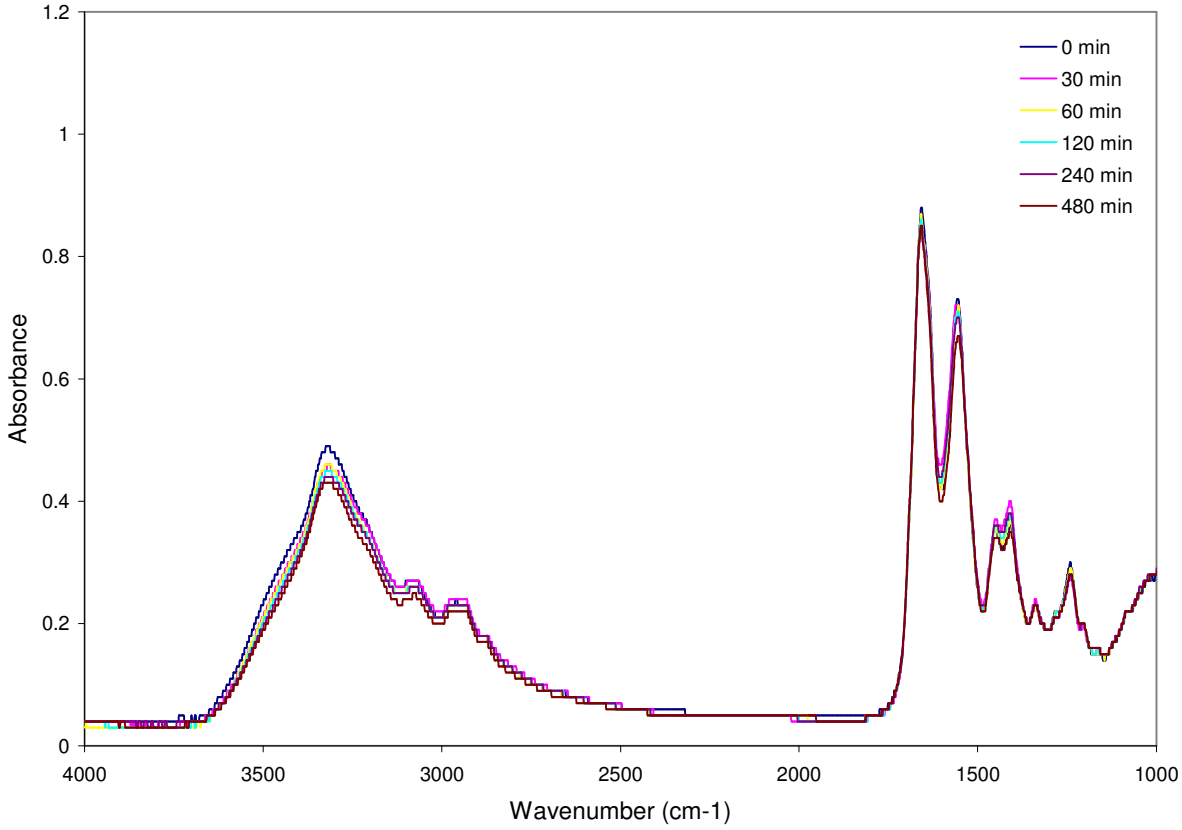

Band	Frequencies of amide bands (cm^{-1})		Change in frequency $\Delta\nu$ (cm^{-1})
	Time of UV irradiation (h)		
	0	8	
Amide A	3323	3321	2
Amide B	3081	3078	3
Amide I	1658	1658	0
Amide II	1556	1556	0

Fig. 7. FT–IR spectra of collagen with ascorbic acid (0.0015 mg / ml) before (0 min) and after (30, 60, 120, 240 and 480 min) radiation.

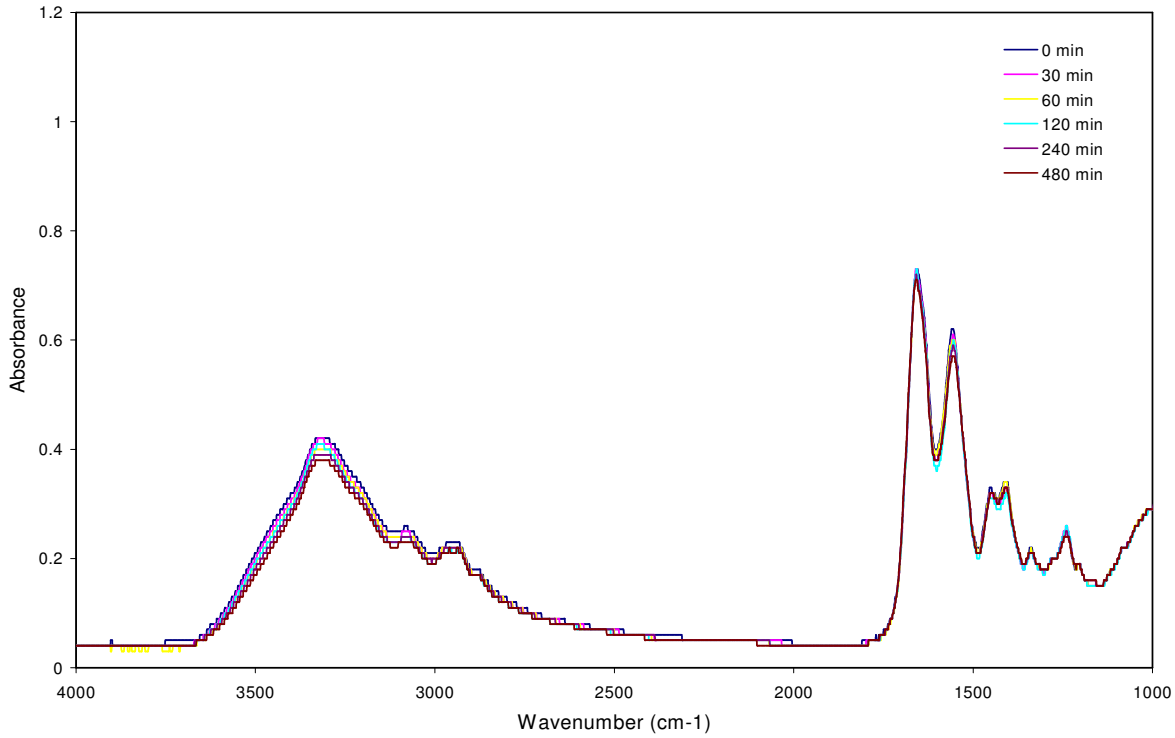

Band	Frequencies of amide bands (cm^{-1})		Change in frequency $\Delta\nu$ (cm^{-1})
	Time of UV irradiation (h)		
	0	8	
Amide A	3318	3316	2
Amide B	3078	3075	3
Amide I	1657	1657	0
Amide II	1556	1556	0

Fig. 8. FT–IR spectra of collagen with ascorbic acid (0.003 mg / ml) before (0 min) and after (30, 60, 120, 240 and 480 min) radiation.

Fig. 9 shows collected IR spectra of non-irradiated samples: pure collagen (curve 1), collagen and ascorbic acid with its 0.0015 mg / ml concentration (curve 2), and collagen and ascorbic acid with its 0.003 mg / ml concentration (curve 3). The intensities of all bands are sharply decreased in the presence of ascorbic acid, and the effect depends on the concentration of the ascorbic acid. All amide bands (A, B, I, and II) are shifted to lower frequencies in the same time (table on Fig. 9).

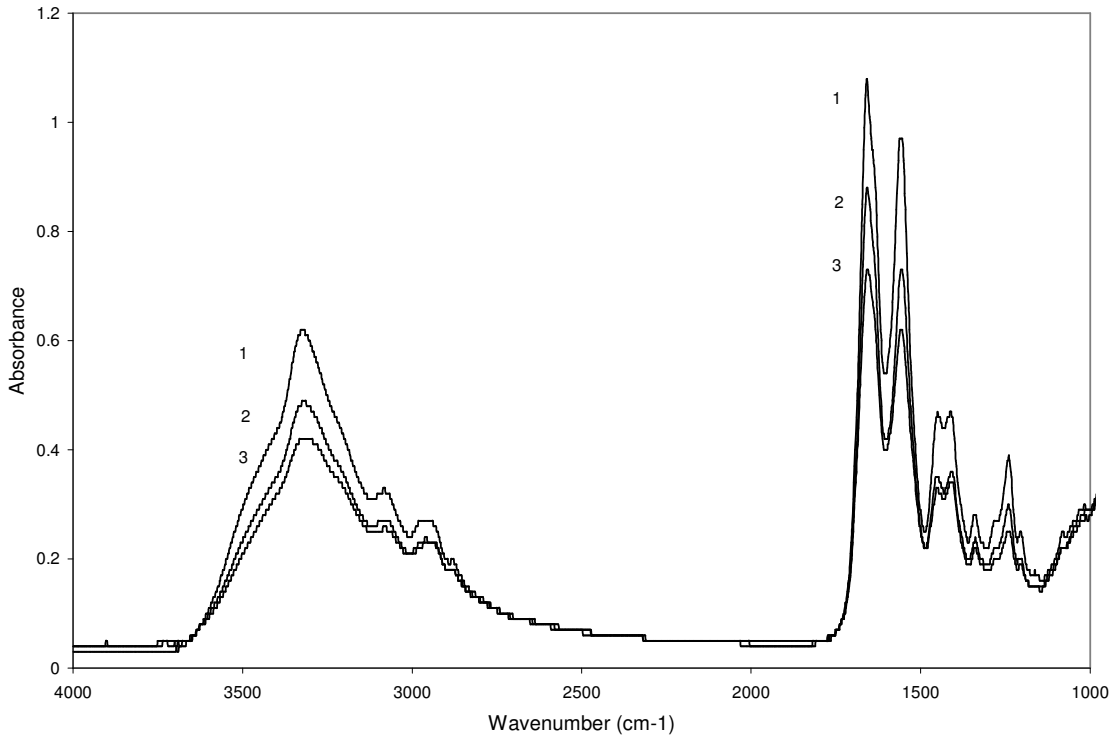

Band	Frequencies of amide bands (cm^{-1})		
	Pure collagen	Collagen with ascorbic acid (0.0015 mg / ml)	Collagen with ascorbic acid (0.003 mg / ml)
Amide A	3330	3323	3318
Amide B	3082	3081	3078
Amide I	1658	1658	1657
Amide II	1558	1556	1556

Fig. 9. FT−IR spectra of non-irradiated samples: collagen – curve 1, collagen with ascorbic acid (0.0015 mg / ml) – curve 2, collagen with ascorbic acid (0.003 mg / ml) – curve 3.

4. DISCUSSION

4.1. UV−Vis absorption spectra

Under UV radiation the conformational changes in collagen – ascorbic acid system occur much more slowly than in pure collagen (Fig. 3). It is likely due to the ascorbic acid's antioxidant feature. Under UV radiation, collagen with ascorbic acid is not as sensitive as collagen alone.

The changes of UV−Vis absorbance profile in the range of (250 – 300) nm (Fig. 4 – 0 min irradiation and Fig. 5 – 0, 5, 10, 15, 30 and 45 min irradiation) might be due to the additional effect of ascorbic acid. We suggest that ascorbic acid connects to collagen with its C = O group. It is possible that OH groups of collagen molecules (mainly of tyrosine amino acid aromatic ring) combine with C = O of ascorbic acid (Scheme 1) to form a hydrogen bond. Another aromatic amino acid is phenylalanine, aromatic ring of which is like that of benzene. It is very hydrophobic and chemically reactive only under extreme conditions. That is why we exclude it from participation in

the mentioned binding reaction. Our previous studies [16,20,22] have been connected with free radicals appearing in collagen water solutions under UV radiation and evoking photodegradation of macromolecule. The aromatic amino acids found in collagen are the primary source of free electrons that form the free radicals. Ascorbic acid, a perfect antioxidant, either donates its electron to restore deleterious free radicals, thus itself becoming a non-toxic free radical, or it impedes aromatics to transit in an excited state under UV radiation, or both. In any case, it is beyond doubt that ascorbic acid changes the environment of a collagen molecule, and the effect depends of the concentration of the ascorbic acid. When increasing the dose of radiation, more molecules of ascorbic acid are hindered, and the antioxidant effect is diminished accordingly.

4.2. FT–IR spectra

Intensities of FT–IR bands have changed under UV radiation. The higher the dose of radiation, the lower the degree of intensities of all bands (amide A, amide B, amide I and amide II) as compared to those of the non-irradiated collagen sample (Fig. 6).

In a previous study [26], it was suggested that under UV radiation, the changes in the amide A and B bands indicate the photodegradation of collagen along its main chains with scission of $-CH_2-N=$ and $=CH_2$ bonds.

There is a noticeable width of the amide A band in the range of (3400 – 3600) cm^{-1}, which sharply narrows during irradiation. It is likely due to the breaking of $N-H\cdots O=C$ inter-chains hydrogen bond as well as losing the bonding water in collagen.

In the presence of ascorbic acid, the intensities of the amide bands of collagen also decrease under irradiation (Figs. 7 and 8), though much more slightly than it occurs for pure collagen. Positions of the amide A and B bands shift to lower frequencies, though in this case, changes in frequencies $\Delta\nu$ are less (see tables on the Figs. 7 and 8) than those for pure collagen (table on Fig. 6). When we have IR spectra of the non-irradiated collagen and the collagen – ascorbic acid system (Fig. 9), intensities of all bands sharply decrease in the presence of ascorbic acid, and the effect depends on the concentration of antioxidant. The reduction of the bandwidth of amide A is presumably due to the restriction of conformational freedom of macromolecules in the presence of ascorbic acid. All amide bands (A, B, I, and II) are shifted to lower frequencies at the same time (table on the Fig. 9). The most remarkable is the amide A band, the shift of which might be due to the formation of a hydrogen bond between N – H group of peptides and C = O group of ascorbic acid (Scheme 1).

Scheme 1.

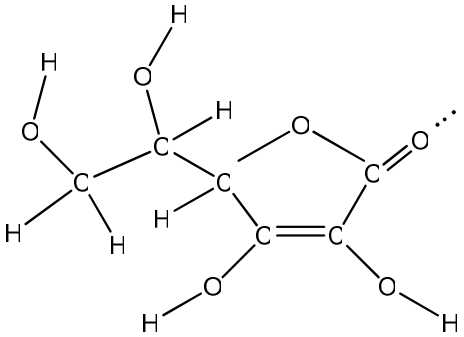

Ascorbic acid

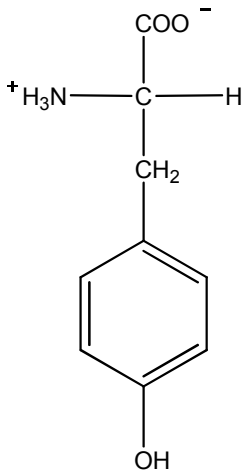

Tyrosine

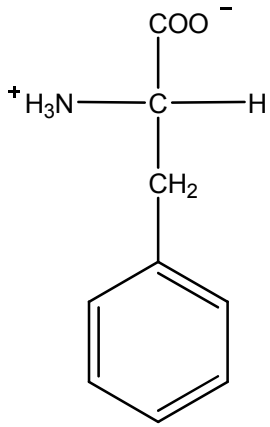

Phenylalanine

Results suggest that ascorbic acid increases the photo-stability of the collagen molecule; and the ascorbic acid interacts with the collagen macromolecule as well.

5. CONCLUSIONS

Structural changes in the collagen molecule occur under UV radiation. Ascorbic acid increases the photo-stability of the collagen molecule, and the molecule becomes less sensitive to the UV radiation. Interaction between collagen and ascorbic acid possibly takes place as well.

ACKNOWLEDGMENT

Financial support from NATO, grant no. CBP.EAP.CLG 982215, is greatfully acknowledged.

REFERENCES

1. B. Alberts, D. Bray, J. Lewis, M. Raff, K. Roberts, J.D. Watson. Molecular Biology of the Cell. New York: Garland Press (1994).
2. D.A.D. Parry, A.S. Craig. In: Ultrastructure of the Connective Tissue Matrix (Eds. A. Ruggery, P.M. Motta). Boston: Martinus Nijhof Publishers (1984).
3. J. Bella, B. Brodsky, H.M. Berman. Structure, **3**, 893 (1995).
4. J. Bella, H.M. Berman. J. Mol. Biol., **264**, 734 (1996).
5. R.Z. Kramer, J. Bella, B. Brodsky, H.M. Berman.. J. Mol. Biol., **311**, 131 (2001).
6. T. Miyata, T. Sohde, A.L Rubin, K.H. Stenzel. Biochimica et Biophysica Acta, **229**, 672 (1971).
7. T. Hayashi, S. Curran–Patel, D. Prockop. Biochem., **18**, 4182 (1979).
8. E. Fujimori. Eur. J. Biochem., **152**, 299 (1985).
9. Ch.A. Miles, A. Sionkowska, S. Hulin, J.S. Trevor, N.C. Avery, A.J. Bailey. J. Biol. Chem., **275**, 33014 (2000).
10. E. Fujimori. Biopolymers, **3**, 115 (1965).
11. E. Fujimori. Biochem., **5**, 1034 (1966).
12. D.V. Crabtree, E. Fujimori. Biopolimers, **19**, 1081 (1980).
13. Y. Kano, Y. Sakano, D. Fujimoto. J. Biochem., **102**, 839 (1987).
14. E. Fujimori. FEBS Lett., **235**, 98 (1988).
15. S.F. Curran, M.A. Amoruso, D.B. Goldstein, A. Berg. FEBS Lett., **176**, 155 (1984).
16. A. Sionkowska, A. Kaminska. Int. J. Biol. Macromol., **24**, 337 (1999).
17. N. Metreveli, L. Namicheishvili, K. Jariashvili, I. Jorjishvili, G. Mrevlishivili. Bull. Georg. Acad. Sci., **164**, 538 (2001).
18. A. Sionkowska. J. Photochem. Photobiol., **124**, 91 (1999).
19. N. Metreveli, L. Namicheishvili, K. Jariashvili, E. Chikvaidze, G. Mrevlishvili. Biophys., **51**, 29 (2006).
20. N. Metreveli, L. Namicheishvili, K. Jariashvili, M. Dgebuadze, E. Chikvaidze, A. Sionkowska. J. Photochem. Photobiol. B: Biol., **93**, 61 (2008).
21. N. Metreveli, L. Namicheishvili, K. Jariashvili, E. Chikvaidze, G. Mrevlishvili. J. Biol. Phys. Chem., **5**, 133 (2005).
22. N. Metreveli, L. Namicheishvili, K. Jariashvili, G. Mrevlishvili, A. Sionkowska. Int. J. Photoenergy, **76830**, 4 pages (2006).
23. A. Sionkowska, A. Kaminska. J. Photochem. Photobiol. A: Chem., **120**, 207 (1999).

24. M.J. Glimcher, C.J. Francois, L. Richards, S.M. Krans. Biochim. Biophys. Acta, **93**, 585 (1964).
25. A. Barth, Ch. Zscherp. Quart. Rev. Biophys., **35**, 369 (2002).
26. A. Kaminska, A. Sionkowska. Polymer Degrad. Stab., **51**, 19 (1996).

MICROBIAL SYNTHESIS OF METAL AND SEMICONDUCTOR NANOPARTICLES

N. Tsibakhashvili [1, 2]

[1] Ilia State University
[2] E. Andronikashvili Institute of Physics
nelly_tsibakhashvili@yahoo.com

Accepted January 31, 2010

Technology based on the use of microbes for the synthesis of nanomaterials is a relatively new and largely unexplored area of research in material synthesis, which has the potential to develop a simple, practical, inexpensive ways to produce novel metallic nanoparticles possessing unique chemical and physical properties.

Biological systems, masters of ambient condition chemistry, synthesize inorganic materials that are hierarchically organized from the nano- to the macroscale. For example, multicellular organisms produce hard inorganic–organic composite materials such as bones, shells, and spicules using inorganic materials to build a complex structure [1,2]. These biominerals are composite materials and consist of an inorganic component and a special organic matrix (proteins, lipids, or polysasharides). The use of microbial systems is very promising approach for assembling nanostructures. Microbial systems may be used as templates for organizing nanoparticles or be programmed to express a set of worker proteins that can synthesize nanoparticles [3,4].Viruses posses hundreds of unique sizes and shapes that may be useful as templates for organizing nanoparticles. Viruses can also be genetically engineered to produce a set of recognition peptides that can selectively identify nanoparticles based on their composition and lattice structure. Microorganisms such as bacteria, fungy, and yeast are recently found as possible eco-friendly nanofactories [5−7], even though they have many biotechnological applications such as remediation of toxic metals [8]. Some microbial cells have developed specific mechanisms for interacting with inorganic ions such as metal and metalloid ions in the surrounding aqueous environment, as a means of protection against toxic metals and / or a means of scavenging trace essential nutrient ions [9]. Sometimes these microbial processes result in metal precipitation, both intracellularly and extracellularly. These mechanisms involved for example, direct redox transformation of ionic species that result in the formation of less soluble species; microbial alteration of the environment (e.g., change in pH) that results in precipitation; microbial excretion or secretion of metabolic products (e.g. carbon dioxide, or sulfide, or phosphate ions) that interact with inorganic species to produce precipitates; and the like. These biomineralization processes have the potential of leading to materials with unusual and / or particularly desirable characteristics. A wide variety of microbially-mediated precipitation mechanisms may be exploited, and wide range of nanoparticles can be prepared. Additionally, by manipulations of key parameters, which control growth and other cellular activities, controlled size and shape of nanoparticles can be achieved.

Below we provide a brief overview of the current research worldwide on the use of microorganisms such as bacteria and actinomycetes (both prokaryotes), as well as algae, yeast, and fungi (eukaryotes) in the biosynthesis of metal and semiconductor nanoparticles and their application.

1. BIOSYNTHESIS OF SILVER (Ag) AND GOLD (Au) NANOPARTICLES

Among the microorganisms, bacteria have received the most attention in the area of biosynthesis of nanoparticles. Biominerals have been formulated by using several bacteria such as

Pseudomonas aeruginosa, *E. coli*, *Citrobacter* sp. [1]. Early studies reveal that bacterium *Bacillus subtilis* 168 is able to reduce Au^{3+} ions to produce octahedral gold particles of nanoscale dimensions, (5 – 25) nm, within bacterial cells by incubation of the cells with gold cloride under ambient temperature and pressure conditions [6,10,11]. Another bacterium – *Pseudomonas stutzeri* AG259 isolated from silver mines accumulates silver nanoparticles in the cell where particle size ranges from 35 to 46 nm [12]. Larger particles (200 nm or more) are formed when *P. stutzeri* AG259 is placed in a concentrated aqueous solution of silver nitrate (50 mM [13]).

Morphological control over the shape of gold nanoparticles has been achieved by using *Plectonema boryanum* UTEX 485, a filamentous cyanobacterium. Expose of *Plectonema boryanum* UTEX 485 to aqueous $Au(S_2O_3)_2^{3-}$ and $AuCl_4^-$ solutions resulted in the precipitation of cubic gold nanoparticles and octahedral gold platelets (6 μm to 10 nm), respectively [14,15]. Another cyanobacterium *Schewanella algae* can reduce Au^{3+} ions in anaerobic environments [16]. In the presence of *S. algae* and hydrogen gas, the Au ions are completely reduced, which results in the formation of 10 to 20 nm gold nanoparticles.

Bacteria not normally exposed to large concentrations of metal ions may also be used to grow nanoparticles. The exposure of *Lactobacillus* strains, which can present in buttermilk, to silver and gold ions resulted to the large-scale production of metal nanoparticles within the bacterial cells [17].

Despite the success and simplicity of biosynthesis methods using bacteria, the resulting silver / gold nanoparticles have large size distribution.

More by chance than by design, it was observed that alkalothermophilic (extremophilic) actinomycete, *Thermomonospora* sp., when exposed to gold ions, reduces the metal ions extracellularly, yielding gold nanoparticles with high polydispersity [18]. A complete reduction of the 10^{-3} M aqueous $HAuCl_4$ solution at pH 9.0 and 50 °C results to spherical and reasonably monodisperse nanoparticles (8 nm size). It was concluded that the monodisperse gold nanoparticles synthesis could be due to extreme biological conditions such as alkaline and slightly elevated temperature conditions used for the synthesis of nanoparticles. The exact reaction mechanisms leading to the formation of silver nanoparticles by this microorganism are not be elucidated. Based on this hypothesis alkalotolerant *Rhodococcus* sp. has been used for intracellular synthesis of good monodisperse gold nanoparticles [19].

Previously, a few yeast strains (*P. jadinii*) have been tested for their ability to produce gold nanoparticles, whereby controlling growth and other cellular activities controlled size (few to 100 nm) and shape of the nanoparticles was achieved [20].Conditions have also been standardized for the synthesis of large quantities of silver nanoparticles, (2 – 5) nm size, by using silver-tolerant yeast strain MKY3 [21].

Nanoparticles with good monodispersity have been obtained by using acidophilic fungus V*erticillum* sp fungi [22]. This has been shown with an experiment where bioreduction of aqueous $AuCl_4^-$ ions was carried out using the fungus *Verticillium* sp. that led to the formation of gold nanoparticles with fairly well-designed dimensions (20 nm) and good monodispersity. Further experiments have documented that the trapping of $AuCl_4^-$ ions on the surface of fungal cells could occur by electrostatic interaction with positively charged groups (such as, lysine residues) in enzymes that are present in the cell wall of the mycelia [23]. Here then gold ions were reduced by enzymes within the cell wall leading to aggregation of metal atoms and formation of gold nanoparticles. However, they could not find the exact mechanism of formation of gold nanoparticles. Other species of fungus specifically, *Fusarium oxysporum, Aspergillus flavus, Trichothecium* sp. are also able to produce gold and silver nanoparticles [24]. However, the monodispersity of produced nanoparticles is much less than that of obtained by acidophilic V*erticillum* sp. In [25] it has been demonstrated that a fungus *Trichoderma asperellum* can be exploited to produce nanocrystalline silver particles with sizes in the range of (13 – 18) nm. It has been established that process of growing silver nanoparticles comprises of two key steps: (a) bioreduction of $AgNO_3$ to produce silver nanoparticles and (b) stabilization and / or encapsulation of the same by suitable capping agents. These nanocrystalls are found to be highly

stable and even after prolonged storage for over 6 months they do not show significant aggregation, which undoubtedly establishes its commercial viability.

Towards elucidating mechanism of nanoparticles formation, an *in vitro* approach was followed where species specific NADH dependent reductase, released by the *Fusarium oxysporum*, were successfully used to carry out the reduction of $AuCl_4^-$ ions to gold nanoparticles [26]. This has first time opened up a novel fungal / enzyme-based in vitro approach for nanomaterial synthesis. Later α-NADPH-dependent nitrate reductase and phytochelatin isolated from *Fusarium oxysporum* has been used for *in vitro* silver nanoparticle production [27].

Apart from individual metal nanoparticles, the bimetallic Au – Ag alloy can be synthesized by *F. oxysporum*. Very recently, it has been shown that by controlling the amount of cofactor NADH, synthesis of quite stable Au – Ag alloy nanoparticles of various compositions have been made possible [28]'s approach can be further employed for producing various other composite nanoparticles.

Nanoparticles have found applications in antibacterial effects [29]. It has been shown that extracellularly produced silver or gold nanoparticles using *Fusarium oxysporum*, can be incorporated in several kinds of materials such as clothes. These clothes with silver nanoparticles are sterile and can be useful in hospitals to prevent or to minimize infection with pathogenic bacteria such as *Staphylococcus aureus*.

Growth medium and conditions play an important role during the production of nanoparticles while using the microorganisms. For example, when gold ions were incubated with the *Trichothecium* sp. (fungus) biomass without shaking this led to the formation of extracellular nanoparticles, while under shaking conditions, this was resulted in the formation of intracellular gold nanoparticles [25]. The possible reason for this could be the enzymes and proteins responsible for the synthesis of nanoparticles. It seems that these proteins did not release under shaking conditions.

2. BIOSYNTHESIS OF SEMICONDUCTORS (QUANTUM DOTS)

In addition to gold and silver nanoparticles, there is much attention in the development of protocols for the synthesis of semiconductor nanoparticles [1,24,30–33]. Semiconductor nanoparticles are an extremely important class of materials. Semiconductor nanocrystalls, also known as "quantum dots" (qdots), are defined as particles with physical dimensions smaller than the Bohr excition radius. Qdots exhibit unique optical and electronic properties that are only observed in an intermediate size region between the size of discrete atoms and that of bulk solids.

The *Candida glabrata* and *Schizosaccharomyces pombe* were used for the first time in the biosynthesis of cadmium sulfide (CdS) nanocrystalls [31–33]. Feeding yeast *Schizosacharomyces pombe* with Cd^{2+}-ions can lead to the expression of a family of proteins that assist in the construction of $(1-3)$ nm CdS-nanoparticles intracellularly [32]. Once, the desired size of nanoparticles is reached, yeast produces a glutathione-like protein to coat the surface of the nanoparticles. This protein helps to stabilize the nanoparticle from aggregation inside the cell and to direct the nanoparticles out of the cell. X-ray scattering data showed that the nanoparticles had a hexagonal lattice structure. Further experiments have been conducted to improve the quantity of semiconductor CdS nanocrystals production that was achieved by using *Schizosaccharomyces pombe* cells [33]. New experiments suggested that the formation of CdS nanocrystals was dependent on the growth phase of yeast. When these cells were incubated with 1 mM Cd during their mid-log phase of growth, maximal nanocrystals were obtained. When Cd was added during stationary phase, its uptake as well as production of CdS nanocrystals was decreased or resulted in no CdS formation. The possible mechanism of decrease in CdS nanocrystals formation was also proposed in this work: upon exposure to Cd as a stress, a series of biochemical reactions were triggered to overcome the toxic effects of this metal. Firstly, an enzyme phytochelatin synthase was activated to synthesize phytochelatins (PC) that chelated the cytoplasmic Cd to form a low

molecular weight PC – Cd complex and ultimately transport them across the vacuolar membrane by an ATP-binding cassette-type vacuolar membrane protein (HMT1). In addition to Cd, sulphide could also be added to this complex in the membrane and that results in formation of high molecular weight PC – CdS^{2-} complex that also allow them to sequestered into vacuole.

According to recent studies [27,34], fungus *Fusarium oxysporum* produces different kinds of semiconductor nanoparticles (CdS, CdSe), however the resulting nanocrystals have low quantum yields (QY < 10 %) and large size distributions (relative standard deviation RSD > 15 %), resulting in broad emission spectra (~ 50 nm full-width at halfmaximum). Exciting is the finding that the exposure of *F. oxysporum* to the aqueous $CdSO_4$ solution yield CdS quantum dots extracellularly [27]. However, reaction of the fungal biomass with the aqueous $CdNO_3$ solution for an extended period of time does not yield CdS nanoparticles, indicating the possibility of the release of a sulfate reductase enzyme into the solutions.

Bacterium *Clostridiumm thermoaceticum* precipitates CdS at the cell surface as well as in the medium from $CdCl_2$ in the presence of cysteine hydrochloride in the growth medium [35]. Most probably, cysteine acts as the source of sulfide. When *Klebsiella aeogenes* is exposed to Cd^{2+} ions in the growth medium, 20 to 200 nm CdS formed on the cell surface [30]. Intracellular CdS nanocrystals, composed of a wurtzite crystalphase, are formed when *E. coli* is incubated with $CdCl_2$ and Na_2S [36]. Nanocrystal formation varies dramatically depending on the growth phase of the cells and increases about 20-fold in *E. coli* grown in the stationary phase as compared with that grown in the late logarithmic phase. The CdS nanoparticles produced within *E. coli* bacteria range in diameter from (2 – 5) nm. Although moderately polydisperse, it was estimated that each bacterium generated greater than 10 000 CdS nanoparticles. Later it was demonstrated that this strain of *E. coli* is able to produce ZnS semiconductor nanoparticles, (20 – 100) nm, as well [36]. In a remarkable investigation, Labrenz et al [37] has shown that spherical aggregates of 2 to 5 nm-diameter (ZnS) particles are formed within natural biofilms dominated by sulfate-reducing bacteria of the family *Desulfobacteriaceae*.

In last years PbS semiconductor nanocrystalls were also synthesized using yeasts and bacteria [38]. It was shown, that *Torulopsis* sp. is capable of synthesizing PbS nanocrystals intracellularly when challenged with Pb^{2+}. Biosynthesized crystalls are (2 – 5) nm in size. In 2007 Gong et al [39] synthesized the uniform nanoparticles PbS with diameters about 13 nm using extremophilic microorganism – thermophilic sulfate-reducing bacterium *Desulfotomaculum* sp. Bacterial cells were exposed to $Pb(NO_3)_2$ action at 15, 25, 35, 40 °C as a batch culture with pH 5-9 for two days. According to experimental observations, Pb^{2+} could directly react with S^{2-} produced by *Desulfotomaculum* sp. and produced PbS nanoparticles immediately. The results also revealed that the PbS crystallites were identical in structure, shape and size under different temperatures while their morphology changed from rod to spheroidal with pH increasing.

3. BIOSYNTHESIS OF METAL OXIDE MATERIALS

Recently the first publications appeared on the synthesis of TiO_2 and ZrO_2 metal oxide materials [40–42]. Bansal et al showed that hexafluorozirconate ions can be reacted with *Fusarium oxysporum* to yield zirconia nanoparticles of average size (3 – 11) nm [40]. Later, they have extended their findings through a detailed study of the reaction of the fungus *Fusarium oxysporum* with aqueous anionic complexes TiF_6^{2-} [41]. The size of titanium particles produced was within the range of (5 – 15) nm. The authors observed that exposure of the fungus to the titanium complexes induced the secretion of proteins of molecular weights 21 and 24 kDa. The molecular weights of these proteins are quite close to those observed on zirconia formation with the same fungus implying that they are the same proteins or their post-translationally modified variants.

4. BIOSYNTHESIS OF MAGNETIC NANOPARTICLES

It is well known that unicellular organisms such as magnetotactic bacteria produce magnetite nanopaerticles. For example, *Magnetospirillum magneticum* produce two types of magnetite nanoparticles; some bacteria produce magnetic (Fe_3O_4) nanoparticles in chains and some produce greigite (Fe_3S_4) nanoparticles [43,44]. Single-domain, uniform magnetic particles (~ 12 nm size) are formed exclusively outside of the bacterial cells by a thermophilic fermentive bacterial strain *Thermoanaerobacter ethanolicus* (TOR-39) [45]. Transition metals such as Co, Cr and Ni may be substituted in thesemagnetic crystals by way of electrochemical processes [46]. In the presence of exogenous electron donor, sulphate reducing bacterium *Desulfovibrio desulfuricans* NCIMB 8307 has been shown to be synthesizing palladium nanoparticles [47].

Overall, the literature suggests that a case for the serious investigation of microorganisms has been made as a possible alternative to the more popular physical and chemical methods that are currently prevalent. Biological methods are simple, practical, and unexpensive for producing novel metallic nanoparticles possessing unique chemical and physical properties. However, number of issues need to be address from the nanotechnology and microbiology points of view before such biosynthetic procedures can compete with the traditional protocols. The surface chemistry of biogenic nanoparticles should be properly recognized (i.e. nature of capping surfactants / peptides / proteins). The elucidation of biochemical pathways leading to metal ion reduction in the different classes of microbes is necessary to develop a rational microbial nanoparticle synthesis procedure. Genetic engineering techniques can potentially be used to improve the particle properties and to control their composition. At present, microbial methods in the synthesis of nanomaterials of varying composition are extreme limited and confined to some metals, semiconductors and very few oxides. Most importantly, the monodispersity of the nanoparticles produced either intra- or extracellularly by tested microorganisms is not very high and far inferior to that obtained through conventional chemical methods. Significant improvement in the monodispersity has been achieved using extremophilic microorganisms.

This work was funded by Grant # STCU–GNSF 5002 from the Ukrainian Science and Technology Centre (STCU) and Georgian National Science Foundation (GNSF).

REFERENCES

1. Biological Nanostructures and Applications of Nanostructures in Biology: Electrical, Mechanical, and optical Properties (Eds. M.A. Stroscio, M. Dutta). New York: Kluwer Academic Publisher (2002).
2. K. Simkiss, K.M. Wilbur. Biomineralization. Weinheim: Wiley-VCH – Academic Press (1989).
3. Ch. Mao, Ch. Flynn, A. Hayhurst, R. Sweeney, J. Qi, G. Georgiou, B. Iverson, A. Belcher. Proc. Natl. Acad. Sci. USA, **100**, 6946 (2003).
4. B. Steinmetz, A. Bize, D. Findlay, G.Y. Lomonosoff, M. Manchester, D.J. Evans, D. Prangishvili. Adv. Func. Mat., **15**, 623 (2008).
5. D.R. Lovley, J.F. Nord, G.L. Philips. Nature, **330**, 252 (1987).
6. G. Southam, T.J. Beveridge. Geochim. Cosmochim. Acta, **58**, 4527 (1994).
7. S. Oliver, A. Kupermann, N. Coombs, A. Lough, G.A. Ozin. Nature, **378**, 47 (1995).
8. G.M. Evans, J.C. Furlong. Environmental Biotechnology: Theory and Applications. Weinhem: Weinheim & Sons (2003).
9. M.R. Bruins, S. Kapil, F. Oehme. Ecotoxicol. Environ. Safety, **45**, 198 (2000).
10. T.J. Beveridge, R.G.E. Murray. J. Bacteriol., **141**, 876 (1980).
11. D. Fortin, T.J. Beveridge. In: Biomineralization (Ed. E. Baeuerien). Weinheim: Wiley-VCH (2000).
12. R.M. Slawson, M.I. van Dyke, H. Lee, J.T. Trevor. Plasmid, **27**, 73 (1992).

13. T. Klaus, R. Joerger, E. Olsson, C.-G. Granqvist. Proc. Natl. Acad. Sci. USA, **96**, 13611 (1996).
14. M. Lengke, M.E. Fleet, G. Southam. Langmuir, **12**, 706 (2006).
15. M. Lengke, B. Ravel, M.E. Fleet, G. Wanger, R.A. Gordon, G. Southam, G. Environ. Sci. Technol., **40**, 6304 (2006).
16. Y. Konishi, T. Nomura, T. Tsukiyama, N. Saitoh. Trans. Mater. Res. Soc. Jpn., **29**, 2341 (2004).
17. B. Nair, T. Pradeep. Cryst. Growth Des., **2**, 293 (2002).
18. A. Ahmad, S. Senapti, M.I. Khan, R. Kumar, M. Sastry. Langmuir, **19**, 3550 (2003).
19. A. Ahmad, S. Senapti, M.I. Khan, R. Kumar, M. Sastry. Nanotechnology, **14**, 824 (2003).
20. M. Gericke, A. Pinches. Hydrometallurgy, **83**, 132 (2006).
21. M. Kowshik, S. Ashtaputre, S. Kharrazi, W. Vogel, J. Urban, S.K. Kulkarni, K.M. Paknikar. Nanotechnology, **14**, 95 (2003).
22. P. Mukherjee, A. Ahmad, D. Mandal, S. Senapti, S.R. Sainkar, M.I. Khan, R. Ramani, R. Parisha, P.A.V. Kumar, M. Alam, M. Sastry, R. Kumar. Angew. Chem. Int. Ed., **40**, 3585 (2001).
23. M. Sastry, A. Ahmad, M.I. Khan, R. Kumar. Cur. Sci., **85**, 162 (2003).
24. S. Oliver, A. Kupermann, N. Coombs, A. Lough, G.A. Ozin. Nature, **378**, 47 (1995).
25. A.Q. Ahmad, S. Senapti, M.I. Khan, R. Kumar, M. Sastry. J. Biomed. Nanotechnol., **1**, 47 (2005).
26. P. Mukherjee, S. Senapti, D. Mandal, A. Ahmad, M.I. Khan, R. Kumar, M. Sastry. Chem. Bio. Chem., **3**, 461 (2002).
27. S.A. Kumar, M.K. Abyaneh, S.W. Gosavi, S.K. Kulkarni, R. Pasricha, A. Ahmad, M.I. Khan. Biotechnol. Lett., **29**, 439 (2007).
28. S. Senapati, A. Ahmad, M.I. Khan, M. Sastry, R. Kumar. Small, **1**, 517 (2005).
29. N. Duran, P.D. Marcato, I.H. Gabriel, O.L. Alves, E. Esposito. J. Biomed. Nanotechnol., **3**, 203 (2007).
30. D. Mandal, M. Bolander, D. Mukhopadhyay, G. Sarkar, P. Mukherjee. Appl. Microbial Biotechnol., **69**, 485 (2006).
31. R.N. Reese, D.R. Winge. J. Biol. Chem., **263**, 12832 (1988).
32. C.T. Dameron, R.N. Reese, R.K. Mehra, A.R. Kortan, P.J. Carroll, M.L. Steigerwald, L.E. Brus, D.R. Winge. Nature, **338**, 596 (1989).
33. M. Kowshik, N. Deshmuck, W. Vogel, J. Urban, S.K. Kulkarni, K.M. Paknikar. Biotechnol. Bioeng., **78**, 583 (2002).
34. A. Ahmad, P. Mukherjee, D. Mandal, S. Senapati, M.I. Khan, R. Kumar, M. Sastry. J. Am. Chem. Soc., **124**, 12108 (2002).
35. D.P. Cunningham, L.L. Lundie. Appl. Environ. Microbiol., **59**, 7 (1993).
36. R.Y. Sweeney, C. Mao, X. Gao, J.L. Burt, A.M. Belcher, G. Georgiou, B.L. Iverson. Chem. Biol., **11**, 1553 (2004).
37. M. Labrenz, G.K. Druschel, T. Thomsen–Ebert, B. Gilbert, S.A. Welch, K.M. Kemner, G.A. Logan, R.E. Summons, G.D. Stasio, P.L. Bond, B. Lai, S.D. Kelly, J.F. Banfield. Science, **290**, 1744 (2000).
38. M. Kowshik, W. Vogel, J. Urban, S.K. Kulkarni, K.M. Paknikar. Adv. Mat., **14**, 815 (2002).
39. J. Gong, Zh. Zhang, H. Bai, G. Yang. Sci. China (Ser. E-Tech. Sci.), **50**, 302 (2007).
40. V. Bansal, D. Rautaray, A. Ahmad, M. Sastry. J. Mater. Chem., **14**, 3303,(2004).
41. V. Bansal, D. Rautaray, A. Bharde, K. Ahire, A. Sanyal. J. Mater. Chem., **15**, 2583 (2005).
42. V. Bansal, P. Poddar, A. Ahmad, M. Sastry. J. Am. Chem. Soc., **128**, 11958 (2006).
43. P. Philipse, D. Maas. Langmuir, **18**, 9977,(2002).
44. H. Lee, A.M. Purdon, V. Chu, R.M. Westervelt. Nano Lett., **4**, 995 (2004).
45. C. Zhang, H. Vali, C.S. Romaneck, T.J. Phelps, S.V. Liu. Am. Mineral., **83**, 1409 (1998).
46. Y. Roh, R.J. Lauf, A.D. Mc Millan, C. Zhang, C.J. Rawn, J. Bai, T.J. Phelps. Solid State Commun., **118**, 666 (2008).
47. P. Yong, N.A. Rowsen, J.P.G. Farr, I.R. Harris, L.E. Macaskie. Biotechnol. Bioeng., **80**, 369 (2008).

ნახშირბადის ნანოსისტემები

ა.პ. ბიბილაშვილი

ი. ჯავახიშვილის სახ. თბილისის სახელმწიფო უნივერსიტეტი
amiranbibilashvili@Tsu.ge

მიღებულია 2010 წლის 2 თებერვალს

1. ნახშირბადისეული კავშირები

ნანოტექნოლოგია იძლევა ფართო პერსპექტივებს ახალი მასალების, ელექტრონიკის, ფიზიკის, ქიმიის, ენერგეტიკის და სხვა დარგების სწრაფი განვითარებისათვის. ამ პროცესში გადამწყვეტ როლს თამაშობენ ფულერენი და ნახშირბადის ნანომილაკები, რომლებშიც ნახშირბადისეული კავშირები თვისებებით უნიკალურია და მრავალსახა. ამ კავშირის ბუნების გაგებისთვის საჭიროა განვიხილოთ ნახშირბადის ატომის ელექტრული სტრუქტურა. ის შეიცავს 6 ელექტრონს, რომლებიც აუღგზნებელ მდგომარეობაში არიან უმდაბლეს ენერგეტიკულ დონეებზე $(1s)^2(2s)^2(2p_x)^1(2p_y)^1(2p_z)$. როცა მოლეკულაში ნახშირბადის ატომი დაკავშირებულია სხვა ატომთან, მისი ელექტრონული სტრუქტურა ასეთია: $(1s)^2(2s)^1(2p_x)^1(2p_y)^1(2p_z)^1$. ელექტრული მუხტი s-მდგომარეობაში განაწილებულია სფერული სიმეტრიით და $1s$-ელექტრონები ქიმიურ ბმაში არ მონაწილეობენ. დანარჩენი 4 ელექტრონი განაწილებულია $n = 2$ დონეებზე. დიდ მანძილებზე ორი ნახშირბადის ატომი ერთმანეთზე არ მოქმედებს და აქვთ დისკრეტული მდგომარეობები. მიახლოებისას დონეები იხლიჩებიან, ქმნიან ზონებს 2 და 6 ელექტრონული მდგომარეობებით, სულ 8 ელექტრონისათვის [1]. ელექტრული მუხტი p-მდგომარეობაში განაწილებულია ჰანტელის ფორმის ურთიერთმართობ ორბიტალებზე. x_0 მანძილზე მიახლოებისას (ნახ. 1) ბმაში მონაწილეობენ გარე p-ორბიტალის ორ-ორი ელექტრონი, რაც იწვევს ზონის ნახევრად შევსებას და მიიღება მეტალი, ანუ გრაფიტი. ატომების უფრო მეტად მიახლოებისას (x_1 მანძილამდე) ნახშირბადის ატომის გარე s-ორბიტალი და სამი p-ორბიტალი ამყარებს კავშირს სხვა ატომებთან. ამ ორბიტალებს შორის მუხტები ერთმანეთში ირევა ანუ, სხვა სიტყვებით, ბირთვიდან ამ ორბიტებზე მყოფი ელექტრონების დაშორება სხვადასხვაა და ხდება მათი ტალღური ფუნქციების ურთიერთ გადაფარვა. ამის გამო ხდება s- და p-მდგომარეობების ტალღური ფუნქციების ჰიბრიდიზაცია. თითოეული ატომიდან ბმაში მონაწილეობს ოთხ-ოთხი ელექტრონი, რაც ავსებს ქვედა სავალენტო ზონას, ხოლო ზედა გამტარებლობის ზონა რჩება ცარიელი. ელექტრონების ასეთი განლაგება იძლევა დიელექტრიკს – მიიღება ალმასი, აკრძალული ენერგეტიკული ზონით 5.3 eV.

ტალღური ფუნქციების ჰიბრიდიზაცია იწვევს s- და p-მდგომარეობების გადაწევას ატომის ბირთვის მიმართ, რასაც ეთანადება შესაბამისი სიდიდის ელექტრული დიპოლური მომენტის წარმოქმნა. მიუხედავად იმისა, რომ ნახშირბადის ატომში $2s$- და $2p$-დონეების ენერგიებს შორის სხვაობა ძალინ მცირეა, ელექტრული დიპოლური მომენტის სიდიდე ($7.33 \cdot 10^{-30}$ C · m) საკმაოდ დიდია და მისი გავლენა ნახშირბადის სხვადასხვა ალოტროპიული (თავიანთი კრისტალური სტრუქტურით განსხვავებული მესერი) მდგომარეობის შექმნის ენერგეტიკაზე არსებითია. ეს მოცემულია ნახ. 2-ზე და ნაჩვენებია, რომ ნახშირბადის სხვადასხვა ალოტროპიული მდგომარეობისათვის დამახასიათებელია სამი ძირითადი ტიპის ქიმიური ბმის წარმოქმნა: sp, sp^2 და sp^3, კავშირებს შორის კუთხეებით 180, 120 და 109.5 °, შესაბამისად [2]. ამ შემთხვევაში არანორმალიზირებული ტალღური ფუნქცია შეიძლება დაიწეროს ასეთი სახით [3]: $\psi = s + \lambda p$, სადაც, p აღნიშნავს p_i ორბიტალების ნარევს, ხოლო λ არის p-მდგომარეობის

s-მდგომარეობაში ფარდობითი შერევის კოეფიციენტი, რომელიცა უდრის, შესაბამისად, 1, 2.5 და 3.5. ასეთი ჰიბრიდიზაციისას *p*-ორბიტალების ბმის მიმართულებები და მათ შორის კუთხე იცვლება λ-ის ცვლილების მიხედვით.

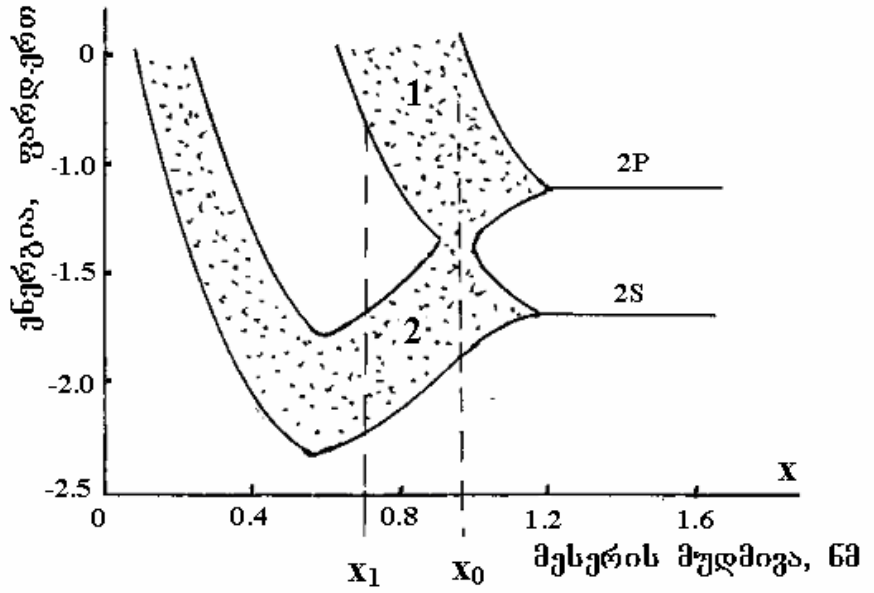

ნახ. 1. ალმასში ენერგეტიკული ზონების შექმნა.
1 – გამტარებლობის ზონა; 2 – სავალენტო ზონა.

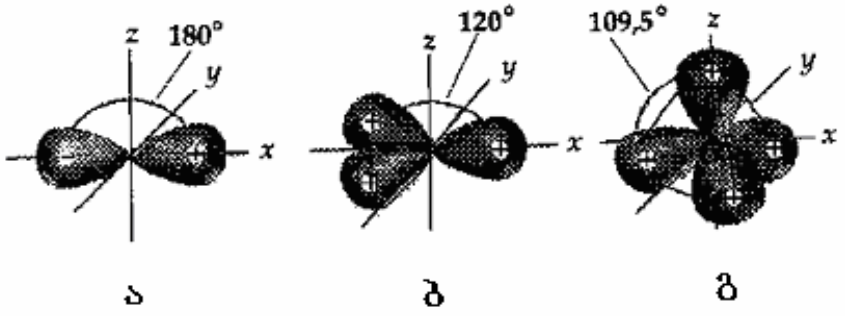

ნახ. 2. ნახშირბადის ქიმიური ბმების ძირითადი ტიპები:
კარბინი (ა), გრაფიტი (ბ), ალმასი (გ).

ნახშირბადის ორატომიანი მოლეკულის შექმნისას აღიძვრება მხოლოდ σ-ბმა, კოვალენტური და იონური კავშირის შესაბამისი წილობითი ენერგიებით 6.83 და 2.2 eV [4]. სავალენტო ელექტრონების ჰიბრიდიზაციით შექმნილი შედარებით დიდი ელექტრული დიპოლის მომენტის გათვალისწინებით დგინდება, რომ დიპოლები განლაგებულია ურთიერთსაწინააღმდეგოდ, რაც ასუსტებს ბმის ენერგიას. წილობითი ენერგიები იცვლება ჯამური ენერგიით და ხდება 6.2 eV-ის ტოლი, ხოლო ბირთვებს შორის მანძილი 1.242 Å-ის ტოლია.

ნახშირბადის ალოტროპიული სახესხვაობანი დამოკიდებულია ნახშირბადის ორატომიან მოლეკულასთან სხვა ატომების მოქმედების სახეზე. ნახშირბადის სამატომიანი მოლეკულა C_3 მიიღება ორატომიან C_2 მოლეკულასთან ნახშირბადის ატომის მოქმედებით. ურთიერთმოქმედების პოტენციალური ენერგიის მინიმუმი ხორციელდება ატომების უმჭიდროესი წყობისას, ანუ

კომპაქტურობის კოეფიციენტის უდიდესი მნიშვნელობისას. ატომების ასეთი განლაგებისას თავს იჩენს ელექტრონ–დიპოლური და დიპოლ–დიპოლური ურთიერთმოქმედებები, რაც ზრდის ბმის ენერგიას. მეორეს მხრივ, ნახშირბადის ატომის მოქმედება C_2 მოლეკულასთან აერთიანებს ყველა სამ ატომს ერთ, საერთო C_3 მოლეკულად. ამის გამო C_2 მოლეკულა განიცდის დეფორმაციას, რაზედაც იხარჯება ენერგია და საბოლოოდ $C_2 - C$ ბმის ენერგია შეადგენს 6.383 eV-ს, საშუალო მანძილით – 1.584 Å. ნახშირბადის ატომისა და ორტომიანი მოლეკულის ურთიერთმოქმედებისას ფორმირდება ალმასის ტიპის სტრუქტურა. მაღალ (დნობის) ტემპერატურაზე ალმასის ტიპის სტრუქტურა იშლება C_2 მოლეკულისა და C ატომის ქიმიური ბმის გაწყვეტის გამო, ხოლო დაბალ ტემპერატურაზე – ორატომიანი მოლეკულის შიგნით ატომთა ბმის გაწყვეტის შედეგად.

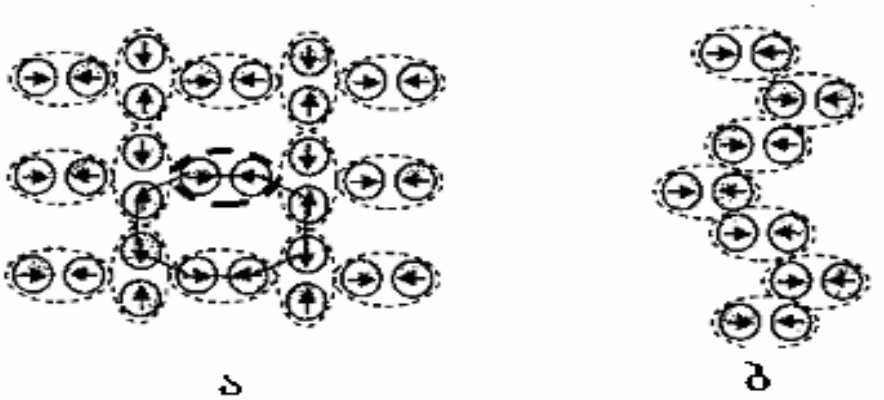

ნახ. 3. მოლეკულების $C_2 - C_2$ ურთიერთმოქმედებისას შექმნილი ნივთიერების ფრაგმენტები. გრაფიტი (ა); ნახშირი (ბ).

ნახშირბადის მოლეკულების $C_2 - C_2$ ურთიერთმოქმედებისას ყალიბდება ჯვარედინი ან ძაფისებური სტრუქტურა ისე, როგორც ეს ნაჩვენებია ნახ. 3-ზე. C_2 მოლეკულების ასეთი ურთიერთგანლაგება იწვევს მათ გაჭიმვას და მოლეკულის შიგნით ატომებს შორის მანძილი გაზრდას 1.242-დან 1.415 Å-მდე. ამ პროცესზე იხარჯება ენერგია და საბოლოო შედეგად ნახ. 3-ზე გამოსახულ შრეში მყოფ C_2 მოლეკულის ბმის ენერგია ფორმირდება დიპოლ–დიპოლური ურთიერთქმედებით და 1.855 eV-ის ტოლია. შრე წარმოადგენს სწორი ექვსკუთხედებისგან შემდგარ ბრტყელ ბადეს, რომელთა ყოველ კუთხეში მოთავსებულია ნახშირბადის ატომი (ჰექსაგონალური კრისტალური სტრუქტურა). ასეთ სიბრტყეს ეწოდება გრაფენი. გრაფენებს შორის ურთიერქმედება მოლეკულურია და ბმის ენერგია შეადგენს 0.29 eV-ს, ხოლო მათ შორის მანძილი – 3.35 Å-ს. მცირეოდენი ძვრის დეფორმაცია იწვევს ასეთი მასალის დაშლას ფენებად. ასეთ თვისებას ამჟღავნებს გრაფიტი. ნახშირს აქვს ძაფისებური სტრუქტურა, რომელიც გამოსახულია ნახ. 3ბ-ზე და რომელშიც ძაფები ერთმანეთის მიმართ წანაცვლებულია ნახშირბადის ერთი ატომის სიდიდით. ამ ალოტროპიულ მდგომარეობაში C_2 მოლეკულებს შორის ბმის ენერგია ~ 2.3 eV-ია, ხოლო ძაფებს შორის კოვალენტური ბმებია და მათი სიდიდე ~ 1.21 eV-ის ტოლია.

ნახშირბადის C_3 მოლეკულის შრეში განლაგების ხასიათი მოცემულია ნახ. 4-ზე. ნახშირბადის შრეში ასეთი წყობა ხასიათდება პოტენციალური ენერგიის მინიმუმით, კომპაქტურობის კოეფიციენტის მაქსიმალური სიდიდით და სტრუქტურა შეიცავს 12 ახლო მყოფ ნახშირბადის ატომს. მათ შორის კოვალენტური ბმა განისაზღვრება გაცვლითი ურთიერთმოქმედებით, ანუ σ-ბმით, 11.5 eV იონიზაციის ენერგიით. ასეთი სახის განლაგების მოცულობითი სტუქტურა ქმნის წახნაგცენტრირებულ კუბურ სტრუქტურას, წანაცვლებულს წიბოს ნახევრით და ატომთა შორის 1.54 Å მანძილით. ბმის ენერგია ძირითადად განისაზღვრება დიპოლ–დიპოლური ურთიერთქმედებით. ასეთი თვისებებით ხასიათდება ალმასი.

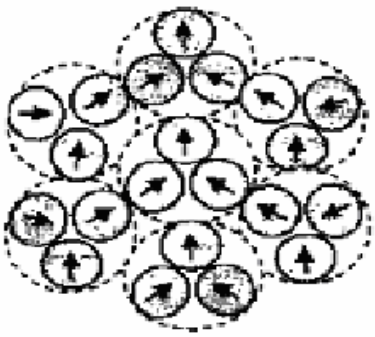

ნახ. 4. ალმასის შრეში C_3 მოლეკულის მდებარეობა დიპოლ-დიპოლური ურთიერთქმედებისას.

2. ფულერენი

დიდი ხნის განმავლობაში ითვლებოდა, რომ ბუნებაში არსებობდა ნახშირბადის სამი ალოტროპიული ფორმა: კარბინი, გრაფიტი და ალმასი. გასული საუკუნის ბოლოს აღმოჩენილ იქნა ე.წ. ჩონჩხედისებური ნახშირბადის სტრუქტურა, რომელიც წარმოადგენს ნახშირბადისეულ შეკრულ ღრუ სფერულ გარსს [3,5]. ის ჰგავს ფეხბურთის ბურთს და შედგება ნახშირბადის 60 ატომისაგან. მისი აღმოჩენა იყო თითქმის შემთხვევითი ვარსკვლავთშორისო სივრცის შესწავლისას. შეისწავლებოდა სინათლის შთანთქმა ვარსკვლავთშორისო არსებული მტვერით, ანუ იქ არსებული მცირე ნაწილაკებით. ცნობილია, რომ ვარსკვლავების სინათლის ინტენსივობა კოსმოსური სივრცის გავლის შემდეგ მცირდება. ესაა ოპტიკური შთანთქმა და ხდება ვარსკვლავებიდან დედამიწისკენ წამოსული სხივის შთანთქმით და გაბნევით მის გზაზე არსებული მტვერის ნაწილაკების მიერ. ეს შთანთქმა შეისწავლება ინტენსივობის გაზომვით მოსული სინათლის სხვადასხვა ტალღის სიგრძეზე, ანუ სხვადასხვა ფერზე. გაზომვების შედეგად აღმოჩნდა, რომ შთანთქმა იზრდება ულტრაიისფერ (უი) დიაპაზონში 220 nm (კვანტის ენერგია 5.6 eV) ტალღის სიგრძესთან ახლოს (ნახ. 5). ამ შთანთქმას ხსნიდნენ ვარსკვლავთშორისო არეში არსებულ ჰიპოთეთიკურად მცირე გრაფიტის ნაწილაკებზე გაბნევით, რომელსაც ასტონომთა შორის მიღებული იყო ჩვეულებრივად და ჰქონდა საერთო აღიარება.

დ. ჰაფმანი და ვ. კრატჩმერი ამ ახსნით ვერ დაკმაყოფილდნენ და განაგრძეს უფრო დაწვრილებით შთანთქმის საკითხის შესწავლა. ლაბორატორიულ პირობებში, ნახშირის ორ ელექტროდს შორის რკალური განმუხტვით, ჰელიუმის ატმოსფეროში, დააფინეს კვარცის მინაზე ჭვარტლის მცირე ნაწილაკები. მას სწავლობდნენ სხვადასხვა ოპტიკური მეთოდებით. მართლაც აღმოაჩინეს გრაფიტის ცნობილი სპექტრული ხაზები უი დიოპაზონში, მაგრამ ინფრაწითელ (იწ) დიაპაზონში მიიღეს ოთხი დამატებითი ხაზიც, რომელთა წარმოშობა არ უკავშირდებოდა გრაფიტს.

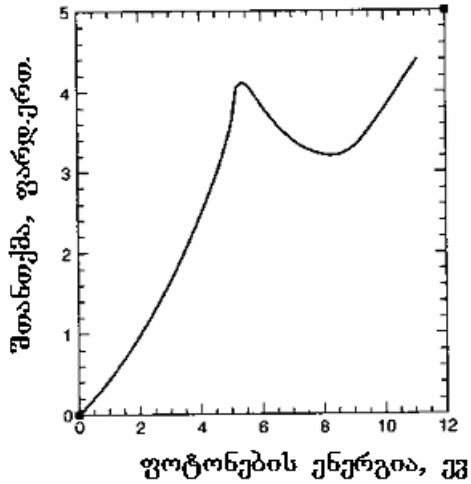

ნახ. 5. ვარსკვლავთშორისი არის გავლით დედამიწაზე მოსული ვარსკვლავის სინათლის ოპტიკური სპექტრი.

ქიმიკოს-თეორეტიკოსების მიერ 60 ატომისაგან შემდგარი ნახშირბადი, ფორმულით C_{60}, რამდენიმე წლის წინათ იყო ცნობილი, მაგრამ მისი არსებობა ექსპერიმენტულად არ იყო დადასტურებული. ამ მოლეკულის ბევრი თვისება გამოთვლილი იყო თეორიულად, მათ შორის იწინასწარმეტყველეს იწ დიაპაზონის შთანთქმის სახეც. ჰაფმანის და კრატჩმერის მიერ აღმოჩენილი ოთხი შთანთქმის ხაზი კარგად ეთანადებოდა თეორიულად ნაწინასწარმეტყველებ C_{60} მოლეკულის შთანთქმის სპექტრს ამ დიაპაზონში. შეიძლება თუ არა ვარსკვლავთა სინათლის შთანთქმა უი დიაპაზონში გამოწვეული იყოს C_{60} მოლეკულით? ამ აზრის დამტკიცებისათვის მეცნიერები იკვლევდნენ შთანთქმას უი დიაპაზონში ნახშირის ელექტროდების რკალით მიღებული ^{13}C-ისათვის და ადარებდნენ ^{12}C-ის სპექტრებს. ცნობილია, რომ ელემენტის საკუთარი იზოტოპით შეცვლისას ანაცვლებს იწ სპექტრს მასათა თანაფარდობიდან კვადრატული ფესვით, ამ შემთხვევაში $\sqrt{13/12} \approx 1.041$-ით. ანუ წანაცვლება უნდა იყოს 4.1 %-ით. ეს ზუსტად ემთხვევა ექსპერიმენტულ მონაცემებს. მაშასადამე, მკვლევარებმა მიიღეს 60 ატომიანი, სფეროს ფორმის ნახშირბადის მოლეკულის არსებობის მყარი დამტკიცება. მასსპექტრომეტრმა დააფიქსირა ნაწილაკები მასური რიცხვით 720, ანუ თითოეული 12 მ.ა.ე. მასის მქონე 60 ნახშირბადის ატომისაგან შემდგარი ნაწილაკები. ეს გააკეთა ჯგუფმა, რომელშიც შედიოდა ჰ. კროტო, რ. კერლი და რ. სმოლი (H. Kroto, R. Curl, R. Smalley), რომლებიც 1996 წელს დაჯილდოვდნენ ნობელის პრემიით [6]. C_{60} მოლეკულის არქიტექტურა შექმნა რიჩარდ ბაკმინისტერ ფულერმა (Richard Buckminster Fuller) და მის საპატივმცემლოდ მას ფულერენი უწოდეს. ის წარმოადგენს ღრუ სფეროს ფორმას, რომელიც შედგება 20 ექვსკუთხა და 12 ხუთკუთხა სიმეტრიულად განლაგებული წახნაგებისგან, სადაც ხუთკუთხედები ერთმანეთს არ ესაზღვრებიან (ნახ. 6). ყოველი ექვსკუთხედი ესაზღვრება სამ ექვსკუთხედს და სამ ხუთკუთხედს, ხოლო ყოველი ხუთკუთხედი – მხოლოდ ექვსკუთხედებს. სფეროს შემქმნელი ნახშირბადის ატომები ერთმანეთს უკავშირდებიან ძლიერი კოვალენტური ბმებით. სფეროს გარსის სისქეა – 0.1, C_{60} მოლეკულის რადიუსი – 0.357, C – C ბმის სიგრძე ხუთკუთხედში – 0.143, ხოლო ექვსკუთხედში – 0.139 nm.

ფულერენის წარმოქმნის დასაწყისში ხდება C_3 მოლეკულასთან ნახშირბადის მოლეკულათა თანდათანობითი მიერთება და ჩაკეტილი კონფიგურაციების შექმნა 5, 8, 34 და ა. შ. ატომისგან, კლასტერის ტიპის მდგრადი კონფიგურაციის სახით. ნახშირბადის შემდგომი ატომები მოქმედებენ ასეთ კლასტერზე, რომელთა ზომები იზრდება. ამიტომ იონური ბმების წვლილი მცირდება და მხედველობაში მიიღება მხოლოდ ელექტრონ–დიპოლური და დიპოლ–დიპოლური ურთიერთქმედება. ნახშირბადის ატომი თავისი დიპოლით მოქმედებს კლასტერის სამ ატომთან,

როგორც ეს ნაჩვენებია ნახ. 3-ზე, ხდება სავალენტო ელექტრონების გაერთიანება და ნახშირბადიანი კავშირების შექმნა ენერგიით 4.664 eV. ფულერენს აქვს მკაცრად განსაზღვრული "გრაფიტის" და "ალმასის" კავშირების წილი, ამიტომ ის იკავებს ადგილს მათ, ე.ი. $sp^2 - sp^3$-მდგომარეობებს შორის.

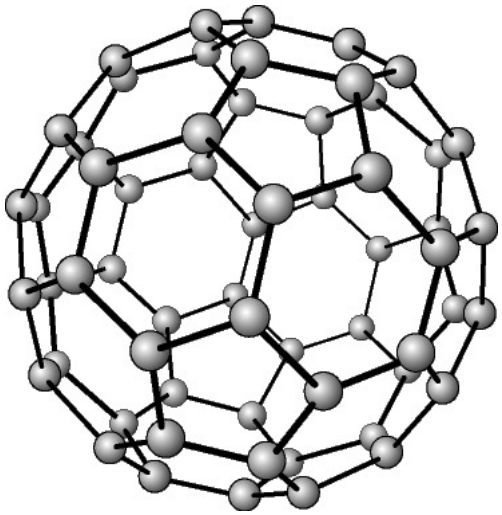

ნახ. 6. C_{60} ფულერენის მოლეკულის სტრუქტურა.

ბუნებაში C_{60}-ის გარდა კიდევ არსებობენ ჰიპერფულერენები (გიგანტური ფულერენები), რომლებიც წარმოადგენენ ერთმანეთში ჩადგმულ გარსებს. მათ შორის ყველაზე მცირე გარსი აქვს C_{60}-ს, რომელიც ასე აღინიშნება $C_{60} @ C_{240} @ C_{540}$ და ა.შ. ყურადღებას იპყრობს შეერთების კიდევ ერთი კლასი, ე.წ. ჰეტეროფულერენები, რომელთა სტრუქტურა შეკრულია და ნახშირბადის ატომები ნაწილობრივ ჩანაცვლებულია სხვა ატომებით. მაგალითად, $C_{59}B$, $C_{57}B_3$, $C_{58}BN$, $C_{59}M$, სადაც M მეტალია, და ა.შ. ზოგადად, C_{60} დიელექტრიკია და მისი სტრუქტურის 26 % სიცარიელეა. ამიტომ საინტერესოა მათი ლეგირება, განსაკუთრებით ტუტემიწა მეტალებით, რომლებიც ადვილად გასცემენ ელექტრონებს. ვაკუუმში 400 °C ტემპერატურაზე შესაძლებელია C_{60}-ის კალიუმით ლეგირება. K ჯდება ტეტრაედრში, გასცემს ელექტრონს, მიიღება C_{60}^{n-}, სადაც ელექტრონები სუსტად არიან დამაგრებულები და მცირე ძაბვაზეც ატარებენ დენს, ანუ ფულერენი ხდება გამტარი. K_3C_{60} ზეგამტარია, რომლის $T_c = 18\,\mathrm{K}$. ასევე ზეგამტარ $CsRuC_{60}$-ისათვის $T_c = 33\,\mathrm{K}$.

ფულერენი, გარდა ვარსკვლავთშორისი სივრცისა, მცირე რაოდენობით აღმოჩენილ იქნა ბუნებრივ მინერალებში (შუნგიტების საბადოში) და მეტეორიტებში. სახელწოდება "შუნგიტები" ეწოდა დასახლება შუნგის გამო, სადაც პირველად აღმოაჩინეს ეს მინერალი. შუნგიტების საბადოში ნახშირის შემცველობა მერყეობს 1-დან 70 %-მდე, ხოლო მასში ფულერენი 10^{-3} %-ია. ნახშირი არის 10 nm ზომის ბურთულების სახით და არა აქვს კრისტალური სტრუქტურა. დედამიწის პირობებში ფულერენი ოზონისა და უი გამოსხივების მოქმედებით განიცდის დეგრადაციას, მაგრამ თუ დაცულია რაიმე გარსაცავი ფენით, ის დიდხანს ინარჩუნებს თავის სახეს. ფულერენი გვხვდება ვულკანის ამონაფრქვევში, მეხის დაცემის ადგილში. ძალიან მცირე რაოდენობით ფულერენს შეიცავს ნავთის ლამფის და ბუხრის ჭვარტლი. მეტეორიტულ ფულერენებში აღმოჩენილ იქნა გაზი ^3He, რომელსაც აქვს კოსმოსური წარმოშობა. ამით მეტეორიტ ალენდეს წლოვანება შეფასდა 4.6 მილიარდი წლით, რომელიც ბევრად მეტია დედამიწის წლოვანებაზე. მთვარის გრუნტში ფულერენი არ იქნა აღმოჩენილი.

3. ფულერენის მიღება

ნახშირბადის სხვადასხვა ალოტროპიული მდგომარეობის მიღებისას ნახშირბადის გაზურ გარემოში, მაღალი ტემპერატურისა და საწყისი პროდუქტების დიდი კონცენტრაციის პირობებში, რეაქცია მიმდინარეობს საკმაოდ ინტენსიურად [4]. ნახშირბადის ატომების მაღალი კონცენტრაცია შესაძლებელია იქნას მიღწეული გრაფიტის სუბლიმაციით მასზე მძლავრი სითბური ან პლაზმური ნაკადის, მზის სხივის ან ლაზერის მოქმედებით. გრაფიტის ფენებს შორის ბმის ენერგია 0.29 eV-ს შეადგენს და მის გასაწყვეტად საჭიროა ~ 3500 K ტემპერატურა, რომელიც ახლოსაა გრაფიტის სუბლიმაციის ტემპერატურასთან (~ 4000 K). ნახშირბადის სხვადასხვა ალოტროპიულ მდგომარეობაში გადაყვანის რეაქციისათვის საჭიროა სუბლიმაციის ტემპერატურაზე მეტი ტემპერატურა და მხოლოდ ნახშირბადის ატომების გარემო, რათა ისინი მინარევულ ატომებთან არ შევიდნენ რეაქციაში და არ დაჯდნენ ასეთი სახით ქვესაფენზე. გარდა ამისა, გრაფიტის მაღალ ტემპერატურამდე გახურებისას არ უნდა ხდებოდეს ამ გარემოს იონიზაცია, ანუ გარემო ტემპერატურის წყაროს არ უნდა ართმევდეს დამატებით ენერგიას. ასეთ გარემოდ აღებულია ჰელიუმი, რომელსაც აქვს მაღალი იონიზაციის ენერგია და მაღალ ტემპერატურაზე არ იონიზირდება.

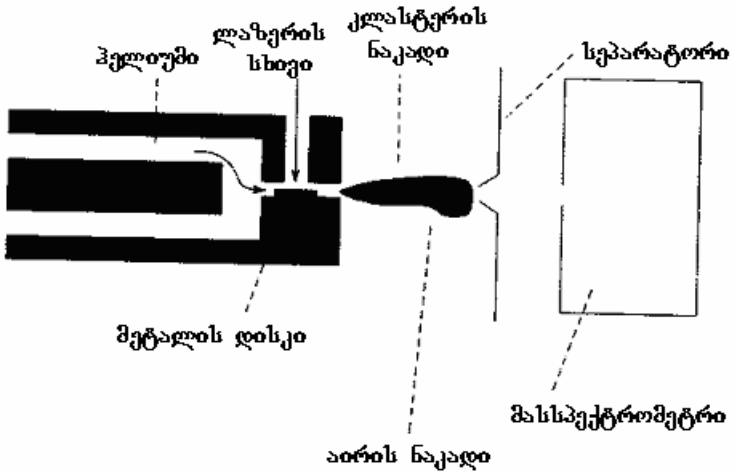

ნახ. 7. მეტალის ზედაპირიდან ლაზერული აორთქლებით ნანონაწილაკის მიღების დანადგარის სქემა.

გრაფიტის გახურება შეიძლება რკალური განმუხტვით ჰელიუმის ატმოსფეროში, რომელიც სრულად აკმაყოფილებს ნახშირბადის სხვადასხვა ალოტროპიულ მდგომარეობების მიღების მოთხოვნებს. მაგრამ, ეს პროცესი ხასიათდება მიღებული პროდუქტის მცირე გამოსავლიანობით, ამიტომ გრაფიტის გასახურებლად გამოიყენება ლაზერი, ენერგიის ნაკადით $10^{12}\,\mathrm{W/m^2}$, რომელიც იძლევა 3000 K ტემპერატურას. ამ დროს გამოსავლიანობა 90 %-ია. ასეთი დანადგარის სქემა მოცემულია ნახ. 7-ზე, რომელიც პირველად შექმნა რ. სმოლიმ [3]. მაღალენერგეტიკული და დიდი ინტენსივობის ლაზერის სხივით ხდება გრაფიტის აორთქლება, გაზური ჰელიუმის ნაკადი წარიტაცებს აორთქლებული ნახშირბადის მცირე ნაწილაკებს მცირე ნახვრეტიან არეში, სადაც ჰელიუმი ფართოვდება, ცივდება ნაკადთან ერთად და კონდენსირდება მცირეატომიან კლასტერებად. შემდეგ ნაკადი გადის კალორიმეტრით მასს-სპექტრომეტრში, სადაც იზომება მოლეკულის ან კლასტერის მასა. ნახ. 8-ზე გამოსახულია მასათა სპექტრი, ზემოთ აღნიშნული ექსპერიმენტით მიღებული ნახშირბადის სხვადასხვა ატომთა რაოდენობის კლასტერებისათვის.

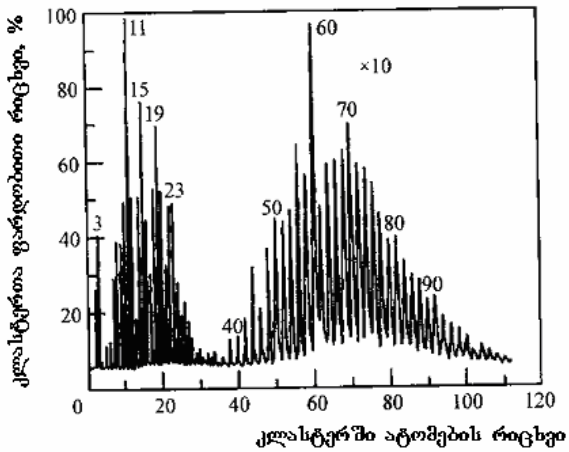

ნახ. 8. გრაფიტის ლაზერული აორთქლებით მიღებული ნახშირბადის კლასტერის მასათა სპექტრი.

4. ნახშირბადის ნანომილაკები

სფეროიდულ ნახშირბადიან სტრუქტურებთან ერთად ფორმირდება ასევე ცილინდრული, წაგრძელებული სტრუქტურაც, ე.წ. ნანომილაკი, რომელიც გამოირჩევა ფიზიკურ-ქიმიური თვისებების მრავალფეროვნებით. იგი პირველად მიიღო 1991 წელს ს. იჯიმამ (S. Iijima). მისი არსებობა და ზოგიერთი თვისებები აღმოჩენამდე თეორიულად იყო ნაწინასწარმეტყველები. ნანომილაკი შეიძლება წარმოვიდგინოთ, როგორც ცილინდრად შეხვეული გრაფიტის ფურცელი, ანუ გრაფენი – ექვსკუთხედის წვეროებში მოთავსებული ნახშირის ატომებით [3–5]. ერთშრიან ნანომილაკს აქვს 2 nm სიდიდის დიამეტრი და 100 μm-მდე სიგრძე. ეს სტრუქტურა კვაზიერთგანზომილებიანია და კარგი ნანომავთულია. ნანომილაკის ერთ-ერთი განზომილებითი პარამეტრია "კირალობა", რომელიც მიუთითებს იმ ექვსკუთხედის კოორდინატებს, რომელიც გრაფენის მილად დახვევისას უნდა დაემთხვეს საწყის ექვსკუთხედს [7]. ტერმინი „კირალობა" შემოიღო 1884 წელს ინგლისელმა ფიზიკოსმა ულიამ ტომსონმა (ლორდი კელვინი, Wiliam Thomson), მაგრამ ამ ტერმინის გავრცელება მოხდა 1966 წელს შვეიცარიელი ქიმიკოსის ვლადიმირ პრელოგის (Vladimir Prelog) მიერ.

ნანომილი წარმოდგინება წყვილი მთელი რიცხვებით (n,m), რომელთა ჯამი დიამეტრზე, წრეწირის გასწვრივ ექვსკუთხედების რაოდენობის ტოლია. გრაფენის მილის ღერძის მიმართ ორიენტაციის კუთხე განსაზღვრავს ნანომილის გამტარებლობის ხასიათს – მეტალურია თუ ნახევარგამტარული. ნახევარგამტარული მილაკის აკრძალული ზონის სიგანე დამოკიდებულია კირალობაზე (შეხვევის კუთხე და მილის დიამეტრი). მეორეს მხრივ, მილის დიამეტრი და შეხვევის კუთხე, ან შეხვევის ბიჯი, ორგანზომილებიანი გრაფენის კრისტალოგრაფიული ელემენტალური უჯრედის ანალოგიაა. ნანომილი მიიღება მისი ტრანსლაციით მილის გასწვრივ (ნახ. 9).

"შეხვევის ანუ კირალური ვექტორი" $\vec{C} = n\vec{a}_1 + m\vec{a}_2$, სადაც $\vec{a}_1$ და $\vec{a}_2$ ჰექსაგონალური უჯრედის ბაზისური ვექტორებია. შეხვევა ისე უნდა მოხდეს, რომ $\vec{C}$ ბოლო და სათავე ერთმანეთს უნდა დაემთხვეს. შეხვევა შეიძლება მოხდეს ზიგზაგურად (როცა $m = 0$), "სავარძლისებურად" (როცა $n = m$) და კირალური მიმართულებით, რაც ჩანს ნახ. 9-დან. ტრანსლაციის $\vec{T}$ ვექტორი მიმართულია მილის გასწვრივ და $\vec{C}$ ვექტორის მართობია. $\vec{T}$-სა და $\vec{C}$-ს შორის არსებული შეხვევის ფართობი ეთანადება ნანომილაკის ერთეულოვან უბანს, რომლის მრავალჯერადი ტრანსლაციით მიიღება ნანომილი.

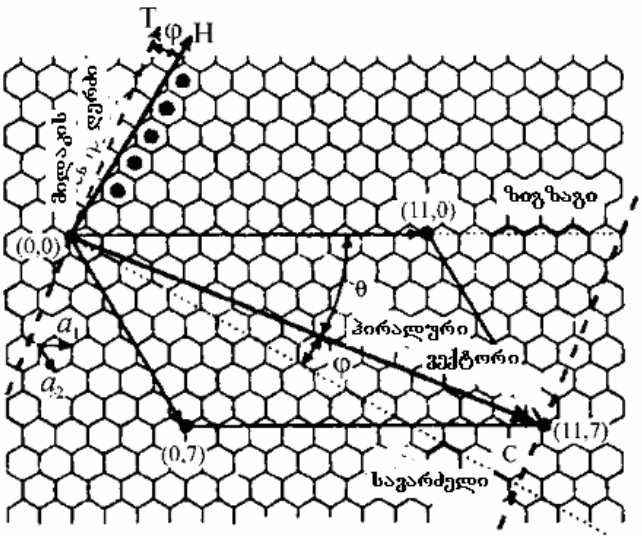

ნახ. 9. გრაფენის ჰექსაგონალური ბადის სხვადასხვა კირალობით ცილინდრად შეხვევით ნანომილაკის ფორმირების მოდელი: $\vec{a}_1$ და $\vec{a}_2$ – ორგანზომილებიანი ელემენტალური უჯრედის ბაზისური ვექტორები; $\vec{T}$ – მილაკის გასწვრივი ღერძის მიმართულება; $\vec{H}$ – გრაფენის სიმეტრიის ღერძის მიმართულება; φ – კუთხე მათ შორის; θ – კირალური კუთხე.

კირალური ინდექსები (n,m) განსაზღვრავენ ნანომილის D დიამეტრს, რომელიც ასე მოიცემა: $D \approx 0.36\sqrt{m^2+n^2+mn}$. მასზედ დამოკიდებულია ნანომილაკის ელექტრული, მექანიკური და სხვა თვისებები.

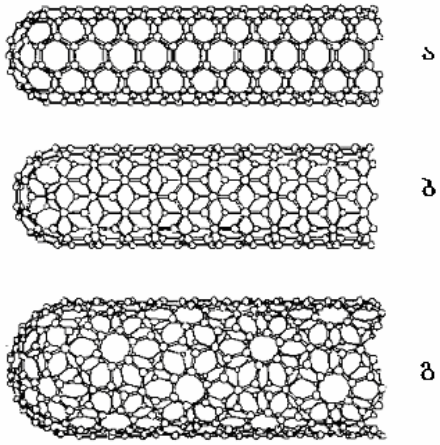

ნახ. 10. გრაფენის შეხვევის მეთოდზე დამოკიდებული ნახშირბადის ნანომილაკის რამდენიმე შესაძლო სტრუქტურა: სავარძელი (ა), ზიგზაგი (ბ) და კირალური (გ).

გრაფენის შეხვევა შესაძლებელია მისი სხვადასხვა ღერძის გარშემო, რითაც მიიღება სხვადასხვა ტიპის ნანომილაკი სხვადასხვა მახასიათებლებით. ნახ. 10-ზე გამოსახულია ასეთი ტიპის სამი შესაძლო ვარიანტი. ნანომილის ზრდის მექანიზმი აქამდე არაა ცნობილი. რადგანაც ერთკედლიანი მილის ზრდისათვის აუცილებელია ნიკელის ან კობალტის კატალიზატორი, შეიძლება ითქვას, რომ კატალიზატორის ატომები უერთდებიან ნახშირბადის ატომებს გაუწყვილებელი ბმებით და ალაგებენ მათ მილის კედლის გარშემო.

ნახ. 11. მრავალშრიანი ნანომილაკის განივიკვეთის მოდელი: ჩადგმულ-კონცენტრიტებული (ა), შეხვეული მთლიანი გრაფენი (ბ), შეხვეული დაჭრილი გრაფენი (გ).

ძაფისებური წანაზარდებით შესაძლებელია ჩამოყალიბებულ იქნან მდგრადი ორ- და მრავალშრიანი ნახშირბადის ნანომილაკები. ამ დროს არსებობს სტრუქტურული სახეობის უფრო მეტი ვარიანტი, რომელთაგან სამი გამოსახულია ნახ. 11-ზე.

ისინი შეიძლება იყვნენ შედგენილი კოაქსიალური ცილინდრებისგან, იყვნენ სხვადასხვა სახის ხვიები, ჰქონდეთ ხახვისებური სტრუქტურა. ყველა შემთხვევაში, ნახშირბადის ორშრიანი ნანომილაკებში (ნონმ) შრეებს შორის მანძილი (ვან დერ ვაალსის ღრეჩო) ახლოსაა გრაფიტის მესერის მუდმივასთან (0.34 nm), ხოლო დეფექტურ ნონმ-ში აღწევს 0.5 nm-ს. ითვლება, რომ ნონმ-ის გარე შრე უმეტესად ნახევარგამტარული მილაკებია, ხოლო შინაგანი შრეები – მეტალური ან ნახევარგამტარული.

ნახშირბადის მოლეკულების $C_3 - C_2$ ურთიერთმოქმედებისას, რომელთა შორის მანძილი 2.664 Å-ია, ფორმირდება ნანომილაკის სტრუქტურა. C_3-ის გარშემო ლაგდებიან C_2 მოლეკულები, რომელთა მიერ შეკრული ჯაჭვი ქმნის შეკრული სტრუქტურის სისტემას. ასეთი სტრუქტურის შიგნით რჩება სიცარიელე, რომლის ზომამ შეიძლება შეადგინოს რამდენიმე ათეული nm. $C_3 - C_2$-ის შიგნით ელექტრონ–დიპოლური და დიპოლურ–დიპოლური ურთიერთქმედების შედეგად ქიმიური ბმის სიდიდე 2.226 eV ხდება.

5. თვისებები და გამოყენება

ნანოსისტემების ბევრი უნიკალური თვისებები განისაზღვრება, ერთი მიმართულებით მაინც, მათი ზომითი შეზღუდვებით. სხვადასხვა თვისებებისათვის (ელექტრული, მექანიკური, მაგნიტური, ქიმიური და სხვა), აგრეთვე, კვანტური ეფექტებისათვის კრიტიკული ზომები შეიძლება იყოს სხვადასხვა, რაც განისაზღვრება ამ მასალის გეომეტრიულ ზომასა და მასში თავისუფალი განარბენის საშუალო მანძილის თანაფარდობით.

ნახშირბადის ნანომილაკების ერთ-ერთი საინტერესო თვისებაა, რომ მისი დიამეტრსა და კირალობაზე დამოკიდებულებით, ის შეიძლება იყოს მეტალი ან ნახევარგამტარი. ნანომილაკის სინთეზის პროცესში შესაძლებელია მილაკში მინარევების შერევა ისე, რომ რაღაც ნაწილი იყოს ნახევარგამტარული თვისებების, ხოლო დანარჩენი – მეტალურის. ჩვეულებრივ, მეტალური თვისებები ახასიათებთ სავარძლისებურ სტრუქტურებს. ნახშირბადის ნანომილაკის ელექტრული თვისებების შესასწავლად იყენებენ მასკანირებელ გვირაბულ მიკროსკოპს (მგმ) ლოკალური ელექტრონული სპექტროსკოპიის რეჟიმში [3]. დიფერენციალური გამტარებლობის ძაბვაზე დამოკიდებულებით დადგინდა, რომ მეტალური გამტარებლობისას სრულდება ომის კანონი, ხოლო ნახევარგამტარულისას – განისაზღვრა აკრძალული ზონის სიგანე, რომელიც შეადგენდა 0.7 eV-ს. დადგინდა, რომ აკრძალული ზონის სიგანე მილაკის დიამეტრის უკუპროპორციულია და დიამეტრის გადიდებით მიისწრაფის ნულისაკენ. ემპირიულად მოცემულია: $E_g \approx 0.9/D$, სადაც E_g აკრძალული ზონის სიგანეა eV-ში და D მილის დიამეტრი nm-ში. ითვლება, რომ E_g იცვლება $(0.4 - 1.0)$ eV ინტერვალში. ნახშირბადის მეტალურ ნანომოლაკს აქვს ძალიან დიდი

ელექტრული გამტარებლობა. დადგენილია, რომ მას შეუძლია გაატაროს კვადრატულ სანტიმეტრზე მილიარდი ამპერი დენი. შესაბამის პირობებში სპილენძის სადენი დნება გამოყოფილი სითბოს ხარჯზე. ნახშირბადის ნანომილაკის ასეთი დიდი გამტარებლობა აიხსნება მათში ძალიან მცირე რაოდენობის დეფექტების არსებობით, რომლებზეც თითქმის არაა გაბნევა, ანუ ელექტრონები არიან ბალისტიკური. ამიტომ დიდი დენი ნანომილაკს არ ახურებს, როგორც ეს ხდება სპილენძში. ამავე მიზეზით ისინი არიან კარგი სითბოგამტარებიც. ნანომილაკი თითქმის ორჯერ უფრო მეტად კარგი სითბოგამტარია, ვიდრე ალმასი. ყოველივე ეს იძლევა საშუალებას, რომ ნახშირბადის ნანომილაკები გამოყენებული იყოს სქემებში ელემენტთაშორის მიმყვანებად. ნახშირბადის ერთშრიან ნახევარგამტარ ნანომილაკებში დენის მატარებლების ძვრადობა აღწევს $15000\ \mathrm{cm}^2 / \mathrm{V} \cdot \mathrm{wm}$-ის ტოლ მნიშვნელობას, რაც მიუღწეველია ჩვეულებრივ ნახევარგამტარებში. დაბალ ტემპერატურაზე ნახშირბადის ნანომილაკებში შეიმჩნევა დენის საფეხურისებური ზრდა (გამტარებლობის დაკვანტვა) მოდებული ძაბვის მიხედვით. გამტარებლობის კვანტია $G_0 = 4e^2 / \hbar$, სადაც e ელექტრონის მუხტია და $\hbar$ – პლანკის მუდმივა. ამიტომ კვანტური გამტარებლობის კოეფიციენტი შეიძლება იყოს მთელი ან არამთელი, მაგალითად, $0.5G_0$. ეს კვანტური მოვლენა გამოიყენება ინფორმაციული სისტემების ნანოელექტრონულ ხელსაწყოებში. IBM-ის (აშშ) თანამშრომლებმა აღმოაჩინეს, რომ დეფექტიანი ნახშირბადიანი ნანომილაკები ასხივებენ იწ სხივებს რამდენიმე რიგით მეტი ინტენსივობით, ვიდრე მასიური ნახევარგამტარები.

პირველივე ცდებმა აჩვენა, რომ ნანომილაკი ხასიათდება უნიკალური მექანიკური თვისებებით. ნანომილის გასწვრივ დრეკადობის მოდულის მნიშვნელობა მდებარეობს $(1.28 - 1.8)$ TPa ინტერვალში. შედარებისათვის უნდა აღინიშნოს, რომ ფოლადისათვის იუნგის მოდული 0.21 TPa-ია, რაც ნიშნავს, რომ ნახშირბადის ნანომილაკის იუნგის მოდული ათჯერ მეტია, ვიდრე ფოლადისა. ე.ი. ნახშირბადის ნანომილი ძნელად უნდა იღუნებოდეს, მაგრამ რადგან მილი ძალიან წვრილია და უდეფექტოა ადვილად იღუნება და არ ტყდება. ამის მიზეზი ისიცაა, რომ ნახშირბადის მილის კედლები შედგება ექვსკუთხედებისაგან, გაღუნვისას ის იცვლის თავის ფორმას, მაგრამ არ ირღვევა. ესაა უნიკალური შედეგი იმ ფაქტისა, რომ C – C ბმამ შეიძლება შეიცვალოს ჰიბრიდიზაციის ხარისხი და $s - p$ შერევის კოეფიციენტი დამოკიდებულია გაღუნვის სიდიდეზე. ნახშირბადის ერთშრიანი ნანომილისთვის ზღვრული ძაბვა მექანიკურ გაჭიმვაზე შეადგენს 45 GPa-ს, მაშინ, როცა ფოლადი ირღვევა 2 GPa-ზე. მექანიკური მახასიათებლებით მრავალშრიანი ნახშირბადის ნანომილაკებიც უკეთესია ფოლადზე, მაგრამ ისეთი არაა, როგორც ერთშრიანის მახასიათებლები. მაგალითად, 200 nm-ის დიამეტრის მქონე მრავალშრიანი ნანომილაკის ზღვრული ძაბვაა 7 GPa და იუნგის მოდული კი – 0.6 TPa. უკანასკნელ ხანს ჩაატარეს ასეთი ექსპერიმენტი: ნანომილაკის დეფორმაციისას მასში გაატარეს დენი, კერძოდ, 12 nm დიამეტრის და 30 nm სიგრძის ნანომილში, სხვადასხვა დეფორმაციისას, გაატარეს $10\ \mathrm{MA} / \mathrm{mm}^2$ სიმკვრივის დენი. ამის შედეგად ნანომილი გახურდა 2000 K ტემპერატურამდე და დაიშალა, როცა ნარჩენი დეფორმაციის შემდეგ ნანომილის დიამეტრი იყო 0.8 nm და სიგრძე 91 nm.

ნახშირბადის ნანომილაკის ღერძის გასწვრივ მცირე ძაბვის მოდებისას მისგან ხდება ელექტრონების ინტენსიური ემისია, რასაც ეწოდება ველითი ემისია. ეს ეფექტი ადვილად დაიმზირება, როცა ორ პარალელურ ფირფიტას შორის, სადაც ერთ-ერთი ნანომილაკია, მოდებულია მცირე ძაბვა. ამ ეფექტის გამოყენება შეიძლება თხელი ბრტყელი დისპლეის გასაუმჯობესებლად და ემისიური კათოდების შესაქმნელად.

ნახშირბადის ნანომილაკის დიდი ელექტრული გამტარებლობა მიუთითებს იმაზე, რომ ისინი ცუდად ატარებენ ელექტრომაგნიტურ ტალღებს. ასეთი ნანომასალისგან შექმნილი კომპოზიციური ფირფიტა ელექტრომაგნიტური გამოსხივებისაგან კარგი დამცველია, რაც მნიშვნელოვანია კომპიუტერული და ელექტრონული ხელსაწყოების წარმოებაში, სამხედრო საქმეში.

დიდ წნევაზე ფულერენი ხდება მკვრივი, როგორც ალმასი. მისი მოლეკულა წარმოადგენს იდეალურად სუფთა წახნაგცენტრირებულ კუბურ მესერში თავისუფლად მოძრავ ბირთვებს. ამ თვისების გამო ფულერენი შეიძლება იქნას გამოყენებული, როგორც მყარი საპოხი და ცვეთამედეგი ნივთიერება. ამიტომ ნახშირბადის ნანომილაკები გამოიყენება ელექტრულ მიკროსკოპებში ზონდებად.

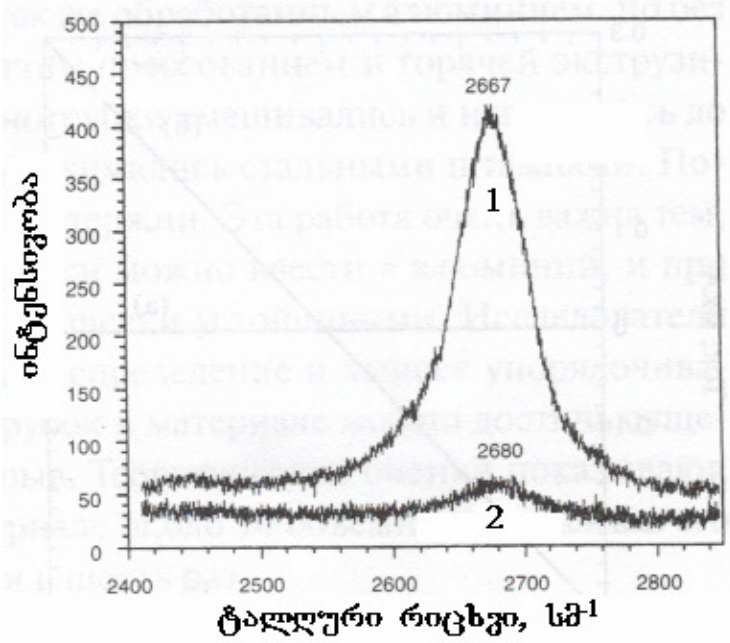

ნახ. 12. ნახშირბადის ნანომილის სპექტრი, მიღებული წყალბადში დამუშავებამდე (1) და მასში დამუშავების შემდეგ (2).

ნახშირბადის ნანომილაკები შეიძლება გამოყენებულ იქნან ლითიუმით მუხტის გადამტანიან ბატარეიებში. გამოთვლებით დადგენილია, რომ მილაკში ნახშირბადის ყოველ ექვს ატომზე შესაძლებელია ლითიუმის ერთი ატომის მოთავსება. ერთ-ერთი საინტერესო შესაძლებლობაა ნახშირბადის ნანომილაკის გამოყენება წყალბადის შესანახად, თბოელემენტების კონსტრუირებისას მომავალი ავტომობილების წარმოებაში ელექტრო ენერგიის წყაროდ (აკუმულიატორად). ნახშირის ნანომილაკის წყალბადით დატუმბვის მარტივი მეთოდი იმაში მდგომარეობს, რომ KOH-ის ხსნარში ერთშრიანი ნანომილაკები ფირფიტის სახით წარმოადგენენ კათოდს. ანოდია $Ni(OH)_2$. ელექტროლიტის დისოციაციისას მიიღება H^+, რომელიც მიემართება კათოდისაკენ, ანუ ავსებს ნანომილაკს, რაც კარგად ჩანს ნახ. 12-ზე. მიღებული მაქსიმალური ტევადობა შეადგენს 1200 $mA \cdot h / kg$. ჩვეულებრივ, ტყვია-მჟავის აკუმულატორის ელექტროდში ნახშირბადის ნანომილაკის შეყვანით იზრდება მისი მუშაობის დრო.

ეფექტური გამოყენება ჰპოვეს ნახშირბადის ნანომილაკებმა სუპერკონდენსატორში, რომელიც წარმოადგენს ელექტროლიტში ჩაშვებულ და ერთმანეთისგან მემბრანა-სეპარატორით გამოყოფილი ორი ელექტროდის სისტემას. მათში გამოიყენება ორმაგი ელექტრული შრის ეფექტი. ნახშირის ნანომილაკებიან სუპერკონდენსატორებში ელექტროდებს შორის მანძილი მცირდება მიკრონიდან ნანომეტრამდე, ფართობი – ასეული m^2 / g-ია და ამიტომ აქვთ მათ ძალიან დიდი ტევადობა ~ 200 F/ g, სიმძლავრის სიმკვრივე 30 kW / kg-მდე და ენერგია ~ 7 $W \cdot h / kg$.

შექმნილია ოთახის ტემპერატურაზე მომუშავე ველის ტრანზისტორი, სადაც ჩამკეტად გამოყენებულია ნახშირბადის ნანომილი [3]. მასზე ძაბვის მცირე ცვლილება იწვევს ნანომილის

გამტარებლობის 10^6-ჯერ და უფრო მეტად ცვლილებას, რაც უკეთესია, ვიდრე სილიციუმიანი ველის ტრანზისტორებისთვის. ასეთი ტრანზისტორის გადართვის დრო შეადგენს რამდენიმე THz-ს, რაც 1000-ჯერ უფრო სწრაფია ზემოთ აღნიშნულთან შედარებით.

ნახშირბადის ნანომილაკების გამოყენება შესაძლებელია ბიოლოგიური და სამედიცინო ტექნოლოგიების ინტეგრაციისათვის. ნანომილაკის და ბიომოლეკულის მოდიფიცირების ბიოლოგიური შეთავსების საკითხი, რომელიც საწყის სტადიაშია, სწრაფად ვითარდება. მოდიფიკაცია შესაძლებელია გახსნილი მილაკის შიგნით – ღრუში დეზოქსირიბონუკლეინის მჟავის (დნმ) შეყვანით, რომელსაც შეუძლია C ციტოქრომის ელექტრონის გადატანა ან ნანომილაკის ღია ბოლოებზე და გვერდებზე ბიომოლეკულის ადსორბცია. მოდიფიცირების საკითხის გადაწყვეტის შემდეგ შესაძლებელი იქნება ამა თუ იმ ორგანოს უჯრედთან ნახშირბადის ნანომილაკით წამლის საშუალების მიტანა, ისე, რომ არ დაზიანდება ჯანმრთელი უჯრედი.

მრეწველობის ერთ-ერთი დარგი, სადაც წარმატებით გამოიყენება ნახშირის ნანომილაკები, არის მშენებლობა. ამ მიმართულებით ყურადღება გადატანილია ახალი, უფრო გამძლე, მსუბუქი და იაფი სამშენებლო მასალის შექმნაზე. როგორც ამ თემატიკაზე სხვადასხვა პუბლიკაციის ანალიზი აჩვენებს, დიდი მიღწევები უკვე სახეზეა. კარგი მექანიკური თვისებების მქონე ნანომილაკური ნახშირის მოცულობითი 5 %-ის შეყვანით ალუმინში, მისი სიმტკიცე იზრდება ორჯერ, 10 %-ის შეყვანით – ექვსჯერ, ხოლო ფოლადის სიმტკიცე იზრდება შვიდჯერ მასში ნანომილაკური ნახშირის – 30 %-ის შეყვანისას.

აგრეთვე, შექმნილია ანტიმიკრობული თვისების მქონე საღებავი, რომელიც უსაფრთხოა სიცოცხლისათვის, გამძლეა გარე ფაქტორების მოქმედების მიმართ და ანტიკოროზიულია.

6. დასკვნა

ნახშირბადის ნანომილაკებს აქვთ უნიკალური ფიზიკურ-ქიმიური, ოპტიკური, მექანიკური და სითბური თვისებები. ბევრი მათგანი ბოლომდე არაა შესწავლილი, შესაძლებელია სხვა თვისებები არცაა აღმოჩენილი. არაა მათი ზრდის მექანიზმი ბოლომდე შესწავლილი და მიღების ტექნოლოგია ჩანერგილი წარმოებაში. მაგრამ, ეს თვისებები იძლევიან დიდ იმედს, რომ შეიქმნება ურთულესი ობიექტები და ძირფესვიანად შეიცვლება თანამედროვე მეცნიერებისა და ტექნიკის დონე, რასაც მოჰყვება განათლების, ხელოვნების და კულტურის სწრაფი ზრდა.

დამოწმებანი

1. К.В. Шалимова. Физика полупроводников. Москва: Энергоатомиздат (1985).
2. Э.Г. Раков. Нанотрубки и фуллерены. Москва: Логос (2006).
3. Ч. Пул мл., Ф. Оуэнс. Нанотехнологии. Москва: Техносфера (2006).
4. Л.И. Гречихин. Наночастицы и нанотехнологии. Минск: ИООО «Право и экономика» (2008).
5. Н.Г. Рамбиди, А.В. Березкин. Физические и химические основы нанотехнологий. Москва: Физматлит (2008).
6. Ю.И. Головин. Введение в нанотехнику. Москва: Машиностроение»(2007).
7. В. И. Балабанов. Нанотехнологии. Москва: Эксмо (2009).

HEAT CAPACITY OF THE 3D AND 2D SYSTEMS ACCORDING TO INTERATOMIC CHEMICAL BONDING

Z. Gogua, G. Kantidze

Georgian Technical University
zgogua@gmail.com

Accepted February 4, 2010

1. INTRODUCTION

The theory of specific heat of solid state, as is known, was created by Einstein [1,2] and then by Debye. Einstein's theory is based on Einstein's model of solid state. According to this model, all the atoms of the solid state have the same oscillation frequency, but in Debye's model atoms' oscillation is presented as the frequency spectrum of isotropic continuum elastic oscillations. So, in the low temperature range the results of Einstein's and Debye's theories do not differ very much from each other, though in some cases Debye's theory is very close to experimental results. In high temperature ranges, the results of Einstein's and Debye's theories are similar, and both turn into Deulong's and Petit's rules (Fig. 1).

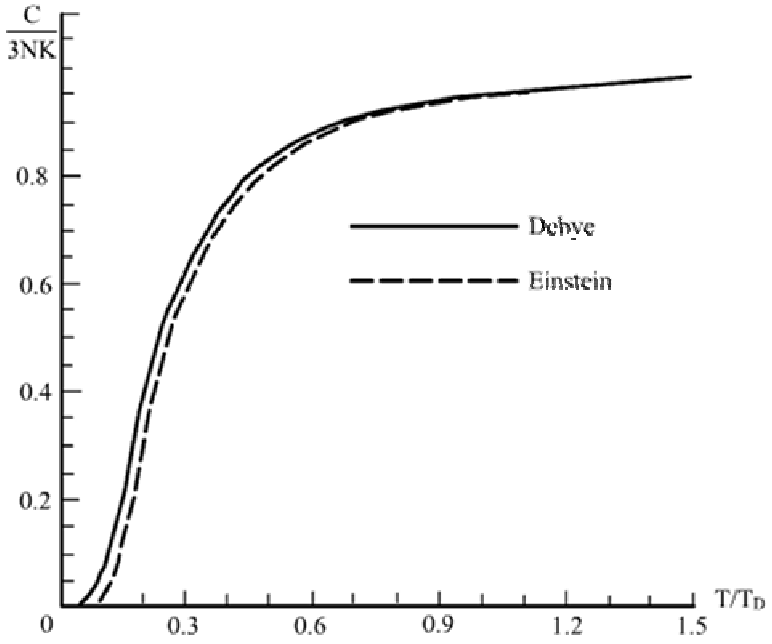

Fig. 1. Temperature-dependence of the crystal lattice heat capacity according to Debye's and Einstein's theories (T_D is the Debye temperature).

According to many experimental data [1,3–5], we can agree to the very important results that in low temperature, as well as in high temperature ranges, in general Deulong's and Petit's rules for three-dimensional crystal states (3D systems) do not work. Neither do Einstein's and Debye's theories in 2D quantized systems [4,6–8]. Heat capacity of any substance depends on the frequency of atomic oscillations. This frequency depends on the interatomic bonding energy. In 1984 a group of some authors offered a conception, which says that interatomic bonding energy depends on the correlation of bonding and anti-bonding quasi-particles (quasi-free electrons and holes in

semiconductors). Actually, this idea is the result of simplest hydrogen molecule analogy: bonding energy in hydrogen molecule is maximal, when it is performed by two, different in spin, electrons. These electrons are called bonding electrons. They are located in the singlet level (bonding level) of molecule. If we transfer one of them to the triplet level (anti-bonding level), then the molecule will collapse. Or if we add third electron to this molecule, (it will take the anti-bonding level, because bonding level is full) bonding energy will decrease. If we view solid as one huge molecule, then, according to type of interatomic bonding and correlation of bonding and anti-bonding quasi-particles we can speak about bonding force. According to the given conception melting, diffusion, defects precipitation, photomechanical and photo-stimulated diffusion occurrences in covalent crystals were investigated successfully in [9–12]. Let us calculate the heat capacity for covalent crystals.

2. CONCEPTION OF COLLECTIVE BONDING FORCE DECREASING IN COVALENT CRYSTALS AND ITS CLARITY

In covalent crystals chemical bonding between neighbor atoms is realized with sp^3 hybrid bonding. Separately, in one atom of covalent substance there are four electrons on the last orbit: two of them are *s* electrons and the other two – *p* electrons. Fig. 2 presents a scheme of converting molecular orbitals to zone pattern. There is ΔE_{sp} energetic difference between these *s* and *p* atoms. There are 2 vacancies in *s* state and 6 in *p* state (Fig. 2a). If the molecule is made of atoms like this, there appears virtual sp^3 hybrid level, where we have 8 places and all 4 (2 *s* and 2 *p*) electrons are virtually situated in them (Fig. 2b). After electrical and magnetic influence, sp^3 hybrid level collapses into bonding σ and anti-bonding σ^* levels. At each of them we have 4 places. All four electrons of the given atom occupy σ bonding level and σ^* anti-bonding level is empty (Fig. 2c). These full σ levels in the whole substance create a valence band which is full with bonding electrons and σ^* levels create an empty conducting band. One part of the collapsed *s* state of atom is the bottom of the conducting band and the other – bottom of the valence band, while one part of the collapsed *p* state is the top of the conducting band and the other part – top of the valence band (Fig. 2d). These results are known from [13].

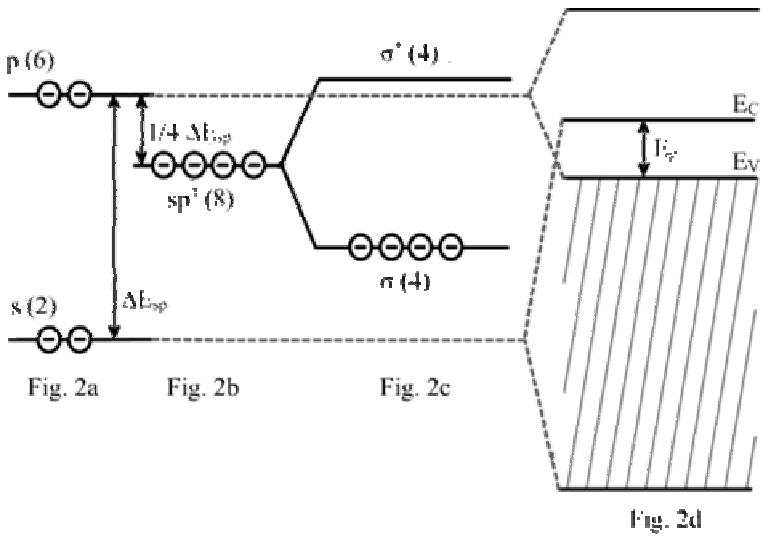

Fig. 2a Fig. 2b Fig. 2c Fig. 2d

When one σ electron moves to the anti-bonding level, there appears another anti-bonding particle: anti-bonding hole. As the top of the valence band is one part of *p* state, the wave function of the electron in this part has *p* symmetry and at the bottom of the conducting band the function has *s* symmetry. So, electron's movement from bonding level to anti-bonding level causes not only a decrease of the interatomic bonding force, but change of bonding symmetry. This means

increasing part of symmetry in linked electrons' wave function (we will consider this question in detail in the next section). According to the conception which was offered by authors of [14], decrease of bonding force and change of bonding symmetry take place between these atoms, where the anti-bonding quasi-particles "travel". Based on this conception, melting of the substance will begin when the concentration of anti-bonding quasi-particles is so great that during one cycle of atomic vibrations, anti-bonding quasi-particles will "travel" in all the atoms of the substance. We think that this conception is essentially valid, but it needs freeing from some inconsistency, which is caused by the conditions listed below: at a given temperature the quasi-impulse of anti-bonding quasi-particles is $p \sim \sqrt{3m^* kT}$, where m^* is the effective mass of the quasi-particle. Based on the given conception $d \sim 1/N^{1/3}$. According to the Heisenberg principle, $p\,d \geq 2\pi\hbar$ which means that $\sqrt{3m^* kT}\big/2\pi\hbar\, N^{1/3} \geq 1$ condition must be met, but even for the highest melting temperature $T = T_m$, e.g. for silicon $\sqrt{3m^* kT}\big/2\pi\hbar\, N^{1/3} \leq 0.1$. So, the Heisenberg principle isn't met. This means that it is unable to use even the classical rules of statistics. As we remain in the frame of conception of collective decreasing of bonding force by anti-bonding quasi-particles [14], our method is based on the wave nature of quasi-particles. In semiconductors quasi-free particles (electrons and holes) wave function in effective mass approximation may be expressed by de Broglie wave instead of Bloch's function. In terms of this, one quasi-particle decreases the bonding force and changes the symmetry not only of one atom but a whole group of atoms that are placed in a definite part of de Broglie wave length. De Broglie wave lengths for quasi-free electrons and holes are $\lambda_{De} = 2\pi\hbar\big/\sqrt{3m_e kT}$ and $\lambda_{Dp} = 2\pi\hbar\big/\sqrt{3m_p kT}$, respectively. Here m_e is effective mass of quasi-free electron and m_p – effective mass of quasi-free hole. The volume of spheres with diameters λ_{De} and λ_{Dp} are $V_{De} = 4\pi\lambda_{De}^3/3$ and $V_{Dp} = 4\pi\lambda_{Dp}^3/3$. As we are focused on semiconductors, so $n = p = n_i$. $2n_i V$ is the number of all anti-bonding quasi-particles in the entire V volume, and $n_i V\left(V_{De} + V_{Dp}\right) = (4\pi/3)\, n_i\left(\lambda_{De}^3 + \lambda_{Dp}^3\right)V$ is the sum of volumes of all the spheres with diameters λ_{De} and λ_{Dp}. At melting temperature $q_D(T_m) = (4\pi/3) n_i(T_m)\left(\lambda_{De}^3(T_m) + \lambda_{Dp}^3(T_m)\right) > 1$, e.g. in silicon $q_D(T_m) \approx 30$, in germanium $q_D(T_m) \approx 52$ and in GaAs $q_D(T_m) \approx 52$. It's definite that $n_i V\left(V_{De} + V_{Dp}\right) > V$. If we consider that anti-bonding quasi-particles decrease interatomic bonding force and change symmetry of wave function in atoms which are located on $\lambda_e = \lambda_{De}/q_D^{1/3}(T_m)$ and $\lambda_p = \lambda_{Dp}/q_D^{1/3}(T_m)$ distances, then the value $q = (4\pi/3)\, n_i\left(\lambda_e^3 + \lambda_p^3\right)$ will change at the melting temperature like this:

$$q(T_m) = \frac{4\pi}{3} n_i(T_m)\left(\lambda_e^3(T_m) + \lambda_p^3(T_m)\right) = 1. \qquad (1)$$

We think that this is the melting condition. It means that the influence of anti-bonding quasi-particles spreads everywhere in the entire crystal. When anti-bonding quasi-particles are not created by thermal energy but in a different way, e.g. by light or pressure etc, then $T \neq T_m$, which means that conditions of changing bonding force and symmetry of wave function look like this:

$$\frac{4\pi}{3} n_k\left(\lambda_e^3(T) + \lambda_p^3(T)\right) = 1. \qquad (2)$$

So, if melting is caused by heat transfer, then critical concentration of anti-bonding quasi-particles is the number of these particles at the melting temperature in a given crystal. If melting is caused by light (laser) etc, then the concentration of quasi-particles must be given with (1) condition:

$$n_k(T) = \frac{3(3kT)^{3/2} q(T_m)}{4\pi^2\hbar^3}\left(\frac{m_e^{3/2} m_p^{3/2}}{m_e^{3/2} + m_p^{3/2}}\right). \quad (3)$$

So,

$$\frac{n_k(T)}{n_k(T_m)} = \left(\frac{T}{T_m}\right)^{3/2} \Rightarrow n_k(T) = n_k(T_m)\left(\frac{T}{T_m}\right)^{3/2}. \quad (4)$$

As is known, in pure semiconductor:

$$n_i = n = p = \frac{\left(2\pi\sqrt{m_{de}m_{dp}}kT_m\right)^{3/2}}{4\pi^3\hbar^3}\exp\left(-\frac{\varepsilon_g}{2kT}\right) \quad (5)$$

and $\varepsilon_g(T_m) = \varepsilon_g(0) - \alpha T_m^2/(T_0 + T_m)$, m_{de} and m_{dp} are effective masses density-of-states of electrons and holes density.

3. CHANGE OF WAVE FUNCTION SYMMETRY AND DECREASE OF BONDING FORCE BY ANTI-BONDING QUASI-PARTICLES IN COVALENT CRYSTALS

As we said above, the bonding between atoms in covalent crystals is affected with sp^3 hybrid wave function. First, let's calculate the energy of covalent bonding in an ideal covalent crystal. When it isn't excited, calculation can be made using the LCAO method. We choose only one direction, because all the other directions are the same. The function of this sp^3 hybrid bonding in direction, which is given in Fig. 3 looks like this [15]:

$$\Phi_{1,2}(r) = \frac{1}{2}\Psi_s(r) + \frac{\sqrt{3}}{2}\Psi_{px}(r). \quad (6)$$

Covalent bonding energy between 1 and 2 atoms is [16]:

$$V_c^{(0)} = <\Phi_1(1)|H|\Phi_1(2)> = -\frac{1}{4}\left(V_{ss\sigma} - 2\sqrt{3}V_{sp\sigma} - 3V_{pp\sigma}\right), \quad (7)$$

where

$$V_{ss\sigma} = <\psi_s(1)|H|\psi_s(2)>,$$

$$V_{sp\sigma} = <\psi_s(1)|H|\psi_{px}(2)> = -<\psi_{px}(1)|H|\psi_s(2)>;$$

$$V_{pp\sigma} = <\psi_{px}(1)|H|\psi_{px}(2)>.$$

These matrix elements are given in [11].

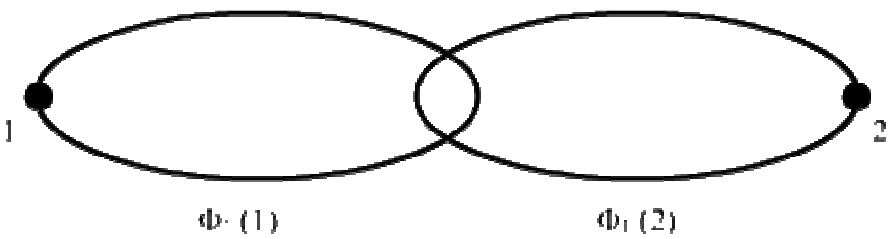

Fig. 3. One of the sp^3 bonding orbital shapes.

Now let's consider the case when an electron tears off the sp^3 hybrid bonding (Fig. 4), moves to interatomic space (in conducting band), and a hole appears in its place. Symbolically, we can call this transition $sp^3 \rightarrow sp^2s^-$, which means that one of the 4 bonding electrons is moved to anti-bonding orbital, which has *s* symmetry. If we choose the general sp^3 hybrid bonding function (6) as

the basic function (as it was in the previous case), we will provide the principle of bonding maximality and the fact that in this state, from where the bonding electron comes, the probability of catching another electron, rises twice. Using the LCAO method, sp^2s^- bonding wave function is given as:

$$\Phi_1^{(1)}(r)=\frac{1}{2\sqrt{5}}\left\{\left(\sqrt{2}+3\right)\Psi_s(r)+\sqrt{3}\left(\sqrt{2}-1\right)\Psi_{px}(r)\right\}. \quad (8)$$

The *s* and *p* functions' coefficients can be considered as "parts of state", when sp^3 hybrid bonding is changed with sp^2s^- one. Generally, in sp^3 hybrid bonding part of *p* state is 3 times greater than part of *s* state, but in the case of sp^2s^- bonding, part of *s* state is $\left(\left(\sqrt{2}+3\right)/\left(\sqrt{3}\left(\sqrt{2}-1\right)\right)\right)^2 \approx 40$ times greater, than the part of *p* state. So this is isotropization of bonding.

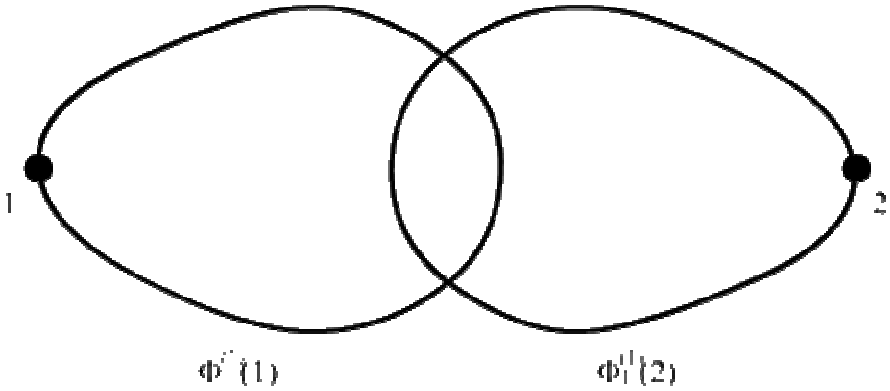

Fig. 4. Shape of sp^2s^- orbital in one of directions.

In regard to covalent bonding energy, for the given state it looks like this:

$$V_c^{(1)}=<\Phi_1^{(1)}(1)|\mathrm{H}|\Phi_1^{(1)}(2)>=\frac{1}{20}\left\{\left(11+6\sqrt{2}\right)V_{ss\sigma}-2\sqrt{3}\left(2\sqrt{2}-1\right)V_{sp\sigma}+3\left(3-2\sqrt{2}\right)V_{pp\sigma}\right\}. \quad (9)$$

4. HEAT CAPACITY CALCULATION

We will calculate the heat capacity for covalent crystals in Einstein's model of solids according to the given results. In this model, in a substance which is built with N number of atoms, the oscillation energy is:

$$\overline{E}=\frac{3N\hbar\omega}{\exp\left(\frac{\hbar\omega}{kT}\right)-1}. \quad (10)$$

In this equation zero-point oscillation energy is ignored, because only these oscillations take part in the interaction with electrons that are caused by energy higher than zero point energy. Generally, atomic oscillation frequency depends on covalent bonding energy [16,17]:

$$\omega=8\sqrt{\frac{V_C}{3d^2M}\left(1+\frac{V_0}{V_C}\right)^{-3/2}}, \quad (11)$$

where $V_0=(\varepsilon_s^{(1)}-\varepsilon_s^{(2)})/2$ is ionic bonding energy on hybridized orbital, $\varepsilon_s^{(1)}$ and $\varepsilon_s^{(2)}$ are terms of the atoms, which have *s* electrons on the last orbital (in Ge and Si, $V_0=0$), d is the distance between atoms, M is the mass of atom. The distance between atoms insignificantly depend on the concentration of anti-bonding quasi-particles [18], but V_C and oscillation frequency depend on it significantly. If $T=0\,\mathrm{K}$, $\omega=\omega_0$ then

$$\frac{\omega(n)}{\omega_0}=\sqrt{\frac{V_C(n)}{V_C(0)}\left(\frac{1+\dfrac{V_0}{V_C(0)}}{1+\dfrac{V_0}{V_C(n)}}\right)^{3/2}}\quad . \tag{12}$$

The probability of the fact that the atoms of the given covalent crystal will bond with each other with decreased bonding force is:

$$W_1=\frac{\left(\dfrac{4\pi}{3}\left(\dfrac{\lambda_e}{2}\right)^3+\dfrac{4\pi}{3}\left(\dfrac{\lambda_p}{2}\right)^3\right)n_i V}{(V/N)N}=\frac{\pi}{6}\left(\lambda_e^3+\lambda_p^3\right)n_i\,. \tag{13}$$

And the probability of occurrence of ordinary bonding is:

$$W_2=1-W_1=1-\frac{4\pi}{3}\left(\lambda_e^3+\lambda_p^3\right)n_i\,. \tag{14}$$

It means that

$$V_C(n)=\left(1-\frac{4\pi}{3}\left(\lambda_e^3+\lambda_p^3\right)n_i\right)V_C^{(0)}+\frac{4\pi}{3}\left(\lambda_e^3+\lambda_p^3\right)n_i V_C^{(1)}\,. \tag{15}$$

Let's say that

$$\gamma=1-V_C^{(1)}/V_C^{(0)},\qquad \xi=\left(\frac{1+V_0/V_C^{(0)}}{1+V_0/V_C^{(n)}}\right)^{3/2},$$

$$\delta=\left(\frac{2\pi}{3}\right)^{3/2}\left(\frac{\pi}{3q(T_m)}\right)\left(\left(\frac{\sqrt{m_{de}m_{dp}}}{m_e}\right)^{3/2}+\left(\frac{\sqrt{m_{de}m_{dp}}}{m_p}\right)^{3/2}\right).$$

According to this we get:

$$\omega_n=\omega_0\sqrt{1-\frac{4\pi}{3}\gamma\xi\left(\lambda_e^3+\lambda_p^3\right)n_i}=\omega_0\sqrt{1-\delta\gamma\exp\left(-\frac{\varepsilon_g(T)}{2kT}\right)}\,.$$

Based on the definition of heat capacity, its expression will be:

$$C=3Nk\left(\left(\frac{\hbar\omega(n)}{kT}\right)^2\frac{\exp\left(\dfrac{\hbar\omega(n)}{kT}\right)}{\left(\exp\left(\dfrac{\hbar\omega(n)}{kT}\right)-1\right)^2}+\frac{1}{4}\frac{\hbar\omega(n)}{kT}\left(\frac{\varepsilon_g(0)}{kT}+\frac{\alpha T T_0}{k(T+T_0)}\right)\times\right.$$

$$\left.\times\frac{\delta\gamma\xi\exp\left(-\dfrac{\varepsilon_g(T)}{2kT}\right)}{\sqrt{1-\delta\gamma\xi\exp\left(-\dfrac{\varepsilon_g(T)}{2kT}\right)}}\left(\frac{1}{\exp\left(\dfrac{\hbar\omega(n)}{kT}\right)-1}-\frac{\hbar\omega(n)}{kT}\frac{\exp\left(\dfrac{\hbar\omega(n)}{kT}\right)}{\left(\exp\left(\dfrac{\hbar\omega(n)}{kT}\right)-1\right)^2}\right)\right). \tag{16}$$

Other constants for some covalent crystals are given in Table 1.

As for the results of this formula for Si, Ge, and GaAs, they are given in Fig. 5. Light dots are the experimental results for Ge and black dots for Si [5].

In the case of low temperatures, when $\hbar\omega >> kT_{(n)}$ and then $\omega_{(n)}\approx\omega_0$, formula (16) will change like this:

$$C=3Nk\left(\frac{\hbar\omega_0}{kT}\right)^2\exp\left(-\frac{\hbar\omega_0}{kT}\right). \tag{17}$$

This result is similar to that of Einstein's theory for low temperature range. In case of high temperature, when $\hbar\omega << kT_{(n)}$, according to (16) formula we get:

$$C = 3N\,k\left\{1+\frac{\hbar\omega(n)}{kT}\left(1+\frac{1}{4}\left(\frac{\varepsilon_g(0)}{kT}+\frac{\alpha T\,T_0}{k(T_0+T)}\right)\right)\frac{\delta\gamma\xi\exp\left(-\frac{\varepsilon_g(T)}{2kT}\right)}{1-\delta\gamma\xi\exp\left(-\frac{\varepsilon_g(T)}{2kT}\right)}\right\}. \qquad (18)$$

Table 1. Covalent crystals' physical constants.

Constants	Ge	Si	GaAs
$\varepsilon_g(0)$, eV	0.74	1.17	1.519
α, eV / K	$4.77 \cdot 10^{-4}$	$4.73 \cdot 10^{-4}$	$5.4 \cdot 10^{-4}$
T_0, K	235	636	204
m_{de} / m_0	0.57	1.08	0.85
m_{dp} / m_0	0.37	0.59	0.53
m_e / m_0	0.18	0.26	0.067
m_p / m_0	0.25	0.38	0.15
$V_2^{(0)}$, eV	– 5.6	– 6.1	– 5.56
$V_2^{(1)}$, eV	– 2.4	– 2.6	– 2.4
ω_0, s^{-1}	$5 \cdot 10^{13}$	$9 \cdot 10^{13}$	$4.7 \cdot 10^{13}$
ω_1, s^{-1}	$3.4 \cdot 10^{13}$	$6 \cdot 10^{13}$	$2.3 \cdot 10^{13}$
$q(T_m)$	52	30	52
$n_i(T_m)$, cm^{-3}	$1.84 \cdot 10^{19}$	$3.2 \cdot 10^{19}$	$7.4 \cdot 10^{18}$
T_m, K	1210	1690	1511
γ	0.57	0.57	0.57
$C(T_m)$, cal / mole · K	9.5	10	7.14

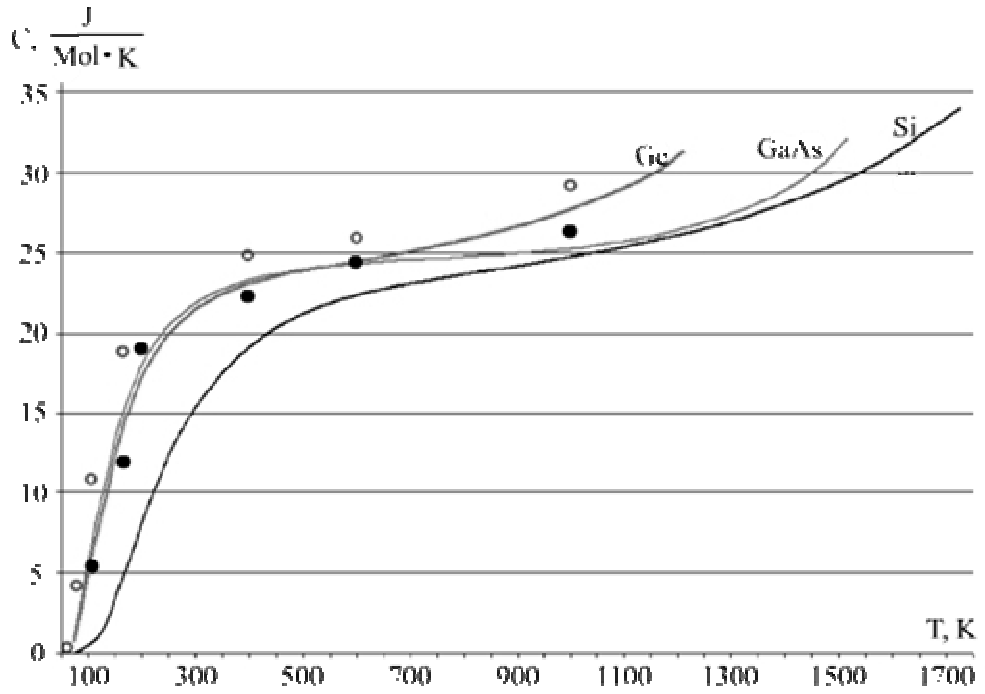

Fig. 5. Dependence between heat capacity and temperature in 3D crystals in Ge and Si according to formula (16) and [5].

In the case of nanostructures, these formulas work well, excepting those in which concentration of charge carriers in pure semiconductors takes place. As all parameters are same, except n_i, we get [19]: $n_i^{2D} = \sqrt{N_C^{2D} N_V^{2D}} \exp\left(-\varepsilon_g(T)/2kT\right)$, where $N_C^{2D} = m_{de} kT/\pi\hbar^2 W$ and $N_V^{2D} = m_{dp} kT/\pi\hbar^2 W$ are densities of quantum states at the edges of conducting and valence bands in 2D systems and W is the thickness of the sample. According to this data, the dependence between temperature and oscillation frequency is:

$$\omega(T) = \omega_0 \sqrt{1 - \delta_1 \gamma \xi \frac{\exp\left(-\dfrac{\varepsilon_g(T)}{kT}\right)}{W\sqrt{kT}}}\ , \tag{19}$$

where

$$\delta_1 = \frac{4\pi^3 \sqrt{m_{de} m_{dp}}}{9\sqrt{3}\, q(T_m)} \left(m_e^{-3/2} + m_p^{-3/2}\right).$$

The final formula for heat capacity will be:

$$C = 3Nk \left\{ \left(\frac{\hbar\omega(n)}{KT}\right)^2 \frac{\exp\left(\dfrac{\hbar\omega(n)}{kT}\right)}{\left(\exp\left(\dfrac{\hbar\omega(n)}{kT}\right) - 1\right)^2} - \frac{1}{4}\left(\frac{\hbar\omega(n)}{kT}\right) \frac{\xi\gamma\delta_1}{\sqrt{kT}\, W} \left(\frac{\varepsilon_g(0)}{kT} + \frac{\alpha T\, T_0}{k(T_0 + T)^2} - 1\right) \times \right.$$

$$\times \frac{\exp\left(-\frac{\varepsilon_g(T)}{2kT}\right)}{\sqrt{1-\delta_1\gamma\xi\frac{\exp\left(\frac{\varepsilon_g(T)}{2kT}\right)}{W\sqrt{kT}}}}\left(\frac{1}{\exp\left(\frac{\hbar\omega(n)}{kT}\right)-1}-\left(\frac{\hbar\omega(n)}{KT}\right)\frac{\exp\left(\frac{\hbar\omega(n)}{kT}\right)}{\left(\exp\left(\frac{\hbar\omega(n)}{kT}\right)-1\right)^2}\right)\Bigg\}. \quad (20)$$

In high temperature range, when $\hbar\omega >> kT$:

$$C = 3Nk\left\{1+\left(\frac{\hbar\omega(n)}{kT}\right)\left(1+\frac{1}{4}\frac{\xi\gamma\delta_1}{\sqrt{kT}W}\left(\frac{\varepsilon_g(0)}{kT}+\frac{\alpha T T_0}{k(T_0+T)}-1\right)\right)\frac{\exp\left(-\frac{\varepsilon_g(T)}{2kT}\right)}{1-\delta\gamma\xi\frac{\exp\left(-\frac{\varepsilon_g(T)}{2kT}\right)}{\sqrt{kT}W}}\right\}. \quad (21)$$

As it seems, in the case of low temperature range in 3D crystals, as well as in 2D systems, dependence between heat capacity and temperature is described with the same equation, but in high temperature range in 2D system, besides this dependence, there appears a dependence on nanocrystal's depth.

Let's see how our equation complies with the first principle. In our calculations we used results based on Maxwell–Boltzmann distribution function (rules of classical statistics). We can use them if between Fermi level and corresponding band level energetic difference is $\sim (2-3)kT$. We consider the semiconductors where location of Fermi level, according to classical statistic rules is given as follows:

$$F = \frac{E_C - E_V}{2} - \frac{3}{4}kT\ln\frac{m_n}{m_p} = \frac{E_C - E_V}{2} - \Delta(T)$$

Even at the highest temperature in Ge and Si $\Delta(T_m) \sim 2kT$ and $\Delta(T_m) \sim 3kT$. This means that we can use rules of classical statistics. As to using basic criteria of a kinetic equation it looks like: $E\Delta t >> \hbar \Rightarrow d >> \lambda_D/2\pi$, where d is the average distance between anti-bonding quasi-particles. $d \sim \lambda_D/q^{1/3}(T_m)$, because $q^{1/3}(T_m) \sim 3-3.6$, $d/\lambda_D > 1$. So, using kinetic equation criteria is met approximately.

5. SUMMARY

The interatomic bonding energy was calculated in covalent crystals in the conditions of $sp^3 \rightarrow sp^2s^-$ excitement (when sp^3 bonding electron takes anti-bonding position). It is shown that part of *s* state increases and *p* state's part decreases many times in sp^3 hybrid bonding in this state. This causes an increase of the degree of freedom of atoms, so this means that the state becomes "fluid" or "soft". Besides, interatomic bonding force decreases and based on this conception, we considered melting process and defined the critical concentration of anti-bonding quasi-particles. This anti-bonding particles form not only by heat transfer, but by any external excitement (light, injection of charge carriers, pressure etc.). The heat capacity in Einstein's model of solid state is calculated according to the dependence between phonon spectrum of atoms and concentration of anti-bonding quasi-particles. These calculations are made for 3D crystals as well as for low-dimensional nanocrystals. Calculations, performed using this method show that, as is seen in Fig. 5, in usual crystals, calculated heat capacity agrees with experimental data better than the calculation results using previous methods. Our method is not very precise but it has other positive sides: this is

a methodologically new principle which can be used in the case of states with different type of chemical bonding in 3D systems, as well as in low-dimensional systems.

REFERENCES

1. Debye Model – Wikipedia. The Free Encyclopedia. 04.05 (2007).
2. K.V. Shalimova. Fizika Poluprovodnikov. Moscow: Energiya (1971).
3. A.R. Regel', V.M. Glazov. Periodicheskij Zakon i Fizicheskie Sdojstva Elektronnykh Rasplavov. Moscow: Nauka (1978).
4. M. A. Aldzhanov, A.A. Abdurragimova, S.G. Sultanova, M.D. Nadzhafzade. Phys. Solid State, **49**, 320 (2007).
5. Tablitsy Fizicheskikh Velichin. Moscow: Atomizdat (1976).
6. V.N. Vasiliev, M.M. Mazkina, A.V. Inyushkin, H. Kadeyama. JEPT Lett., **73**, 633 (2001).
7. A.G. Gusev. Nanokristallicheskie Materialy: Metody Polucheniya i Svojstva. Ekaterinburg: URO RAS (1988).
8. A.V. Markin, N.N. Smirnova, A.G. Lyapin, M.V. Kondrin. Phys. Solid State, **48**, 1016 (2006).
9. I.G. Gverdtsiteli, A.B. Gerasimov, Z.G. Gogua, M.G. Pkhakadze, Z.V. Jibuti. Bull. Acad. Sci. Georg. SSR, **127**, 517 (1987).
10. I.G. Gverdtsiteli, A.B. Gerasimov, Z.G. Gogua, M.G. Pkhakadze, Z.V. Jibuti. Bull. Acad. Sci. Georg. SSR, **128**, 293 (1987).
11. A.B. Gerasimov, G.D. Chivadze, N.G. Kutivadze, A.P. Bibilashvili, B.G. Bokochadze. Phys. Solid State, **41**, 2017 (1999).
12. A.B. Gerasimov, G.D. Chivadze, N.G. Kutivadze, A.P. Bibilashvili, B.G. Bokochadze. Phys. Solid State, **42**, 683 (2000).
13. M. Kastner. Phys. Rev. Lett., **28**, 355 (1972).
14. I.G. Gverdtsiteli, A.B. Gerasimov, M.G. Phakadze, A.A. Tsertsvadze. Bull. Acad. Sci. Georg. SSR, **115**, 8 (1985).
15. K. Dei, D. Selbin. Teoreticheskaya Neorganicheskaya Khimiya. Moscow: Khimiya (1976).
16. W.A. Harrison. Electronic Structure and the Properties of Solids. The Physics of the Chemical Bond. San Francisco: W.H. Freeman & Co (1980).
17. A.B. Gerasimov, G.D. Chivadze, Z.G. Gogua. Ukr. J. Phys., **51**, 785 (2006).
18. http://ece-www.colorado.edu/~bart/book/book/chaPetitr2/ch2_3.htm. - 30.01.2007.
19. V.P. Dragunov, I.G. Nejzvestnyj, V.A. Grudchin. Osnovy Nanoelektroniki. Novosibirsk: NGTU (2004).

თულიუმის, პრაზეოდიუმისა და ნეოდიუმის სულფიდების თხელი ფირების ლეგირება

ქ.დ. დავითაძე [1], თ.ა. მინაშვილი [2], გ.ნ. ილურიძე [2]

[1] საქართველოს საავიაციო უნივერსიტეტი,
ketketi@mail.ru
[2] საქართველოს ტექნიკური უნივერსიტეტი
tamazminashvili@rambler.ru

მიღებულია 2010 წლის 8 თებერვალს

ქიმიური ვალენტობის წესით შექმნილი იშვიათმიწა ელემენტების (იმე) ერთნახევრიანი სულფიდები გაჯერებული ნაერთებია, სადაც კათიონური მესრის ყოველი მეცხრე კვანძი ვაკანტურია. Ln_2X_3 ტიპის შენაერთები დაბალ ტემპერატურაზე იზოლატორებია. ოთახის ტემპერატურაზე მათი კუთრი წინაღობა 10^8 Ohm · m-ს უახლოვდება. უფრო დაბალი წინაღობები გამოწვეულია ან მინარევული ატომების არსებობით ან სტექიომეტრიიდან გადახრით [1]. რაღა თქმა უნდა, სტექიომეტრიული შემადგენლობის მქონე სუფთა მასალების გამოყენება შეუძლებელია მიკროელექტრონული ხელსაწყოს შესაქმნელად. სწორედ ამიტომ არის საინტერესო ამ შემადგენლობის ფირების ლეგირება.

ერთნახევრიან სულფიდებში იშვიათმიწა ელემენტებს სამის ტოლი ვალენტობა აქვთ. ამიტომ მათი ჩანაცვლების გზით განსაზღვრული გამტარებლობის ტიპის მისაღწევად მალეგირებელ ელემენტებად გამოყენებულ უნდა იყოს პერიოდული სისტემის მეორე ან მეოთხე ჯგუფის ელემენტები. ამ დროს აქცეპტორის როლი უნდა შეასრულონ II ჯგუფის ელემენტებმა, ხოლო დონორის – IV ჯგუფის ელემენტებმა, რომელთა ლოკალიზაცია ხდება სამვალენტიანი იმე-ის სუბმესრის კვანძებში. თუ მალეგირებელი ატომი მოთავსდა კრისტალური მესრის კვანძებს შორის, ამ შემთხვევაში არსებობს ალბათობა იმისა, რომ II და IV ჯგუფის ელემენტებმა დონორის როლი შეასრულონ. ეს ალბათობა დამოკიდებულია გეომეტრიულ და ელექტროქიმიურ ფაქტორებზე.

მინარევული ატომების კრისტალური მესრის კვანძებში განლაგება შესაძლებელია, როცა მინარეული ატომების r_{imp} რადიუსებსა და მატრიცის ატომების r_{REE} რადიუსებს შორის სხვაობა არ აღემატება 15 %-ს. ამ დროს საქმე გვაქვს ჩანაცვლების მყარ ხსნართან და $0.85 < r_{imp} / r_{REE} < 1.15$.

ჩანერგვის მყარ ხსნარში მინარეული ატომების კვანძებს შორის განთავსების პირობაა $r_{imp} < r_{\text{Ln–S}}$, სადაც $r_{\text{Ln–S}}$ იმე-სა და გოგირდის უახლოეს ატომებს შორის მანძილია. Tm_2S_3-ში ეს მანძილია 12.46, Nd_2S_3-ში – 2.85, ხოლო Pr_2S_3-ში – 8.9 Å. ჩანაცვლების მყარი ხსნარების წარმოქმნის პირობაა მინარევული და მატრიცული ატომების ელექტროქიმიური მსგავსება – ელემენტები ქიმიური დაძაბულობის რიგში ერთმანეთთან ახლოს უნდა იმყოფებოდნენ, რადგანაც, წინააღმდეგ შემთხვევაში, ადგილი ექნება ქიმიური ნაერთის წარმოქმნას.

ყოველივე ამის საფუძველზე ჩატარებული ანალიზის, ლეგირების პროცესის სიმარტივის და მალეგირებელი ელემენტის ტოქსიურობის გათვალისწინებით ჩვენს მიერ მიღებული თულიუმის, პრაზეოდიუმისა და ნეოდიუმის ერთნახევრიანი სულფიდების თხელი ფირების მალეგირებელ ელემენტებად შერჩეულ იქნა II ჯგუფის ელემენტი კადმიუმი და IV ჯგუფის ელემენტი ტყვია [2].

ფირების მიღების ტექნოლოგია საშუალებას არ იძლევა ფირის მიღების პროცესის პარალელურად განხორციელდეს მისი ლეგირებაც, რადგან ძალიან მაღალია მალეგირებელი ელემენტის მიერ ახალი ქიმიური ნაერთის შექმნის ალბათობა. ამიტომ ასეთ პროცესად ჩვენს მიერ შერჩეულ იქნა წინასწარ მიღებული ფირის ლეგირება მინარევის დიფუზის მეთოდით, კერძოდ, დიფუზიით დახურულ მოცულობაში, რომელიც გამოირჩევა პროცესის სიმარტივით და ფირის გაჭუჭყიანების ნაკლები ალბათობით.

ვინაიდან კადმიუმი ხასიათდება ორთქლის მაღალი დრეკადობით [3], ლეგირებისას ადგილი აქვს ორთქლის ფაზაში მყოფი კადმიუმის ატომების ადსორბციას ფირის ზედაპირზე და შემდეგ მათ დიფუზიას ფირის სიღრმეში. ამ დროს, როგორც წესი აირად ფაზაში მყოფი ატომების რაოდენობა გაცილებით მეტია ფირში დიფუნდირებული ატომების რიცხვზე. დიფუზიის ტემპერატურისა და დროის ვარირებით შესაძლებელია საკმაოდ ფართო დიაპაზონში ვცვალოთ მინარევის ზედაპირული კონცენტრაცია. წონასწორული კონცენტრაცია პროპორციულია ორთქლის წნევის და მყარდება არა მყისიერად, არამედ გარკვეული დროის შემდეგ. თუკი წონასწორობა დიფუზიის დროზე ნაკლებ დროში მიიღწევა, ზედაპირული კონცენტრაცია შეიძლება ჩაითვალოს მუდმივად. დახურულ მოცულობაში დიფუზიის ჩატარებისას ეს პირობა უმრავლეს შემთხვევაში სრულდება. ამავე დროს გათვალისწინებული უნდა იყოს დიფუზანტის ორთქლის წნევის ტემპერატურაზე დამოკიდებულება. ზოგიერთი მინარევისთვის დიფუზიის ტემპერატურაზე ორთქლის წნევა იმდენად მაღალია, რომ შეიძლება მოხდეს ამპულის რღვევა.

აირადი ფაზიდან ლეგირების მეთოდი ტყვიით ლეგირებისას არ გამოდგება, რადგან ტყვიის წონასწორული წნევა ძალიან დაბალია იმ ტემპერატურებზე, რომლებზეც ფირის მასალის დაშლას ადგილი არა აქვს. ამიტომ ფირზე წინასწარ ვაკუუმურ-თერმული აორთქლებით ეფინება ტყვია, შემდეგ კი ვატარებთ დიფუზიური გამოწვის პროცესს კვარცის დახურულ ამპულაში ინერტული აირის გარემოში. ეს მეთოდი შეესაბამება დიფუზიას სასრულო სიმძლავრის წყაროდან.

აღნიშნული ფირების ფოტოგამტარებლობის სპექტრალური და ტემპერატურული დამოკიდებულების გაზომვა პირველად შესაძლებელი გახდა მათი კადმიუმით და ტყვიით ლეგირების შემდეგ.

Tm_2S_3-ის, Pr_2S_3-ის და Nd_2S_3-ის თხელი ფირების ტყვიის ატომებით ლეგირება ჩატარებულ იქნა დახურულ მოცულობაში მინარევის შემოსაზღვრული წყაროდან დიფუზიის მეთოდით. ამ მეთოდის განსახორციელებლად ფირებს ტყვიით წინასწარ ვფარავთ 10^{-6} mm Hg-იან ვაკუუმში თერმული აორთქლების მეთოდით. დაფენის პროცესში ფუძეშრის ტემპერატურა ~ 400 K-ის ტოლია, ხოლო ტყვიის ამაორთქლებლის ტემპერატურა – ~ 1300 K-ის, ხოლო დაფენილი ტყვიის ფენის სისქე (8 – 15) μm-ის რიგისაა. დაფენის შემდეგ ფირს ნელა ვაცივებთ ოთახის ტემპერატურამდე ვაკუუმში, რის შემდეგაც მას ვათავსებთ წინასწარ მარილმჟავას, აზოტმჟავასა და მლღობი მჟავას ნარევით 1 h-ის განმავლობაში ქიმიურად დამუშავებულ კვარცის ამპულაში, რომელშიც 10^{-5} mm Hg-მდე ვაკუუმია. ამპულას ვავსებთ სპექტრალურად სუფთა არგონით და მისი განრჩილვის შემდეგ მას ვათავსებთ დიფუზიურ ღუმელში, რომელსაც ვახურებთ ~ 900 K-მდე და ვაწარმოებთ დიფუზიურ გამოწვას (8 – 25) h-ის განმავლობაში.

პროცესის დასრულების შემდეგ ნიმუშს ვაციებთ ოთახის ტემპერატურამდე და ფირის ზედაპირიდან ტყვიის ნარჩენს ვაცილებთ მექანიკური პოლირებით.

Tm_2S_3-ის, Pr_2S_3-ის და Nd_2S_3-ის თხელი ფირების კადმიუმით ლეგირება ხდება დახურულ მოცულობაში აირადი ფაზიდან. ზემოთ ნახსენები მეთოდით ქიმიურად დამუშავებული ამპულის სხვადასხვა მხარეს ვათავსებთ ფირს და ~ (10 – 15) g რაოდენობის მაღალი სისუფთავის კადმიუმს. ამის შემდეგ ამპულას ვტუმბავთ და განრჩილვის შემდეგ ვათავსებთ სპეციალურად აწყობილ ორსექციან ჰორიზონტალურ ღუმელში, რომელსაც

ვახურებთ ~ 900 K-მდე. ამ ტემპერატურაზე კადმიუმის ორთქლის წნევა საკმაოდ მაღალია ~ $1.3 \cdot 10^{-2}$ mm Hg. დიფუზიურ გამოწვას ვაწარმოებთ (15 – 45) h-ის განმავლობაში. ამის შემდეგ ოთახის ტემპერატურამდე გაციებულ ფირს მექანიკური პოლირებით ვაცილებთ ზედმეტ კადმიუმს.

რენტგენოგრაფიული და ელექტრონოგრაფიული მეთოდებით ხდება ფირების ფაზური შემადგენლობის კონტროლი ლეგირებისას შესაძლო მეორე ფაზის გაჩენის გამოსავლენად. როგორც კვლევებმა გვიჩვენეს, არც ტყვიით და არც კადმიუმით ზემოთ ნახსენებ რეჟიმებში ფირების ლეგირებისას დამატებითი ფაზის წარმოქმნას ადგილი არა აქვს.

დამოწმებანი

1. А.В. Голубков, Е.В. Гончарев, В.П. Жузе, Г.М. Логинов, В.М. Сергеева, И.А. Смирнов. Физические свойства халькогенидов редкоземельных элементов. Ленинград: Наука (1973).
2. Z.U. Jabua, K.D. Davitadze, T.O. Dadiani, A.V. Gigineishvili, M.I. Stamateli. Georg. Engin. News, **3**, 27 (2004).
3. З.У. Джабуа, Л.Н. Глурджидзе, Т.О. Дадиани, В.В. Санадзе. Сообщ. АН ГССР, **104**, 669 (1981).

STIMULATED PHENOMENA IN GLASS DOPED WITH CdSe QUANTUM DOTS

G. Dekanozishvili [1], D. Driaev [1], T. Kalabegishvili [1, 2], V. Kvatchadze [1]

[1] E. Andronikashvili Institute of Physics
vkvachadze@yahoo.com
[2] Ilia State University

Accepted February 10, 2010

1. INTRODUCTION

Thermo-stimulated luminescence of aluminoborosilikate glass doped with CdSe quantum dots (average radii $R \sim 28$ and 47 Å) and irradiated by ionizing radiation was studied first in [1]. Compound peaks at 100 and 150 °C, respectively, were observed on thermo-stimulated luminescence (TSL) curves of these samples. The intensities of these peaks increased with irradiation dose growth so, that dose-effect linear correlation was revealed. Consequently there is a prospect of CdSe QDs-doped glass application as a dosimetric material.

One of the severe requirements to such materials is high stability of properties, which is expressed on the one hand in the possibility of long-term storage of dosimeteric information [1] and on the other hand in reproducibility of results during repeated irradiation – reading cycles. The last-named question will be studied in the article presented.

Optically stimulated luminescence (OSL) [2] is even more sensitive method for solution of similar tasks, but in the case under investigation application of this method for samples containing semiconducting CdSe was hampered and available thermo-optical luminescence (TOL) method [3] was used only for studies of photoluminescence and its temperature quenching [4].

Results of ultraviolet light (UV) effect on the material under investigation are also given.

2. SAMPLES AND METHODS

Measurements of TSL and photoluminescence temperature quenching were performed on the modernized unit [1] that performs selective measurements of CW–OSL (a constant illumination intensity mode) and high-temperature TSL, ((300 – 775) K, a constant heating rate) as well as TOL. The luminescence was recorded by photoelectric multiplier integrally over all wavelengths. The source of exiting light is blue LED, $\lambda = 447$ nm.

The investigated samples were prepared by growth of quantum dots in glass [5]. The average radii (28 Å) of CdSe nanoparticles were determined by the transmission electron microscope. For comparison, along with the activated samples the "pure" ones i.e. samples not doped with nanoparticles were studied.

The samples in the presented paper were the same as in [1]. Previously they underwent repeated cycles of ionizing radiation action and high-temperature TSL measurement. In the experiments with application of UV were also used the same samples.

Irradiation was carried out at room temperature by X-rays on the URS–55M device with X-ray tube BSV–2Cu with a copper anticathode (50 kV, 20 mA).

The UV light irradiation was performed by the mercury-quartz lamp DRT–220 application.

3. RESULTS AND DISCUSSION

TSL curves of irradiated samples with CdSe QDs having radii of 28 Å (curves 3-8 [1]) are given in Fig. 1a. An intensive compound peak in the temperature range (50– 300) ºC (with maximum at 150 ºC) as well as a low intensity peak at 375 ºC was observed. With irradiation time growth the intensities of both peaks rise with constant rate. Prior to TSL detection spontaneous post-radiation luminescence was also observed – very intensive signals that extinct exponentially with time.

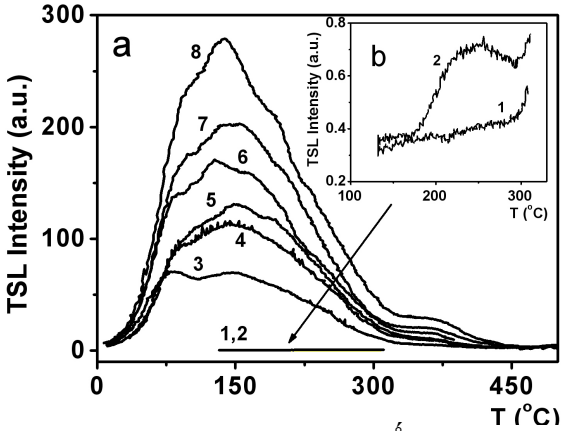

Fig. 1. TSL curves of CdSe quantum dots (28 Å) doped glass irradiated by X-rays (curves 3 – 8) and UV light (curve 2). Irradiation time: curve 2 – 5 h; 3 – 10; 4 – 15; 5 – 20; 6 – 40; 7 – 60; 8 – 80min. Curve 1 refers to the undoped glass after X-irradiation (30 min).

Intensities of TSL curves obtained this time (sample exposure times are 30, 40 and 60 min) are almost by (20 – 25) % lower than similar curves in Fig. 1a. However linear correlation between TSL peak intensity and exposure time is retained. Consequently, possibility to measure doses of ionizing radiation with samples of CdSe QDs doped glass does not vanish.

For investigated samples irradiance responsivity decrease for repeated cycles of "irradiation-reading" is possibly due to internal changes that are caused by thermal load in the process of high temperature TSL measurement. It is encouraging that temperature location of the main peak in Fig. 1a is considerably remote from the high temperature zone and fatigue effect will have a little impact on dosimetric memory of the material.

UV light effect in TSL of investigated samples is negligible compared with X-ray impact.

After 5 h irradiation one negligible peak is observed at ~ 250 ºC (curve 2, Fig. 1b), i.e. in the temperature range that is overlapped by intensive TSL peak (150 ºC) of X-rayed samples (see Fig. 1a). Curve 1 refers to the undoped glass after X-irradiation (30 min).

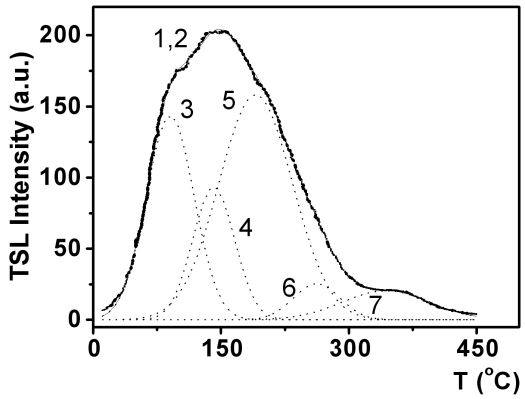

Fig. 2. TSL curve of X-irradiated sample – curve 1 (the same as curve 7, Fig. 1) and components of its resolution (curves 3, 4, 5, 6 and 7) and summed curve of components – curve 2.

In Fig. 2 the result of formal resolution of TSL peak at 150 ºC (curve 7, Fig. 1a) into elemental components is given. Curves 3, 4, 5 and 6 display presence of spectrum of trapping sites for charge carriers that are released at temperatures 90 (3), 141 (4), 190 (5) and 262 ºC (6). In our opinion, it is real to isolate the most low-temperature peak (3) from this peak group by combined TSL + OSL (TOL) method and "develop" operating peak of prospective detector on its basis.

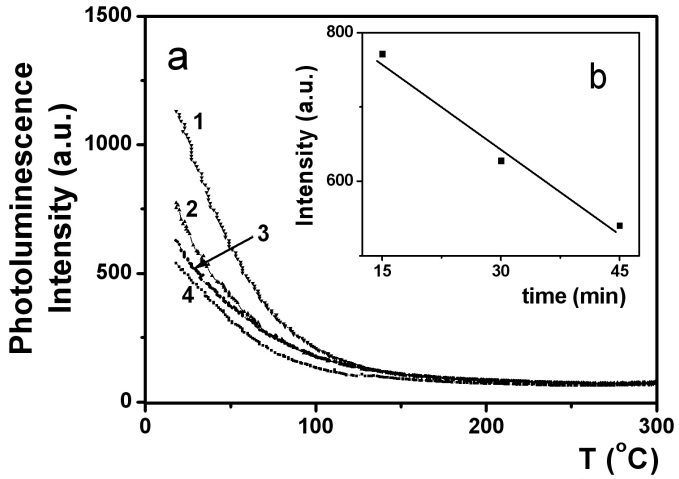

Fig. 3. Luminescence quenching curves of CdSe quantum dots (28 Å) doped glass before (curve 1) and after irradiation by X-rays (irradiation time: curve 2 – 15, 3 – 30 and 4 – 45 min) (a) and photoluminescence intensity dependence on sample exposure time (b).

Curves, shown in Fig. 3a were formally obtained by TOL method, but actually they are curves of photoluminescence temperature quenching, as it was noted in Introduction. Curve 1 applies to glass sample with CdSe QDs before irradiation; curves 2, 3 and 4 refer to the same sample after X-raying (exposure times are 15, 30 and 40 min, correspondingly). In all the cases, both before and after irradiation the effect of temperature quenching of photoluminescence prevails (charge transfer between energetic levels of CdSe), and weaker TSL effect (charge transfer between CdSe luminescence centers and glass trapping centers) does not become apparent.

Luminescence quenching curve lies progressively lower when increasing irradiation dose. This, evidently is caused by the fact that the more X-ray intensity is, the more charge carriers leave QDs and are captured by glass traps. As a result the efficiency of photoluminescence processes should decrease (that is actually observed in Fig. 3a), whereas TSL which is caused by the process of carriers return to QDs, should increase (see Fig. 1a). Proceeding from such pattern of charge carriers' behavior and from the radiation growth trend of TSL intensity, photoluminescence intensity should decrease with exposure time growth, which is actually shown in Fig. 3b.

4. CONCLUSIONS

The investigation of glass samples doped with CdSe nanoparticles and X-rayed showed that:

- Peak at 150 ºC on the TSL curve is a compound one and originates from superposition of at least four elemental peaks.
- When repeating cycle "irradiation-reading" multiply possibility to identify dose of ionizing radiation is retained.
- Photoluminescence efficiency decreases with irradiation dose increase.

UV radiation effect on the specified samples is negligible.

REFERENCES

1. G. Dekanozishvili**,** D. Driaev, T. Kalabegishvili**,** V. Kvatchadze**.** Thermoluminescence and absorption spectra of CdSe quantum dot doped glass irradiated by X-rays. J. Luminescence, **129**, 1154 (2009).
2. E.M. Yoshimura, E.G. Yukihara. Nucl. Instr. Meth. Phys. Res. B, **250,** 337 (2006).
3. L. Botter–Jensen, S.W.S. Mc Keever, A.G. Wintle. Optically Stimulated Luminescence Dosimetry. Amsterdam: Elsevier (2003).
4. D. Curie. Luminescence Cristalline. Paris: Dunod (1960).
5. U. Woggon. Optical Properties of Semiconductor Quantum Dots. Berlin: Springer–Verlag (1997).

ПРЕДЛОЖЕНИЯ ПО СОЗДАНИЮ ЦЕНТРА НАНОТЕХНОЛОГИИ В ГРУЗИИ

Р.И. Чиковани

Грузинский технический университет
rchikovani@mail.ru

Принята 10 февраля 2010 года

1. НЕКОТОРЫЕ ВОПРОСЫ РАЗВИТИЯ НАНОТЕХНОЛОГИИ

В последнее время во всём мире стремительно развивается новое направление науки и техники, названное нанотехнологией.

Нанотехнологию можно определить как набор технологий и методов, основанных на манипуляциях с отдельными атомами и молекулами в масштабах (1 – 100) nm (1 нанометр = 10^{-9} метра). Эти методы, регулируя структуру и состав вещества позволяют создавать наноматериалы, наноструктуры, наноэлементы и нанооносистемы для применения в разных отраслях науки, техники и промышленности.

А термин нанонаука, по определению международной организации по стандартизации "ASTM International" означает "изучение материалов, процессов, явлений или устройств в нанометровом диапазоне".

Несмотря на маленький срок развития, нанотехнология, основываясь на достижениях физики, химии, биологии и других фундаментальных наук, намечает невиданные ранее перспективы и невероятные возможности её применения во многих сферах деятельности человека (рис. 1). По прогнозу, нанотехнология радикально изменит жизнь человеческого общества и повлияет на процессы, протекающие в природе. По данным экспертов США развитие нанотехнологии через 10 – 15 лет позволит создать новую отрасль экономики с оборотом 1 триллион долларов и миллионы рабочих мест, а к 2030 году половина производимой продукции в мире будет изготовлена с применением нанотехнологии. Многое из сфер применения нанотехнологии неизвестно даже учёным.

Исходя из этого, нанотехнология может быть определена ещё как совокупность прикладных исследований нанонауки и их практических применений, включая промышленное производство и социальные приложения.

Нанотехнология признана специалистами всех стран наиболее всеобъемлющей основой дальнейшего роста материального производства и благосостояния людей.

О популярности нанотехнологии указывает то, что в настоящее время ежегодно проводятся сотни конференций, посвящённых различным аспектам нанотехнологии. Опубликованы сотни тысяч статьей и монографий, созданы специальные сайты в интернете, идёт интенсивная подготовка к созданию наноэлектронных элементов и различных функциональных устройств от простейших до нанокомпьютеров.

Можно убедительно сказать, что XXI век – это век нанотехнологии и эта технология во многом определит не только научно-технический прогресс, но и социально-экономическое благосостояние общества. Нанотехнология радикально преобразует человеческую жизнь в целом, и это по прогнозам экспертов всего за 30 – 50 лет.

Необходимо отметить, что возникновение нанонауки и нанотехнологии не обусловлено только уменьшением геометрических размеров материалов (частиц) до нанометрового уровня. Основным фактором является появление у этих материалов совершенно новых, уникальных свойств, которые не объясняются в рамках классической физики и требуют привлечения квантовой физики. Для объяснения и исследования процессов и явлений, протекаю-

щих в нанообъектах понадобились новые идеи, подходы, новая измерительная аппаратура и технологическое обеспечение получения наноматериалов и наноструктур.

Размерные эффекты, проявляющиеся в наномасштабных объектах разнообразны (изменение электрической проводимости, магнитных свойств, механической прочности, излучательной способности, оптических характеристик, химических свойств, биологической активности и др., а также характер их изменений) и они определяют свойство и применение этих нанообъектов. Важно отметить, что при переходе на наноразмеры меняется структура твердых тел (в т.ч. полупроводников), меняется ширина запрещенной зоны, иногда и характер химической связи.

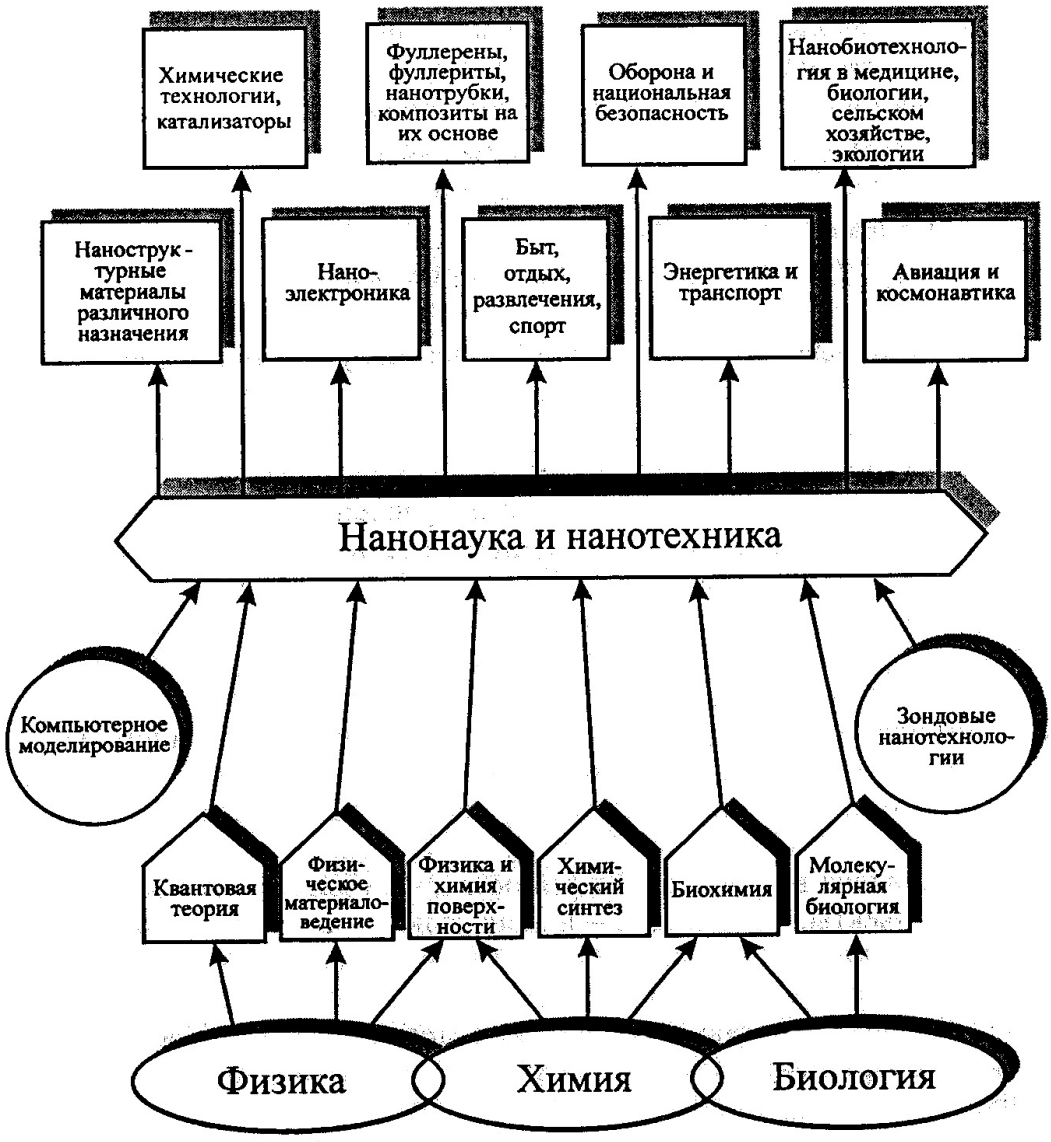

Рис. 1. Фундаментальные основы и области применения нанонауки и нанотехники.

Среди размерных эффектов весьма важным эффектом, определяющим технологию и дизайн создания нанопродукции, является резкое увеличение доли поверхности наночастиц по сравнению с объёмом, т.е. доля атомов, находящихся в поверхностном слое растёт с уменьшением размера частиц вещества. Известно, что поверхностные атомы обладают свойствами, отличающимися от «внутренних», поскольку они связаны с соседями иначе, чем внутри вещества. В результате, на поверхности велика вероятность протекания процессов атомной реконструкции и возникновения других структур расположения атомов и их

свойств. Современные методы позволяют создавать разные наноструктуры из отдельных атомов и молекул.

Материалы, в основе которых лежат различные наноразмерные структуры, во многих случаях обладают комплексом уникальных свойств, существенно отличающихся от характеристик объёмных материалов с таким же химическим составом. Например, золото приобретает способность излучать свет, слой серебра толщиной 10 nm проводит видимый свет и отражает инфракрасные лучи и т.д. Таким образом, чтобы получить материал с существенно новыми свойствами, применяемыми в нанотехнологии, его необходимо наноструктурировать.

Классификация наноматериалов в основном следующая. По составу наноматериалы делятся на неорганические (керамика, металлы и сплавы), органические (в том числе полимерные и биологические наноструктуры), а также органо-неорганические (в том числе металло-органические и металло-полимерные) (рис. 2).

Рис. 2. Основные типы наноматериалов.

По фазовому состоянию они делятся на:

– однофазные (нанокристаллиты, островковые плёнки и т.д.);

– двухфазовые однокомпонентные системы (аморфно-кристаллические, микродоменные структуры).

Подавляющее большинство наноструктурированных материалов включает два или более компонента и носят название нанокомпозитов. Они обычно состоят из сплошной твёрдой матрицы (полимерной, металлической, углеродной, керамической и др.), наполненной твёрдыми же наночастицами, состав, размеры и форма которых могут быть различными. Нанокомпозиты классифицируются по фазовой структуре следующим образом:

– двухфазные бикомпонентные системы (например, металл–окисел (Fe / Fe_2O_3) или полупроводник–окисел (Si / SiO_2));

– многофазные системы (многослойные нанотолщинные плёнки, сплавы и т.д.).

В настоящее время интенсивнее всего исследуются и представляются наиболее перспективными прежде всего:

– наноструктурированные металлы и сплавы;

– нанокерамика;

– углеродные материалы, компонентами которых служат аллотропные формы углерода – фуллерены или нанотрубки (рис. 3), имеющие весьма широкую сферу применения в нанотехнологии (заметим, что углерод будет иметь в нанотехнологии такое же значение, какое имеет кремний в микроэлектронике);

– наноструктурированные полимерные материалы (в т.ч. наиболее высокомолекулярный линейный полимер – молекула ДНК).

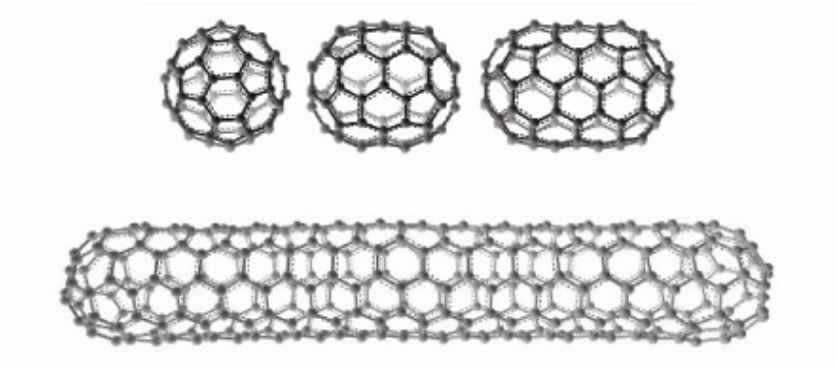

Рис. 3. Фулерены и нанотрубки.

Мощный научный фундамент, созданный в последней трети XX века, позволил всего за несколько лет разработать сотни наноструктурных продуктов и реализовать десятки способов их получения и промышленного производства.

Разработка, создание, исследование и эффективное применение разнообразных наноструктур немыслимо без большого арсенала средств, методов и технологических процессов, поддерживаемых соответствующей аппаратурой и приборами.

Мощным, многофункциональным, почти универсальным средством исследования наноструктур, манипулирования атомами и молекулами, создания из них структур и позволяющим визуализацию и контроль созданных наноструктур, является сканирующая зондовая микроскопия.

В последнее время создано множество таких микроскопов, основанных на разных физических явлениях. Особенно надо отметить туннельную микроскопию, атомно-силовую микроскопию и оптическую микроскопию ближнего поля.

Из технологических методов получения наноструктур (в основном полупроводниковых структур для наноэлектроники) необходимо отметить:

– молекулярно- лучевую эпитаксию;

– жидкофазную технологию;

– химическое осаждение размножением.

Изучение наноразмерных явлений и конкретных наносистем на протяжении последних лет подтверждает невероятные перспективу и значимость нанотехнологии для будущего человеческой жизни.

Современное состояние дел можно по праву можно назвать нанотехнологическим бумом, который охватил большинство областей деятельности общества.

Возникли новые понятия: «наноэлектроника», «нанофизика», «нанохимия», «нанобиология», «наномедицина».

Очень важным фактором развития нанотехнологии является экономика нанопромышленности. Дело в том, что технология создания любой продукции имеет два подхода: технология «сверху–вниз», когда получаем изделие из более крупных заготовок путем

отделения ненужных частей и технология «снизу–вверх», когда изготовление изделия осуществляется из элементов «низшего порядка» (атомов, молекул, фрагментов биологических клеток и т.п.), располагаемых в требуемом порядке. По этому принципу работает природа при построении сложных биологических систем.

Современное производство работает по принципу «сверху–вниз», которое очень неэффективно по сравнению с природными процессами как по доле полезно используемой массы первичного сырья, так и по затратам энергии. В конечный потребительский продукт превращается ~ 1.5 % массы добываемого сырья, а доля полезно используемой энергии и того меньше.

Природа действует неизмеримо экономнее. Она широко использует безотходную сборку и самосборку очень сложных систем из простых молекул. Самосборка и самоорганизация играют ключевую роль в жизни всего живого.

Нанотехнология идет по пути технологии «снизу–вверх». Последние исследования показали возможность реально создавать промышленные технологии получения наносистем. Эксперты прогнозируют, что через 10 – 15 лет успехи нанотехнологии позволят создавать роботы – ассемблеры, которые будет создавать наносистему и собирать свой аналог по заданной программе, без непосредственного вмешательства человека.

Принципиальная цель нанотехнологии состоит в создании и применении стратегий, напоминающих те, которые существуют и действуют в природе, что придает нанотехнологии особое значение. Нанотехнология фактически стирает границы между исскуственным и природным.

Интересно отметить, что люди издавна исторически применяли нанотехнологии (например., известны Дамаскский мечь, содержащий углеродные нанотрубки, Кубок Ликура IV века, покрытый частицами золота и серебра размером 70 nm, имеющий способность разноцветного ораження и др.). Известны, также, в природе наноэффекты (например, лотос-эффект – самоочищающися слой, феномен ящерицы Гекон, свободно ходить по потолку, вертикальной стене, стеклу (рис. 4)). Все это нашло объяснение.

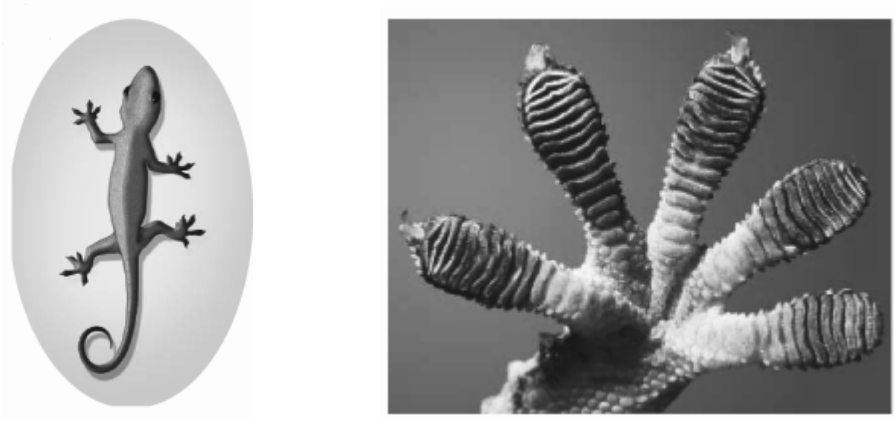

Рис. 4. Ящерица «Гекон» и ее лапка.

Нанотехнология, нанонаука является междисциплинарной областью и требует проведение междисциплинарных исследований на основе срастающихся и взаимно дополняющих друг друга наук и технологий, в результате чего неожиданно появляются новые продукты и методы.

Таким образом, нанотехнология системно связана с множеством научных дисциплин и уже существующих технологий, и эта специфика отражается как на исследовании структур и явлений на нанометрическом уровне, так и на процесс обучения и подготовки кадров в области нанонауки и нанотехнологии.

Несмотря на малый срок развития, нанотехнология вплотную подошла к задачам практического конструирования и создания приборов, машин, интегрированных систем с

нанометровыми размерами деталей, компонентов и узлов. Для освоения этого нового для инженерной практики поля деятельности нужны более фундаментальные основания и подходы, чем традиционные при производстве макропродукции. Они должны основывается на законах квантовой физики, биохимии, молекулярной биологии и др.

Пока в этом направлении сделаны только самые первые шаги. Однако грандиозные перспективы стимулируют ученых и инженеров к быстрейшему использованию почти безграничного потенциала, заложенного природой в наноструктуры, для решения широкого спектра жизненно важных задач развития общества.

Нанотехнология открывает перед человечеством возможность принципиального изменения современного состояния науки и техники и создает предпосылки новой научно-технической революции.

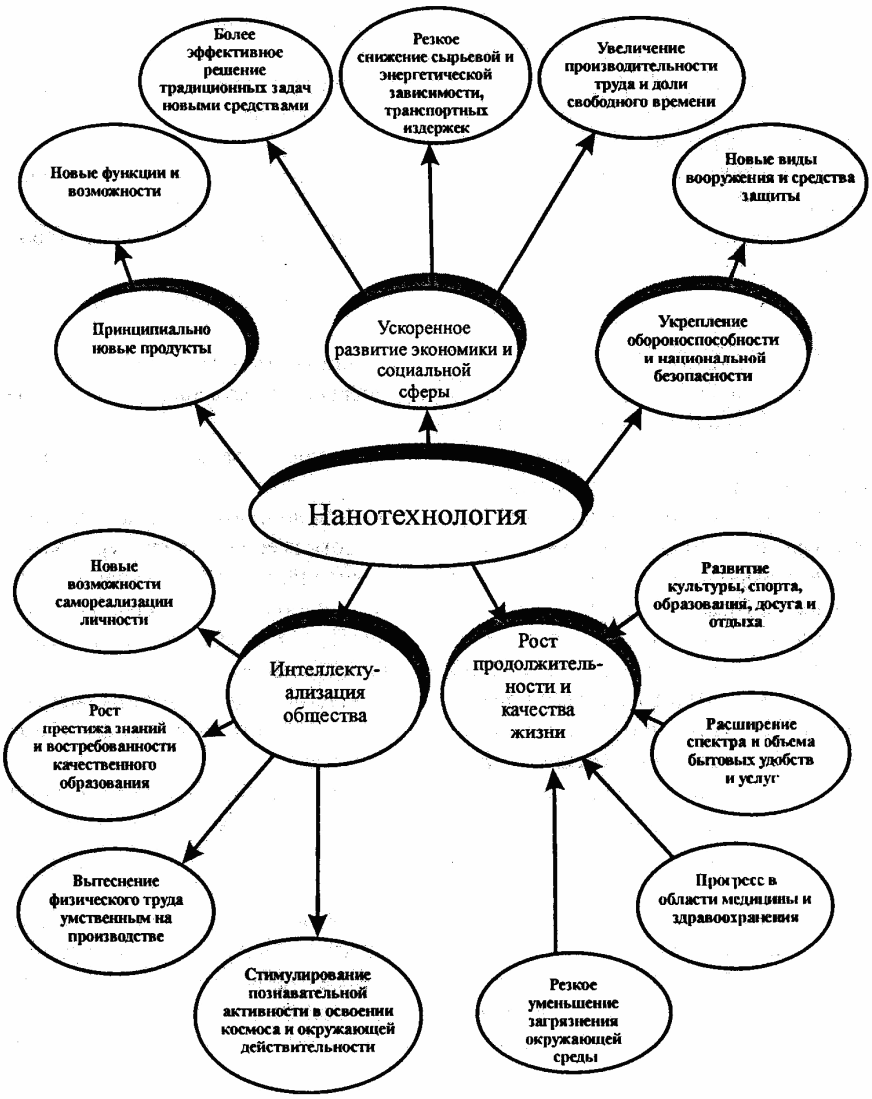

Рис. 5. Прогнозируемые социально-экономические последствия нанотехнологической революции.

Фантастическим, почти сказочным является перспектива развития нанотехнологии и ее влияния на все сферы человеческой деятельности, а именно, на развитие науки и техники, экономики, промышленности, сельского хозяйства, военной техники, социальной сферы, культуры, улучшение экологического состояния окружающей среды, интеллектуализации общества и др. (рис. 5).

Благодаря нанотехнологии постоянно будет подниматься уровень жизни и благосостояние человека.

Большие возможности обещает нанотехнология в развитии биотехнологии и медицины, электроники и информационной технологии, энергетики, транспорта, вооружения и т.д.

Приведем некоторые наиболее вероятные научные прорывы на нанотехнологии:

– увеличение производительности компьютеров, увеличение быстродействия (до нескольких терагерц (10^{12} Hz) и памяти (до нескольких Tbit (10^{12} bit) на cm^2), резкое уменьшение размеров;

– создание квантовых компьютеров;

– воостановление человеческих органов с использованием вновь созданной ткани. Создание искусственных органов, замена органов и «ремонт организма»;

– создание ДНК-чипов, позволяющих осуществить анализ генетической информации и проведение лечения;

– осуществление «адресной» доставки лекарств в организме, позволяющая устранить большие (например, раковые) клетки, убивать их;

– создание специальной диагностической аппаратуры, которая будет обнаруживать болезни в организме человека на самых разных стадиях;

– молекулярные нанороботы непосредственно из атомов и молекул будут создавать любой предмет (продукты питания, одежда и др.), будут возникать нанофабрики вместо современных заводов;

– будут созданы лёгкие и более прочные материалы;

– более эффективными и безопасными станут транспортные средства;

– переход на водородную энергетику, более эффективное использование солнечной энергии (КПД ~ 90 %);

– снижение уровня потребления ископаемого топлива (нефти и угля), значит и вредных выбросов в атмосферу;

– значительно повысится урожайность сельского хозяйства путём выведения растений, устойчивых к вредителям, обогащение малоурожайных земель;

– создание высококачественных фильтров для очистки воды и воздуха от промышленных загрязнений;

– будут создаваться «умные» машины, микронаноэлектромеханические системы;

– появятся связанные с интернетом устройства, возникнет глобальная система связи;

– резко изменится техника вооружения и способы борьбы с противником;

– появятся космические наноаппараты, позволяющие выполнять новые замыслы в освоении космоса.

Приведённый перечень содержит лишь отдельные аспекты применения нанотехнологии в разных областях человеческой деятельности. Имеются ещё много перспективных (отчасти фантастических) вопросов использования нанотехнологии.

Для примера в таблице 1 показана связь нанотехнологии с биологией и медициной, а в таблице 2 – возможности применения нанотехнологии в сельском хозяйстве.

Очевидно, развитие нанотехнологии (как каждой иновации) содержит потенциальные опасности её применения в разных областях (в медицине, военной технике и т.д.).

Возникают и этические вопросы, которые требуют детального обсуждения, анализа и принятия соответствующих решений для защиты людей от потенциально возникших опасностей.

Несмотря на это, в настоящее время нанотехнология стремится вперёд. Её воздействие на общественную жизнь обещает иметь всеобщий характер и затронуть все стороны жизни, быта, социальных отношений.

Нанотехнология – это не просто новая совокупность приёмов. Это новые концепция, парадигма и философия практической деятельности.

Как пишут некоторые авторы «те, кто владеют методами нанотехнологии, владеют миром».

Таблица 1. Связь нанотехнологий с биологией и медициной (по данным Института «Хитати Сокэн»).

Область исследований	Возможные практические применения нанотехнологий	Социальные, экономические и технические последствия
Здравоохранение и медицина	Создание наноустройств (автономных и вводимых в организм) Биодатчики (создание органических и неорганических материалов, превосходящих ткани организма по функциональным возможностям) Создание биомеханизмов, способных осуществлять измерения и требуемые медицинские действия	Новые парадигмы в медицине Создание долгосрочных и эффективных систем контроля здоровья Измерения уровня загрязнения окружающей среды Революционные изменения в медицинском обслуживании (возникновение медицины «малого» вмешательства и даже медицины «без вмешательства») Измерение содержания различных веществ в организме, лечебные операции при необходимости (детектирование и уничтожение раковых клеток и т. п.)
Лекарственные препараты	Практическое использование результатов проекта «Геном человека» «Адресная доставка» лекарств Получение новых биоматериалов Искусственные ферменты и антитела Искусственные функциональные полимеры (заменители тканей организма и т. п.)	Реализация идей «индивидуальной» медицины Организация полного курса лечения на основе личной генетической информации о пациенте Значительный прогресс в здравоохранении и фармацевтике Непрерывный контроль за состоянием организма Полная победа над раковыми заболеваниями, СПИДом и т. п. Разработка лекарственных препаратов с новым механизмом действия (например, препаратов, активизирующихся при повышении температуры у пациента)
Восстанавливающая медицина	Производство биологически активных нановеществ методами самосборки	Реализация идей восстанавливающей медицины Производство искусственных тканей и органов, не вызывающих реакцию отторжения Развитие рынка медицинских услуг (до 50 миллиардов иен) к 2020 году

Таблица 2. Возможности применения нанотехнологий в сельском хозяйстве (по данным Института «Хитати Сокэн») .

Рост населения планеты и проблема недостатка продуктов питания!
Население Земли в 1999 году составляло 6 миллиардов человек!
К 2050 году население Земли может составить 100 миллиардов человек!
Как обеспечить жителей планеты продуктами питания?

Проблемы сельского хозяйства	Возможные практические применения нанотехнологий	Социальные, экономические и технические последствия
Недостаток продуктов питания	Методы генетической модификации: • создание более устойчивых к сорнякам и вредителям сортов растений • увеличение урожайности • повышение питательной ценности (калорийности) получаемых продуктов • анализ генетической информации растений, генная модификация • применение ДНК-чипов и т. п.	Решение проблемы нехватки питания Создание стабильного и достаточного сельскохозяйственного производства Широкое применение техники ДНК-чипов и ДНК-анализа

Несмотря на малый срок развития, нанотехнология уже нашла свое применение в разных областях хозяйства. Ниже приводим некоторые примеры применения нанотехнологии.

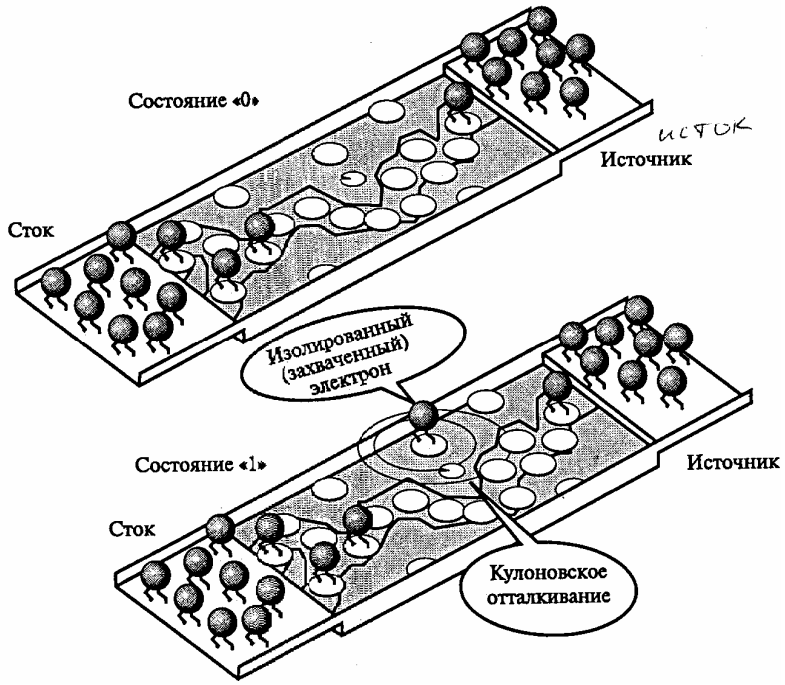

Рис. 6. Одноэлектронный транзистор.

В области наноэлектроники создан одноэлектронный транзистор (рис. 6), работающий при комнатной температуре. Создание одноэлектронного транзистора имеет огромное значе-

ние для дальнейшего развития электроники, т.к. он позволяет создать интегральные схемы (например, схему памяти) с 1000-раз большей емкостью, чем современные сверхбольшие интегральные схемы. Т.е. память такой схемы будет 1 Tbit (10^{12} бит) и займет площадь ~ 6 cm^2. Быстродействие схем на одноэлектронных транзисторах составит 10^{12} операций в секунду (!).

Созданы нанометрические порошки серебра, имеющие уникальнее свойства, которые могут использоваться в различных видах продукции. Наносеребро является высокоэффективным антибактерицидным средством. Спектр действия частиц серебра распространяется на 650 видов бактерий и микроорганизмов (для сравнения – антибиотики подавляют не болле 10 видов и даже для них со временем наступает привыкание и требует создания новых препаратов). Имея наносеребро, получаем антибиотик, к которому нет привыкания и нет отрицательного влияния на человеческий организм. Наносеребро незаменимо для профилактики и борьбы с инфекционными процессами, включающими антисептическую промывку, аппликацию, обеззараживание воды, сохранение пищевых продуктов, фильтрацию воздуха, антимикробную защиту одежды, обуви, предметов быта.

На основе наносеребра с концентрациями (10^{-5} – 10^{-2}) % можно производить множество товаров народного потребления с ярко выраженными антибактерицидными свойствами (зубные пасты, кремы, шампуни, стиральные порошки, лаки, краски, ткани, гигиенические принадлежности и т.д.

Одной из областей практического применения нанотехнологии – это специальная одежда. Созданная из материалов на основе нановолокон одежда не пропускает ультрафиолетовые лучи, практически не промокает под дождем и почти не пачкается. Такая одежда обладает антибактериальными и антигрибковыми свойствами.

Обширное применение нашла нанотехнология в создании самых разнообразных лакокрасочных материалов. Уникальное свойство наноматериалов позволило создать краски со свойствами, отличными от сушествуюших. Они оказались очень эффективными для окраски автомобилей, поездов, зданий и др. Лакокрасочные иновационные материалы, разработанные на основе применения нанотехнологии обладают уникальными характеристиками. Благодария сверхмалым размерам частиц достигается высокая адгезия, прочность и стойкость покрития к внешным воздействиям, устойчивость к ультрафиолетовому излучению. Коэффициент влагопоглашения гарантирует зашиту от дождя. Покрытия являются грязеоттакливаюшими, обладают самоочишаюшимся эффектом. Поверхность становится настолко гладкой, что никакие другие краски не могут закрепиться. Новый нанолак обеспечивает высокую и длительную прочность покрытия, а также образцовую сохранность автомобилей.

Использование принципов нанотехнологии в форме введения в моторное топливо наноразмерных частиц оксида церия, позволило уменьшить вредные вибросы в отработавших газах автомобиля. Соответствующая технология разработана английской фирмой “Oxonica”. Рабочая концентрация оксида церия в топливе – 5 миллионных долей на литр, т.е. на железнодорожную цистерну топлива достоточно (150 – 200) g нанопорошка. Эффект от применения наночастиц – экономия топлива ~ 15 % и резкое снижение выбросов оксидов азота.

Уже полученные результаты и перспективы работ в области нанотехнологий привели к тому, что в разных странах на уровне правительства и частных крупнейших фирм (бизнесменов) приняты и успешно выполняются программы по практическому использованию результатов научно-практических исследований для нужд не только науки, но государства и общества в целом. Эти программы представляют собой национальные стратегии по нанотехнологии.

Правительственные структуры более чем 35 стран мира, осознавая роль нанотехнологии в XXI веке, выделяют значительные ресурсы на формирование человеческого капитала, развитие научного потенциала, ускорение коммерциализации научных исследований, вывод научных результатов на рынок и занятие отдельных сегментов мирового нанорынка.

Пионером развития нанотехнологии является США, которые в 2000 г. провозгласили программу – «Национальная нанотехнологическая инициатива», которая являлась стимулом для разработки аналогичных программ в других странах мира.

Сегодня США являются лидером в нанотехнологии. В 2007 г. правительство США вложило в её развитие 1.3 млрд. долларов. Университеты США широко готовят студентов для наноиндустрии. США занимают лидирующую позицию и на мировом нанорынке.

Страны ЕС, осознавая важность нанотехнологий для обеспечения конкурентоспособности и безопасности в Европе, разработали стратегию развития нанотехнологии, которая финансируется как из средств Европейской комиссии, так и из бюджетов отдельных государств, а также по различным программам.

Япония является лидером во многих нанообластях. Здесь нанотехнология находится в центре внимания как властей, так и бизнес-сообщества. В 2005 г. только из бюджетных источников было выделено почти 1 млрд. долларов. В пятилетнем плане развития науки и технологий на период 2006 – 2010 гг. нанотехнология рассматривается как один из ключевых приоритетов.

За лидерство в области нанотехнологии борется Китай. В 2003 г. Китай поставил ряд стратегических целей, в числе которых является аккумулирование усилий для превращения нанотехнологии в основу китайской промышленности.

Китайское правительство также как правительство США, считает что обороноспособность страны в значительной степени будет предопределяться развитием нанотехнологии. Сегодня Китай лидер по количеству патентов, а также фирм (более 800), работающих в области нанотехнологии. Внутренний рынок нанопродукции в Китае составляет несколько млрд. долларов и неуклонно растёт.

На азиатском континенте, кроме Китая и Японии, продвинутыми странами в области нанотехнологии являются Южная Корея, Тайвань и Сингапур.

Осознавая важность нанотехнологии, как основы технологического развития в XXI веке, страны Латинской Америки (Бразилия, Аргентина, Мексика) начали предпринимать конкретные шаги для аккумулирования ресурсов государственного сектора и корпорации с целью развития научного потенциала, кооперируясь при этом с более продвинутыми странами, прежде всего с США. Эти страны разработали программу и выработали стратегию развития нанотехнологии, выделяя десятки млн. долларов за эти цели.

В 2001 г. в Израиле была разработана Национальная инициатива развития нанотехнологии. За 2001 – 2005 гг. бюджетные ассигнования на нанотехнологии составили 45 млн. долларов, которые были направлены главным образом на создание центров и оснащение их первоклассным оборудованием.

В Южной Африке Программа развития нанотехнологии стартовала в 2003 г. Общие расходы на нанонауку оцениваются в 3 млн. долларов.

Примечательно, что нанотехнология поднята до государственного приоритета даже в таких маленьких странах как Дания, Финляндия и Голландия.

Начинает активизироваться в области нанотехнологии Индия, обладающая хорошими возможностями её развития.

Расширение работ во всём мире в области нанотехнологии, принятие национальных программ и увеличение финансирования обусловлено пониманием того, что нанотехнологии являются базисными технологиями XXI века.

Отличительной особенностью всех национальных программ развития нанотехнологии является то, что развитие инфраструктуры выделяется в них отдельным блоком. Все страны создают специальные междисциплинарные центры нанотехнологии и учреждают центры коллективного пользования.

Среди других особенностей этих программ отметим следующие:

– выделение проблемы формирования человеческого капитала в качестве приоритетного, формирование кадрового потенциала для проведения междисциплинарных исследований;

– партнёрство с частным сектором, которое обусловлено необходимостью быстрой коммерционализации научных разработок;

– включение в качестве отдельной задачи изучения последствий использования нанопродукции и наноуслуг, определение возможного отрицательного воздействия на здоровье человека и экологию.

Наконец, практически во всех национальных программах сформированы направления международного сотрудничества.

Российское правительство, распоряжением 2006 г. одобрило программу координации работ в области нанотехнологии и наноматериалов в РФ, хотя научно-исследовательские работы проводились намного раньше в научно-исследовательских институтах АН РФ и в ВУЗ-ах РФ. Фундаментальные научно-исследовательские работы по нанотехнологии проводятся по нескольким программам, наиболее крупными из которых являются программы: «Физика наноструктур» под руководством лауреата Нобелевской премии, академика Ж.И. Алферова и «Перспективные технологии и устройства в микро- и наноэлектронике» под руководством академика К.А. Валиева. Кроме того, в России для развития нанотехнологии организована корпорация «Роснанотех» и выделено финансирование.

В конце для примера приведем обзор рыночных цифр и прогнозов по нанотехнологии (Таблица 3).

Таблица 3. Обзор рыночных цифр и прогнозов по НТ.

Объем продаж на мировом рынке (год)	**Вид продукта**
493 млн долларов США (2000) 900 млн долларов США (2005)	Неорганические наночастицы и порошки (SiO_2, TiO_2, металлы и т. д.)
40 млрд долларов США (2002)	Синтетические наночастицы как полуфабрикаты
23 млрд долларов США (2003) 73 млрд долларов США (2003)	Наноматериалы Инструменты; компоненты нанобиотехнологии
54 млрд евро (2001) 100 млрд евро (2005)	НТ продукты (по убывающей): наноматериалы, нанослои, наноаналитические препараты, сверхточная обработка поверхности, латеральные наноструктуры
66 млрд долларов США (2005) 148 млрд долларов США (2003)	НТ продукты
до 200 млрд евро (2005)	НТ продукты
225 млрд долларов США (2005) 700 млрд долларов США (2008)	НТ продукты
1 триллион долларов США (2015)	НТ продукты вообще

Таким образом, нанотехнология в перспективе вырисовывается как одна из судьбаносных технологий для человечества.

2. ВОПРОСЫ СОЗДАНИЯ ЦЕНТРА НАНОТЕХНОЛОГИИ В ГРУЗИИ

Анализ развития нанотехнолгогии в разных странах мира, особенно в малых, слаборазвитых и развивающихся странах показывает, что Грузия ни в коем случае не может (и не должна) обойти развитие нанотехнологии, если не хочет навсегда остаться в числе самых отсталых и без перспективных стран.

Не увидев уже ощутимые результаты развития нанотехнологии и игнорирование влияния нанотехнологической революции на общество приведет к безвозратному упадку научно-технического уровня и ухудшению социально-экономического состояния Страны.

Необходимо, в первую очередь, как произошло в других странах – на всех уровнях (особенно, на парламентском, правительственном уровне) признать нанотехнологию, осознать ее как основную технологию XXI века, определяющую развитие общества и понять необходимость срочной подготовки соответствующих кадров.

В связи с ожидаемым поступлением и нарастанием количества нанопродукции в Грузии, немаловажным является также необходимость квалифицированно разъяснить населению не только положительные, но и отрицательные стороны пользования нанопродукцией и наноуслугой.

Проведение мероприятий по развитию нанотехнологии в Грузии безусловно благоприятно скажется на повышение научно-технического уровня страны, оживление фундаментальных наук (особенно приоритетных направлений) и улучшении социально-экономического состояния страны.

Необходимо отметить, что в Грузии имеется ряд факторов, способствующих развитию нанотехнологии, а именно:

– имеется пока еще достаточно высокий научный потенциал фундаментальных наук (физики, химии, биологии) являющиеся основой развития нанотехнологии;

– сохранились кадры, имеющие многолетний опыт в области микроэлектроники (как в науке, так и в производстве полупроводниковых интегральных схем и оптоэлектронных приборов).

Здесь же отметим, что микроэлектронная технология является основой развития наноэлектроники. Можно сказать, что сама наноэлектроника, используя технологические методы изготовления микроэлектронных приборов, представляет собой продолжение развития микроэлектроники:

– в физике, химии и биологии ведутся интересные научные исследования, являющиеся перспективными для использования в нанотехнологических разработках;

– в Тбилиси имеются отдельные научные группы в институтах, работающие в области нанотехнологии и получившие интересные результаты;

– немаловажным фактором, являющимся стимулом развития нанотехнологии в Грузии, является ее геополитичесое положение;

– имеются определенные связи наших ученых с институтами развитых стран, положительно влияющие на проведение исследовании в области нанотехнологии.

Самым эффективным и важнейшим мероприятием для развития нанотехнологии в Грузии и реализации возможностей с учетом этих факторов является создание коллективного центра наноэлектроники в Грузии.

Основной целью наноцентра является создание базиса нанотехнологии в Грузии для дальнейшего его развития.

Основные задачи наноцентра можно сформулировать следующим образом:

– проведение научных исследований в области нанонауки и нанотехнологии по выбранным приоритетным направлениям, имеющим самое важное значение для Грузии;

– подготовка научных кадров в области нанотехнологии, особенно большое внимание будет уделено формированию кадрового потенциала для проведения междисциплинарных исследований. Оказание помощи и услуг ВУЗ-ам страны в этом направлении;

– предоставление возможности проведения исследований по нанотехнологии разным исследователям (в том числе и иностранным) по согласованным тарифам финансирования;

– установление и развитие научного сотрудничества и партнерства с центрами микроэлектроники в разных странах;

– определение возможности внедрения результатов исследований в промышленность;

– изучение последствий использования нанопродукции и наноуслуг, выполнение роли эксперта в этом направлении;

– оказание консультаций по вопросам применения нанопродуктов;

– участие в разработке разных (в том числе правительственных) программ по нанотехнологиям;

– популяризация нанотехнологий, привлечение молодежи к нанонауке;

– разработка планов работы наноцентра.

Исходя из анализа состояния разных отраслей науки и их значимости для страны, кажется оптимальным сосредоточить усилия центра на следующих приоритетных направлениях нанотехнологии (см. рис. 7):

– наноэлектроника (включая полупроводниковые преобразователи солнечной энергии высокой эффективности);

– нанохимия (включая получение некоторых наноматериалов);

– нанобиология (в том числе вопросы использования результатов в медицине);

– экология (выбросы, сельскохозяйственные вредители).

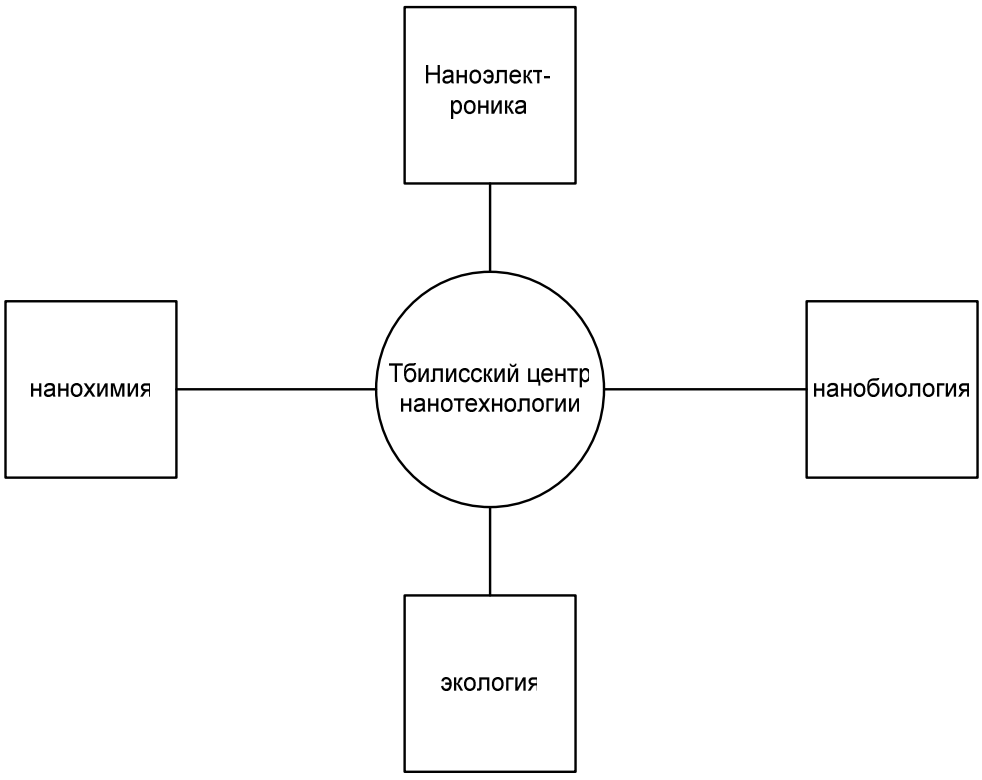

Рис. 7. Предполагаемые приоритетные направления нанотехнологии в Грузии.

Для квалифицированного выполнения поставленных задач наноцентр должен иметь возможность:

– командировать сотрудников при острой необходимости в разные страны, в том числе для участия в конференциях, выставках;

– вернуть из разных стран молодых специалистов, граждан Грузии для работы в Наноцентре;

– приглашать ученых на кратковременный период (консультации, доклады);

– вызывать специалистов из фирм для ремонта поставленного ими оборудования;

– проводить рабочие семинары, конференции;

– напечатать необходимую научно-техническую литературу (малым тиражом);

– заключить договора с разными организациями по вопросам, касающимся деятельности Наноцентра.

3. ОСНАЩЕНИЕ ЦЕНТРА

Центр должен быть укомплектован современным первоклассным оборудованием по всему технологическому циклу.

Кроме того, в связи с необходимостью проведения предварительных измерений, обучения кадров, прохождения практики и выполнения дипломных работ по нанотехнологии, требуется оборудовать Наноцентр более дешовым оборудованием по всему циклу (есть фирмы, которые продают использованное, но работающее оборудование по низким ценам).

Структура Центра в основном определяется количеством приоритетных направлений. В предложенном варианте рассматривается четыре отдела: наноэлектроники, нанобиологии, нанохимии и экологии и вспомогательные подразделения.

Для создания Наноцентра возможно привлечение инвесторов (в т.ч. внутри страны). Главное – чтобы не произошло распыление сил; это будет губительным. Смело можно утверждать, что развитие нанотехнологии в Грузии внесет значительный вклад в возрождение экономики (сельского хозяйства, производства на основе новых технологий) и что самое главное, в формирование основанного на знание общества в Грузии.

Кроме основной литературы [1−12], приведенной в конце, в статье использованы несколько десятков разных материалов, взятых из Интернета.

ССЫЛКИ

1. Ю.И. Головин. Введение в нанотехнику. Москва: Машиностроение (2007).
2. М. Рыбалкина. Нанотехнологии для всех. nanonewsnet.ru (2007).
3. Н. Кобаяси. Введение в нанотехнологию. Москва: Бином (2007).
4. У. Хартман. Очарование нанотехнологии. Москва: Бином (2008).
5. Н.Г. Рамбиди, А.В. Берёзкин. Физические и химические основы нанотехнологии. Москва: Физматлит (2008).
6. А.А. Абрамян, В.И. Балабанов, В.И. Беклемышев, Р.В. Вартанов, И.И. Махонин, В.А. Солодовников. Основы прикладной нанотехнологии. Москва: Издателский дом Магистр-Пресс (2007).
7. ს. დადუნაშვილი. ნანოტექნოლოგიების შესავალი. თბილისი: გამომცემლობა “ტექნიკური უნივერსიტეტი” (2002).

8. დ. ჯიშიაშვილი. ნანოტექნოლოგიის შესავალი. საგამომცემლო სახლი "ტექნიკური უნივერსიტეტი". (2007).
9. ა. გერასიმოვი. ნანოტექნოლოგიების საწყისები. თბილისი (2009).
10. Н. Гапоненко. Экономические стратегии, **01**, 44 (2008).
11. И.В. Мелихов. Вестн. РАН, **77**, 987 (2007).
12. Нанотехнологии и этика, политика и направления деятельности. Всемирная комиссия по этике научных знаний и технологий. UNESCO (2008).

О РАЗРАБОТКЕ ОПТОЭЛЕКТРОННЫХ ЭЛЕМЕНТОВ С ИСПОЛЬЗОВАНИЕМ СВОЙСТВ НАНОКРЕМНИЯ НА СТРУКТУРЕ «КРЕМНЫЙ НА САПФИРЕ»

Р.Е. Казаров [1], Р.И. Чиковани [2], Д.И. Гарибашвили [3], Г.И. Годердзишвили [2], Т.И. Хачидзе [2]

[1] Тбилисский государственнй университет И. Джавахишвили
Rkazarov@yahoo.com
[2] Грузинский технический университет
rchikovani@mail.ru
gela49@mail.ru
tengo7777@mail.ru
[3] Институт физики Э. Андроникашвили.
devigar@mail.ru

Принята 10 февраля 2010 года

Уникальные свойства наноматериалов поставили вопрос в повестку дня об использовании этих свойств для создания разных перспективных приборов наноэлектроники.

Одним из интересных направлений в облости наноэлектроники открывается перед разработчиками в связи обнаружением у нанокремния эффективной люминесценции. Это позволяет использовать кремний наряду микроэлектроники и в оптоэлектронике. Особенно заманчивым и перспективным представляется использование нанокремныя в структуре «кремный на сапфире» (КНС).

Конкретно предлагается изготовление структуры с использованием сапфировой подложки. На одной стороне сапфира изготавливается микросхема на основе диодной матрицы, или МОП транзисторов, которые служат фотоприемниками светового излучения. На протовоположной стороне сапфира наносится нанокремний, способный излучать свет, который проходит через сапфировую подложку и регистрируется фотоприомниками. Созданию такой структуры спасобствует свойство и параметры самого сапфира. Он представляет собой оптически прозрачный материал, прекрасный изолятор, химически инертный, механически прочный и радиационно стойкий, это очень важно для фукционирования разных оптоэлектронных приборов.

Возможность создания оптоэлектронных элементов на основе предлогаемых структур – нанокремный (излучатель) – сапфир (световод) а инегральная схема (фотоприемник), обусловлена следующими факторами:

– Обнаружение у наноструктурированного кремния способности излучать свет сделал его перспективным оптоэлектронным материалом. Исследования в этом направлении развиваются преимушественно в области компонентов для нано-оптоэлектроники. Судя по опубликованным работам [1], а также публикациям в Интернете прогнозируется разное перспективное применение нанокремния и процессов на его основе: использование кремниевых излучателей для интегральных оптических схем, в запоминающих устройствах, в качестве световолновых компонентов, матричных излучателей и оптопар, лазеров и др.;

– В Грузии, в институте «Мион» была проведена серия НИР и ОКР по созданию диодных интегральных схем для запоминаюшего устройство на основе структур кремний на сапфире.

Схемы были выполнены на основе вертикальных диодных структур [2], которые обеспечивают минимизацию паразитной емкости, стойкость к радиационной, температурной, химической и другим возможным воздействиям. Как следствие этого обстоятельства схемы

характиризуются малой потребляемой мощностью, высоким быстродействием и надежностью. На рис. 1 показана последовательность основных технологических операций при создании КНС-диодов с торцевым p-n переходом.

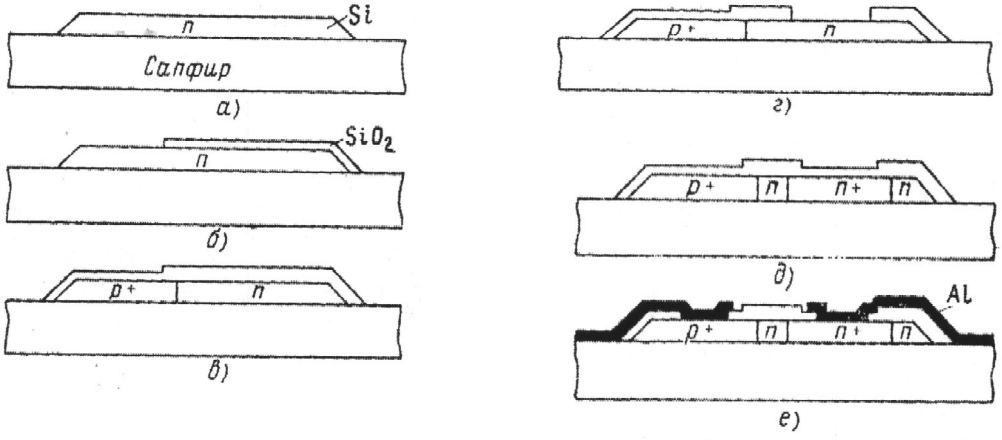

Рис. 1. Последовательность основных технологических операций создания КНС-диодов с торцевым p-n переходом.

НИИ «Мион» был разработан весь технологический цикл получения КНС интегральих схем и в течение рада лет осуществлялось изготовление электрически программируемых диодных матриц (712 ВВ 1 и др.), которые использовалиь в блоках постоянной памяти радиоэлектронной аппаратуры в космических аппаратах, а также в подводных лодках. Здесьже отметим, что среди авторов данной статьи являются основные создатели указанных выше схем (в т.ч. и руководитель).

По указанным КНС интегральным схемам НИИ «Мион» был головным исполнителем.

– В свое времия в НИИ «Мион» были проведены интересные исследования использования диодной матрицы, сформированной на основе структуры КНС в качестве матрицы фоточувствительных элементов [3]. Создание матриц фоточувствительных элементов в интегральном исполнении считается перспективным направлением в оптоэлектронике, так как оно позволит конструировать координатно-чувствительные устройства высокого разрешения, распознавания образов, цифровой записи голограмм и т. д.

В работе [3] исследовано спектральное распределение фототока короткого замыкания и фото-э.д.с структуры при разных температурах. К сожалению из-за отсутствия излучающего кремния, работа не нашла развития (применение других излучающих материялов, например, соединения $A^{III}B^{V}$ или $A^{II}B^{VI}$ не являлись реальным из-за сложности технологии применения их в КНС структуре).

Именно обнаружение эффективного излучения у нанокремния даёт возможность вернуться к вопросу создания оптоэлементов на КНС структурах.

– Имеется высокий научньй потенциал и кадры в области разработки разных оптоэлектронных приборов (светодиоды, излучающие матрицы, знако-цифровые индикаторы шкалы и др.). Это позволяет совмесно со специалистами по КНС структурам более эффективно вести работу по созданию оптоэлектронных элементов на КНС.

Очевидно, решение этой перспективной задачи требует заново осмыслить и отработать целый ряд технологических процессов. Потребуется корректировка технологии получения КНС интегральних схем, проведение соответствующих исследований и установление неизвестных до сих пор режимов отдельных технологических процессов получения кремния (как нано-, так и микрокремния) на КНС структурах.

Отметим, что проведение предусмотренных работ по использованию нанокремния в структуре КНС будет способствовать возникновению новой сферы их применения.

ССЫЛКИ

1. A.T. Fiory, N.M. Ravindza. J. Electr. Mat., **32**, 1043 (2003).
2. Р.Е. Казаров, Г.В. Маглакелидзе, В.В. Микадзе. Авт. свид. № 597282, 15 ноября (1977).
3. М.Б. Воскобойник, Т.В. Джахуташвили, Р.Е. Казаров, Д.А. Кюрджиев, И.Е. Пекар, Р.И. Чиковани. Электр. тех. (Сер. 2: Полупровод. приб.), **108**, 106 (1976).

AlGaAs ჰეტეროსტრუქტურის ფოტოელემენტის ფოტოელექტრული პარამეტრების განსაზღვრა უკონტაქტო მეთოდით

ა.ბ. გუჩმაზოვი, გ.ნ. ილურიძე, თ.ა. მინაშვილი,
გ.ვ. რთველიაშვილი მ.ს. თაქთაქიშვილი

საქართველოს ტექნიკური უნივერსიტეტი
an_guch@mail.ru

მიღებულია 2010 წლის 11 თებერვალს

როგორც ცნობილია, გარკვეული ტიპის ნახევარგამტარულ სტრუქტურებში, კერძოდ სტრუქტურებში, რომელთაც გააჩნიათ მაღალი შინაგანი კვანტური გამოსავლიანობის გამოსხივებითი რეკომბინაციის მქონე ფოტოაქტიური ფენა, არსებობს პირდაპირი კავშირი ამ სტრუქტურების ფოტოელექტრულ პარამეტრებსა და მათ ლუმინესცენციურ მახასიათებლებს შორის [1]. აღნიშნული კავშირი საშუალებას იძლევა განისაზღვროს ნახევარგამტარული სტრუქტურის ფოტოელექტრული პარამეტრები ნაკეთობის დამზადების ადრეულ ეტაპზე, ჯერ კიდევ კონტაქტების ფორმირებამდე. ეს მეტად მნიშვნელოვანია საბოლოო გამოსავლიანობის გაზრდისა და შესაბამისად თვითღირებულების შემცირების თვალსაზრისით. იგულისხმება ისეთი ნაკეთობების დამზადება, როგორებიცაა მაღალეფექტური ფოტოელემენტები, ფოტოტრანზისტორები, Al – Ga – As სისტემის ტრანზისტორები და ა.შ. [2].

ექსპერიმენტებისათვის გამოყენებულ იქნა დაბალტემპერატურული თხევადფაზიანი ეპიტაქსიის მეთოდით მიღებული n-GaAs – p-GaAS – p-AlGaAs ჰეტეროსტრუქტურის ფოტოელემენტების ნიმუშები. მუშაობა წარმოებდა რუსული წარმოების ფოტოელექტროლუმინესცენციის საკვლევი დანადგარის SDL – 2-ის ბაზაზე შექმნილ დანადგარზე. ადგილი ჰქონდა ნიმუშის სელექციურ ფოტოაგზნებას ინტენსიური სინათლის ნაკადით.

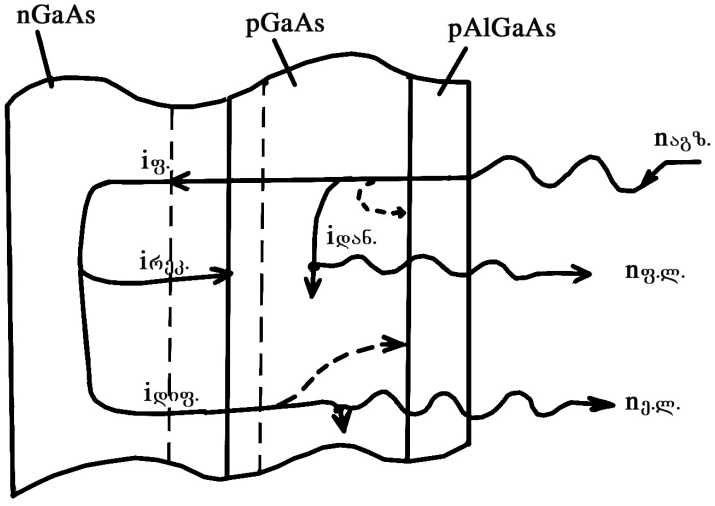

ნახ. 1. უქმი სვლის რეჟიმში AlGaAS ფოტოელემენტში მოქმედი დენების სქემატური გამოსახულება.

ფოტოაგზნებული საკვლევი ნიმუშის აქტიურ ფენაში არაწონასწორული მუხტის მატარებლების გადაადგილება სქემატურად შეიძლება ისე გამოვსახოთ, როგორც ეს ნახ. 1-ზეა ნაჩვენები.

ნიმუშის ზედაპირზე დაცემული n_{exc} ინტენსივობის სინათლის ნაკადი, შთაინთქმება რა p-GaAs-ის ზონაში, წარმოქმნის მუხტის არაწონასწორულ მატარებლებს. მათი ერთი ნაწილი, რომელიც შეიძლება წარმოვიდგინოთ როგორც დანაკარგის დენი i_{loss}, ისევ განიცდის რეკომბინაციას იგივე არეში და იძლევა ლუმინესცენციურ გამოსხივებას n_{phl}.

მუხტის მატარებლების მეორე ნაწილი, რომელმაც ვერ მოასწრო რეკომბინაცია, წარიტაცება p-n გადასასვლელის მოცულობითი ველის მიერ და ქმნის ფოტოდენს i_{ph}. შედეგად ხდება კონტაქტური ძაბვის პირდაპირი წანაცვლება და ელექტრონების ინჟექცია n-დან p-არეში.

ინჟექტირებული ელექტრონების ერთი ნაწილი, რომლებიც ქმნიან დენს i_{rec}, განიცდის არაგამოსხივებად რეკომბინაციას p-n გადასასვლელის გაღარიბებულ არეში, ხოლო მეორე ნაწილი, რომელთაც შეესაბამებათ დიფუზიური დენი i_{diff}, ისევ გადმოდის რა p-GaAs არეში განიცდის რეკომბინაციას, i_{loss}-ის მსგავსად, და იძლევა n_{el} ლუმინესცენციურ გამოსხივებას, რომელსაც პირობითად ელექტროლუმინესცენციური კომპონენტი შეიძლება ვუწოდოთ.

მუხტის მატარებლების გარკვეული ნაწილი, როგორც დიფუზიური i_{diff} დენიდან, ისევე ამგზნები სინათლის შთანთქმით მიღებული მატარებლებიდან, განიცდის არაგამოსხივებად რეკომბინაციას ზედაპირულ დონეებზე, მაგრამ მათი პროცენტული წვლილი ერთნაირად შეიძლება ჩაითვალოს და ვერ ცვლის სქემაზე ნაჩვენები ძირითადი დენების თანაფარდობას.

ნახ. 2-ზე მოყვანილია ექსპერიმენტული ნიმუშის სელექციური ფოტოაგზნებისა და ნიმუშიდან გამომავალი ლუმინესცენციურ გამოსხივებაზე დაკვირვების სქემა.

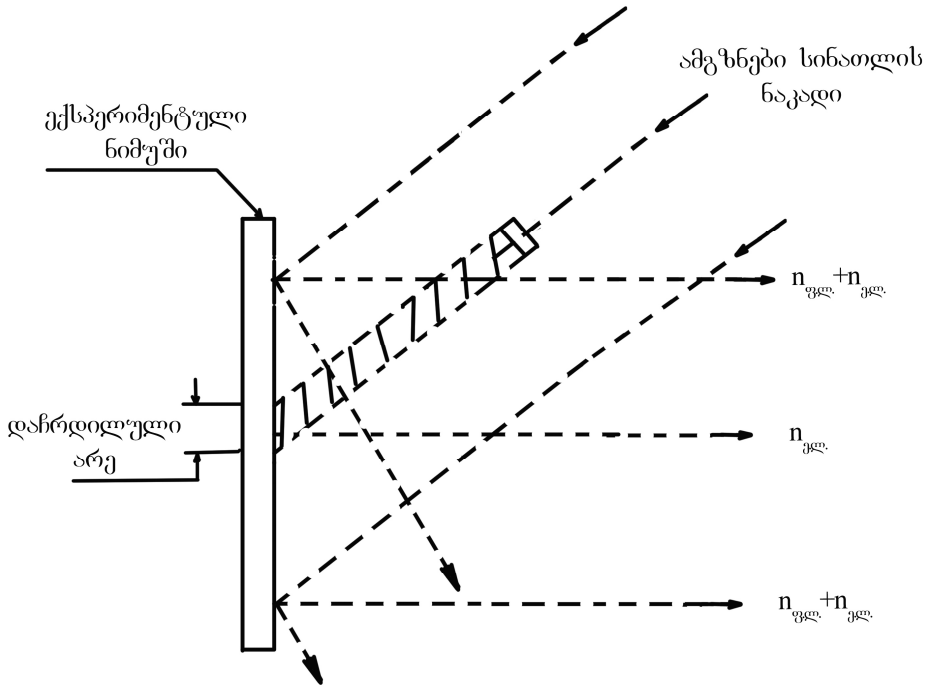

ნახ. 2. ექსპერიმენტული ნიმუშის ფოტოაგზნების სქემა.

წინა ნახაზზე მოყვანილი მუხტის მატარებლების განაწილების სურათიდან გამომდინარე, ბუნებრივია, რომ ნიმუშის დაჩრდილულ არეში ადგილი ექნება მხოლოდ n_{el} ლუმინესცენციურ გამოსხივებას, ხოლო განათებულ არეში ფიქსირდება $n_{phl}+n_{el}$ ჯამური მნიშვნელობა.

ექსპერიმენტულად განისაზღვრებოდა ცალკეული არეებიდან ლუმინესცენციური გამოსხივებების აგზნების ინტენსივობაზე დამოკიდებულების მრუდები, საიდანაც [3]-ში წარმოდგენილი მეთოდიკით ხდებოდა ჰეტეროსტრუქტურის p-n გადასასვლელის მიერ ფოტოგენერირებული მუხტის მატარებლების შინაგანი შეგროვების კოეფიციენტის – Q_i-ის გამოთვლა.

შედარებისთვის სტანდარტული მეთოდით ვზომავდით მუხტის ფოტოგენერირებული მატარებლების შინაგანი შეგროვების კოეფიციენტის აბსოლუტურ მნიშვნელობას საექსპერიმენტო ნიმუშებისათვის მათზე არსებული ელექტრული კონტაქტების მეშვეობით. გაზომვა წარმოებდა $He-Ne$-ის გაზური ლაზერის ($\lambda = 632.8\,nm$) გამოყენებით საექსპერიმენტო ნიმუშისა და სილიციუმის ეტალონური ფოტომიმღების ფოტოდენების შედარების გზით (არეკვლის კოეფიციენტის გათვალისწინებით).

ქვემოთ მოყვანილი ცხრილი 1-დან ჩანს, რომ ორი განსხვავებული მეთოდით მიღებულ შედეგებში საკმაოდ კარგი ხარისხობრივი თანხვედრაა.

ცხრილი 1.

ნიმუშის ნომერი	შეგროვების კოეფიციენტი Q_i	
	ლუმინესცენციის მეთოდით, abs. units	ყალიბრებული ფოტოელემენტის გამოყენებით, abs. units
1	0.91	0.86
2	0.84	0.81
3	0.87	0.83

ამრიგად, გამოკვლევის შედეგებმა აჩვენა, რომ ამ ტიპის ჰეტეროსტრუქტურებში კონტაქტების დამზადების სტადიამდე მხოლოდ ლუმინესცენციის საშუალებით შესაძლებელია შეფასდეს ჰეტეროსტრუქტურის ზოგიერთი ძირითადი ელექტრული და ფოტოელექტრული პარამეტრი. მისი გამოყენება საშუალებას იძლევა უფრო სრულყოფილი გახდეს შესაბამისი ელექტრონული ნაკეთობის წარმოების პროცესი და შემცირდეს თვითღირებულება.

დამოწმებანი

1. Ю.А. Аношин, В.М. Базин, М.И. Герценштейн, А.С. Даревский, С.С. Кабак, Л.М. Панасюк В сб.: Тез. докл. XI Всесоюз. конф. по физ. п/п-ов. Кишинев, 187 (1988).
2. В.Р. Ларионов, Т.Б. Попова, В.Д. Румянцев, Л.И. Флакс, Ш.Ш. Шамухамедов. В сб.: Тез. докл. IV Всесоюз. конф. по физ. проц. в п/п-овых гетероструктурах. Часть 2. Минск, 220 (1988).
3. А.Б. Гучмазов, Х.А. Родригес, В.Д. Румянцев. ФТП, **25**, 143 (1991).

COMPETITIVE NANOTECHNOLOGIES FOR NANOELECTRONICS, PIEZOENGINEERING, PHOTOCATALYSIS AND COMPOSITES PARTICULARLY USING ELECTROLESS DEPOSITION

T.N. Khoperia, T.I. Zedginidze

E. Andronikashvili Institute of Physics
teimurazkhoperia@yahoo.com
tinikozedginidze@yahoo.com

Accepted February 12, 2010

Electroless metallization technology which allowed replacing adequately Au and Ag with Ni – P or Ni – B alloys and simplifying significantly the metallization process was developed [1–6].

The proposed patentable nanomethods for the first time allow one to produce nanochips and photomasks with nano-sized adjacent elements by single optical UV photolithography [7].

The proposed nanomethods are much more advantageous and simpler than other expensive and complicated methods such as e-beam, X-ray lithography or fabrication of nanoelements using light-phase-shift photomasks.

The proposed methods of metallization are widely used in electronics**,** piezoengineering and instrument-making. As a result Au, Ag and Pd were replaced with the alloys of non-precious metals; usage of toxic substances was eliminated [1–6].

1. INTRODUCTION

The term "electroless plating" denotes the method of deposition of metals and alloys without using the external electric current source. This method could find a wide application in accomplishment of the above mentioned tasks and resolution of other problems in various fields of industry such as nanoelectronics, microelectronics, fabrication of ICs, printed circuit boards, hard memory discs, instrument-making, machine-building, plating of plastics, etc.

The first edition of T.N. Khoperia's monograph – Electroless Deposition of Nickel on Nonmetallic Materials (in Russian). Moscow: Metallurgiya, 144 pages (1982), edited by K.M. Gorbunova – was distributed in a very short time. The research and development results presented in this monograph facilitated the implementation of new methods of metallization [1].

A new monograph has been prepared for publishing [8]. In our opinion, this monograph will promote reaching a new level of nanotechnology.

The present monograph contains new data on the proposed nanotechnologies for fabrication of fine-grained powder-like particles, films, bulk materials, nanocomposites, nanochips, devices for microelectronics, nanoelectronics, photonics and photocatalysis.

The development of a competitive nanotechnology for fabrication of nanochips is compared to "building the first atomic bomb or sending a person to the Moon" (Scientific American, April 2004, p. 49).

In this monograph, there is presented the technology providing the replacement of precious metals by nonprecious ones and the exclusion of the use of toxic substances and some undesirable production processes. The mechanism, the kinetics and the thermodynamics of reactions of electroless nickel deposition on various materials are described. The results of systematic investigations of the mechanism and kinetics of sensitization, activation prior to electroless metallization of nonmetallic materials are presented. The monograph can help the readers to use

efficiently wide possibilities of electroless deposition for fabrication of powder-like particles, bulk materials and films with specified properties.

This book will be helpful for scientists and engineers involved in the investigation and application of nanoelectronics, microelectronics, catalysis, photocatalysis, instrument-making, medicine etc.

The proposed monograph [8] consists of the following chapters:

Chapter I. Problems of the electroless nickel deposition on the various materials;

Chapter II. Reaction mechanism and kinetics of electroless nickel deposition using hypophosphite as reducing agent;

Chapter III. Some factors affecting the kinetics of electroless nickel deposition and properties of the coatings (using hypophosphite as reducing agent);

Chapter IV. Electrochemical investigations of the mechanism of electroless nickel deposition and the corrosion resistance of coatings;

Chapter V. Investigation of kinetics of the reactions and magnetic properties of electrolessly deposited Ni, Ni – P and Ni – Re – P coatings by using hydrazine or hypophosphite as reducing agents;

Chapter VI. Electroless metallization of nonmetallic materials;

Chapter VII. Industrial application of electroless nickel deposition in microelectronics, nanoelectronics, piezoengineering and instrument-making;

Chapter VIII. Nanotechnologies for fabrication of semiconductor powder-like photocatalysts with a uniform size distribution and their spectrophotometric investigation.

The developed methods of metallization of various materials have been widely used at the enterprises of the NIS for production of quartz resonators and filters, monolithic piezoquartz filters, photomasks, piezoceramic devices for hydroacoustics and delay lines of color TV sets (several hundreds million devices were produced), casings of integrated circuits and semiconducting devices, ceramic microplates, precise microwire and film resistors, capacitors, catalysts, etc.

As a result of usage of the developed technology Au, Ag and Pd were adequately replaced with non-precious metal alloys; a time for production of piezoquartz and piezoceramic devices was reduced by a factor of 4 (in the case of fabrication of piezoquartz devices).

2. SPECIFIC FEATURES OF ELECTROLESS METALLIZATION OF NONMETALLIC MATERIALS

The process of electroless deposition of nickel alloy using hypophosphite as a reducing agent is characterized by the following specific features revealed experimentally [1–6,8–18]:

1) The reduction of metal ions with hypophosphite proceeds on the surface of metals belonging to group VIII of the Periodic Table, which are capable to catalyze this process;

2) The rate of the process depends sharply on the solution temperature, obeying the exponential law;

3) In the acid solutions, the acidity and buffer properties of the solution affect significantly the rate of the process;

4) In alkaline solutions, the rate of the process depends on the concentration of hypophosphite, while in acid solutions such dependence manifests itself only under specific conditions;

5) The reduction of nickel ions is always accompanied by the release of gaseous hydrogen;

6) The concentration of the components of the solution for electroless nickel deposition is low, about (0.1 – 0.2) m / l;

7) The layer formed as a result of reactions does not consist of pure metal, but always contains phosphorus, the amount of which depends on the process conditions, in particular, on the pH value of the solution.

For electroless deposition of metals on nonmetallic materials, it is often necessary to give them the catalytic properties that would provide the initiation of the reaction of the metal ion reduction on nonmetallic surfaces. This is usually done with the help of two sequential processes (nowadays, often combined) called sensitization and activation [1–6]. The sensitization is generally performed by immersion of nonmetallic materials into the acid solution of bivalent tin. The activation is generally carried out by immersion of nonmetallic materials in the solution of palladium chloride.

Both the formulations of the solutions for surface treatment – sensitization and activation and the conditions of electroless nickel deposition depend on the nature and structure of the materials to be coated.

It is possible to increase the amount of the products remaining on the surface by rinsing the sensitized samples with sodium carbonate or ammonia solutions; in this case the hydrolysis proceeds faster and more completely. The activation can be carried out together with the sensitization with "conjugated" solutions containing salts of tin and palladium, platinum or gold. The solution suggested for this purpose contained salts of palladium and tin. The solutions prepared separately were combined immediately before the activation.

Metallization of disperse and porous materials by the electroless method at low temperature can be of a practical significance for obtaining, for example, the powder-like catalysts.

3. THE MECHANISM OF SENSITIZATION AND ACTIVATION

It is shown that the existence of adsorbed tin ions on the surface provides both a greater number of palladium ions on the glass and a greater strength of bonding of palladium to the surface at subsequent activation [1-6].

The experimental results show that the application of sensitization becomes less essential in the case of electroless metallization of non-metallic materials with greater surface roughness. With the increase in the substrate roughness (ground surface), the surface concentration of the adsorbed Sn and Pd ions increases.

The conditions of activation such as the pH value of palladium chloride solution, the concentration, temperature and surface roughness determine whether the sensitization is necessary or not.

The sensitization reduces the induction period of the nickel deposition reaction, promotes complete coverage of the surface and improves the coating quality [1–3].

At adding HCl (1 milliliter of concentrated acid per gram of $PdCl_2 \cdot 2H_2O$), chloropalladic acid is formed according to the reaction:

$$2HCl + PdCl_2 = H_2PdCl_4 \quad (1)$$

which affects favorably the activation process.

The mechanism of sensitization and activation was established, involving the concept of an equilibrium shift towards formation of complex palladium anions and predominance of the number of palladium ions over tin ions on the surface [1,2,8].

It was established that the part of palladium ions not reduced by sensitization-activation:

$$Sn(II) + Pd(II) = Sn(IV) + Pd \quad (2)$$

can be partially reduced at subsequent interaction with hypophosphite in the solution of electroless deposition according to the reaction:

$$PdCl_4^{2-} + H_2PO_2^- + H_2O = Pd + H_2PO_3^- + 2H^+ + 4Cl. \quad (3)$$

The investigation results showed for the first time that, when the aqueous-alcoholic solution is used as a solvent for tin chloride at the sensitization, at subsequent activation the amount of adsorbed palladium ions increased as compared with the application of the aqueous solvent for tin chloride. This can be referred to the fact that the addition of the organic compound to water changes the solvent configuration and the solvation degree of dissolved substances. Under these conditions,

dissolvation of Sn ions is simplified, because the ion-solvent (dipole) interaction is stronger in a water solvent than in a water–spirit solvent. Besides, it is more difficult for ethyl alcohol molecules, than for water molecules, to displace the tin ions at the interface. The small size of water molecules makes their presence at the interface energetically favorable.

A new mechanism of sensitization and activation in the mixed solvent, the effect of the solvent and the possibility of obtaining the nanometer-scale pore-free films can be explained by the interpretation with consideration of the reduction in the ionic strength in the mixed solvent and the increase in the ionic-activity coefficient.

As is known, the composition of the solution and the origin of the solvent affect the ionic strength I of electrolyte and, the ionic-activity coefficient. Taking into consideration this circumstance, the increase in the adsorption of palladium ions and the deposition of a denser film of palladium clusters after using a water–spirit solvent for sensitization could be explained on the basis of the Debye–Hückel theory. The relation between the ionic-activity coefficient γ_i and the ionic strength is expressed by the Debye–Hückel equation:

$$\lg \gamma_i = -A z_i^{\,2} \sqrt{I} \ . \qquad (4)$$

The use of the water-spirit solvent for the sensitization solution reduces the total number of ion charges $z_i^{\,2}$ in the solution and the ionic strength as compared to the water solvent. The decrease in the total number of electric charges in the solution is likely to promote a decrease in the force of attraction between the ions and the solvent, a decrease in the interaction between the ion and the dipole and an increase in the ionic-activity coefficient. It was established that the addition of NaCl to palladium chloride solution was favorable for the activation process.

To investigate the influence of chlorine ion concentration on the sign of the charge of complex palladium ions, a series of experiments was performed on the transfer of ions in the electric field. $PdCl_2 \cdot 2H_2O$ was dissolved in water with the minimum amount of HCl. The obtained solution was poured into the electrolyser divided into several compartments by porous glass diaphragms. In other series of experiments, electrolysis was carried out in 1 g / l solution of $PdCl_2 \cdot 2H_2O$ with some amount of NaCl added. In both cases, after electrolysis, portions of the solution taken from the cathodic, anodic and middle compartments of the electrolyser were subjected to polarographic analysis for palladium content. The results of the investigation showed that palladium was present in the form of a complex anion in the solution with minimum amount of hydrochloric acid with or without NaCl. But in the solution containing sodium chloride, Pd (II) was completely transformed into complex anions. As a result of the electrolysis, the concentration of palladium ions in the cathodic compartment was found to be much lower than that in the anodic compartment of the electrolyser.

The effect of addition of sodium chloride to the palladium chloride solution on the enhancement of adsorption of palladium ions and the increase in the activation effectiveness can be explained as follows. At adding NaCl to the $PdCl_2$ solution, small palladium cations (Pd^{2+}) transform into the palladium complex anion $PdCl_4$. In this case, the energy of interaction between the palladium anion and the solvent molecules, and the number of solvation molecules decrease. The reduction in the attraction forces between the palladium ion and the surrounding solvent molecules promotes an increase in the ion activity coefficient. As a result, the palladium ions easily get rid of their solvation shield. Under these conditions, the adsorption of palladium ions and the efficiency of activation increase. The application of the abovementioned methods allowed us to establish the mechanisms of sensitization and activation.

4. REPLACEMENT OF AU AND AG WITH THE NI – P AND NI – B ALLOYS IN ELECTRONICS

A new method of production of precise piezoelectric quartz resonators and filters, and monolithic piezoquartz filters with electrodes, made of electroless nickel-phosphorous alloy**,** for spacecraft, hydroacoustics and communication devices was developed [1–8]. Electrical characteristics of quartz resonators with the deposited Ni – P coating are better than when gold and silver were used as electrode layers. It is owing to the fact that:

1) For assembling the quartz oscillator at Ni – P plating, preliminary fusing of the silver sublayer (made from paste), causing undesirable changes in piezoquartz physical properties, is not necessary;

2) The improvement in the frequency characteristics of piezoquartz resonators is owing to the fact that the specific weight of the Ni – P alloy (7.8) is less than that of Ag (10.5) and Au (19.3). Therefore, the Ni – P electrode film does not deteriorate the oscillation properties of the piezoelement.

3) Adhesion between Ni – P electrode and piezosubstrate is higher than that between Ag or Au and the piezosubstrate. This decreases the electrical resistance between the electrode and the piezosubstrate and consequently the quality of the resonator increases.

A method of electroless deposition on polished quartz, glass and other nonmetallic polished materials was developed. The optimal conditions of metallization were established and the technology of electroless nickel deposition on piezoelectric quartz elements with smooth surfaces, including polished ones, was developed [8]. This technology for the first time provided high adhesion of Ni deposited by the electroless method to polished nonmetallic substrates and high ductility, deposition of thick films on polished piezoquartz being the most important for obtaining the monolithic quartz filters, in which the effect of energy capturing is necessary.

Bulk and miniature resonators of piezoquartz and lithium niobate manufactured on the basis of the developed technology of electroless deposition of a nickel-phosphorus alloy, instead of gold and silver plating, were successfully used in communication equipment, microprocessor devices, TV and video devices, quartz balances, ultrahigh frequency (UHF) equipment, UHF transducers of surface acoustic waves, watch industry, etc.

Basic advantages and innovations of the developed technologies in the field of electroless nickel deposition on piezoquartz and lithium niobate as compared to silver and gold plating are the following: 1) Frequency stability of piezoquartz devices increases by a factor of 1.8; 2) The absolute value of dynamic resistance of piezoquartz resonators decreases by 30 %, and the resistance scattering decreases by (40 – 50) %, as compared to the resonators with silver-plated piezoelements; 3) The quality and the long-term stability of piezoquartz devices improve.

The technology was developed for the production of piezoceramic and ceramic devices by electroless deposition of electrode layers made of Ni – P or Cu for hydroacoustic equipment of submarines and ships, delay lines of colour TV sets, capacitors, etc. As a result of using the developed technology, the time for production of the piezoceramic and ceramic devices was reduced by a factor of 60 as compared to high-temperature fusing of silver-containing paste, and Ag was adequately substituted with non-precious metals. The developed electroless methods allow producing films with specified electrical, mechanic, magnetic, optical and chemical properties.

The proposed methods of metallization of various materials are widely used at the enterprises of the Commonwealth of Independent States (CIS) for production of quartz resonators and filters (several tens of millions piezoquartz devices were produced), monolithic piezoquartz filters, photomasks, piezoceramic and ceramic devices for hydroacoustics and delay lines of color TV sets (several hundred of million piezoceramic and ceramic devices were produced), casings of integrated circuits and semiconductor devices, ceramic microplates, precise microwire and film resistors and other devices. The application of the proposed technologies has given a large economical effect. As a result of the use of this method, the technology was significantly simplified; the labor intensity of

the process decreased sharply; the production volume per square meter of production increased 8 times as compared to metallization by fusing the silver paste; the reliability, the quality and operational characteristics of photomasks produced by deposition of the semitransparent masking elements improved significantly and the accuracy of fitting precise microwire resistors, increased 10-fold.

Many companies produce various devices on the basis of ceramics and piezomaterials with gold and silver plating. To produce the same devices by the developed technologies, precious metals have already been adequately replaced with non-precious ones.

5. NEW NANOTECHNOLOGY FOR FABRICATION OF NANOCHIPS AND PHOTOMASKS WITH NANOSIZED ELEMENTS BY OPTICAL PHOTOLITHOGRAPHY

The proposed patentable nanomethods for the first time allow one to produce nano-sized adjacent elements of different thickness made of various materials (particularly of Si) by single optical UV photolithography (Fig. 1). These advantages significantly extend the functional capabilities of the devices and simplify the removal of undesirable gases and heat dissipation.

The proposed patentable nanomethods are much more advantageous and simpler than other expensive and complicated methods such as e-beam and X-ray lithography or fabrication of nano-sized elements by a light phase shift photomasks. The proposed method allows us to eliminate surface treatment by e-beam. It can save about 4 000 000 USD (the price of e-beam exposure equipment). It also eliminates the application of X-ray masks with gold masking elements.

Scientific basis of the new method of fabrication of photomasks with semitransparent elements and devices with nano-sized elements consists in the fact that the technology is carried out in such a way that the difference between boundary properties of the modified materials and bulk properties of the same materials are revealed to the utmost.

The proposed nanotechnology helps to solve one of the main problems of the modern microelectronics. It simplifies and makes cheaper the technology of microfabrication of the devices with the nano-sized elements [4,5,7].

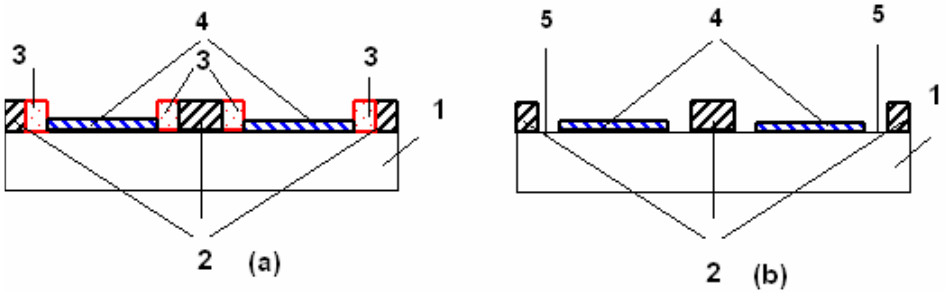

Fig. 1. Photomask with nano-sized semitransparent elements of different thickness fabricated by single conventional optical photolithography: (a) intermediate sample, (b) final product. 1 – transparent substrate; 2 – semitransparent masking elements of the first group; 3 – boundary layers of the masking elements of the first group; 4 – semitransparent masking elements of the second group; 5 – nano-sized transparent sections.

For application of this nanomethod, the elements of the first group, having the micron-sized value, are fabricated by conventional optical photolithography after deposition of the first masking film of semitransparent materials – transparent in the spectral region of visible light and non-transparent for UV exposing radiation.

The upper and lateral boundaries of the first group elements are oxidized in the nano-sized depth equal to the lateral nano-sized dimensions of the transparent elements of the photomask,

obtained afterwards. After the oxidation of the boundaries of the first-group masking elements, the secondary masking film is deposited on the intermediate sample. The secondary film is deposited on the part of the transparent substrate between the oxidized sections of the first-group elements and on the upper layer of the oxidized sections of the first-group elements.

The unnecessary upper layers of the second deposited masking film are removed selectively by chemical-mechanical polishing (CMP) or subsequent selective etching for exposing the lateral oxidized sections of the first-group elements.

Then the oxidized sections of the fist-group elements selectively etched. The remained part of the secondary layer is to be used for fabrication of masking elements of the second group between the masking elements of the first group.

Thus the first- and second-group masking elements and nano-sized lateral transparent elements between them are fabricated. The masking elements have a semitransparent character because they are transparent in the spectral region of visible light and non-transparent for UV exposing radiation. Owing to the transparency of the masking elements in the visible light, the precision of elements alignment significantly improves.

As a result of high-productive group method of single optical photolithography, by means of modification of the element boundaries and their subsequent selective etching, the sizes of masking elements and transparent sections are changed. This allows us to fabricate the photomask with nano-sized elements by using a standard photomask with micron-sized elements.

The proposed invention differs from the prior art, for example, in the following.

In the prior art:

I. It was not disclosed clearly how to fabricate the photomask with nano-sized transparent and nano-sized masking elements, moreover with the nano-sized adjacent masking elements of different thickness by conventional UV optical single photolithography;

II. It was not disclosed how to fabricate the working copies of the photomasks with nano-sized masking and transparent elements using a standard photomask with the element size more than a micron by conventional UV optical single photolithography;

III. It was not clearly explained how to break the contact between the layers of the secondary masking film deposited on the transparent substrate and at different levels. In the proposed International Application, five alternative solutions of this problem are described for the first time (see [7]);

IV. The formation of the layers of different chemical nature on the boundaries of the semitransparent masking elements of the first and second groups was not proposed;

V. The method of increasing the reliability of CMP and decreasing the damage to the thin layer by CMP and the method of thinning of the secondary masking film were not disclosed;

VI. In the prior art, the method and the conditions of increasing the strength of adhesion and the wear resistance of the deposited masking elements were not disclosed.

6. THE INDUSTRIAL APPLICATION OF ELECTROLESS NI FOR FABRICATION OF TWO-LAYER PHOTOMASKS WITH SEMITRANSPARENT EDGES OF MASKING ELEMENTS IN THE LOWER LAYER

A method of production and a new design of defect-free two-layer (Si – Ni) photomasks with semitransparent edges of the Si masking elements in the lower layer of the pattern based on single conventional optical UV photolithography is proposed (Fig. 2). This photomask has a number of advantages over the existing ones: 1) much less porosity; higher optical density; less thickness and higher wear resistance of the masking elements, and 2) semitransparence of the masking elements, which simplifies and enhances the alignment precision [18]. These photomasks were widely introduced in the microelectronic industry with a large economical effect.

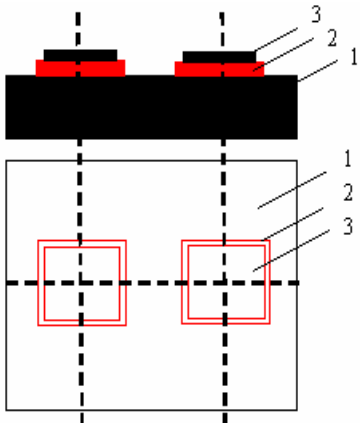

Fig. 2. Two-layer photomask metallized by the electroless method: 1 – glass substrate; 2 – semitransparent Si layer; 3 – opaque masking layer of Ni – P alloy.

7. FABRICATION OF PHOTOCATALYSTS

By means of selective local electroless deposition of nanocrystals having specified properties on high-dispersive powder-like semiconductor photocatalysts, many problems of solar energy applications and photocatalytic splitting of water can be overcome or mitigated [19]: I. Recombination of the photoexcited electrons and holes; II. Simultaneous proceeding of oxidation and reduction reactions at the same sites of photoelectrodes. III. The possibility of using the low-energetic visible-light irradiation; IV. Low quantum efficiency of energy conversion; V. Difficulty in deposition of nano-sized clusters on nano- and meso-sized particles.

The following methods are used for overcoming the problems in this field: 1) Electroless deposition of nanoclusters with specified properties on semiconductor photocatalysts; 2) Reduction in the recombination of photoexcited electrons and holes by means of nanotraps; 3) Separation of the active centers of reduction and oxidation reactions; 4) Changing the solvent structure and the increase in the ionic-activity coefficient in the mixed solvent.

We developed a local electroless method of deposition of amorphous and crystalline quantum dots and also nanocrystals on high-dispersive powder like nanoparticles. The method provides both low and high degree of covering of nanoparticle surfaces. The high-dispersive particles with low surface covering with nanocrystals are characterized by high catalytic activity.

It was established for the first time that the irradiation with γ-rays increased sharply the light absorption ability of semiconductor powders.

It was demonstrated that the selection of optimal sizes of powder particles could also enhance the optical absorption over the specified wavelength range. By using purposefully the above mentioned factors, it is possible to shift the optical absorption spectra of high-dispersion NiB / TiO_2 (anatase) powders to the visible light region, i.e. to the wavelength range of (400 – 800) nm. This allows bringing the optical properties of Ni – B / TiO_2 powders closer to the requirements of photocatalytic reaction, which will promote the production of hydrogen and oxygen from water by using the light energy, the conversion of light energy into electric power, the destruction of undesirable bacteria, for cancer treatment and other applications.

The comparison of the peaks of optical absorption spectra of the obtained photocatalysts revealed the following. We obtained the photocatalysts having the peak of optical absorption spectra 3 times higher than that of ordinary TiO_2 photocatalysts (St-01 and P-25).

A new method of size selection of pure TiO_2 particles and micro-, meso- and nanocrystal-coated powder-like semiconductor photocatalysts with aim obtain of a uniform size distribution was developed. This method is important because the quantum size effect is a challenge.

A patentable method of fabrication of self-cleaning tunnel-lamps, windows and automobile screening windows from exhaust (organic contaminants and fumes) is being developed. The proposed method blocks the diffusion of Na^+ cations (or removes them) from the glass substrate into titanium, which have an adverse effect on photocatalytic-cleaning activity of TiO_2. The proposed layer also provides the enhancement of glass transparency. Coated glass stays transparent much longer and can be cleaned by rainfall.

8. FABRICATION OF MESO- AND NANO-SIZED MAGNETIC PARTICLES FOR CANCER TREATMENT

The competitive method of fabrication of thermo-absorbing meso- and nano-sized magnetic particles (coated with biologically compatible material) was developed. Applications of high-dispersive magnetic particles could include information storage systems, biomedical fields, targeted delivery of drugs for cancer treatment, sensors, etc.

In the magnetic field with specific frequency, the magnetic nano- and meso-particles can absorb energy. As a result, an increase in the local temperature around the high-dispersive powder-like particles takes place. This effect could be applied to selective destruction of cancer tumors at 42 °C by means of irradiation (their selective heating) with infrared light or with an alternating magnetic field, while leaving nearby tissues unharmed.

The possibility of electroless deposition of metals on nonmetallic, high-dispersive dielectric and semiconductor particles without their preliminarily activation by palladium chloride, demonstrated in our works, could be explained theoretically in the following way. In the boundary layer, at the solid-water interface, the following factors manifest themselves:

1. The dielectric constant of water in the thin boundary water layer adjacent to the solid surface is lower by an order of magnitude than in the bulk water;
2. The configuration of solvent changes;
3. The ion–dipole interaction changes, owing to which the ions attract water dipoles;
4. The activity coefficient of the ions dissolved in the solution increases;
5. On the surface of fine-grained particles, the wettability increases and the attraction and the ion adsorption are stimulated under the influence of the surface molecular field and the non-saturated surface forces;
6. The degree of hydration decreases with the decrease the size of particles;
7. The above mentioned factors could lead to reduction in the energy, which is necessary for adsorption and introduction of metallic ions into the surface monolayer of oriented molecules of the solvent at the solid surface–solution interface;
8. There exists the quantum size effect of high-dispersive semiconductor particles and nano-sized clusters on the reaction;
9. Under the effect of the large surface area of high-dispersive particles, the presence of a large number of unsaturated surface forces and defects on the surface, the adsorption and the breaking of bonds among the reductant atoms happen more readily, which is essential for the course of heterogenic catalysis reaction of electroless metal deposition.

9. METALLIZATION OF THE INTERNAL PORCELAIN SURFACE OF THE VACUUM CHAMBER OF ELECTRON SYNCHROTRON

It is possible to deposit the Ni – Re – P coatings with specified electrical surface resistance by the electroless method. The results of this investigation were used for metallization of the internal porcelain surface of the vacuum chamber of electron synchrotron “Pakhra”, installed at the Laboratory of Photomeson Processes of P. Lebedev Institute of Physics, Moscow (Fig. 3). As is

well known, one of the main parts of the electron synchrotron is the porcelain vacuum chamber, the internal surface of which is metallized for removal of static charge, which deteriorates the process of acceleration of elementary particles in the electron synchrotron. The requirements to the electric resistivity of the conducting layer deposited on the internal surface of the vacuum chamber of electron synchrotron are defined, on the one hand, by the possibility of rapid discharge of the static charge and, on the other hand, by the admissible value of eddy currents. Based on these requirements, the estimated value of the surface resistance is about 2 kOhm / sq. cm. Until recently, for formation of the conducting layer of ceramic chambers of electron synchrotrons, the methods of baking or thermoelectric deposition were used. Those methods involved the use of expensive equipment and took quite a long time.

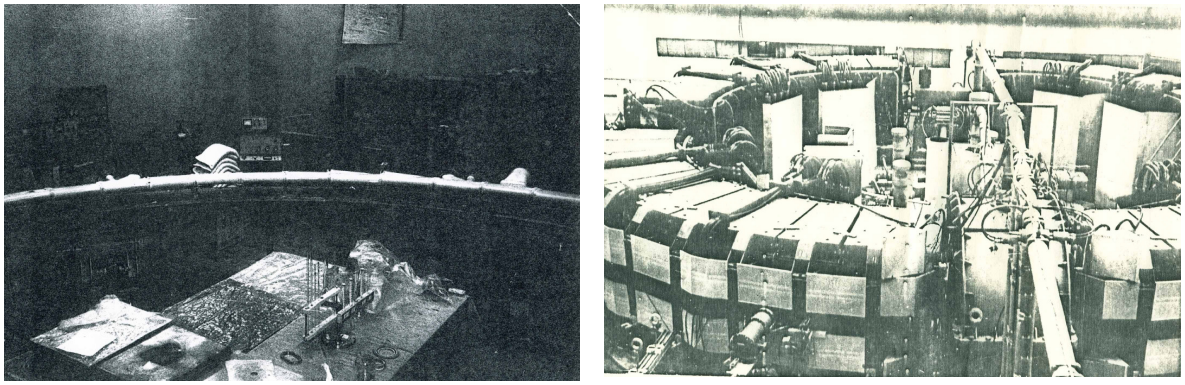

Fig. 3. The ceramic vacuum chamber of electronic synchrotron at P. Lebedev Institute of Physics, Moscow, Russia. Inner surfaces of ceramic pipes were metallized with Ni – P – Re alloy (for removal of electrostatic charge) by the electroless method developed by T.N. Khoperia.

The results of testing of the vacuum chamber of electron synchrotron metallized with the Ni – Re – P alloy by the method developed by T.N. Khoperia were quite good. The tests verified the high efficiency of the proposed method of metallization with the specified surface resistance, its simplicity and the reliability of adhesion of the conducting layer to the internal surface of the vacuum chamber of electron synchrotron. The tests pointed to one more of its advantages – its high productivity. For example, it took a few minutes to metallize a porcelain section, whereas it took several hours to deposit the conducting layer by the method of burning. Besides, it should be noted that the application of the proposed method made simpler the operation of the vacuum chamber as compared to the method used before, due to the deposition of the conducting layer with low gas emission and the elimination of the need in long-time pumping to vacuum of the chamber before its operation each time.

10. CONCLUSIONS

1. The present work contains new data on the nanotechnologies for fabrication of fine-grained powder-like particles, films, bulk materials, nanocomposites, devices for microelectronics, nanoelectronics, photocatalysis and photonics.

2. The nanotechnologies using the electroless deposition are much more advantageous and simpler than other expensive methods of nanotechnology and allow the fabrication of photocatalysts and catalysts by means of deposition of nanocrystals having the specified properties on high-dispersive semiconductors.

3. The developed methods of metallization of various materials have been widely used at the enterprises of the Commonwealth of Independent States for production of quartz resonators and filters, monolithic piezoquartz filters, photomasks, piezoceramic devices for hydroacoustics and

delay lines of color TV sets (several hundreds of millions of devices were produced), casings of integrated circuits and semiconductor devices, ceramic microplates, microwire and film resistors, capacitors and catalysts.

4. As a result of application of the developed technology, Au, Ag and Pd were adequately replaced with non-precious metal alloys; the time for production of piezoquartz and piezoceramic devices was reduced by a factor of $4 - 60$; labor intensity of the technology was reduced significantly; the frequency stability of piezoquartz devices was increased 1.8 times; the absolute value of dynamic resistance of piezoquartz resonators became lower by 30 % and the resistance scattering became lower by $(40 - 50)$ % as compared to resonators with silver-plated piezoelements.

5. A new patentable nanotechnology of production of photomasks and microdevices (with nano-sized adjacent elements of different thickness made of various materials) on the basis of single conventional optical photolithography was developed.

6. Theoretical interpretation of the increase in the amount of palladium ions adsorbed during the activation after preliminary sensitization in aqueous-alcoholic solution is presented.

7. The possibility of electroless deposition of metals on nonmetallic, high-dispersive dielectric and semiconductor particles without their preliminarily activation is explained theoretically, taking into account various physical-chemical phenomena.

REFERENCES

1. T.N. Khoperia. Electroless Nickel Plating of Non-Metallic Materials. Moscow: Metallurgiya (1982).
2. T.N. Khoperia. In: Proc. 10th World Congress of Metal Finishing (Interfinish'80). Kyoto, 147 (1980).
3. T.N. Khoperia, T.J. Tabatadze, T.I. Zedginidze. Electrochim. Acta, **42**, 3049 (1997).
4. T.N. Khoperia. Microelectron. Eng., **69**, 384 (2003).
5. T.N. Khoperia, T.J. Tabatadze, T.I. Zedginidze. In: Proc. Int. Conf. Micro Materials. Berlin, 818 (1997).
6. T.N. Khoperia. Microelectron. Eng., **69**, 391 (2003).
7. T. Khoperia, N. Khoperia. A photomask and Devices with Nano-Sized Elements, International Publication Number: WO 2009 / 106903. Georgian Patent P 4788 (2009).
8. T.N. Khoperia. Electroless Deposition of Metals and Alloys for New Challenges in Nanotechnologies, Electronics and Photocatalysis (Monograph in English, which is presented for publication).
9. K.M. Gorbunova, A.A. Nikiforova, G.A. Sadakov, V.P. Moiseev, M.V. Ivanov. Physical-Chemical Bases of the Process of Electroless Cobalt Plating. Moscow: Nauka (1974).
10. G.G. Gawrilov. Chemical (Electroless) Nickel Plating. Redhill: Portcullis Press Ltd (1979).
11. Kh.B. Petrov. Galvanizirune na Plastmasi. Sofia (1982).
12. M.I. Shalkauskas, AY. Vashkyalis. Electroless Metallization of Plastics. Leningrad: Khimiya (1977).
13. Electroless Plating: Fundamentals and Applications (Eds. G.O. Mallory, J.B. Hajdu). Orlando: AESFS (1990).
14. W. Riedel. Electroless Nickel Plating. Hertfordshire: ASM Int. Materials Park – Finishing Publication Ltd (1991).
15. C.J. Sambucetti, E. O'Sullivan, L.T. Romankiw. In: Abs. 40th Int. Soc. Electrochem. Meeting. Kyoto (1989).
16. T. Osaka, T. Homma. Interface, **4**, 42 (1995).

17. S. Lopatin, Y. Shacham–Diamand, V.M. Dubin, P.K. Vasudev, B. Zhao, J. Pellerin. In: Electrochem. Soc. Proc. Series (Eds. M. Paunovic, D.A. Scherson). Pennington, 271, (1997).
18. T. Khoperia, T. Zedginidze, G. Mamniashvili, A. Akhalkatsi. Bull. Georg. Natl. Acad. Sci., **2**, 92 (2008).
19. M.M. Nadarishvili, K.A. Kvavadze, G.I. Mamniashvili, T.N. Khoperia, T.I. Zedginidze, E-print arXiv: Cond-mat / 0903.5104 (2009).

BORON NITRIDE NANOSTRUCTURES: MOLECULES, SHEETS, TUBES, FULLERENES (AN OVERVIEW)

L. Chkhartishvili

Georgian Technical University
chkharti2003@yahoo.com

Accepted February 13, 2010

1. INTRODUCTION

Boron nitride with the chemical formula BN can be found in form of one-dimensional diatomic molecule, two-dimensional nanotubes and fullerenes, three-dimensional crystals like the layered hexagonal h-BN and rhombohedral r-BN, cubic zinc-blende c-BN and wurtzite w-BN modifications etc. Boron and nitrogen atoms are tetrahedrally surrounded in both denser c-BN and w-BN crystals. However, unlike the zinc-blende case, in the wurtzite structure there are two different types of nearest-neighbor bonds: one perpendicular to the hexagonal atomic planes and three equal bonds forming these planes. For a stable wurtzite-type structure ratio of the lattice constants and internal parameter value are correlated in such a way that all bond lengths are almost equal, whereas the tetrahedral angles are distorted.

Any constituent atom of h-BN crystal, which corresponds to the boron nitride ground state, may be considered as a 3-coordinated because the strong chemical (covalence with deal of ionic) binding occurs only within the layers. Weak van der Waals forces are mostly responsible for interlayer binding. h-BN crystal has a "graphitic" structure with two-layer stacking sequence, while r-BN is characterized by a three-layer stacking (Fig. 1). The layers in these layered structures consist of regular hexagons (i.e. 6-membered atomic rings) with vertexes alternatively occupied by B and N atoms. In h-BN crystal, B atoms are placed directly above N atoms and on the contrary. Hence, it would be possible to think that in interlayer bonding there is a deal of ionicity. However, actually electrostatic component is insignificant due to the large interlayer distance. It is argued also by the existence of layered r-BN crystal in which each subsequent layer is turned on angle of $\pi/3$, and also by the isolated plane defects and their bundles included in real h-BN crystals, in which any given atom can be placed above the like atom. Besides, it is possible to obtain turbostratic t-BN and amorphous structures in form of mixes of the various boron nitride crystalline phases, and multi-walled nanotubular and multi-shelled fullerene-like BN structures. Strong chemical bonding between atoms in given layer and weak interlayer interaction in layered boron nitrides specify an opportunity of the physical and chemical intercalations by the various atoms and molecules.

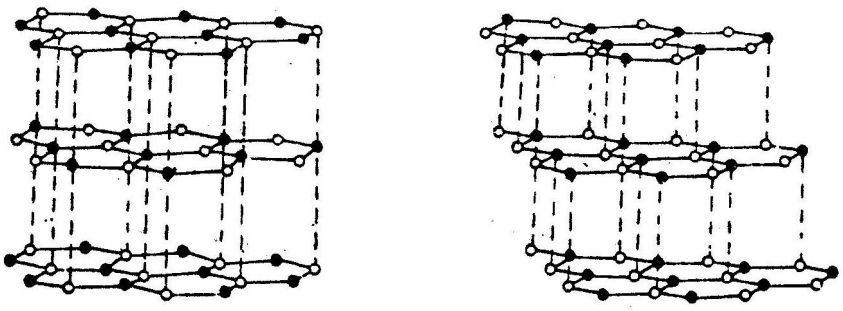

(1) **(2)**

Fig. 1. Two- (1) and three-layer (2) stacking sequences in h-BN and r-BN layered crystals.

Based upon the similarity of structures of the above specified boron nitride phases with graphite, it was assumed [1], that alongside with carbon C nanotubes and fullerenes, it should be stable BN nanotubes and fullerenes, the fragments of hexagonal or mixed BN layers wrapped into cylinders or spheres, respectively. A modified-neglecting-of-diatomic-overlap (MNDO) study of BN analogues of C fullerenes was presented in [2] and $B_{30}N_{30}$ molecule was predicted to be stable and, consequently, relatively simple to synthesize. And in fact, by means of arc-discharge BN nanosystems had been obtained both from carbon nanotubes [3] and in carbon-free plasma [4].

Classification scheme of the 3D nanostructures useful for boron nitride was suggested in [5]. It is based on crystallite and grain boundary forms and chemical composition. According to the extended classification [6], *l*D, *m*D, and *n*D structures may serve as building blocks for any *k*D structure if $k \geq l,m,n$ ($k,l,m,n = 0,1,2,3$ are dimensions of the nanostructures).

2. BORON NITRIDE MOLECULES

2.1. Diatomic molecule

Diatomic molecule BN (Fig. 2, (1)) can be considered as a simplest (degenerated) form both for boron nitride nanotubes and boron nitride fullerenes. In general, electronic theory of substance considers a diatomic molecule as a special problem for its intermediate structural and, consequently, electronic properties between mono- and polyatomic systems [7]. Peculiarities mainly are related with the system axial symmetry and uniqueness of the structural parameter – interatomic distance d. Unlike the solid state and nanoscale boron nitrides, which are materials with a diversity of technical and industrial applications, BN molecule existing under the extreme conditions is only of special scientific interest being the "building block" for two- and three-dimensional boron nitride structures. From the standard thermochemical data, the energy of B–N bond at the equilibrium length is known to be considerably higher in comparison with those of B–B and N–N bonds. Besides, any stable regular BN structure is a network of atomic rings with alternating atoms such that the nearest-neighbor environment of both B and N atoms consists of only B–N bonds. Therefore, B–N bond length is a key interatomic distance in the analysis of boron-nitrogen binding.

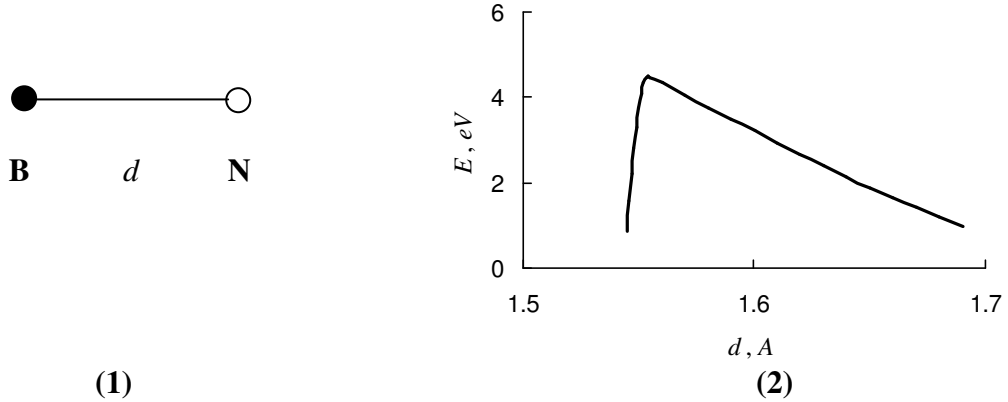

(1) **(2)**

Fig. 2. BN diatomic molecule (● – B; ○ – N), the isolated B–N bond (1) and quasi-classically calculated [15] B–N binding energy versus interatomic distance in the vicinity of equilibrium (2).

There are known some first principles and semiempirical investigations for boron-nitrogen interaction (see [8,9]). Applying a self-consistent-field (SCF) procedure to the BN molecule in [10], it was calculated molecular orbitals (MO) in order to minimize total energy of the diatomic system. Then using the spectroscopic data available for the corresponding ground state, the BN molecule dissociation energy value E was found as 4.6 eV. According to the original theoretical approach of

[11], equilibrium interatomic distance in this molecule equals to 1.307 Å. At the same time, spectroscopic parameters characterizing the calculated boron-nitrogen interaction potential curve lead to the dissociation energy estimation of 5.05 eV. Nearly the same bond length theoretical value of 1.320 Å was suggested in [12]. In [13] a short-ranged classical-force-field (CFF) modeling of BN modifications was performed on the basis of experimental and first principles solid-state and diatomic-molecular data. In particular, assuming that CFF can be correctly determined by a sum of only two-body interaction terms, the B–N potential energy had been expressed analytically via Morse potential, what gave $d \approx 1.32521$ Å and $E \approx 5.50007$ eV. However, it was noted [14] that standard forms of the pair interatomic potentials, like the Morse, Mee–Grüneisen, Buckingham, and others, converge slowly and hence a cutoff procedure should be used. But, in such case non-physical jump on the potential radial function can arise. To eliminate this problem, based on the embedded atom method it was elaborated new B–N interatomic potential, which fulfills the conditions for smooth end: the potential function and its derivative (i.e. interatomic force) vanish at the cutoff radius. The equilibrium bond length of 1.4457 Å and binding energy of 4.00 eV were found to reproduce correctly relative stabilities of the boron nitride layered structures.

We also suggested [15] the theoretical, namely, quasi-classical method of calculation of the B–N interatomic binding energy E in dependence on the bond length d. The constructed $E = E(d)$ curve was shown to be useful for estimations of BN crystalline structures cohesion parameters as well. This function reveals standard behavior characteristic for the central pair potentials. $E(0) = -\infty$, and $E(d) \equiv 0$ if d is equal or more than sum of B and N quasi-classical atomic radii $r_{(B)} \approx 2.30$ and $r_{(N)} \approx 1.70$ Å, i.e. $d \geq r_{(B)} + r_{(N)}$ (note that quasi-classical B–N interatomic potential automatically fulfills the conditions for the smooth end at $d = r_{(B)} + r_{(N)} \approx 4.00$ Å), while within the intermediate region $0 < d < r_{(B)} + r_{(N)}$ it is an oscillatory function with several maxima. Among them only one is kinetically available and, therefore, corresponds to the equilibrium. Piece of the quasi-classical $E = E(d)$ curve for BN diatomic molecule, in the vicinity of this maximum, is presented in Fig. 2, (2). Its analysis yields the values of bond length of 1.55 Å and binding energy of 4.51 eV. Same dependence determined earlier [16] within the frames of another quasi-classical parameterization scheme (for this purpose the screening factor of the potential affecting the given electron in interacting atom was approximated by the radial polynomial, not by the constant) is relatively flat and leads to estimations of 1.58 Å and 4.79 eV.

Thus, the spread in theoretical and semiempirical values for BN molecule binding energy is (4.0 – 5.5) eV, which overlaps with the recommended [17] experimental dissociation energy value of (4.0 ± 0.5) eV. The available first principles and semiempirical calculations and thermochemical experimental data lead to the binding energy values of about (4 – 7) eV per B–N bond for various, differently coordinated, BN modifications (for sheet and layered structures see below). Such kind of estimations may be considered to be in qualitative agreement with quasi-classically calculated B–N bond energy as the ground state energetic parameters are quite sensitive to the atomic coordination. By reason of this, we focus our attention on the differences in the bond length values between BN molecular and crystalline phases. Isolated B–N bond length quasi-classical values and other concerned theoretical and semiempirical data, which lie over the range (1.307 – 1.580) Å, are overestimated in comparison with 1.281 Å measured in $^{11}B^{14}N$ molecule [18]. The explanation may be that this molecule has a triplet ground state, but with a low-lying singlet state with longer bond.

Theoretical estimates show some redistribution of the valence electron density between B and N atoms bonded in diatomic molecule. Calculation of the quasi-molecular minimal unit cell of h-BN crystal within the two-dimensional approximation, i.e. the B_1N_1 system, yields following occupancies for the valence electron states: s(B) – 0.88, p_{xy}(B) – 0.23, p_z(B) – 0.69, s(N) – 1.12, p_{xy}(N) – 1.77, and p_z(N) – 1.31 [19]. Therefore, for B and N atoms one can find charges of $3-(0.88+0.23+0.69)=+1.20$ and $3-(1.12+1.77+1.31)=-1.20$, respectively, i.e. $B^{+1.20}N^{-1.20}$

configuration. From the electronegativity scale, charge transfer direction is valid, but ionic charge value of 1.20 seems to be overestimated. There are known wave-function calculations [20,21] leading to the $B^{+0.47}N^{-0.47}$ configuration with physical meaning for transferred charge of 0.47. These discrepancies seem to be arisen from the ambiguousness of an ionicity scale [22,23].

According to all available theoretical studies, BN molecule ground state identifies with $X^3\Pi$ triplet-state [10-13,18,24]. However, molecular spectra [25] verifying this ground state at the same time reveal low-lying $A^1\Sigma^+$ singlet-state. Applying SCF MO method at the experimental bond length, the 1σ, 2σ, 3σ, 4σ, $1\pi^+$, 5σ, 6σ, and $2\pi^+$ electron-states energies in BN molecule were found [10] as −425.1769, −209.320, −28.9767, −12.251, −10.970, +0.1001, +21.527, and +0.25772 eV, respectively. Consequently, the first ionization potential (IP) is estimated as 10.970 eV. Using the extended Slater basis, the MO configuration of BN molecule in frames of SCF approach also was considered in [25]. Our non-self-consistent quasi-classical calculations [26] gave two upper occupied electron levels: −31.66 and −10.93 eV, i.e. IP = 10.93 eV. Another quasi-classical value of the B–N bond IP of 6.2 eV we obtained [15] self-consistently – at the equilibrium bond length of 1.55 Å calculated within the same approach.

Work function (WF) is known as a solid-state counterpart of the molecular IP. To the best of our knowledge, there are no experimental data neither for boron nitride crystalline modifications WF, nor for BN diatomic molecule IP itself. It were suggested only semiempirical WF values of 11.8 [27], 11.5 [28], and 10.6 eV [29] predicted for BN sheet; and theoretical estimations of 11.0 and 10.9 eV determined for BN molecule using SCF MO method [10] and quasi-classical approach within the another parameterization scheme [26], respectively. All of these values have the same order of magnitude ≥ 10 eV, but somewhat more than IP found in [15]. In this connection, it would be noted that the earlier quasi-classical calculations [26] were performed employing the experimental values of B–N bond lengths in h-BN crystal layers or in BN molecule, i.e. non-self-consistently. However, according to the Harrison interpolative conception [30], the bond-length-dependence of any energetic gap in substance electronic structure may be approximated as $\sim 1/d^2$. Consequently, non-self-consistent IP of BN molecule should be corrected by the $\sim (d_{\exp}/d)^2$ factor, where $d_{\exp} \approx 1.28$ Å is the experimental length of the isolated B–N bond. For the case of another quasi-classical parameterization scheme with $d \approx 1.58$ Å and IP ≈ 10.9 eV it leads to the IP of 7.1 eV, which is in better agreement with the new quasi-classical result of 6.2 eV.

Quasi-classically calculated interatomic vibration energy in B–N diatomic system of 0.178 eV / mole (corresponding vibration quantum equals to 1435 cm^{-1}) was found by fitting quasi-classical B–N potential curve with parabola [16,31]. This value is in good agreement (with deviations of ~ 5 %) with the values experimentally obtained for neutral BN molecule of 0.187 (1514.6) [18] and 0.188 eV / mole ((1519.0 ± 0.2) cm^{-1}, from the absorption spectra Fourier analysis for laser-induced molecular fluorescence) [25]. According to the SCF theoretical method of [11], the ground state vibration energy in molecular BN estimated as 0.179 eV / mole (1446 cm^{-1}), which is almost the quasi-classical result. In [12] it was suggested the higher theoretical value of 0.217 (1750), what is close with 0.216 eV / mole (1740 cm^{-1}) measured in ionized molecule BN^+ [32].

2.2. Polyatomic molecules

Studies on the complex molecular clusters of B and N also are of interest for deeper insight into the defect formation processes in boron nitride nanosystems. High-temperature Knudsen cell mass spectrometry was used to study the equilibria involving the B_2N molecule [33]. Thermal functions needed in the evaluation of the mass spectrometric equilibrium data had been calculated from available experimental and theoretical molecular parameters. In particular, the enthalpy changes in some reactions with B_2N formation had been measured. Room temperature atomization

and formation enthalpies were determined as 10.84 and 5.71 eV, respectively. At the same time, the first principles calculations were performed to estimate B_2N electronic parameters, like the ionization energy and electron affinity. Mixed clusters of B and N atoms – B_2N, BN_2, B_3N, B_4N, B_2N_2, and B_3N_2 – can be produced by sputtering of a solid state BN [34]. Atom ordering in assumed linear species had been derived from measurements of the mass distribution of both the positive and negative products from the fragmentation of the anionic clusters in a gas target. The neutral configurations were calculated as $B^{+0.28}B^{-0.11}N^{-0.17}$, $N^{+0.03}B^{-0.06}N^{+0.03}$, $B^{+0.08}B^{+0.14}B^{-0.03}N^{-0.19}$, $B^{-0.04}B^{+0.07}B^{+0.05}B^{+0.03}N^{-0.11}$, and $B^{-0.07}B^{+0.02}N^{+0.02}N^{+0.03}$. It was found tendency that the structure with the most number of B–N bonds is most stable both in neutral and anionic species (exception is BN_2 molecule). In the contrast with this, the specie with the most number like atoms adjacent to each other (except for triatomic chains) has the largest electron affinity.

First principles ground-state calculations of the infinite one-dimensional chain of alternating B and N atoms were performed [35] using the restricted Hartree–Fock (HF) approach, while the many-body effects were taken into account by second-order perturbation theory and coupled-cluster model. Both at the HF and the correlated levels boron–nitrogen chain exhibits equidistant bonds. Structural, electronic, and transport properties of atomic chains of a groups III–V binary compound were studied [36] using the first principles plane-wave (PW) pseudopotential (PP) method. Compound wires of BN revealed semiconductor or insulating properties. It was proposed [37] that BN polymers, with the same structure as organic polymers, will allow the idea to be a cheap alternative to inorganic semiconductors for designing of the modern electronic devices, and demonstrated some related potential innovations, including band gap tuning.

3. BORON NITRIDE SHEETS

3.1. Structure

The facts that boron nitride layered crystals, nanotubes, and fullerenes may be prepared urge on analysis of hypothetic isolated infinite hexagonal layer, i.e. BN sheet. Corresponding two-dimensional BN crystal is represented as a planar layer composed of regular hexagons with vertexes alternately occupied by B and N atoms (Fig.3, (1)). In this crystal, $\vec{t}_1 = a(1/2, \sqrt{3}/2)$ and $\vec{t}_2 = a(-1/2, \sqrt{3}/2)$ are the basis vectors, where a is the lattice constant determined as the shortest distance between like atoms. Unit cell contains one B and one N atom with radius vectors of $\vec{d}_{(B)} = a(0, 1/\sqrt{3})$ and $\vec{d}_{(N)} = a(0, -1/\sqrt{3})$ with respect to the center of a hexagon (Fig. 3, (2)).

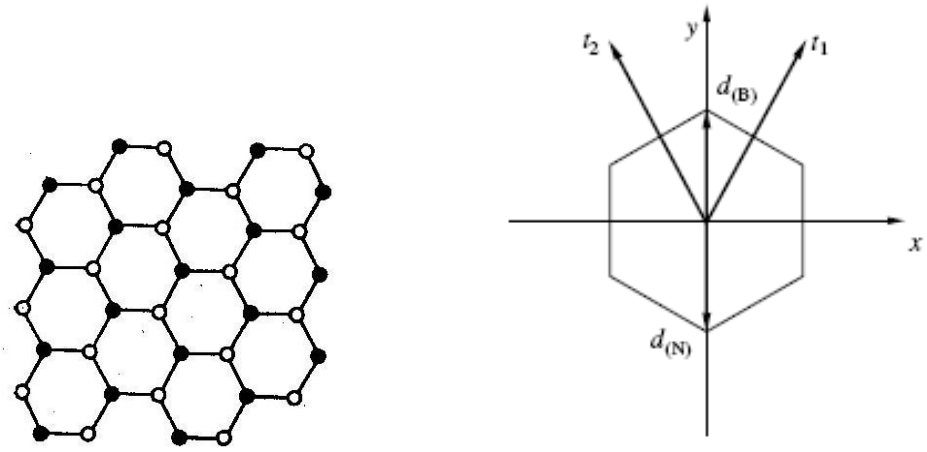

(1) **(2)**

Fig. 3. BN hexagonal sheet (1) and its unit cell (2).

Classification and consideration of the BN haeckelite sheet structures consisting of not only hexagonal atomic rings, but also other even-membered rings, one can find in [38].

3.2. Binding

For the first time, the truncated crystal approach in form of two semiempirical (standard and extended iterative Hückel) methods was employed [28] to the two-dimensional hexagonal boron nitride structure and found bond length to be equal to 1.48 or 1.50 Å. But, when semiempirical calculations were performed on two-dimensional periodic small cluster of the h-BN layer the equilibrium B–N distance was computed as 1.441 Å [29]. In [39] the 3-coordinated $B_{12}N_{12}$ network of 6-membered atomic rings was examined theoretically. Namely, the total energy calculated using HF approach and density functional theory (DFT) in local and gradient-corrected forms was minimized with respect to B–N bond length. But, "graphitic" isomer $B_{12}N_{12}$ is only a fragment of the BN sheet and its geometry appears to be somewhat distorted because of finite sizes. As should be expected, the smallest deviations of the bonds angles from the ideal value of 120° were observed for the bonds of atoms forming the central hexagon: –(2.52 – 2.65)° for B atoms and +(2.52 – 2.65)° for N atoms. There were also obtained number of unequal bond lengths: (1.266 – 1.283), (1.371 – 1.378), (1.427 – 1.442), (1.434 – 1.444), (1.520 – 1.536), and (1.553 – 1.576) Å. The finiteness of the quasi-classical atomic radii allowed us to obtain the B–N bond length for infinite boron nitride sheet within the initial quasi-classical approximation [40]. The calculated dependence of the molar binding energy on the lattice constant (Fig. 4) exhibits a maximum of 23.0 eV at the 2.64 Å, which should correspond to the equilibrium state for an isolated hexagonal layer (analytical optimization [41] of the lattice parameter using the binding energy calculated in quasi-classical approximation, which is possible only neglecting by the vibration energy, yields slightly different values: 23.2 eV and 2.66 Å, respectively). The lattice constant of 2.64 Å means B–N bond length of 1.52 Å. Correction introduced by zero-point vibrations was estimated as 0.242 eV / mole [31,40].

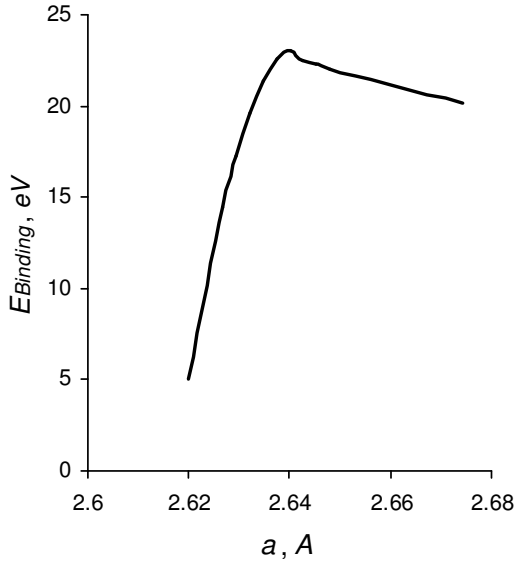

Fig. 4. Quasi-classically calculated [40] dependence of the molar binding energy on the lattice constant for BN sheet.

The quasi-classical bond length of 1.52 Å in isolated BN sheet is in reasonable agreement (with deviation of 4.6 %) with the bond length of 1.45 Å observed in layers of real h-BN crystals. At first glance, the surprising thing is that the theoretical result for the isolated layer is in better agreement (deviations of (2.6 – 3.8) %) with the bond lengths in tetrahedrally coordinated modifications c-BN (1.57 Å) and w-BN (1.56 and 1.58 Å). However, it is worth nothing that in some respects two-dimensional boron nitride looks like three-dimensional crystals c-BN and w-BN: these three structures do not contain weak interlayer bonds, which occur in the h-BN layered modification. The lengths of (1.52 – 1.54) and (1.55 – 1.58) Å obtained in [39] for the bonds of

atoms forming the central (almost undistorted) hexagon in $B_{12}N_{12}$ plane-fragment are also in good agreement with the quasi-classical result found for an idealized infinite BN sheet. Another quasi-classical approach using different scheme of parameterization, employed for the calculation of h-BN binding and zero-point vibration energies, somewhat underestimates the intralayer bond length [42]. The plausible reason may be that the crystalline equilibrium configuration was selected maximizing its static binding energy with respect only to the layer lattice parameter, while the interlayer distance was fixed.

Summarizing other theoretical and semiempirical results concerning intralayer bond lengths in h-BN (and r-BN) one can state that all of them are in agreement with the experimental value of 1.446 Å [43]. For instance, in [44] the total energy of h-BN crystal as a function of unit cell volume V had been calculated using orthogonalized linear-combinations-of-atomic-orbitals (LCAO) method within the local-density-approximation (LDA). The equilibrium was found at $V/V_{\exp} = 0.998$, where $V_{\exp}$ is the experimental value of V. Such result corresponds to the intralayer B–N distance of 1.438 Å. The calculations of [45] were also based on DFT within LDA, but PW expansion was used both for PP and wave-function. Computed total energies and, consequently, the intralayer bond lengths in h-BN and r-BN were nearly the same: 1.441 and 1.439 Å, respectively. The short-ranged CFF modeling of boron nitrides leads to exactly the same intralayer B–N bond lengths in both of layered structures: 1.454 Å [13]. The results presented show satisfactory accuracy for the quasi-classically determined boron-nitrogen binding characteristics: accuracies of quasi-classical approaches to determination of isolated B–N bond length and length of bonds in solid state structure make up a few percents, 7.2 and 5.1 %, respectively. Thus, the obtained B–N binding curve and its parameters (namely, equilibrium bond length, binding energy, and vibration frequency) would be useful for investigations of compounds containing B–N bonds and, especially, BN nanosystems.

As for the BN sheet binding and vibration energies, it is also expedient to analyze correctness of the given predictions by comparing them with data available on the cohesion characteristics of h-BN layered crystals. As follows from standard thermochemical data, the binding energy of h-BN equals to 13.0 eV / mole [46]. The binding energies of 14.5, 16.0, and 14.4 eV / mole were determined from semiempirical calculations performed using two variants of the semiempirical LCAO method and an approach based on a periodic small-sized cluster [28,29]. Within a CFF potential model, the lower semiempirical estimate of 11.5 eV / mole was obtained [13]. In the framework of DFT, optimization of the structural parameters led to the theoretical binding energy of 12.5 eV / mole [45]. Therefore, it should be expected that the molar binding energy for h-BN layered crystal lies in the range from 11.5 to 16.0 eV. The binding energy of 23.0 eV / mole found by the quasi-classical method for the isolated layer is considerably higher. However, when comparing these energies, it should be taken into account that interlayer bonds are substantially weaker than intralayer ones and that each atom in layered BN structures is involved in the formation of 5 bonds, of which only 3 are intralayer bonds. Consequently, if the interlayer energy is ignored as compared to the intralayer energy, we can assume that the molar binding energy of similar modifications is equal to 3 / 5 of the molar binding energy of the isolated layer. With use result 23.0 eV / mole for layer, we find the molar binding energy of $3/5 \times 23.0$ eV = 13.8 eV. Indeed, this energy is close to the midpoint (13.75 eV) of the aforementioned energy range. On the other hand, the vibration energies of the isolated layer and layered crystals can be directly compared because the atoms of the low-dimensional system can execute vibrations in three independent directions in physical space. Quasi-classical result of 0.242 for two-dimensional BN agrees well with analogous calculations of 0.266 [31], with the semiempirical estimate of 0.225 for zero-point vibrations energy in h-BN [13], and coincides in order of magnitude with the estimate of 0.350 eV / mole from the theoretical phonon spectrum [45].

Let take a quick look at defects in BN layer. Using methods of model PP and expanded unit cell, it was found that N-vacancies in BN sheet, as well as di- and trivacancional clusters including

neighbor defects in BN layer, are characterized by small binding energies [47]. Calculated spectra and oscillator strengths allow interpreting local bands of the optical absorption in real (pyrolitic) layered h-BN crystals before and after irradiation by fast-neutrons, protons, and C-ions. Charge contour maps of defects also were given. By first principles calculations the 20 structures $B_xC_yN_z$, derived from a hexagonal layer by placing B, N, or C atoms on each site, were considered [48] to investigate their relative stabilities. First principles simulations on the interaction of molecular hydrogen H_2 with the native and substitutional defects of single hexagonal BN sheet were performed in [49]. The adsorption of H_2 on structures found to be endothermic with respect to dissociation. In planar sheets, vacancies reduce the barriers for H_2 dissociation.

The geometries of the haeckelite BN sheets were constructed by DFT [50]. Their molar energy of cohesion is higher (by ~ 0.6 eV / mole) than for regular one.

3.3. Electronic structure

The first Brillouin zone of two-dimensional boron nitride (like its unit cell in configuration space) is hexagonal in shape (Fig. 5, (1)). There are known number of calculations performed to obtain BN sheet electronic structure. In [51] parameters of the electronic structure of two-dimensional BN were calculated in the framework of standard HF method, HF method with inclusion of the weighting function in the exchange part of the Fock matrix, and DFT. The band gap equals to 13.7 for both HF variants and 4.30 eV in the case of DFT. It was emphasized that the DFT systematically underestimates the band gap. This circumstance is most likely one of the two possible reasons for the discrepancy in results. The second reason is that the value of 13.7 eV determined by the HF methods seems to be extremely overestimated for the band gap in any BN modification. When calculating the electronic structure of two-dimensional BN by the LCAO method within the initial quasi-classical approximation [40], the piecewise constant approximations of the 2*s* and 2*p* valence orbitals of B and N atoms served as the basis set. The lattice constant was taken equal to 2.64 Å. Within the approximation under consideration, this value should correspond to the equilibrium state. The calculated densities-of-states (DOS) in the valence and conduction bands are depicted in Fig. 5, (2) with respect to the Fermi level. According to these results, two-dimensional boron nitride, like its three-dimensional crystalline modifications, is a dielectric: the band gap is determined to be 6.22 eV.

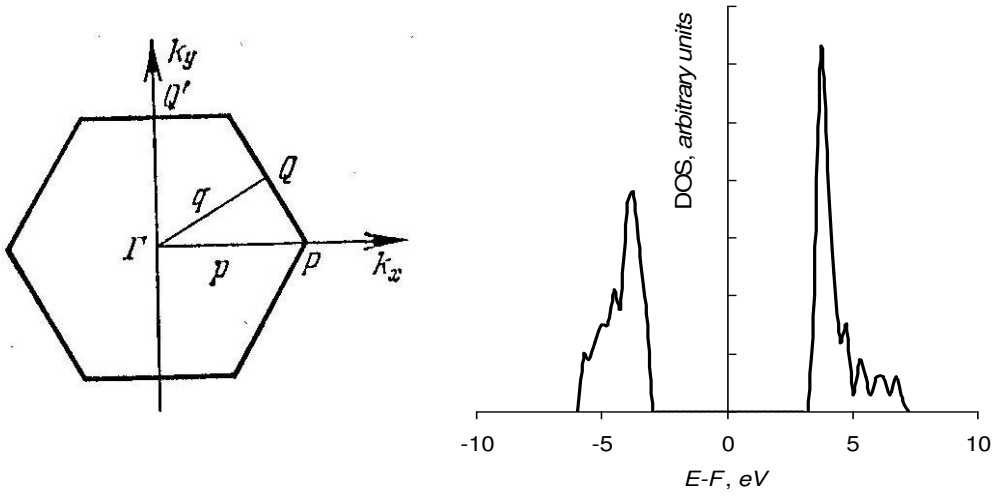

(1) **(2)**

Fig. 5. First Brillouin zone of BN sheet (1) and its quasi-classically calculated [40] DOS (2).

DOS obtained for the isolated BN layer should be compared with the corresponding data for the h-BN layered modification: the DOSs in the valence and conduction bands were calculated by

the orthogonalized-plane-wave (OPW) method [52,53], in the tight-binding approximation [54], by the full-potential linear augmented-plane-wave (APW) method [55], and in the framework of LDA with the use of orthogonalized LCAOs [44]. Moreover, the theoretical results were corrected with due regard for the experimental data on X-ray photoemission [56] and X-ray photoelectron spectroscopies [57]. In [26], the DOS for h-BN was also calculated by the quasi-classical method, but with a different from [40] parameterization scheme. A comparison of the above results suggests that, in general terms, the DOS for two-dimensional BN is similar to that for h-BN crystals. However, the data available for h-BN three-dimensional crystals do not allow to interpret specific features of the DOS for the two-dimensional BN layer or to estimate characteristic energy gaps. The calculated electronic structure of two-dimensional BN can also be compared with the electronic structure of nanotubes, which are characterized by their own specific features (see below). According to calculations, multi-walled BN nanotubes are also dielectrics [4]. For example, within the LDA their band gap was estimated at 5.5 eV. One more class of BN structures somewhat related to the isolated layer is represented by fullerene molecules B_mN_m ($m = 1,2,3,...$), which are approximately spherical in shape and are faceted by flat rings comprising B and N atoms (see below). With an increase in the number m of atoms the so-called HOMO–LUMO band gap, which is defined as the energy interval between the highest occupied MO and the lowest unoccupied MO, is stabilized at approximately 9 eV [14]. This estimate is larger than that obtained for isolated layer. However, the former band gap should be overestimated, because, when changing over to the infinite periodic structure, the HOMO and LUMO levels are split into the valence and conduction bands, respectively. Furthermore, the error introduced in such an assignment of molecular states to crystalline ones is associated with the fact that not only 6-membered atomic rings serve as faces of the B_mN_m fullerenes. Finally, it should be noted that all the above calculations of the electronic structure of h-BN, BN nanotubes, B_mN_m fullerenes, and BN sheet were performed using the intralayer bond lengths d corresponding to the real h-BN structure. This bond length is approximately 5 % shorter than the bond length obtained in two-dimensional BN by the quasi-classical method. According to the above mentioned Harrison interpolative scheme [30] for energy parameters of solids, we can assume that band gap $E_g \sim 1/d^2$. Then, substitution by the quasi-classical bond length leads to a decrease in the aforementioned estimates by ~ 10 %.

Some electronic and magnetic properties of hexagonally bonded honeycomb ribbons consisting of B and N with zigzag edges terminated by H atoms had been studied [58] using first principles total-energy electronic structure calculations within the local-spin DFT. The energy gap of BN ribbons is dominated by the edge states and it decreases monotonically with increasing ribbon width.

Using methods of model PP and expanded unit cell, it was calculated deep electron levels series for N-vacancies, and small di- and trivacancional clusters including neighbor defects in BN layer [47]. Calculated spectra allow interpreting luminescence and photoconductivity in real (pyrolitic) layered h-BN crystals before and after irradiation by fast-neutrons, protons, and C-ions. The magnetic properties of vacancies in a BN sheet were calculated in [59]. Applying a full spin-polarized description to the system, it was demonstrated that both B vacancy (V_B) and N vacancy (V_N) can induce spontaneous magnetization. Using first principles calculations the 20 structures $B_xC_yN_z$ derived from a hexagonal layer by placing B, N, or C atoms on each site were considered [48] to investigate their electronic structures. In general, structures with large values of the band gap were observed to have a B / N (i.e. x/z) ratio of ~ 1. In [60] it was performed first principles calculations to investigate the possible magnetism induced by different concentrations of nonmagnetic impurities and vacancies in a BN sheet. Atoms of Be, B, C, N, O, Al, and Si were used to replace either B or N. The changes in the DOS as well as the extent of the spatial distribution of the defect states, the possible formation of magnetic moments, the magnitude of the magnetization energies, and the exchange energies were discussed. It was shown that the

magnetization energy tends to increase as the concentration of the defects decreases in most of the defect systems, which implies a definite preference for finite magnetic moments.

The electronic properties of the haeckelite BN sheets were considered by DFT [50]. They are dielectrics with band gaps less than that for hexagonal sheet. The DOSs were given for various plane structures including hexagonal sheet.

4. BORON NITRIDE NANOTUBES

4.1. Synthesizing

For the first time, the arc-discharge methods were used to produce $B_xC_yN_z$ nanotubular structures [3] identified by the high-resolution transmission-electron-microscopy (TEM) together with *K*-edge electron-energy-loss-spectrometry (EELS) determining the local atomic composition. Multi-walled pure BN tubes with inner diameters on the order of 1 to 3 nm and with lengths up to 200 nm were produced [4] in a carbon-free plasma discharge between a BN-packed W-rod and a cooled Cu-electrode. EELS of individual tubes yielded B / N ratio of approximately 1. At present time various methods of synthesis of the BN nanotubular structures are developed.

The arc discharge under the atmosphere of molecular nitrogen N_2 between electrodes from graphite and refractory boron compounds, for example, from hafnium diboride HfB_2 forms BN–C nanotubes with strong phase separation between BN and C layers along the radial direction [61,62]. If both of electrodes are made from HfB_2 rods, there are formed single- or double-walled chemically pure BN nanotubes with the structure close to stoichiometric B / N ~ 1 [63]. Most obtained tube ends are closed by flat layers perpendicular to the tube axis. A closure by a triangular facet, resulting from three 120°-disclinations was proposed to account for this specific shape. In a greater part, the multi-walled BN nanotubes are formed at use as electrodes zirconium diboride ZrB_2 [64,65]. In this case, most of the nanotube had diameters from 3 to 40 nm and lengths on the order of 100 nm. Single-layer tubes with diameters of 2 to 5 nm were also formed as a minority. The morphology of the tube tips suggests the presence of pentagons and heptagons, which are energetically less favorable compared with squares.

A laser melting of the solid-state boron nitride (of any crystal structure, not only layered, but also amorphous) at high nitrogen pressure, (5 – 15) GPa, forms nanotubes free from inclusions, containing from 3 up to 8 walls, and having a characteristic outer diameter of (3 – 15) nm [66]. BN nanotubes have been also obtained by pyrolysis of the molecular precursor at use of Co catalysts [67]. Bundles of single-walled (or containing few layers) BN nanotubes of almost stoichiometric structure can be formed in substitution reactions – by thermal treatment of a mixture of boron trioxide or trichloride and bundles of single-walled C-nanotubes at high-temperatures, (1250 – 1350) °C, in a nitrogen flow [68,69]. BN nanotubes also grow in solid-state process that involves neither deposition from the vapor phase nor chemical reactions [70]. The nanotubes were produced by first ball-milling layered h-BN powder to generate highly disordered or amorphous nanostructures and followed by annealing at temperatures up to 1300 °C. The annealing leads to the nucleation and growth of hexagonal BN nanotubes both of cylindrical and bamboo-like morphologies. Multi-walled BN nanotubes have been obtained by carbothermal reduction of the ultra-dispersive amorphous boron oxide B_2O_3 at simultaneous nitriding at the high temperatures, (1100 – 1450) °C [71,72]. For large tubes it was found dependence of the factor of form on radius. Besides of arc-melting, pyrolysis, and chemical reactions, boron nitride nanotubular structures were created by means of ballistic nuclear displacements caused in h-BN layered crystal structure by an electron irradiation in TEM [73,74].

High growth temperatures (above 1100 °C), a low production yield, and impurities have prevented progress in applications of BN nanotubes in the past decade. Relatively recently, it was

shown that these tubes can be grown on substrates at lower temperatures (of about 600 °C) [75]. It was constructed high-order tubular structures, which can be used without further purification.

Boron nitride fiber-like clusters and nanotubes were synthesized by evaporation of the layered BN under the nitrogen atmosphere [76]. Their diameters and lengths equal to (0.05 – 200) and (100 – 3000) μm, respectively. Applying TEM, there were obtained their associations in tree- and coral-like aggregates.

4.2. Structure

Elementary form for BN nanotube is a wrapped closed hexagonal surface inscribed in the cylinder. Such BN nanotubes (Fig. 6, (1-3)) can be found in regular, i.e. zigzag (n,0) or armchair (n,n), and also in chiral (n,m) forms. Here n and m are the tube indexes. Their symmetry operators have been identified in [77]: each type belongs to different family of the non-symmorphic rod groups; armchair tubes with even n are found to be centrosymmetric. The types and structures of the non-carbon, in particular, BN nanotubes were overviewed in [78]. Besides, the deformed regular or haeckelite nanotubes can exist (Fig. 6, (4-5)). Concerning the haeckelite structures of BN tubes, a variety of chiral angles, including zigzag and armchair types, were observed. Depending on the structure formation kinetics characteristic for given technology, BN nanotubes quite often take the bamboo-like morphology, forms of a nanoarch (i.e. half-tube at the ends closed by planes) etc. Real nanotubular structures are not infinite in length: they are definitely truncated.

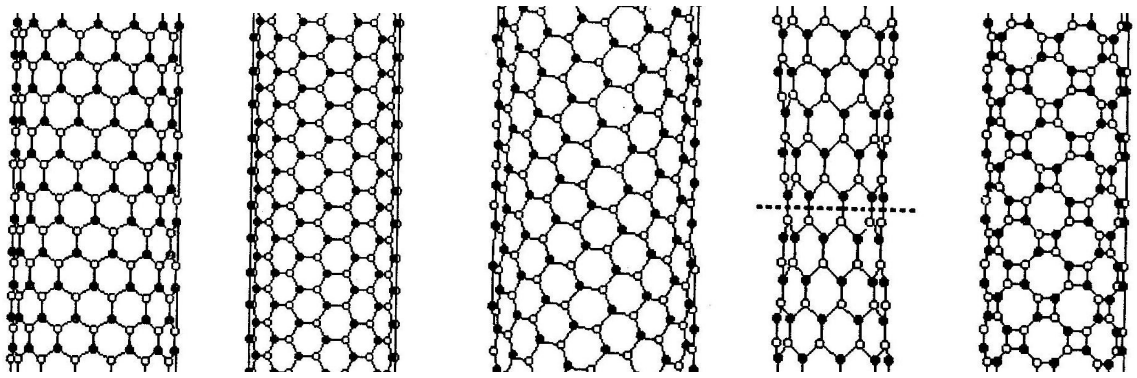

Fig. 6. Zigzag (1), armchair (2), chiral (3), and deformed (stretched) (4) hexagonal, and haeckelite (5) BN nanotubes.

The three main different possible morphologies of the cylindrical tube closing with flat [65] (Fig. 7, (1)), conical, and amorphous ends, as observed in experiments, were shown [79] to be directly related to the tube chirality. There are also possible rectangular BN nanotubes with linear defects on edges and with tips in the form of triangular flags [65] (Fig. 7, (2)). Such kind morphologies suggest presence of the energetically unfavorable odd-membered atomic rings (i.e. pentagons and heptagons) in addition to favorable even-membered rings (e.g. squares).

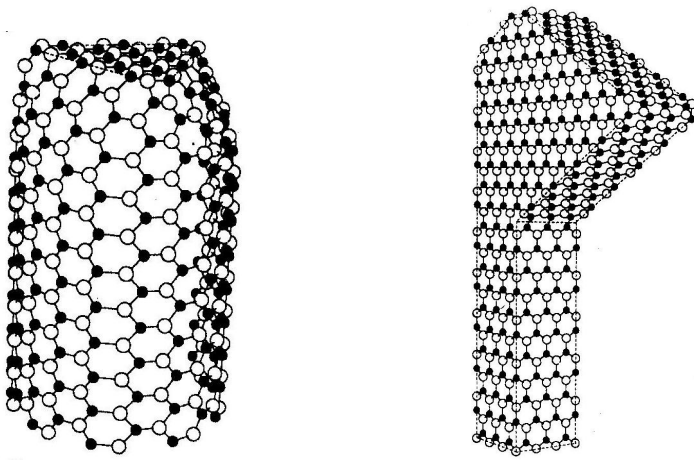

(**1**) (**2**)

Fig. 7. BN cylindrical nanotube with flat end [65] (1) and rectangular nanotube with tip in form of truncated flag [65] (2).

As the growth of BN nanotubes cannot be directly observed and, consequently, the underlying microscopic mechanism is a controversial subject, in [80] it was performed first principles molecular dynamical (MD) simulation of the single-walled nanotube edges. The behavior of growing BN nanotubes was found to be strongly depending on the nanotube network chirality. In particular, open-ended zigzag tubes close rapidly into an amorphous tip, preventing further growth. In the case of armchair tubes, the formation of squares traps the tip into a flat cap presenting a large central even-membered ring. This structure is metastable and able to revert to a growing hexagonal framework by incorporation of incoming atoms. These findings are directly related to frustration effects, namely that B–N bonds are energetically favored over B–B and N–N bonds.

For purposeful designing devices based on nanotubular BN it is important to be able to predict reliably the sizes of the nanotubes with given indexes. This task was solved for the most stable forms. Namely, the expressions of radiuses and lengths of the zigzag and armchair BN nanotubes in terms of B–N bond length were obtained. The formulas determining (*n*,0) and (*n*,*n*) BN nanotubes radii $R_{(n,0)}$ and $R_{(n,n)}$, and lengths $L_{(n,0)}$ and $L_{(n,n)}$, have been derived in [81]:

$$R_{(n,0)} = \frac{a}{4\sin\pi/2n},$$

$$R_{(n,n)} = \frac{\sqrt{5+4\cos\pi/2n}\ a}{4\sqrt{3}\sin\pi/2n},$$

$$L_{(n,0)} = \sqrt{3}ka,$$

$$L_{(n,n)} = ka.$$

Here parameter a corresponds to lattice constant of the boron nitride layered crystals, i.e. intralayer B–B or N–N bonds lengths. Therefore, B–N bond length d equals to $a/\sqrt{3}$. Nanotube index $n = 1,2,3,...$ determines the number of atoms as nanotube unit cell consists of $2n$ formula units BN; and $k = 1,2,3,...$ is the number of unit cells in a finite-length nanotube. On basis of this, sizes of the small single-walled BN nanotubes (1,0), (1,1), (2,0), (3,0), …, (17,0), (10,10) were estimated and also their most stable aggregates in form of double-walled nanotubes predicted (assuming $d = 1.4457$ Å what is the experimental value of the B–N bond length in h-BN layers): (1,0)@(9,0), (1,0)@(10,0), (1,1)@(10,0), (1,1)@(6,6), …, (8,0)@(17,0), (5,5)@(17,0), (5,5)@(10,10). Therefore, the estimations of radii of the single-walled BN nanotubes, from its part, can be used for a prediction of their most probable combinations in multi-walled structures. At the

analysis of the given problem, it is necessary to take into account that basically it is a question of the average radii, as the detailed research [79] performed by a generalized tight-binding MD method revealed that dynamic relaxation (similar the reconstruction at atomically clean surfaces of III-V crystalline semiconductors) results in a wave-like or "rippled" surface, in which B atoms rotate inward and N atoms more outward. But, a general feature of BN nanotubular systems is that the stronger surface potentials are associated with regions of higher curvature [82]. Thus, interlayer interaction in BN nanotubes differs from bonding in three-dimensional layered crystals. However, most likely, the distinctions are weak enough to change essentially the equilibrium interlayer distances, which are observed in h-BN and r-BN crystals. Given conclusion is also argued by the results of an experimental study of the multi-walled nanotubes applying high-resolution electronic microscopy [83]. In these structures, like the three-dimensional layered BN crystals, hexagonal and rhombohedral stacking sequences in nanotube wall-assembly can freely coexist. There are also possible some different cross-section flattening, as well as ordering of layers in non-spiral zigzag. According to first principles total-energy calculations [84], the most favorable double-walled BN nanotubes are structures in which the interwall distances are about 3 Å, i.e. as interlayer distances in layered BN crystals. So, because of weakness of the interlayer van der Waals forces various types of multi-walled BN nanotubes can exist. From here follows, that there is more probable formation of such multi-walled boron nitride nanotubes in which adjoin regular tubes with difference in radii close to interlayer distance in layered boron h-BN crystal, i.e. to half of height of the hexagonal unit cell $c \approx 6.6612$ Å [85]. Thus, the type of next nanotube has no crucial importance.

In view of these factors, from above calculated single-walled nanotubes it had been chosen the listed pairs most suitable for formation of the stable double-walled BN nanotubes. Remaining small divergences in sizes of the neighboring regular nanotubes can be compensated by defects and small chiral distortions. Such transformations of the zigzag and armchair nanotubes into chiral one will be accompanied, respectively, by increase and decrease in their radii. Hence, if the difference in radii between regular nanotubes is more (less) than $c/2$, the realization of structure in which the internal wall will be zigzag (armchair) and external – armchair (zigzag) is more probable. Based on estimations of sizes of the single-walled BN nanotubes, it is possible to predict successfully the most stable double-walled forms. But, how it will be solved the same problem for multi-walled nanotubes? Let shortly stop on the given problem. In this case, all over, it will be necessary to calculate radii of nanotubes with high indexes to choose sequences of single-walled nanotubes, whose radii are close to terms of arithmetical progression with arithmetic ratio of $c/2$. However, now only geometrical consideration will be insufficient. The matter is that unlike double-walled nanotubes in multi-walled ones there are also medial layers. For this reason, the choice of the most stable structure should be made on the basis of comparison of reduction in energy caused by deviation from the equilibrium interlayer distance with its gain caused by the chiral distortions.

Finally, about the detailed regular geometries of the zigzag and armchair BN nanotubes described in [86] using cylindrical coordinates (ρ, φ, z), which are useful in electronic calculations.

Unit cell of the zigzag $(n,0)$-nanotubes consists of 4 atomic rings in parallel planes perpendicular to the axis. There are 2 pairs of rings and each consists of 2 planes with n boron or n nitrogen atoms. Evidently, cylindrical coordinate ρ for all atomic sites equals to tube radius:

$$\rho_{\mathrm{B}} = \rho_{\mathrm{N}} = R_{(n,0)}.$$

As for the coordinates φ and z in the first and second pairs of atomic rings, they equal to

$$\varphi_{\mathrm{B}} = \varphi_{\mathrm{N}} = 2l\pi / n,$$

$$z_{\mathrm{B}} = (6m+1)a / 2\sqrt{3},$$

$$z_{\mathrm{N}} = (6m-1)a / 2\sqrt{3},$$

and

$$\varphi_{\mathrm{B}} = \varphi_{\mathrm{N}} = (2l+1)\pi / n,$$

$$z_{\mathrm{B}} = (3m-1)a/\sqrt{3},$$
$$z_{\mathrm{N}} = (3m+1)a/\sqrt{3},$$

respectively. Here $l = 0,1,2,...,n-1$ and $m = 0,\pm1,\pm2,...$ number atomic pairs in given pair of the atomic rings and these rings themselves, respectively. Unit cell of the armchair (*n*,*n*)-nanotubes consists of 2 atomic rings in parallel planes perpendicular to the tube axis. From its part, each ring consists of n boron and n nitrogen atoms. Coordinate ρ for all atomic sites equals to tube radius:

$$\rho_{\mathrm{B}} = \rho_{\mathrm{N}} = R_{(n,n)},$$

while the rest cylindrical coordinates in the first and second atomic rings equal to

$$\varphi_{\mathrm{B}} = \varphi_1 + 2l\pi/n,$$
$$\varphi_{\mathrm{N}} = -\varphi_1 + 2l\pi/n,$$
$$z_{\mathrm{B}} = z_{\mathrm{N}} = ma,$$

and

$$\varphi_{\mathrm{B}} = -\varphi_1 - 2\varphi_2 + 2l\pi/n,$$
$$\varphi_{\mathrm{N}} = \varphi_1 + 2\varphi_2 + 2l\pi/n,$$
$$z_{\mathrm{B}} = z_{\mathrm{N}} = (2m+1)a/2,$$

respectively. Here

$$\sin\varphi_1 = \frac{2\sin\pi/2n}{\sqrt{5+4\cos\pi/2n}},$$
$$\sin\varphi_2 = \frac{\sin\pi/2n}{\sqrt{5+4\cos\pi/2n}},$$

and $l = 0,1,2,...,n-1$ and $m = 0,\pm1,\pm2,...$ number B or N atoms in atomic rings and these rings themselves. On the basis of this, it was found the distances between given atomic site and sites in so-called central atomic pairs in zigzag ($l = m = 0:\ \varphi_{\mathrm{B}} = \varphi_{\mathrm{N}} = 0$, $z = a/2\sqrt{3}$, and $z = -a/2\sqrt{3}$),

$$\frac{({}^{lm}_{(n,0)}\mathrm{B1} - {}^{00}_{(n,0)}\mathrm{B1})^2}{a^2} = \frac{\sin^2 l\pi/n}{4\sin^2\pi/2n} + 3m^2,$$
$$\frac{({}^{lm}_{(n,0)}\mathrm{B2} - {}^{00}_{(n,0)}\mathrm{B1})^2}{a^2} = \frac{\sin^2(2l+1)\pi/2n}{4\sin^2\pi/2n} + \frac{3(2m-1)^2}{4},$$
$$\frac{({}^{lm}_{(n,0)}\mathrm{N1} - {}^{00}_{(n,0)}\mathrm{B1})^2}{a^2} = \frac{\sin^2 l\pi/n}{4\sin^2\pi/2n} + \frac{(3m-1)^2}{3},$$
$$\frac{({}^{lm}_{(n,0)}\mathrm{N2} - {}^{00}_{(n,0)}\mathrm{B1})^2}{a^2} = \frac{\sin^2(2l+1)\pi/2n}{4\sin^2\pi/2n} + \frac{(6m+1)^2}{12},$$
$$\frac{({}^{lm}_{(n,0)}\mathrm{B1} - {}^{00}_{(n,0)}\mathrm{N1})^2}{a^2} = \frac{\sin^2 l\pi/n}{4\sin^2\pi/2n} + \frac{(3m+1)^2}{3},$$
$$\frac{({}^{lm}_{(n,0)}\mathrm{B2} - {}^{00}_{(n,0)}\mathrm{N1})^2}{a^2} = \frac{\sin^2(2l+1)\pi/2n}{4\sin^2\pi/2n} + \frac{(6m-1)^2}{12},$$
$$\frac{({}^{lm}_{(n,0)}\mathrm{N1} - {}^{00}_{(n,0)}\mathrm{N1})^2}{a^2} = \frac{\sin^2 l\pi/n}{4\sin^2\pi/2n} + 3m^2,$$
$$\frac{({}^{lm}_{(n,0)}\mathrm{N2} - {}^{00}_{(n,0)}\mathrm{N1})^2}{a^2} = \frac{\sin^2(2l+1)\pi/2n}{4\sin^2\pi/2n} + \frac{3(2m+1)^2}{4};$$

and armchair ($l = m = 0:\varphi_{\mathrm{B}} = \varphi_1, \varphi_{\mathrm{N}} = -\varphi_1$, and $z_{\mathrm{B}} = z_{\mathrm{N}} = 0$) tubes,

$$\frac{(\,{}^{lm}_{(n,n)}\mathrm{B1}-{}^{00}_{(n,n)}\mathrm{B1})^2}{a^2}=\frac{(5+4\cos\pi/2n)\sin^2 l\pi/n}{12\sin^2\pi/2n}+m^2,$$

$$\frac{(\,{}^{lm}_{(n,n)}\mathrm{B2}-{}^{00}_{(n,n)}\mathrm{B1})^2}{a^2}=\frac{(5+4\cos\pi/2n)\sin^2(2l-1)\pi/2n}{12\sin^2\pi/2n}+\frac{(2m+1)^2}{4},$$

$$\frac{(\,{}^{lm}_{(n,n)}\mathrm{N1}-{}^{00}_{(n,n)}\mathrm{B1})^2}{a^2}=\frac{(2\sin(2l-1)\pi/2n+\sin l\pi/n)^2}{12\sin^2\pi/2n}+m^2,$$

$$\frac{(\,{}^{lm}_{(n,n)}\mathrm{N2}-{}^{00}_{(n,n)}\mathrm{B1})^2}{a^2}=\frac{(\sin(2l+1)\pi/2n+2\sin l\pi/n)^2}{12\sin^2\pi/2n}+\frac{(2m+1)^2}{4},$$

$$\frac{(\,{}^{lm}_{(n,n)}\mathrm{B1}-{}^{00}_{(n,n)}\mathrm{N1})^2}{a^2}=\frac{(2\sin(2l+1)\pi/2n+\sin l\pi/n)^2}{12\sin^2\pi/2n}+m^2,$$

$$\frac{(\,{}^{lm}_{(n,n)}\mathrm{B2}-{}^{00}_{(n,n)}\mathrm{N1})^2}{a^2}=\frac{(\sin(2l-1)\pi/2n+2\sin l\pi/n)^2}{12\sin^2\pi/2n}+\frac{(2m+1)^2}{4},$$

$$\frac{(\,{}^{lm}_{(n,n)}\mathrm{N1}-{}^{00}_{(n,n)}\mathrm{N1})^2}{a^2}=\frac{(5+4\cos\pi/2n)\sin^2 l\pi/n}{12\sin^2\pi/2n}+m^2,$$

$$\frac{(\,{}^{lm}_{(n,n)}\mathrm{N2}-{}^{00}_{(n,n)}\mathrm{N1})^2}{a^2}=\frac{(5+4\cos\pi/2n)\sin^2(2l+1)\pi/2n}{12\sin^2\pi/2n}+\frac{(2m+1)^2}{4}.$$

4.3. Binding

We can specify some theoretical results on binding properties and stabilities of BN nanotubes. Stabilities of the boron nitride nanotubular structures were studied by means of non-orthogonal tight-binding formalism [87]. The radii and energies of the BN nanotubes also were estimated [14] by MD simulation within the embedded atom model in which parameter d took the experimental value 1.4457 Å of the intralayer B–N bond length in real h-BN crystals. In [38] binding energy of the regular BN nanotubes had been calculated within frames of DFT in generalized gradient approximation (GGA). By search of equilibrium values of B–N bond length and radii, the geometry of the tubular supercell consisting of 32 atoms was optimized. For (8,0), (10,0) and (4,4) tubes, it has been found $d \approx 1.46$ Å, and for (5,5) tube, $d \approx 1.45$ Å. Within frames of semiempirical MNDO calculations of the nanotubular piezoelectric characteristics [88], their radii also were determined. In this case energies in dependence on bond length were calculated for the molecular fragments containing 3 or 4 elementary layers. Most likely, in this work for d the empirical value known for h-BN crystals was fixed as equilibrium value too.

The deal of ionicity of binding in boron nitride structures is important in explaining the electronic differences between BN tubes and similar C tubes [1]. To help understand and predict nanotube interactions in multi-walled structure the electrostatic potentials on both outer and inner surfaces of some single-walled BN nanotubes had been calculated at a HF Slater-type-orbital level [82]. Structures were optimized computationally. Fictitious hydrogen atoms were introduced at the ends of the open tubes, to satisfy the unfulfilled valences. It was found that BN tubes have stronger and more variable surface potentials than graphitic ones. There are characteristic patterns of positive and negative sites on the outer lateral surfaces, while the inner ones are markedly positive.

The binding and vibrations in small-radius single-walled BN nanotubes in [89] were studied by DFT using LDA. The results show that the chirality preference observed in experiments may be explained from the relative stability of the corresponding BN strips: the zigzag strips have larger binding energies and thus may be more easily formed. The smallest stable BN nanotube is found to

be the (5,0) zigzag nanotube. Dependence of the tube deformation energy on its radius R was approximated by the formula ΔE [eV / mole] = 5.82 / (R [Å]) $^{2.09}$. The phonon dispersions of BN nanotubes were calculated and the frequency of the radial breathing mode is found to be inversely proportional to the nanotube radius. The geometries of the BN nanotubes were also constructed in DFT [50]. Molar energy of cohesion is higher (by ~ 0.6 eV / mole) then for sheet. It was found similar relation for deformation energy dependence on tube radius $\sim C / R^{\alpha}$ with different C and $\alpha \approx 2$ for different structures.

Using the symmetry properties in [77] it was determined the numbers of Raman- and IR-active vibrations in single-walled BN nanotubes. In contrast to the regular carbon nanotubes, zigzag boron nitride tubes possess almost twice vibrations as armchair ones. An extensive first principles study of the phonons in BN nanotubes using perturbation DFT in the LDA was performed in [90]: based on the non-symmorphic rod group symmetry of the tubes, the Raman- and IR-active modes at the point of the one-dimensional Brillouin zone were evaluated. For zigzag and chiral nanotubes, the set of IR-active modes is a subset of the Raman-active modes. In particular, the radial breathing mode is not only Raman-, but also IR-active. However, for armchair tubes, the sets of IR- and Raman-active modes are disjoint. The frequencies of the active modes of zigzag, chiral, and armchair tubes were presented as a function of the tube diameter and compared with the frequencies obtained by the zone-folding method (i.e. by rolling of a BN sheet into a tube). Except for the high-frequency tangential modes, the zone-folding results are in very good agreement with the first principles calculations. The radial breathing mode frequency can be derived by folding a sheet of finite width. Finally, the effects of bundling on the phonon frequencies are shown to be small. First principles calculations of the nonresonant Raman spectra of zigzag and armchair BN nanotubes were presented in [91]. In comparison, a generalized bond-polarizability model, where the parameters are extracted from first principles calculations of the polarizability tensor of a BN sheet, was implemented. For light polarization along the tube axis, the agreement between model and first principles spectra is almost perfect, but for perpendicular polarization, depolarization effects have to be included in the model in order to reproduce Raman intensities.

Based on the analytically described nanotubular geometries, binding energies (including both electrostatic and zero-point vibration terms) per mole of the ultra-small-radius BN nanotubes (1,0), (1,1), (2,0), (3,0), (2,2), (4,0), (5,0), and (3,3) were calculated within the quasi-classical approach [86]. It was found out the molar binding energy oscillatory-dependence on the tube radius (Fig. 8). According to obtained values, the formation probabilities for BN tubes with indexes (5,0) and (3,3) and higher are almost same that for the layered BN crystals. Ultra-small-radius BN nanotubes (1,1), (2,0), (2,2), and (4,0) seem to be a metastable as their molar binding energies are positive, but less than that for layered BN crystals, while smallest (1,0) tube structure degenerated in zigzag atomic strip should be instable (with negative binding energy). Exception is the (3,0) tube, formation of which was predicted energetically preferable than layered crystal growth.

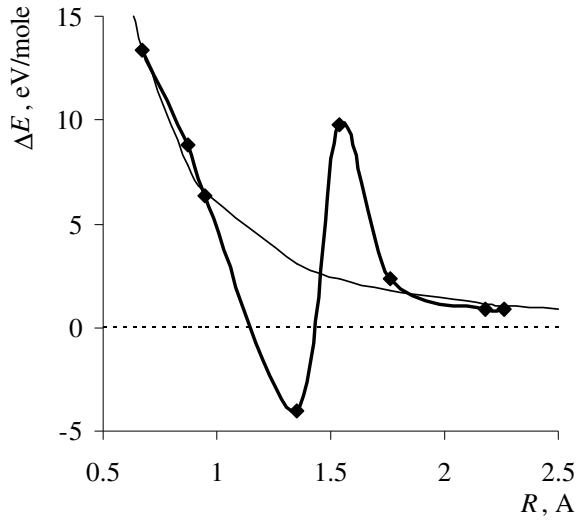

Fig. 8. Energy difference between infinite- (dashed line) and ultra-small-radius BN nanotubes calculated by quasi-classical method [86] (heavy solid line) and by the extrapolating formula [89] (regular solid line).

The possible dislocation dipoles as defect nuclei under tension in BN nanotubes were identified by dislocation theory and MD simulations [92]. Formation energies of the dipoles evaluated by gradient-corrected DFT are high and remain positive at large strains, thus suggesting great yield resistance of BN nanotubes. The dipole appears to be more favorable in spite of its homoelemental B–B and N–N bonds. The resonant photoabsorption and vibration spectroscopy combined with scanning tunneling microscopy unambiguously identify the presence of Stone–Wales defects in BN nanotubes [93]. Based on extensive time-dependent DFT calculations, it was proposed to resonantly photoexcite such defects in the IR and UV regimes as a means of their identification. Intrinsic defects in zigzag BN nanotubes, including single vacancy, divacancy, and Stone–Wales defects, were systematically investigated using DFT calculation in [94]. It was found that the structural configurations and formation energies of the topological defects are dependent on tube diameter. The results demonstrate that such properties are originated from the strong curvature effect in BN nanotubes. The scanning tunneling microscope images of intrinsic defects in the BN nanotubes also were predicted. The defected BN tubes with C-substitutions were considered in [88].

Based on DFT calculations [38], it was found that energies of haeckelite BN nanotubes exceed by ~ 0.6 eV / mole that for corresponding hexagonal nanotubes. They are less stable in comparison with corresponding haeckelite sheets as well, but they are stable and can be synthesized. Energy of deformation (i.e. energy needed to wrap nanotube from its sheet prototype) for large haeckelite BN tubes extrapolated by the formula $\sim 1/R^2$ where R is the tube radius.

The theoretical studies carried out using a total-energy non-orthogonal tight-binding parameterization on the elastic properties of single-walled BN nanotubes were reported in [95]. It was considered tubes of different diameters, ranging from 0.5 to 2 nm, and found that in the limit of large diameters the mechanical properties of nanotubes approach those of the graphite-like sheet. The stiffness and plasticity of BN nanotubes was investigated [96] using generalized tight-binding MD and first principles total-energy methods. Due to B–N bond rotation effect, the compressed zigzag nanotubes were found to undergo anisotropic strain release followed by anisotropic plastic buckling. The strain is preferentially released toward N atoms in the rotated B–N bonds. The tubes buckle anisotropically toward only one end when uniaxially compressed from both. Based on these results, a skin-effect-model of smart nanocomposite materials is proposed, which localizes the structural damage toward the surface side of the material. B–N bond-rotation mode of plastic yield in BN nanotubes in [97] was investigated combining first principles computations with a probabilistic rate approach to predict the kinetic and thermodynamic strength. BN nanotubes yield

defects have low activation, but high formation energies. Elastic characteristics of BN nanotubes in [88] also were calculated applying MNDO method.

4.4. Electronic structure

Tunneling spectroscopy indicates that band gap of BN nanotubes grown on substrates ranges from 4.4 to 4.9 eV [75]. The photoluminescence decay process in multi-walled BN nanotubes is characterized by 2 time-constants that are attributed to intra- and interwall charge recombination, respectively [98]. A comparison of the photoluminescence of BN nanotubes to that of h-BN is consistent with the existence of a spatially indirect band gap in multi-walled BN. Optical absorption spectra of small-radius single-walled BN nanotubes obtained by first principles calculations in the framework of time-dependent DFT were presented in [99]. They were compared with those obtained for the BN layered structures and hexagonal sheet focusing on the role of depolarization effects, anisotropies, and interactions in the excited states. The main features of the spectra are reproduced well by the random phase approximation, when crystal local field effects are correctly included. Results are relevant for the interpretation of experimental data obtained for nanotube characterization, such as optical and fluorescence spectroscopes.

A systematic first principles study of the optical and electronic properties of BN nanotubes within DFT in the LDA was performed in [100]. Specifically, the optical dielectric function and the band structure of the single-walled zigzag (5,0), (6,0), (9,0), (12,0), (15,0), (20,0), and (27,0); armchair (3,3), (4,4), (6,6), (8,8), (12,12), and (15,15); and chiral (4,2), (6,4), (8,4), and (10,5); as well as the double-walled zigzag (12,0)@(20,0) nanotubes were calculated. The underlying atomic structure of the BN nanotubes was determined theoretically. It was found that though the band gap of all the single-walled nanotubes with a diameter larger than ~ 15 Å is independent of diameter and chirality, the band gap of the zigzag nanotubes with smaller diameters decreases strongly as the tube diameters decrease and that of the armchair nanotubes has only a weak diameter dependence, while the band gap of the chiral nanotubes falls in between. It was also found that for the electric field parallel to the tube axis, the absorptive part of the dielectric function for all nanotubes except a few with very small diameters, is very similar to that of bulk layered h-BN with the electric field parallel to the layers. In other words, in the low-energy region, (4 – 9) eV, the absorptive part consists of a single distinct peak at ~ 5.5 eV, and in the high-energy region, (9 – 25) eV, it exhibits a broad peak centered near 14.0 eV. For the electric field perpendicular to the tube axis, the absorptive part of spectrum of all the nanotubes (again except the ultra-small-diameter nanotubes) in the low-energy region also consists of a pronounced peak at ~ 6.0 eV, while in the high-energy region it is roughly made up of a broad hump starting from 10.0 eV. The magnitude of the peaks is in general less than half of the magnitude of the corresponding ones for electric field parallel to the tube axis, showing a moderate optical anisotropy in the nanotubes that is smaller than in h-BN. Interestingly, the static dielectric constant for all the nanotubes is almost independent of diameter and chirality. For both electric-field polarizations, the static polarizability is roughly proportional to the tube diameter, suggesting that the valence electrons on the BN nanotubes are tightly bound. The calculated EELS of all nanotubes studied for both electric field polarizations were similar to those of h-BN, being dominated by a broad $\pi+\sigma$-electron plasmon peak at ~ 26 eV and a small π-electron plasmon peak at ~ 7 eV. Interwall interaction was found to reduce the band gap slightly and to have only minor effects on the dielectric functions and EELS. The calculated dielectric functions and EELS were found to be in reasonable agreement with the available experimental data. A systematic study of the second-order nonlinear optical properties of BN nanotubes within DFT in LDA had been performed in [101] (see also [102]) using highly accurate full-potential projector APW method. Specifically, the second-harmonic generation and linear electro-optical coefficients of a large number of the single-walled zigzag, armchair, and chiral BN nanotubes as well as the double-walled zigzag (12,0)@(20,0) nanotube and the single-walled zigzag (12,0) bundle had been calculated. Though

the interwall interaction in the double-walled BN nanotubes was found to reduce the second-order nonlinear optical coefficients significantly, the interwall interaction in the single-walled tube bundle has essentially no effect on the nonlinear optical properties. The prominent features in the spectra of BN nanotubes were correlated with the features in the linear optical dielectric function in terms of single-photon and two-photon resonances.

The EPR and ^{11}B NMR studies of multi-walled BN nanotubes were reported in [103]. EPR and x-ray photoelectron spectra are comparable to those of powder BN, while the quadruple coupling constant and asymmetry parameter determined from the NMR are close of these parameters in bulk h-BN. The spectra correspond to the axial symmetry of the boron site. The data obtained reflect a very similar local symmetry of the B-site and charge distribution over the B–N bond in nanotubes and bulk boron nitride. These facts explain why BN nanotubes hold the electronic properties of the bulk compound.

At the first time, a simple Slater-Koster tight-binding scheme had been applied to calculate BN nanotubes electronic strictures [1]. All examined nanotubes were found to be semiconductors: the band gaps were larger than 2 eV for most tubes. Depending on the chirality, the calculated band gap can be direct or indirect. In general, the larger radius corresponds to the larger band gap, with a saturation value corresponding to the band gap of h-BN. Within the special semiempirical approach [104] pure BN nanotubes were shown to present a very stable quasiparticle with band gap around $(5.5 - 6.0)$ eV, nearly independent of the tube radius and chirality. The electronic properties of small-radius single-walled BN nanotubes were studied using DFT method with the LDA [89]. The energy gap of small zigzag BN nanotubes was showed decreasing rapidly with the decrease of radius. The electronic properties of the BN nanotubes also were constructed in DFT [50]. They are dielectrics with band gaps of $(3.2 - 4.2)$ eV that is less than for hexagonal sheet. Within DFT employing self-interaction-corrected PPs in [105] it was investigated dependence of electronic structure on BN nanotube diameter and compound ionicity. The calculated band gap energies of zigzag tubes vary much stronger for small and medium diameters than those of their armchair counterparts showing a significant narrowing of the band gaps. The collective π-electronic excitations in individual BN single-walled nanotubes with a zigzag wrapping were investigated in [106], treating the dynamic dielectric response within a SCF approach and using the one-electron states derived from a simple two-band tight-binding model. Explicit analytic expressions for the real and imaginary parts of the frequency- and wave-number-dependent dielectric function of the system were obtained, whereby the EELS-function can easily be calculated. In good agreement with the experiment, each tube was found to support only one branch of the wave-number-dispersed collective π-plasmon mode for each transferred quantum angular momentum. Band-gap modification by radial deformation in BN nanotubes through first principles PP DFT calculations was investigated in [107]. In zigzag BN nanotubes, radial deformations that give rise to transverse pressures of about 10 GPa decrease the gap from 5 to 2 eV. The band gap of armchair nanotube was found to be insensitive to radial deformations. This different behavior between zigzag and armchair nanotubes was attributed to the different characteristics of states near the gap.

First principles calculations providing by the electronic structures of double-walled BN nanotubes had been performed in [84]. The electronic energy bands around the Fermi energy found to be depend interestingly on the tube radii due to the hybridization between σ- and π-states. The nearly-free-electron-states of the nanotubes can induce peculiar charge redistribution in the interwall region. According to available calculations, multi-walled BN nanotubes also are dielectrics [4]. Within LDA their band gap was estimated at 5.5 eV. It was noted that it only slightly depends on the tube radius, chirality, and number of layers. DFT calculations [38] showed that haeckelite BN nanotubes are dielectrics with gap in range of $(3.24 - 4.09)$ eV. Band gap depends on tube radius tending (reducing) to that for corresponding haeckelite sheet as radius increases.

Modeling of the electronic structure of $B_xN_xC_y$ nanotubes ($x, y > 0$) with various atom dispositions in the hexagonal lattice points on cylinder surfaces had been fulfilled in [108].

Electronic spectra of such systems with a quasi-one-dimensional superlattice had been investigated in the topological and valence approximations supposing that such mixed nanotubes consist of alternating C and BN ring-like or chain-like structures. These systems with different extent of minizones in the electronic spectrum can be produced by means of a change of belt-like fragment width. Quasi-localized nanotubular states were found out too. In [109] the C-substitutionals, antisites, and vacancy defects in BN nanotubes had been investigated by first principles total-energy calculations based on a DFT spin-polarized method. All these defects introduce localized energy levels inside the band gap. For some open-shell systems, like the C-substitutionals and vacancies, the levels present an exchange splitting > 0.5 eV. The C_B and N_B defects in N-rich growth condition and C_N in B-rich growth condition are the ones that present the lower formation energies. The binding energy of H atoms to a (10,0) single-walled BN nanotube was calculated at 25, 50, 75, and 100 % coverage using the DFT [110]. The average binding energy is highest at 50 % coverage, when H atoms are adsorbed on the adjacent B and N atoms along the tube axis and the value is −2.34 eV / mole, which is similar to 1 / 2 of the H−H binding energy. The band gap of 4.29 eV of the pristine (10,0) tube is decreased up to 2.01 eV for the H-adsorbed one with 50 % coverage. In [111] it was performed first principles calculations to study the effect of molecular oxygen O_2 adsorption on the electronic properties of (5,5) pristine and C-doped BN nanotube. The binding energies of oxygen molecules physisorbed at different sites were determined by considering both short- and long-range interactions. Spin-polarized calculation within the DFT yielded the triplet ground state for oxygen physisorbed on pure BN nanotube; the large energy gap between the unoccupied oxygen levels and the top of the valence band indicates the absence of hole doping. The introduction of substitutional C impurity increases the reactivity of BN nanotube toward molecular oxygen and stable O_2 chemisorption states exist on both C-substituted C_N and C_B defect sites. Chemisorbed O_2 on the C_N defect is found to impart metallicity on the BN nanotube.

4.5. Applications

At once behind synthesizing BN nanotubes, for them it was offered a number of probable applications in techniques [4]. For example, the system of the collinear BN nanotubes forms a boron nitride fiber. At the same time, the theory [112] developed for structural and electronic properties of nanotubular heterojunctions, in which one of layers is nanotubular boron nitride (namely, for C / BN and BC_2N / BN systems), leads to a conclusion that on basis of it a different electronic devices can be elaborated. In particular, sandwich nanostructures with C-layers both in the center and at the periphery separated by a few BN-layers may allow creation of nanotubular electronic devices [61]. Within the special semiempirical approach [104] C / BN superlattices and isolated junctions had been investigated as specific examples by the wide variety of electronic devices that can be realized using such nanotubes. The bottom of the conduction bands in pure BN nanotubes is controlled by a nearly-free-electron-state localized inside the tube suggesting interesting electronic properties under doping.

Other opportunities of application of the BN nanotubes are connected with features of their phonon spectrum [14]. Such dielectric tubes without inversion center can be used as phonon laser in GHz – THz range or hypersound quantum generator. Because of presence special nanotubular oscillatory modes, there is strong enhancement of electron-phonon interaction in comparison with a bulk material and it is not excluded that close-packed one-dimensional BN nanotubes will serve as high-temperature superconductors.

The band gap progression with BN nanotube diameter, which is of crucial importance for device applications, was presented and analyzed in detail in [105]. In zigzag BN nanotubes, radial deformations that give rise to transverse pressures decrease the gap from 5 to 2 eV, allowing for optical applications in the visible range [107]. Importantly, both the zigzag and chiral tubes are found [101] (see also [102]) to exhibit large second-order nonlinear optical behavior with the

second-harmonic generation and linear electro-optical coefficients being up to 15-times larger than that of bulk BN in both denser zinc-blende and wurtzite structures, indicating that BN nunotubes are promising materials for nonlinear optical and optoelectronic applications. Electronic structure of BN nanotubes can be tuned in a wide range through covalent functionalization [113] (see also [114]). The UV and visible absorption spectra indicate that their electronic structure drastically changes under functionalization. First principle calculations revealed that the covalently functionalized BN nanotubes can be either n- or p-doped depending on the electronegativity of molecules attached, and their energy gap can be adjusted from UV to visible optical range by varying concentration of functionalizing species.

BN from C distinguishes partial heteropolarity of the chemical bonding and for this reason one more sphere of the possible applications for BN nanotubes can become elaboration of new piezoelectric materials. The 3-fold symmetry of BN sheet, the III-V analog to graphite, prohibits an electric polarization in its ground state. But, this symmetry is broken when the sheet is wrapped to form of a BN tube. It was shown [115] that this leads to an electric polarization along the nanotube axis which is controlled by the quantum-mechanical boundary conditions of its electronic states around the tube circumference. Thus, the macroscopic dipole moment has an intrinsically nonlocal quantum-mechanical origin from the wrapped dimension. Combining first principles and tight-binding methods, and analytical theory, the piezoelectricity of a heteropolar (in particular, BN) nanotube was found [116] to depend on its chirality and radius. Effect can be understood starting from the piezoelectric response of an isolated sheet, along with a structure specific mapping from the sheet onto the tube surface. It was demonstrated that a linear coupling between the uniaxial and shear deformations occurs for chiral nanotubes, and the piezoelectricity of nanotubes is fundamentally different from its counterpart in bulk material. First principles calculations of the spontaneous polarization and piezoelectric properties of BN nanotubes showed [117] that they are excellent piezoelectric systems with response values larger than those of piezoelectric polymers. The intrinsic chiral symmetry of the nanotubes induces an exact cancellation of the total spontaneous polarization in ideal, isolated nanotubes of arbitrary indexes. But, the breaking of this symmetry by the intertube interaction or elastic deformations induces spontaneous polarization comparable to that of wurtzite bulk semiconductors [88].

Multielement nanotubes comprising multiple SiC-core, an amorphous SiO_2-intermediate layer, and outer shells made of BN and C layers separated in the radial direction, with diameters of a few tens of nm and lengths up to 50 μm, were synthesized by means of reactive laser ablation [118]. This resembles a coaxial nanocable with a semiconductor-insulator-semiconductor geometry and suggests applications in nanoscale electronic devices that take advantage of this self-organization mechanism for multielement nanotube formation.

A theoretical description of electron irradiation of single-walled BN nanotubes was presented in [119]. In a first step, the anisotropy of the atomic emission energy threshold was obtained within extended MD simulations based on the DFT tight-binding method. In a second step, total cross section for different emission sites as a function of the incident electron energy was numerically derived. Two regimes were then described: at low irradiation energies (below 300 keV), the atoms are preferentially ejected from the upper and lower parts of the tube while at high energies (above 300 keV) the atoms are preferentially ejected from the side walls. Typical values from a fraction of barn (at side wall for 150 keV electron) up to around 20 barn (for 1 MeV electrons) are obtained for the total cross section of knock-on processes. In BN nanotubes, the emission energy threshold maps were reported to show B sputtering to be more favorable for low irradiation energies, while N sputtering is more favorable at high energies. These calculations of the total knock-on cross section for nanotubes can be used as a guideline for TEM experimentalists using high energy focused beams to shape nanotubes, and also more generally if electron irradiation is to be used to change nanotube properties such as their optical behavior or conductivity.

One-dimensional crystals of potassium halides, including KI, KCl, and KBr, were inserted into BN nanotubes [120]. High-resolution TEM and energy-dispersive X-ray spectrometry were

used to characterize their microstructures and compositions. The fillings are usually single crystals with lengths up to several μm. The wetting properties (static contact angles of the liquids and surface tension) of individual BN nanotubes were studied [121] experimentally using a nanotube-based force to measure the interactions between nanotubes and liquids in situ. First principles simulations on the interaction of molecular hydrogen H_2 with the native and substitutional defects of small-diameter (8,0) BN nanotubes were performed in [49]. The adsorption of H_2 on structures found to be endothermic with respect to dissociation, with the small-diameter nanotube possessing the smaller barrier. Although chemisorption along the tube axis is energetically preferred, the barrier for dissociation is lower for chemisorption across the tube axis, implying that chemisorbed hydrogen can be kinetically trapped in a higher energy state. Dopants that maximize the localization of the HOMO and LUMO states maximize hydrogen binding energies. C-dopants do not enhance H_2 binding, whereas Si-dopants for N provide H_2 binding energies of 0.8 eV, at the upper end of the range required for hydrogen storage. The formation energy of most defects is reduced with increasing curvature except for the C-substitutionals. Vacancies do not reduce the barriers for H_2 dissociation for strongly curved nanotubes. The surface stress induced by nanotube curvature boosts the hydrogen storage capabilities of vacancies, with the nitrogen vacancy chemisorbing 4H and allowing a H_2 molecule to enter the interior of the tube. The hydrogen binding properties of BN systems are strongly dependent on the defects and dopants present. Pretreating of these systems so as to partially remove nitrogen should enhance H_2 adsorption properties. The hydrogen absorption capacity of Ti-covered single-walled BN nanotube was investigated using first principles PW method [122]. The weak interaction of H_2 molecules with the outer surface of bare nanotube can be significantly enhanced upon functionalization by Ti atoms: each Ti atom adsorbed on tube can bind up to four H_2 molecules with an average binding energy suitable for room temperature storage.

5. BORON NITRIDE FULLERENES

As alternative nanostructures to tubular boron nitride serve the boron nitride cages having form of the fullerene-like molecules. However, from consideration of a corresponding geometrical problem it is known that, in contrast to tubes, such closed structures cannot be faceted only by hexagons. Terms “fullerene” and “fullerite”, as well as “fulleride”, have been introduced and affirmed for a designation of carbon cage-molecules and corresponding molecular crystals. It was offered [14] that the similar structures constructed of atoms of boron and nitrogen, be called “fulborenes” and “fulborenites”. But, during discussion at 13th International Symposium on Boron, Borides and Related Compounds (5-10 September, 1999, Dinard, France) it had been drawn attention on the inadmissibility of such terminology breaking the surname of individual as Fuller is inventor of a geodetic dome. It seems preferable do not introduce the new terms, but to expand the contents of concepts “fullerene” and “fullerite” that they be characterizations of the atomic structures instead of their chemical composition.

5.1. Synthesizing

Polyhedral “graphitic” nanoparticles made of C and BN layers were obtained in the soot collected on the anode deposit formed by arching an HfB_2 rod with graphite in N_2 atmosphere [14].

It was demonstrated that from boron nitride it can be synthesized fullerene-like hollow nanoparticles with polyhedral morphology [123]. Together with BN nanotubes the Zr-compound nanoparticles encapsulated in BN cages were formed by arc-discharge between ZrB_2 electrodes in an N_2 atmosphere [64]. By the carbothermal synthesis there were obtained multi-shelled fullerenes – BN onions [14]. Boron nitride fullerene materials like the clusters, onions, intercalations, nanopolyhedra, and nanocapsules also can be synthesized by polymer pyrolysis, various chemical

reactions, arc-melting, electron-beam irradiation etc [74]. Corresponding fullerene clusters and atomic nanoclouds formed on the surface of BN fullerene material provided angular and spherical nanocage structures, which consist of 4-, 5-, 6-, and 7-membered atomic rings bonding.

In [124] it was described in situ synthesis and characterization of single-walled BN nanotubes terminated by fullerene-like structures onto polycrystalline W-substrates using electron-cyclotron resonance nitrogen and electron-beam boron sources. Analysis of the structures as a function of film thickness indicated that they were grown by addition of atoms to the exposed ends of single sheets, not at the substrate / nanostructure interface.

BN polymorphic modification with diamond-like structure with $B_{12}N_{12}$ molecules instead atomic sites has been obtained [125] by synthesis in the supercritical flow. Prismatic BN nanorods have been grown [126] on single-crystal Si-substrates by mechanical ball-milling followed by annealing at 1300° C. Growth takes place by rapid surface diffusion of BN molecules, and follows heterogeneous nucleation at catalytic particles. Growth terminates with a clear cuneiform tip. Growth, structure, and dominating facets were shown to be consistent with a system which seeks lowest bulk and surface energies.

5.2. Structure

For any structural analysis of BN fullerene-like systems it is obligatory presence certain model of the atomic structure. Modeling of the BN fullerene structures as well as fullerites and fullerides constructed of them are based on several empirically established rules [14]. By comparison of the measured values of formation enthalpies it yields that B–N chemical bonds are essentially stronger than B–B and N–N bonds. For this reason, it is believed that structure of the stable BN fullerenes is close with stoichiometric one, i.e. ratio $B / N \approx 1$. But, such systems can be built up only from atomic rings with even number of vertexes, which are alternatively occupied by atoms B and N. The stated is the Rule 1. Further, the structures of spherical BN fullerenes are searched among Archimedean polyhedra, all vertexes of which lie at a sphere surface, under the additional condition that for each atom 3 nearest neighbors are available. It is essence of the Rule 2. Search of the BN fullerite structures is governed by two additional rules. Rule 3: the coordination and type of molecular lattices are determined by a number and orientation of faces of the constituent molecules. Rule 4: the number of covalent double-bonds on both conjugated faces equals to a necessary number of intermolecular single-bonds between two adjacent faces. Conditions of formation of covalence crystals from the binary fullerene-like molecules, in particular, B_nN_n recently have been more detailed [127]: these clusters should be the hollow convex polyhedra satisfying Euler's rule; their faces should be constructed only by even-membered rings and satisfy so-called isolated ring's rule; the number of the isolated faces should be coincided with the symmetry of the forming crystal; it should exist only alternating chemical bonds (i.e. B–N bonds). In case of 4, 6, 8 or 12 isolated faces, these conditions lead to tetrahedral, cubic, and hexagonal symmetries. Thus, bonding of the clusters with similar faces form close-packed crystal structures with sphalerite-like, rock salt, bcc, fcc, and hcp lattices. For experimental determination of structure of the nanometric hollow BN spheres it can be applied a technique of the electron inelastic scattering cross-section analysis developed in [128] for a layered crystal h-BN. During the growth, the structures of BN onions are observable by means of TEM and x-ray microstructural analysis [14]. Atomic structures and the mechanisms of formation for various BN fullerene systems (clusters, onions, nanoinclusions, nanocapsules etc) in [74] were studied by means of high-resolution TEM and EELS. On this basis a number of structural models of similar systems have been offered. In particular, $B_{36}N_{36}$ cluster should be built up from 6 4-membered and 24 6-membered rings. Besides, it has been noticed that BN nanocages possess more acute-angled form and specific internal structure in comparison with carbon cages. Listed methods also allow detecting of the impurity atoms in boron nitride metal-fullerides. Particularly, it has been found out Ag nanoparticles packed in BN spherical capsules. On

surfaces of similar materials there are formed fullerene clusters and atomic clouds in the form of nearly spherical and faceted nanocage structures consisting of 4- and 6-membered rings. Images of the fullerene-like kinks and bends terminating substrate-grown BN nanotubes can be obtained by high-resolution TEM [124]. High-resolution TEM together with nanobeam electron diffraction allowed determining of the orientation of BN hexagons in cone-shelled particles [129].

The structures of some regular (determination see below) BN fullerenes and predicted [14] fullerite species are shown in Figs. 9, 10, and 11.

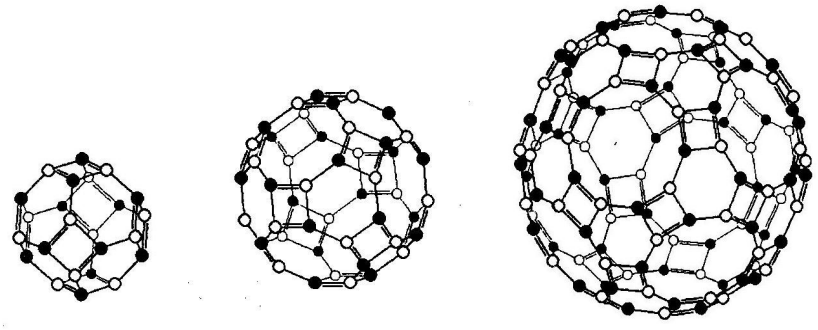

(1) **(2)** **(3)**

Fig. 9. Regular $B_{12}N_{12}$ (1), $B_{24}N_{24}$ (2), and $B_{60}N_{60}$ (3) fullerenes.

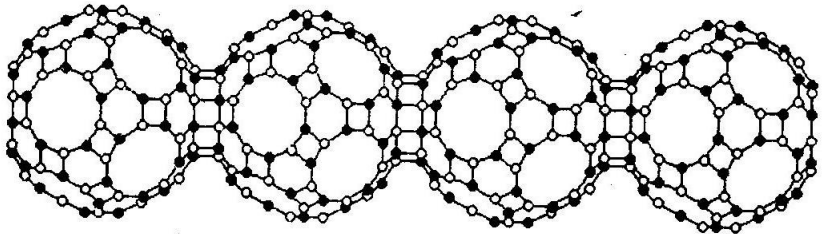

Fig. 10. Predicted [14] inorganic polymeric chain consisted of $B_{60}N_{60}$ fullerenes.

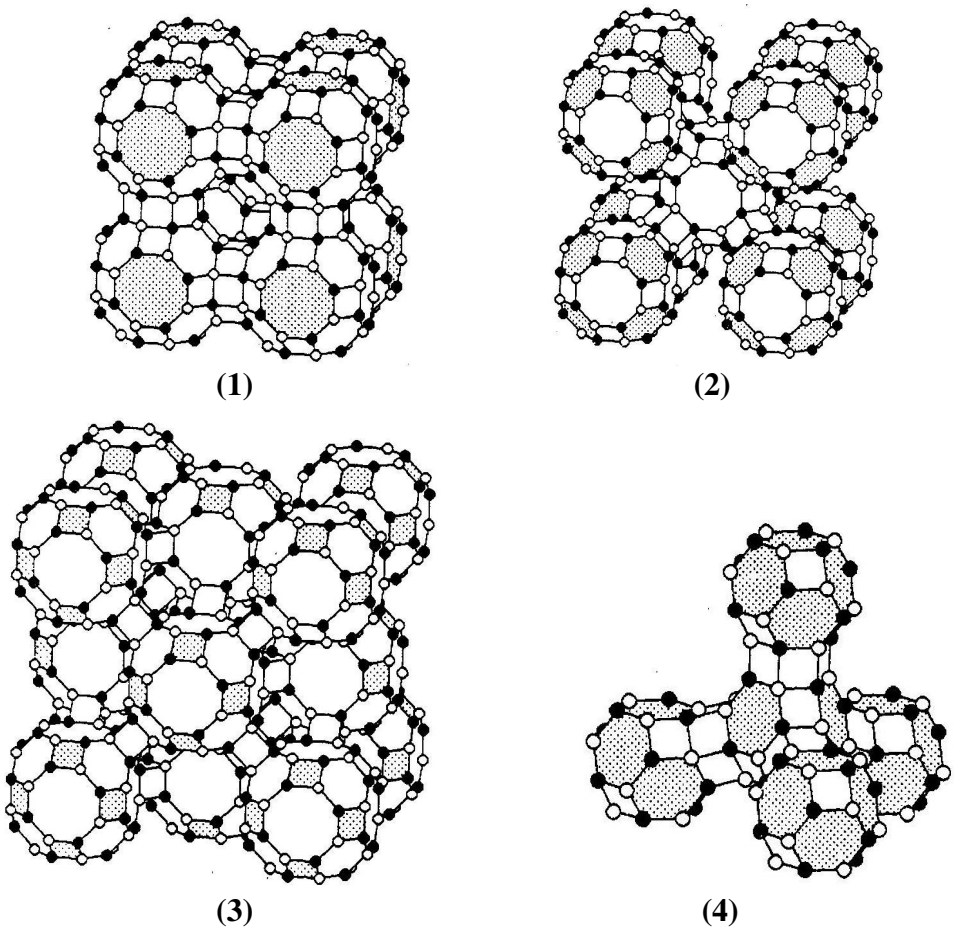

Fig. 11. Unit cells of predicted [14] $B_{24}N_{24}$ fullerites with sc (1), bcc (2), and fcc (3) lattices; and $B_{12}N_{12}$ coordination tetrahedron (4), the building block of zinc-blende and wurtzite lattices.

Concept of a regular boron nitride fullerene has been introduced in [130]. Structure of the BN fullerene is considered as regular if it meets certain conditions: (1) structure consists of equal numbers of B and N atoms; (2) only 3-fold chemical bonds are realized (i.e. analogs of the bonds in layers of h-BN, r-BN, and t-BN layered crystals, as well as in regular BN nanotubes, but with distinguished valence angles); (3) atomic rings represent plane or broken (along diagonals between B and N sites) regular polygons with even number of vertexes alternatively occupied by B and N atoms. Given definition yields equal B–N bond lengths. Let denote this only structural parameter for n-fullerene ($n = 1,2,3,...$) by d_n. The chemical formula of a regular BN fullerene should be $B_{2n(n+1)}N_{2n(n+1)}$. As the regular fullerene is inscribed in sphere, the spherical or, more precisely, geographical (r, φ, λ) coordinates are useful to describe atomic sites positions.

Evidently, the geographical coordinate r for all atomic sites equals to fullerene radius r_n,

$$r_{\mathrm{B}} = r_{\mathrm{N}} = r_n .$$

The latitudes φ are determined as

$$\varphi_{\mathrm{B}} = \varphi_{\mathrm{N}} = \operatorname{sgn} m \arccos \frac{r_{n,m}}{r_n},$$

while longitudes λ as

$$\lambda_{\mathrm{B}} = \arcsin \frac{d_{\mathrm{B}\,n,m}}{r_{n,m}} + \pi \left(\frac{4l - 3 + (-1)^m}{2n} - 1 \right),$$

$$\lambda_{\mathrm{N}} = \arcsin\frac{d_{\mathrm{N}\,n,m}}{r_{nm}} + \pi\left(\frac{4l-3-(-1)^m}{2n} - 1\right).$$

Here indexes $m = \pm 1, \ldots, \pm(n+1)$ and $l = 1, \ldots, n$ number atomic rings in parallel planes and B and N atoms in planes, respectively. Radius $r_{n,m}$ of the ring in m-plane can be calculated from following relation

$$r_{n,m}^2 = \frac{d_{\mathrm{B}\,n,m}^2 + 2d_{\mathrm{B}\,n,m}d_{\mathrm{N}\,n,m}\cos\pi/n + d_{\mathrm{N}\,n,m}^2}{4\sin^2\pi/n}.$$

For planes with $m \neq \pm 1$, $d_{\mathrm{B}\,n,m}$ and $d_{\mathrm{N}\,n,m}$ are certain interatomic distances in m-plane, which equal to one of a diagonals $d_{n,k,j}$ between certain B and N vertexes in regular $2k$-gon ($k = 1,2,3,\ldots$ and $j = 1, \ldots, k$) with vertexes alternatively occupied by B and N atoms and side d_n:

$$\frac{d_{n,k,j}}{d_n} = \frac{\sin\pi j/2k}{\sin\pi/2k}.$$

But, if $m = \pm 1$, i.e. in planes adjacent or coincident with equatorial plane, one from the parameters $d_{\mathrm{B}\,n,m}$ and $d_{\mathrm{N}\,n,m}$ equals to d_n, while another equals to parameter D_n expressed as

$$\frac{D_n}{d_n} = \frac{\sin\pi j_{\mathrm{B}}/2k_{\mathrm{B}}}{\sin\pi/2k_{\mathrm{B}}} + \frac{\sin\pi j_{\mathrm{N}}/2k_{\mathrm{N}}}{\sin\pi/2k_{\mathrm{N}}} - 1,$$

where j_{B} and j_{N} are the j-values in planes with $m = \pm 2$.

And finally, radius of regular n-fullerene is determined as

$$\frac{2r_n^2}{d_n^2} = 1 + \frac{1}{8\sin^2\pi/n}\left(\frac{\sin\pi j_{\mathrm{B}}/2k_{\mathrm{B}}}{\sin\pi/2k_{\mathrm{B}}} + \frac{\sin\pi j_{\mathrm{N}}/2k_{\mathrm{N}}}{\sin\pi/2k_{\mathrm{N}}}\right)^2.$$

In particular, in case of $n = 2^0, 2^1, 2^2, \ldots$, i.e. for fullerenes B_4N_4, $B_{12}N_{12}$, $B_{24}N_{24}$ etc, planes with $m = \pm 1$ coincide with equatorial one and one can obtain simplified formula:

$$\frac{r_n^2}{d_n^2} = \frac{1}{\sin^2\pi/2n}\left(\frac{3}{4} + \frac{\cos\pi/2n}{\sqrt{2}}\right).$$

On basis of the stated relations, the explicit expressions (in term of B–N bond length d_n) of the interatomic distances in regular boron nitride fullerene have been obtained:

$$\begin{aligned}
&(\mathrm{B}\,n,m',l' - \mathrm{N}\,n,m'',l'')^2 = \\
&= 2r_n^2 - 2\,\mathrm{sgn}\,m'm''\sqrt{(r_n^2 - r_{n,m'}^2)(r_n^2 - r_{n,m''}^2)} - \\
&- \left(d_{\mathrm{B}\,n,m'}d_{\mathrm{N}\,n,m''} + d_{\mathrm{N}\,n,m'}d_{\mathrm{B}\,n,m''}\right)\times \\
&\times\frac{\cos\left(4(l'-l'') + (-1)^{m'} + (-1)^{m''}\right)\pi/2n}{4\sin^2\pi/2n} + \\
&+ \left(d_{\mathrm{B}\,n,m'}d_{\mathrm{B}\,n,m''} - d_{\mathrm{N}\,n,m'}d_{\mathrm{N}\,n,m''}\right)\times \\
&\times\frac{\sin\left(4(l'-l'') + (-1)^{m'} + (-1)^{m''}\right)\pi/2n}{2\sin\pi/n},
\end{aligned}$$

$$\begin{aligned}
&(\mathrm{N}\,n,m',l' - \mathrm{B}\,n,m'',l'')^2 = \\
&= 2r_n^2 - 2\,\mathrm{sgn}\,m'm''\sqrt{(r_n^2 - r_{n,m'}^2)(r_n^2 - r_{n,m''}^2)} - \\
&- \left(d_{\mathrm{N}\,n,m'}d_{\mathrm{B}\,n,m''} + d_{\mathrm{B}\,n,m'}d_{\mathrm{N}\,n,m''}\right)\times \\
&\times\frac{\cos\left(4(l'-l'') - (-1)^{m'} - (-1)^{m''}\right)\pi/2n}{4\sin^2\pi/2n} +
\end{aligned}$$

$$+\left(d_{\mathrm{N}\,n,m'}\,d_{\mathrm{N}\,n,m''}-d_{\mathrm{B}\,n,m'}\,d_{\mathrm{B}\,n,m''}\right)\times$$
$$\times\frac{\sin\left(4(l'-l'')-(-1)^{m'}-(-1)^{m''}\right)\pi/2n}{2\sin\pi/n},$$
$$(\mathrm{B}\,n,m',l'-\mathrm{B}\,n,m'',l'')^2=$$
$$=2r_n^2-2\operatorname{sgn}m'm''\sqrt{(r_n^2-r_{n,m'}^2)(r_n^2-r_{n,m''}^2)}-$$
$$-\left(d_{\mathrm{B}\,n,m'}\,d_{\mathrm{B}\,n,m''}+d_{\mathrm{N}\,n,m'}\,d_{\mathrm{N}\,n,m''}\right)\times$$
$$\times\frac{\cos\left(4(l'-l'')+(-1)^{m'}-(-1)^{m''}\right)\pi/2n}{4\sin^2\pi/2n}+$$
$$+\left(d_{\mathrm{B}\,n,m'}\,d_{\mathrm{N}\,n,m''}-d_{\mathrm{N}\,n,m'}\,d_{\mathrm{B}\,n,m''}\right)\times$$
$$\times\frac{\sin\left(4(l'-l'')+(-1)^{m'}+(-1)^{m''}\right)\pi/2n}{2\sin\pi/n},$$
$$(\mathrm{N}\,n,m',l'-\mathrm{N}\,n,m'',l'')^2=$$
$$=2r_n^2-2\operatorname{sgn}m'm''\sqrt{(r_n^2-r_{n,m'}^2)(r_n^2-r_{n,m''}^2)}-$$
$$-\left(d_{\mathrm{N}\,n,m'}\,d_{\mathrm{N}\,n,m''}+d_{\mathrm{B}\,n,m'}\,d_{\mathrm{B}\,n,m''}\right)\times$$
$$\times\frac{\cos\left(4(l'-l'')-(-1)^{m'}+(-1)^{m''}\right)\pi/2n}{4\sin^2\pi/2n}+$$
$$+\left(d_{\mathrm{N}\,n,m'}\,d_{\mathrm{B}\,n,m''}-d_{\mathrm{B}\,n,m'}\,d_{\mathrm{N}\,n,m''}\right)\times$$
$$\times\frac{\sin\left(4(l'-l'')-(-1)^{m'}+(-1)^{m''}\right)\pi/2n}{2\sin\pi/n}.$$

5.3. Binding

At the first time, it was calculated [131] $B_{36}N_{24}$ fullerene which is the boron nitride structural analogue of the well-studied carbon C_{60} fullerene. It is very difficult for synthesizing, because of a strong deviation from the stoichiometric composition: its traces are hardly observable by mass-spectrometry. For this reason, the bonds lengths in $B_{36}N_{24}$ molecule were not measured. The B(1) – B(1), B(2) – B(2), B(1) – N, and B(2) – N distances were only estimated by means of MD: 1.972, 2.016, 1.670, and 1.695 Å, respectively. Here B(1) designates the sites constituent the pairs of adjacent B atoms, which form sides of the 5-membered rings; and B(2) are sites constituent the pairs, which form common side of the adjacent 6-membered rings (unlike B sites, all N sites in this structure are equivalent).

Semiempirical MO method calculation performed for the $B_{12}N_{12}$ of fullerene-like spheroid geometry had led to the following values of structural parameters [132]. Valence angles B–N–B in rhombuses and hexagons equal to 79.92 and 106.44 °, while bonds lengths equal to 1.504 and 1.418 Å, respectively. The same lengths tested by first principles HF method fall in intervals (1.475 – 1.508) and (1.433 – 1.438) Å confirming semiempirical results. These calculations testify in favor of presence of stationary points on potential-energy-surfaces of $(BN)_{12}$ fullerenes. The molar heat of formation is estimated as 0.86 eV / mole. HF test calculations also confirm a conclusion about their stability: system total energy is negative and its absolute HF value ranged in an interval from 945.77688 up to 950.56265 eV.

Atomic structures for various BN fullerene systems (clusters, onions, nanoinclusions, nanocapsules etc) in [74] also had been optimized by means of MO method. Optimization of the possible structures generated from the completely deformable B_3N_3 and B_4N_4 graphs carried out by DFT method shows [133] that these systems are competitive by stability with any final BN structure, in particular, fullerenes. It had been noticed that boron nitride fullerene-like systems

mainly obtained in experimental conditions are $B_{36}N_{36}$ molecules. The comparative analysis of some possible structural models of BN fullerenes indeed leads to a conclusion [134] that unlike the isolated atomic rings $B_{36}N_{36}$ cluster is a stable structure in spite of the existence of distorted 6- and 4-membered rings. It is an explanation for the other similar BN microstructures too [135]. Total and cohesion energies of the smallest stoichiometric boron nitride fullerene-like clusters also were considered by the HF method in Gaussian-orbitals basis [127]. Calculations revealed their stability.

The structure and the growth mechanism for BN fullerenes in [14] had been investigated theoretically – by means of MD using original B–B, B–N, and N–N interatomic potentials. In particular, the diameters of $B_{12}N_{12}$, $B_{24}N_{24}$, and $B_{60}N_{60}$ molecules along the radial axes, which are passing through tetragonal (or hexagonal) faces have been predicted as 4.089 (3.541), 6.382 (6.045), and 10.804 (10.609) Å. It has been pointed that the difference between effective radiuses of spheroid molecules $B_{12}N_{12}$ and $B_{60}N_{60}$ equal to 3.36 Å is close to interlayer distance of 3.33 Å in h-BN. The analogy extends on bonds between fullerene-surfaces: in calculations of parameters of the fullerene molecules $B_{12}N_{12}$, $B_{24}N_{24}$, and $B_{60}N_{60}$, interatomic B–N potential with equilibrium distance of 1.4457 Å (which corresponds to the intralayer bond length in bulk h-BN crystal) was used with success. Semiempirical MNDO method predicts stability of $B_{12}N_{12}$, $B_{24}N_{24}$, and $B_{60}N_{60}$ fullerenes as their total potential energies are negative. On magnitude they equal to 10.26, 11.12 and 11.26 eV / mole, respectively (at heats of formation of 6.857, 8.098, and 29.280 eV / mole).

Calculations of the boron nitride isomers performed within the frames of various variances of HF method and DFT both in LDA and with gradient corrections show [136] that the small-sized B_nN_n molecules are characterized by the one-dimensional geometry. At the average sizes, $n \le 8$, they are more stable in the form of rings, but at the relatively high number of constituent atoms, $n \ge 11$, when at least 2 from 4-membered rings from each other are separated by hexagons, they prefer the form of a cage. As for B_9N_9 and $B_{10}N_{10}$ cages, their structures by the stability are comparable with corresponding ring-structures. In [39] the energy of $B_{12}N_{12}$ fullerene-like cages with respect that for isomer in the form of a ring had been obtained. By HF method variances it had been given the values: –1.58, –1.06, and –0.88; by DFT within LDA: –8.21, –7.46, and –7.35; and by DFT with gradient corrections: –1.93, –1.10, and –1.00 eV. Despite of essential discrepancies in absolute values of energy-differences obtained their negative sign and hence stability of the $B_{12}N_{12}$ fullerene does not cause any doubt.

In [137] the first principles DFT calculations within the GGA were applied to study structure and relative stabilities of stoichiometric fullerenes $B_{16}N_{16}$, $B_{36}N_{36}$, and $B_{64}N_{64}$, as well as non-stoichiometric ones $B_{12}N_{16}$, $B_{32}N_{36}$, $B_{60}N_{64}$, $B_{16}N_{12}$, $B_{36}N_{32}$, and $B_{64}N_{60}$. Overall tendency for formation of octahedrally faceted shapes as the atomic number increases, with more spherical shapes being prevalent only for small nonstoichiometric cages, was obtained. BN fullerenes of diameters of ~ 12 Å or larger are expected to be polyhedrally faceted regardless of their stoichiometry. For the small molecules (with a diameter of ~ 5 Å) it was found that stoichiometric $B_{16}N_{16}$ structure is more stable than nonstoichiometric ones with similar dimensions, in both boron-rich and nitrogen-rich environments. For the larger sizes, the nonstoichiometric $B_{32}N_{36}$ and $B_{60}N_{64}$ are found to be more stable than their stoichiometric counterparts in a nitrogen-rich environment, while the stoichiometric structures are most stable under the boron-rich conditions. These conclusions remain largely unchanged when one considers the gas-phase limit of atomic reservoirs. Following classification of BN fullerenes have been offered in [137]. As small, intermediate, and large ones it should be considered the fullerenes with a diameters of ~ 5, 8, and 12 Å, respectively. Quantitatively the relative stabilities of BN fullerenes with nearly the same sizes were estimated based on calculated molar energies of formation: $B_{12}N_{16}$ – 8.28, $B_{16}N_{16}$ – 8.54, and $B_{16}N_{12}$ – 8.08; $B_{32}N_{36}$ – 8.77, $B_{36}N_{36}$ – 8.77, and $B_{36}N_{32}$ – 8.61; $B_{60}N_{64}$ – 8.89, $B_{64}N_{64}$ – 8.89 and $B_{64}N_{60}$ – 8.11 eV. Generalization of similar results leads to the conclusion that for large fullerenes (i.e. with diameters more than ~ 12 Å) dependence of the molar energy of formation on number n of B–N pairs is expressed by the formula $E/n = A + B/n + C/\sqrt{n}$, where A is the energy of formation per

B–N pair in isolated BN plane sheet with respect of layered h-BN crystal (it corresponds to a limit of fullerene with infinite diameter); B/n describes contributions from the stresses caused by presence of "wrong bonds"; and the term $C/\sqrt{n}$ is caused by edges-formation after achievement the sizes when polyhedral form becomes more suitable.

According to the semiempirical MO calculations [132], the lowest vibration frequency for $(BN)_{12}$ fullerene spheroids is estimated as 340.3 cm^{-1}, while by another semiempirical method MNDO frequencies of the vibration modes dominant over the BN fullerenes IR-spectra are found [14] as following: $B_{12}N_{12}$ – 1294 and 825; $B_{24}N_{24}$ – 1356, 1336, and 772 cm^{-1}. Studies of the $B_nN_n^+$ ionized clusters at numbers of atoms $n = 3 - 10$ performed within DFT had showed [138] that like the case of their neutral analogues lower energies are characteristic for systems with even indexes.

Detailed comparisons between the experimental (high-resolution electron microscopy) images of fullerene-like structures terminating single-walled substrate-grown BN nanotubes and MD simulations showed [124] a dominance of kinks and bends involving 4- and 8-fold ring structures. Sometimes there are also such hollow structures of boron nitride which in form strongly differ from sphere. For example, in [129] it has been discovered nanoscale BN cone particles, which consist of an ordered stacking of seamless conical shells. In all but one case, the results of structural analysis confirmed with a model of orderly stacked 240 °-disclinations, which is the smallest cone geometry ensuring the presence of B–N bonds only. One case of a nanoscale cone constituted of 300 °-disclination was found, implying that structures containing line defects of B–B or B–B bonds may be formed. MD studies of the BN nanotubular structures by the tight-binding method show that various experimentally observable fullerene-like morphologies, including conic, flat, amorphous etc of their ends are directly connected with chirality of the given tube [79]. Optimization of the BN cage molecules configuration by a gradient-search method specifies an opportunity of distortions in real structures in bond lengths and valence angles from the regular geometrical values together with "rippling" surfaces [127].

In [139] the two-dimensional lattice of BN shells was treated with a first principles method. The demonstrated robustness of continuum elasticity up to very small length-scale allows one to define and compute the in-plane stiffness and flexural rigidity moduli of the representative BN nanoshells, including limit structure of the plane BN sheet. Only small deviations from the linear elasticity are observed. BN shells can associate in systems of collinear spherical surfaces. Arising interlayer interactions are much weaker than intralayer ones as they are caused by van der Waals polarization forces. Correspondingly, interlayer bonds appear to be more than twice longer in comparison with intralayer bonds. As it has been noticed [14], interlayer interactions in multi-shelled BN cages, onions etc are almost the same as in three-dimensional layered boron nitride crystals and multi-walled nanotubes.

It is possible to obtain some inequalities between total ground state energies of polyhedral carbon clusters and their derivatives with substitution by boron and nitrogen atoms $(BN)_xC_{n-2x}$ ($n - 2x \geq 0$), which do not depend on a used theoretical method of analysis, and on this reason are suitable in first principles calculations as well as for semiempirical estimations [140]: difference between these energies is expressed by the simple sign-variable sum over substituted sites. The energetics and thermal stability of storing hydrogen in BN-based nanostructures had been studied using first principles DFT formalism [141]. It was shown that H_2 molecule enters through the hexagonal face of the $B_{36}N_{36}$ cage and prefers to remain inside the cage in molecular form. The energy barriers for the H_2 molecule to enter or escape from the cage are, respectively, 1.406 and 1.516 eV. As the concentration of hydrogen inside the cage increases, the cage expands and the bond length of the hydrogen molecule contracts, resulting in significant energy cost. There were performed first principles calculations for the interactions between transition metal atoms Fe, Co, and W, as well as for FeO molecule with the $B_{36}N_{36}$ fullerene [142]. The stable structure of complexes may have the dopant atom either at the center of the cage or making covalent bonds with

the fullerene wall, with similar total energies. FeO molecule has a binding energy with the fullerene 2.5 eV larger than those of the transition metal atoms and produces larger distortions in the cage.

Molecular and solid forms of BN, based on stoichiometric and nonstoichiometric fullerenes, were predicted in [143] by means of first principles calculations. Study of the energetics of dimmer formation indicates that the reactivity of BN fullerenes depends strongly on the stoichiometry. The stoichiometric fullerenes form strong covalence bonds between the tips of neighboring cages, while the tips of nitrogen-rich fullerenes "repeal" each other. Calculations predict the large interstitial channels (with diameters of (5 – 8) Å), but the hardness comparable to that of hard metals. In contrast, nitrogen-rich units (with the exception of $B_{12}N_{16}$) should form loosely bound molecular solids (like the standard carbon fullerenes). Following values of binding energy per intermolecular bond were predicted: $B_{12}N_{16}$ and $B_{16}N_{16}$ dimmers – 0.47 and 0.45; and $B_{12}N_{16}$, $B_{16}N_{16}$, and $B_{36}N_{36}$ fullerite-crystals – 0.34, 0.30, and 0.29 eV.

Consideration of $B_{12}N_{12}$, $B_{24}N_{24}$, and $B_{60}N_{60}$ molecules as analogues of carbon fullerenes allows to predict [14,127,144,145] existence of inorganic polymeric chains and at least 10 boron nitride fullerite crystals and calculate their lattice parameters and density. It have been constructed a number small clusters B_nN_n (with $n = 12$, 16, 18, 14, 36, and 60) able to form zeolite-like covalence crystals. Comparison between these structural calculations and available experimental data allows identifying the fullerite with simple cubic symmetry constructed from $B_{12}N_{12}$ molecules with BN intermediate explosive phase. As for BN polymorphic modification with diamond-like structure with the same molecules instead atomic sites [125], which structure earlier called by an E-phase, it has been named [14] as "hyperdiamond" of $B_{12}N_{12}$. Experimental value for its lattice parameter, 11.14 Å is in good agreement with predicted one, 11.52 Å. Calculation of the bulk modulus of elasticity leads to a conclusion that it should be a superhard semiconductor.

Analysis of the atomic orbitals population in nonstoichiometric molecule $B_{36}N_{24}$ (with structure like the carbon C_{60} fullerene) carried out [131] by X_α-method gives following values of the atomic charges – B(1): +0.47, B(2): +0.41, and N: −0.66 (for B sites determination see above). Atomic charges in fullerene spheroids $B_{12}N_{12}$ were calculated by the MO method [132] and also semiempirically using MNDO method [14]. The averaged charges on B (positive) and N (negative) atoms constituent $B_{12}N_{12}$, $B_{24}N_{24}$, and $B_{60}N_{60}$ fullerenes have been estimated as ±0.26, ±0.31 and ±0.30, respectively [14]. Electron density distribution maps in diamond-like $B_{12}N_{12}$ fullerite have been calculated in [125] by the full-potential APW method. Optimization of the smallest BN cage molecules configuration by a gradient-search method also leads to the necessity to transfer certain electron charge from B atoms to N atoms and, hence, to certain deal of ionicity in interatomic bonds together with formation of "rippling" surfaces [127]. Because positive B ions leave inside, while negative N ions leave outside, it results in formation of the thin dipole-layer.

5.4. Electronic structure

Electronic states in nonstoichiometric $B_{36}N_{24}$ cluster (structural analog of carbon C_{60} fullerene) was calculated in HF X_α-method MO approach [131]. Fermi level had appeared to be located at 5.5 eV below the zero-level that specifies the electron-deficiency and, therefore, electron affinity of the system. HOMO–LUMO gap has turned out to be equal to 1.9 eV, while valence band width about 20 eV. The electronic structure, namely valence electrons energies, of the fullerene-like spheroid with chemical formula $B_{12}N_{12}$ in [132] had been calculated by the semiempirical MO method. HOMO–LUMO gap was estimated as 8.9 eV. First principles test-calculations confirm presence of an energy gap, but overestimate its width, (13.5 – 14.5) eV. Results of the first principles calculations performed in [146] for $B_{36}N_{36}$ fullerene-like cluster (its form and sizes are comparable with these of fullerene experimentally obtained by the electron irradiation of BN) show that BN fullerenes should have wider energy gaps than BN nanotubes of similar diameter. This fact emphasizes the stability property of such kind molecules as they have been formed. For $B_{36}N_{36}$

cluster the electronic structure had been calculated by the discrete-variation X_α-method [74]. The energy gap is estimated as ~ 4 eV what is close to value for bulk BN. For $B_{12}N_{12}$, $B_{24}N_{24}$, and $B_{60}N_{60}$ fullerenes, the HOMO–LUMO band gap (at B–N bonds lengths of 1.4457 Å as it takes place in h-BN layers) was calculated by the semiempirical MNDO method in [14]. They were equal to 7.98, 8.34, and 8.73 eV, respectively. Therefore, the inference can be made that, with an increase in the number m of atoms the HOMO–LUMO band gap is stabilized at approximately 9 eV. Ionization bands and electron affinities of boron nitride B_nN_n clusters of the average sizes ($n = 3$, 4, 5) have been investigated in [147] within Green-function approach for external electrons. It was found that $B_3N_3^-$ anion is poorly stable concerning the electron loss, whereas for B_4N_4 and B_5N_5 it was observed negative adiabatic electron affinities.

As one would expect, the DOS distribution calculated for $B_{36}N_{36}$ cluster is similar to that of layered h-BN crystal [134]. Applying DFT within GGA, the band structure of various BN fullerites had been calculated in [143]. For gap width of the simple cubic structures constructed from $B_{12}N_{12}$, $B_{16}N_{16}$, and $B_{36}N_{36}$ fullerenes, the estimations of (4.0 – 4.5), 4.5, and 3.8 eV were made. Thus, a spread of gap value was estimated as ~ 0.5 eV. A zone-folding construction was applied [148] to the honeycomb lattice band structure to yield explicit expressions for the Hückel π-type MO energies and symmetries of trivalent polyhedra consisting of hexagons and squares with octahedral symmetry. The numerical Hückel calculations on a large set of cages also had been performed. A clear distinction in electronic structure between leapfrog, nonleapfrog type 1, and nonleapfrog type 2 cages was revealed. The results are relevant for attaining boron-nitrogen cages. Quantum-chemical calculations on $B_{36}N_{36}$ confirm the results. Recently electronic structure of small B_nN_n fullerene-like clusters, including forbidden gap width and DOS distribution map, has been calculated by HF X_α-method using Gaussian orbitals basis [127].

First principles calculations of the $B_{36}N_{36}$ fullerene electronic structure show that doping by the transition metals like Fe, Co and W, and also by molecule FeO can lead to occurrence of several new forbidden states [142]. Fragments of carbon rings which can be placed on the ends of BN nanotubes playing a role of the ending of a tube or connection of two tubes theoretically can be considered as quantum dots [149]. Electronic spectra of these fullerene-like objects had been calculated by Hückel method using Bloch periodic boundary condition.

Band structure and DOS distribution of the boron nitride fullerite in diamond-like structure with $B_{12}N_{12}$ molecules instead atomic sites in [125] had been calculated by first principles full potential APW method. For the energy gap width the estimate of ~ 1.9 eV was found.

5.5. Applications

It was marked that cluster BN fullerene-like materials are intrigued both for scientific researches and from the point of view of practical applications what are: cluster protection, cluster separation, producing of nanoball bearings, catalysis, and biotechnologies [74]. Governing the sizes, number of layers, cluster types, chirality, and structure, it is possible to achieve that non-magnetic C–B–N nanocage structures with the gap in a range of (0 – 5) eV showed useful electronic, optical, and magnetic properties such as Coulomb blocking, photoluminescence, supermagnetism etc.

A number of ideas regarding fullerene-like BN have been offered in [14]. On the basis of $B_{12}N_{12}$ fullerite with zinc-blende lattice, it can be elaborated “hyperdiamond”, while on the basis of $Me_2B_{12}N_{12}$ fulleride (Me is atom of an appropriately chosen metal) with bcc lattice – “superdense diamond”. Boron nitride fullerites with nanoporous channels of molecular sizes in regular simple cubic lattice are attractive as a molecular sieves or nanomembranes. Various encapsulated BN fullerites (i.e. BN fullerides) can serve as new nanocomposite materials. BN fullerenes based materials are capable to combine some such properties that is impossible in common crystals. For example, as it is predicted by the DFT within GGA the stoichiometric fullerenes should form

covalence-bonded low-dense crystals with channels with a diameters of (5 – 8) Å, but on hardness comparable with hard metals [143]. On the contrary, non-stoichiometric (nitrogen-rich) fullerenes (except for $B_{12}N_{16}$) should form more brittle molecular solids similar with usual carbon fullerites.

At zero temperature, up to 18 hydrogen molecules can be stored inside $B_{36}N_{36}$ cage [141]. However, at room temperature high weight percentage hydrogen storage can not be achieved. Doping of the $B_{36}N_{36}$ fullerene by the transition metals etc can lead to several new forbidden states [142]. But, there no additional cage magnetic moment: such kind hybrids possess the same magnetic moments as the isolated dopants. Measurements of the photoluminescence and magnetic properties of BN nanocapsules show significant energy shifts and supermagnetism [74].

6. CONCLUDING REMARKS

Description made for the various boron nitride nanosystems geometries, binding, electronic structure etc may serve as basis for further investigations. In particular, with this purpose it planned application of the quasi-classical approach (the physical theory see in [150–153], and for related mathematical problems like calculations of matrix elements and solving of secular equation see in [154–158]), which with success has been realized for other structural modifications of boron nitride – diatomic molecule, isolated plane sheet, hexagonal h-BN, cubic c-BN, and wurtzite-like w-BN crystals [15,16,26,31,40–42,159–165]. On the basis of geometry description for regular BN nanotubes [81] recently by this approach it has been studied relative stability of the ultra-small nanotubes and complex dependence of the molar energy from radius is found out [86]. Similar calculations for BN fullerenes based on their geometry [130] should give answers to such questions as: the spheroid form is stable or flattened BN fullerenes containing defects are energetically more preferable; what are the maximal sizes of regular boron nitride fullerenes; in what combination they can form multi-shelled fullerenes etc. Such consideration needs to take into account features characterizing BN nanosystems, in view of general equations derived [166] for fluctuations in energy of the small completely open systems, which show that the fluctuations should be unusually large, because there are no restraints on the size of the system and fluctuations in total number or partial numbers of atoms in binary systems indirectly contribute to the fluctuations in their energy.

REFERENCES

1. A. Rubio, J.L. Corkill, M.L. Cohen, Phys. Rev. B, **49**, 5081 (1994).
2. X. Xia, D.A. Jelski, J.R. Bowsner, Th.F. George. J. Am. Chem. Soc., **114**, 6493 (1992).
3. Z. Weng–Seih, K. Cherrey, N.G. Chopra, X. Blasé, Y. Miyamoto, A. Rubio, M.L. Cohen, S.G. Louie, A. Zettl, R.Gronsky. Phys. Rev. B, **51**, 11229 (1995).
4. N.G. Chopra, R.J. Luyken, K. Cherrey, V.H. Crespi, M.L. Cohen, S.G. Louie, A. Zettl. Science, **269**, 966 (1995).
5. H. Gleiter. Acta Mater., **48**, 1 (2000).
6. V.V. Pokropivnyj, V.V. Skorokhod. In: Proc. 4th Int. Conf. “Mater. & Coat. Extr. Perf.”. Kiev: IPMS, 235 (2006).
7. N.P. Borisova. Methods of Non-Empirical Calculations of Diatomic Molecules within Ellipsoidal Basis. Leningrad: LU (1986).
8. I.V. Weiz. In: [18], Supplement to the Russian Translation, 295 (1984).
9. O.I. Bukhtyarov, S.P. Kurlov, B.M. Lipenskikh. In: Abs. 8th Int. Symp. Boron, Borides, Carbides, Nitrides & Rel. Comp Tbilisi: Metsniereba, 135 (1984).
10. J.L. Masse, M. Bärlocher. Helv. Chim. Acta, **47**, 314 (1964).
11. Yu.G. Khajt, V.I. Baranovskij. J. Str. Chem., **21**, 153 (1980).
12. H. Bredohl, J. Dubois, Y. Houbrechts, P. Nzohabonayo. J. Phys. B, **17**, 95 (1984).

13. Ch.M. Marian, M. Gastreich, J.D. Gale. Phys. Rev. B-I, **62**, 3117 (2000).
14. V.V. Pokropivnyj, V.V. Skorokhod, G.S. Oleinik, A.V. Kurdyumov, T.S. Bartnitskaya, A.V. Pokropivnyj, A.G. Sisonyuk, D.M. Sheichenko. J. Solid State Chem., **154**, 214 (2000).
15. L. Chkhartishvili. In: Proc. 2nd Int. Boron Symp. Eskişehir: OGU, 165 (2004).
16. L. Chkhartishvili, D. Lezhava, O. Tsagareishvili, D. Gulua. Trans. AMIAG, **1**, 295 (1999).
17. A. Gaydon. Dissociation Energies and Spectra of Diatomic Molecules. London: Chapman & Hall (1947).
18. K.P. Huber, G. Herzberg. Molecular Spectra and Molecular Structure. IV. Constants of Diatomic Molecules. New York: van Nostrand Reinhold Co (1979).
19. R.A. Evarestov. Quantum-Chemical Methods in Solid State Theory. Leningrad: LU (1982).
20. G. Will, A. Kirfel. AIP Conf. Proc., **140**, 87 (1986).
21. G. Will, A. Kirfel, B. Josten. J. Less-Comm. Met., **117**, 61 (1986).
22. A. Garcia, M.L. Cohen. Phys. Rev. B-II, **47**, 4215 (1993).
23. A. Garcia, M.L. Cohen. Phys. Rev. B-II, **47**, 4221 (1993).
24. Zh. Zhang, Sh. Zhou, Y. Xiong. Yunnan Daxue Xuebao (Ziran Kaxueban), **20**, 407 (1998).
25. M. Lorenz, J. Agreiter, A.M. Smith, V.E. Bondybey. J. Chem. Phys., **104**, 3143 (1996).
26. L. Chkhartishvili, D. Lezhava, O. Tsagareishvili. J. Solid State Chem., **154**, 148 (2000).
27. E. Doni, E. G. Pastori Parravicini. Nuo. Cim. B, **64**, 117 (1969).
28. A. Zunger. J. Phys. C, **7**, 76 (1974).
29. A. Zunger. J. Phys. C, **7**, 96 (1974).
30. W.A. Harrison. Electronic Structure and the Properties of Solids. The Physics of the Chemical Bond. San Francisco: W.H. Freeman and Co (1980).
31. Chkhartishvili, L. 2006, Proc. TSU (Phys.), **40**, 130.
32. V.I. Vedeneev, L.V. Gurvich, V.N. Kondrat'ev, V.A. Medvedev, E.A. Frankevich. Chemical Bonds Breaking Energies. Ionization Potentials and Electron Affinities. Moscow: Acad. Sci. USSR (1962).
33. G. Meloni, M. Sai Baba, K.A. Gingerich. J. Chem. Phys., **113**, 8995 (2000).
34. R. Vanderbosch. Phys. Rev. A, **67**, 013203 (2003).
35. A. Abdurahman, A. Shukla, M. Dolg. Phys. Rev. B, **65**, 115106 (2002).
36. R.T. Senger, S. Tongay, E. Durgun, S. Ciraci. Phys. Rev. B, **72**, 075419 (2005).
37. M. Côté, P.D. Haynes, C. Molteni. Phys. Rev. B, **63**, 125207 (2001).
38. S.V. Lisenkov, G.A. Vinogradov, T.Yu. Astakhova, N.H. Lebedev. JETP Lett., **81**, 431 (2005).
39. D.L. Strout. J. Phys. Chem. A, **104**, 3364 (2000).
40. L.S. Chkhartishvili. Phys. Solid State, **46**, 2056 (2004).
41. L.S. Chkhartishvili. Phys. Solid State, **48**, 846 (2006).
42. L. Chkhartishvili, D. Lezhava. Trans. GTU, **439**, 87 (2001).
43. Boron Nitride (BN). In: Landolt-Börnstein. Neue Serie. Gruppe III, Band 17, Teiband a (Ed. O. von Madelung). Berlin: Springer–Verlag, 148 (1982).
44. Y.-N.Xu, M.Y. Ching. Phys. Rev. B-I, **44**, 7784 (1991).
45. K. Albe. Phys. Rev. B-II, **55**, 6203 (1997).
46. Boron Nitride. In: Selected Values of Chemical Thermodynamic Properties (Eds. D.D. Wagmann, W.H. Evans, V.B. Parker, J. Halow, S.M. Bairly, R.L. Shumn). Washington: NBS, 270 (1968).
47. S.N. Grinyaev, F.V. Konusov, V.V. Lopatin. Phys. Solid State, **44**, 275.(2002).
48. M.S.C. Mazzoni, R.W. Nunes, S. Azevedo, H. Chacham. Phys. Rev. B, **73**, 073108 (2006),.
49. S.A. Shevlin, Z.X. Guo. Phys. Rev. B, **76**, 024104 (2007).
50. S.V. Lisenkov, G.A. Vonogradov, Y, Yu. Astakhova, N.G. Lebedev. Phys. Solid State, **48**, 179 (2006).
51. R.A. Evarestov, I.I. Tupitsyn. Phys. Solid State, **44**, 1656 (2002).
52. M.S. Nakhmanson, V.P. Smirnov. Phys. Solid State, **13**, 752 (1971).

53. M.S. Nakhmanson, V.P. Smirnov. Phys. Solid State, **13**, 2763 (1971).
54. J. Zupan. Phys. Rev. B, **6**, 2477 (1972).
55. K.T. Park, K. Terakura, N. Hamada. J. Phys. C, **20**, 1241 (1987).
56. J. Barth, C. Kunz, T.M. Zimkina. Solid State Commun., **36**, 453 (1980).
57. D.J. Joyner, D.M. Hercules. J. Chem. Phys., **72**, 1095 (1980).
58. J. Nakamura, T. Nitta, A. Natori. Phys. Rev. B, **72**, 205429 (2005).
59. M.S. Si, D.S. Xue. Phys. Rev. B, **75**, 193409 (2007).
60. R.-F. Liu, Ch. Cheng. Phys. Rev. B, **76**, 014405 (2007).
61. K. Suenaga, C. Colliex, N. Demoncy, A. Loieseau, H. Pascard, F. Willaime. Science, **278**, 653 (1997).
62. K. Suenaga, F. Willaime, A. Loieseau, C. Colliex. Appl. Phys. A, **68**, 301 (1999).
63. A. Loiseau, F. Willaime, N. Demoncy, G. Hug, H. Pascard. Phys. Rev. Lett., **76**, 4737 (1996).
64. Y. Saito, M. Maida, T. Matsumoto. Jpn. J. Appl. Phys. 1A, **38**, 159 (1999).
65. Y. Saito, M. Maida. J. Phys. Chem. A, **103**, 129 (1999).
66. D. Golberg, Y. Bando, M. Eremets, K. Tekemura, K. Kurashima, H. Yusa. Appl. Phys. Lett., **69**, 2045 (1996).
67. R. Sen, B.C. Satishkumar, A. Govindaraj, K.R. Harikumar, G. Raina, J.-P. Zhang, A.K. Cheetham, C.N.R. Rao. Chem. Phys. Lett., **287**, 671 (1998).
68. D. Golberg, Y. Bando, W. Han, K. Kurashima, T. Sato. Chem. Phys. Lett., **308**, 337 (1999).
69. D. Golberg, W. Han, Y. Bando, L. Bourgeois, K. Kurashima, T. Sato. J. Appl. Phys., **86**, 2364 (1999).
70. Y. Chen, L.T. Chadderton, J.F. Gerald, J.S. Williams. Appl. Phys. Lett., **74**, 2960 (1999).
71. T.S. Bartnitskaya, G.S. Olejnik, V.V. Pokropivnyj, N.V. Danilenko, V.M. Vershchaka, A.V. Kotko. Superhard Mat., **6**, 71 (1998).
72. T.S. Bartnitskaya, G.S. Olejnik, A.V. Pokropivnyj, V.V. Pokropivnyj. JEPT Lett., **69**, 145 (1999).
73. C. Colazo–Davila, E. Bengu, L.D. Marks, M. Kirk. Diam. Rel. Mat., **8**, 1091 (1999).
74. T. Oku, T. Hirano, M. Kuno, T. Kusunose, K. Niihara, K. Suganuma. Mat. Sci. Eng. B, **74**, 206 (2000).
75. J. Wang, V.K. Kayastha, Y.Kh. Yap, Zh. Fan, J.G. Lu, Zh. Pan, I.N. Ivanov, A.A. Puretzky, D.B. Geohegen. Nano Lett., **5**, 2528 (2005).
76. A.A. Frolov, L.L. Sartinskaya, N.I. Danilenko, M.M. Nishchenko, V.I. Patoka. In: Proc. 4th Int. Conf. “Mater. & Coat. Extr. Perf.”. Kiev: IPMS, 344 (2006).
77. O.E. Alon. Phys. Rev. B, **64**, 153408 (2001).
78. V.V. Pokropivnyj. Powd. Metall. Met. Cer., **11/12**, 51 (2001).
79. M. Menon, D. Srivastava. Chem. Phys. Lett., **307**, 407 (1999).
80. J.-C. Charlier, X. Blasé, A. de Vita, R. Car. Appl. Phys. A, **68**, 267 (1999).
81. L.S. Chkhartishvili. In: Thin Films in Optics and Nanoelectronics. Kharkiv: KhPTI, 367 (2006).
82. Z. Peralta Inga, P. Lane, J.S. Murray, S. Boyd, M.E. Grice, Ch.J. O’Connor, P. Politzer. Nano Lett., **3**, 21 (2003).
83. D. Golberg, Y. Bando, L. Bourgeois, K. Kurashima, T. Sato. Appl. Phys. Lett., **77**, 1979 (2000).
84. S. Okada, S. Saito, A. Oshiyama. Phys. Rev. B, **65**, 165410 (2002).
85. Yu.B. Kuz’ma, N.F. Chaban. Binary and Ternary Systems Containing Boron. Handbook. Moscow: Metallurgiya (1990).
86. L.S. Chkhartishvili. Nano Str. Mater. Sci., **1**, 33 (2009).
87. E. Hernández, C. Goze, P. Bernier, A. Rubio. Phys. Rev. Lett., **80**, 4502 (1998).
88. N.G. Lebedev, L.A. Chernozatonskij. Phys. Solid State, **48**, 1909 (2006).
89. X.J. Xiang, J. Yang, J.G. Hou, Q Zhu. Phys. Rev. B, **68**, 035427 (2003).

90. L. Wirtz, A. Rubio, R.A. de la Concha, A. Loiseau. Phys. Rev. B, **68**, 045425 (2003).
91. L. Wirtz, M. Lazzeri, F. Mauri, A. Rubio. Phys. Rev. B, **71**, 241402(R) (2005).
92. H.F. Bettinger, T. Dumitrică, G.E. Scuseria, B.I. Yakobson. Phys. Rev. B, **65**, 041406 (2002).
93. Y. Miyamoto, A. Rubio, S. Berber, M. Yoon, D. Tománek. Phys. Rev. B, **69**, 121413(R) (2004).
94. G.Y. Gou, B.C. Pan, L. Shi. Phys. Rev. B, **76**, 155414 (2007).
95. E. Hernandez, C. Goze, P. Bernier, A. Rubio. Appl. Phys. A, **68**, 287 (1999).
96. D. Srivastava, M. Menon, K.-J. Cho. Phys. Rev. B, **63**, 195413 (2001).
97. T. Dumitrică, B.I. Yakobson. Phys. Rev. B, **72**, 035418 (2005).
98. J. Wu, W-Q. Han, W. Walukiewicz, J.W. Ager III, W. Shan, E.E. Haller, A. Zettl. Nano Lett., **4**, 647 (2004).
99. A.G. Marinopoulos, L. Wirtz, A. Marini, V. Olevano, A. Rubio, L. Reining. Appl. Phys. A, **78**, 1157 (2004).
100. G.Y. Guo, J.C. Lin. Phys. Rev. B, **71**, 165402 (2005).
101. G.Y. Guo, J.C. Lin. Phys. Rev. B, **72**, 075416 (2005).
102. G.Y. Guo, J.C. Lin. Phys. Rev. B, **77**, 049901(E) (2008).
103. A.M. Panich, A.I. Shames, N. Froumin, C.C. Tang, Y. Bando. Phys. Rev. B, **72**, 085307 (2005).
104. X. Blasé, J.-C. Charlier, A. de Vita, R. Car. Appl. Phys. A, **68**, 293 (1999).
105. B. Baumeier, P. Krüger, J. Pollmann. Phys. Rev. B, **76**, 085407 (2007).
106. V.A. Margulis, E.E. Muryumin, E.A. Gaiduk. Phys. Rev. B, **77**, 035425 (2008).
107. Y.-H. Kim, K.J. Chang, S.G. Louie. Phys. Rev. B, **63**, 205408 (2001).
108. E.G. Gal'pern, V.V. Pinyaskin, I.V. Stankevich, L.A. Chernozatonskii. J. Phys. Chem. B, **101**, 705 (1997).
109. T.M. Schmidt, R.J. Baierle, P. Piquini, A. Fazzio. Phys. Rev. **B**, 67, 113407 (2003).
110. S.S. Han, S.H. Lee, J.K. Kang, H.M. Lee. Phys. Rev. B, **72**, 113402 (2005).
111. J. Zhang, K.P. Loh, J. Zheng, M.B. Sullivan, P. Wu. Phys. Rev. B, **75**, 245301 (2007).
112. X. Blasé, J.-C. Charlier, A. de Vita, R. Car. Appl. Phys. Lett., **70**, 197 (1997).
113. Ch. Zhi, Y. Bando, Ch. Tang, D. Golberg. Phys. Rev. B, **74**, 153413 (2006).
114. Ch. Zhi, Y. Bando, Ch. Tang, D. Golberg. Phys. Rev. B, **74**, 199902(E) (2006).
115. E.J. Mele, P. Král. Phys. Rev. Lett., **88**, 056803 (2002).
116. N. Sai, E.J. Mele. Phys. Rev. B, **68**, 242405(R) (2003).
117. S.M. Nakhmanson, A. Cazolari, V. Meunier, J. Bernholc, M. Buongiorno Nardelli. Phys. Rev. B, **67**, 235406 (2003).
118. Y. Zhang, K. Suenaga, C. Colliex, S. Iijima. Science, **281**, 973 (1998).
119. A. Zobelli, A. Gloter, C.P. Ewels, G. Seifert, C. Colliex. Phys. Rev. B, **75**, 245402 (2007).
120. W.-Q. Han, C.W. Chang, A. Zettl. Nano Lett., **4**, 1355 (2004).
121. K. Yum, M.-F. Yu. Nano Lett., **6**, 329 (2006).
122. E. Durgun, Y.-R. Jang, S. Ciraci. Phys. Rev. B, **76**, 073413 (2007).
123. W. Han, Y. Bando, K. Kurashima, T. Sato. Jpn. J. Appl. Phys. II, **38**, L755 (1999).
124. E. Bengu, L.D. Marks. Phys. Rev. Lett., **86**, 2385 (2001).
125. V. Pokropivnyj, A. Smolyar, A. Pokropivnyj, V. Bekenev, V. Kutsc, R. Partch. In: Abs. 15th Int. Symp. Boron, Borides & Rel. Mat. Humburg: UH, 46 (2005).
126. H. Zhang, J.D.F. Gerald, L.T. Chadderton, J. Yu, Y. Chen. Phys. Rev. B, **74**, 045407 (2006).
127. L.I. Ovsianikova, V.V. Pokropivnyj. In: Proc. Int. Conf. High Mat Tech. Kiev: IPMS, 118 (2007).
128. C. Souche, B. Jouffrey, G. Hug, M. Nelhiebel. Micron, **29**, 419 (1998).
129. L. Bourgeois, Y. Bando, W.Q. Han, T. Sato. Phys. Rev. B, **61**, 7686 (2000).
130. L.S. Chkhartishvili. Nanomaterials 2. Kharkiv: KhPTI, 23 (2008).

131. J. Kawai, Y. Muramatsu, M. Kobayashi, I. Higashi, H. Adachi. Jpn. J. Appl. Phys. Ser., **10**, 72 (1993).
132. M.E. Zandler, E.C. Behrman, M.B. Arrasmith, J.R. Myers, T.V. Smith. J. Mol. Str.: TheoChem., **362**, 215 (1996).
133. P.W. Fowler, K.M. Rogers, T. Heine, G. Seifert. AIP Conf. Proc., **486**, 170 (1999).
134. T. Hirano, T. Oku, K. Suganuma. Diam. Rel. Mat., **9**, 625 (2000).
135. T. Hirano, T. Oku, K. Suganuma. Met. Inst. Sci. Ind. Res., **57**, 181 (2000).
136. D.L. Strout. J. Phys. Chem. A, **105**, 261 (2001).
137. S.S. Alexandre, H. Chacham, R.W. Nunes. Phys. Rev. B, **63**, 045402 (2001).
138. M.G. Giuffreda, M.S. Deleuze, J.-P. Francois. J. Phys. Chem. A, **104**, 5855 (2000).
139. K.N. Kudin, G.E. Scuseria, B.I. Yakobson. Phys. Rev. B, **64**, 235406 (2001).
140. I.V. Stankevich, R. Seto. Phys. Solid State, **43**, 1916 (2001).
141. Q. Sun, Q. Wang, P. Jena. Nano Lett., **5**, 1273 (2005).
142. R.J.C. Batista, M.S.C. Mazzoni, H. Chacham. Phys. Rev. B, **75**, 035417 (2007).
143. S.S. Alexandre, R.W. Nunes, H. Chacham. Phys. Rev. B, **66**, 085406 (2002).
144. V.V. Pokropivnyj, A.V. Pokropivnyj, V.V. Skorokhod, A.V. Kurdyumov. Reps. Ukr. Natl. Acad. Sci., **4**, 112 (1999).
145. V.V. Pokropivnyj, V.V. Skorokhod, A.V. Kurdyumov, G.S. Oleinik, T.S. Bartnitskaya, A.V. Pokropivnyj. Proc. SPIE, **3790**, 213 (1999).
146. S.S. Alexandre, M.S.C. Mazzoni, H. Chacham. Appl. Phys. Lett., **75**, 61 (1999).
147. M.S. Deleuze, M.G. Giuffreda, J.-P. Francois, L.S. Cederbaum. J. Phys. Chem. A, **104**, 1588 (2000).
148. S. Compernolle, A. Ceulemans. Phys. Rev. B, **71**, 205407 (2005).
149. L.A. Chernozatonskij, Ya.K. Shimkus, I.V. Stankevich. Phys. Lett. A, **240**, 105 (1998).
150. L. Chkhartishvili. Sci. Trans. TSUB, **1**, 195 (2003).
151. L. Chkhartishvili. Quasi-Classical Theory of Substance Ground State. Tbilisi: GTU (2004).
152. L. Chkhartishvili. In: Proc. Int. Sci. Conf. FMNS. Blagoevgrad: SWU, 45 (2005).
153. L. Chkhartishvili. Quasi-Classical Method of Calculation of Substance Structural and Electronic Energy Spectrum Parameters. Tbilisi: TSU (2006).
154. L.S. Chkhartishvili. Math. Notes, **69**, 421 (2001).
155. L.S. Chkhartishvili. Trans. GTU, **452**, 15 (2004).
156. L.S. Chkhartishvili. Math. Notes, **77**, 273 (2005).
157. L. Chkhartishvili. In: Proc. Georg. Math. Union's 4th Cong. Tbilisi: IM, 151 (2005).
158. L.S. Chkhartishvili. Math. Notes (in press).
159. L. Chkhartishvili, D. Lezhava, O. Tsagareishvili. In: Abs. 13th Int. Symp. Boron, Borides & Rel. Comp. Rennes: CNRS, 55 (1999).
160. L. Chkhartishvili, D. Lezhava. In: Abs. 13th Int. Symp. Boron, Borides & Rel. Comp. Rennes: CNRS, 56 (1999).
161. L. Chkhartishvili. In: Proc. 1st Int. Boron Symp. Kütahya: DU, 139 (2002).
162. L. Chkhartishvili. In: Abs. 14th Int. Symp. Boron, Borides & Rel. Comp. Saint Petersburg: PTI, 68 (2002).
163. L. Chkhartishvili. J. Solid State Chem., **177**, 395 (2004).
164. L. Chkhartishvili. Sci. Res. ICTU, **1**, 296 (2005).
165. L. Chkhartishvili. Mat. Sci.: An Ind. J., **2**, 18 (2006).
166. T.L. Hill, R.V. Chamberlin. Nano Lett., **2**, 609 (2002).

ПОЛУЧЕНИЕ НАНОЧАСТИЦ ОКСИДА ЖЕЛЕЗА МЕТОДОМ ЛАЗЕРНОЙ АБЛЯЦИИ

В.Г. Квачадзе [1], Т.И. Павлиашвили [1], Г.Г. Абрамишвили [1], Т.Л. Калабегишвили [1, 2], В.М. Габуния [3]

[1] Институт физики Э. Андроникашвили
vkvachadze@yahoo.com
[2] Государственный университет Илии
[3] Институт металургии и материаловедения Ф. Тавадзе

Принята 19 февраля 2010 года

1. ВВЕДЕНИЕ

В настоящее время интенсивно изучаются свойства магнитных наночастиц и магнитных жидкостей коллоидных суспензий однодоменных магнитных частиц в жидкости. Физические свойства магнитных жидкостей определяются содержанием дисперсной фазы, агрегативной устойчивостью дисперсных частиц и напряжением внешнего магнитного поля, с помощью которого и формируются их магнитные свойства. Последнее позволяет целенаправленно изменять свойства магнитных жидкостей в соответствии с прикладными задачами [1,2]. Имеется в виду применение магнитных жидкостей в антифрикционных узлах и демпферах, в ультразвуковой дефектоскопии, магнитных сепараторах редких элементов, в механизмах роботов и т.д.

Синтез магнитных жидкостей возможен различными методами [1]: методом измельчения магнитных частиц, электрохимическим методом, путем конденсации паров металлов в жидкости, методом химического осаждения и др. Нами для синтеза наночастиц а-оксида железа использовался метод лазерной абляции, В этом случае возможно получение наночастиц, свободных от посторонних примесей [3]. Именно «чистые» наночастицы необходимы для перспективного их применения в области биомедицины (например, адресной доставки лекарств в терапии рака), что определяет цель данной работы.

2. ЭКСПЕРИМЕНТ И ОБСУЖДЕНИЕ РЕЗУЛЬТАТОВ

Порошок a-Fe_2O_3 (гематит) помещался в кварцевый стакан с дистиллированной водой и подвергался воздействию рубинового лазера ОГМ – 20 (694.3 nm). Мощность импулса составляла $3 \cdot 10^6$ W; длительность на уровне 0.5 максимальной интенсивности излучения не более $3 \cdot 10^{-8}$ s. Частота следования импульсов – 1 Hz.

В результате многократного воздействия лазерных импульсов в дистиллированной воде был получен взвесь аблированных частиц. Размеры наночастиц определялись методом Дебая–Шерера, согласно которому, дифрактометр регистрирует кристаллический образец в параллельном пучке монохроматического рентгеновского излучения.

На рис. 1 представлена дифрактограмма исследуемых наночастиц.

Согласно расчетам, которые проводились по формуле:

$\Delta B = K \lambda R L \cos\theta$,

где $\Delta B = B - B_0$ – прирост ширины линии, B – измеренная ширина линии, B_0 – ширина линии для кристаллов оптимальных размеров (около 10^4 Å), L – линейный размер полученных нанокристаллов, K – величина, близкая к 1, R – радиус камеры в mm [4], средний размер полученных нанокристаллов не превышает (80 – 100) nm. Однако исследования,

которые проводились с помощью растрового микроскопа (Nanolab – 7, OPTON), показали, что в магнитной жидкости наряду с крупными агломератами наблюдаются наночастицы с размерами порядка 20 nm (рис. 2).

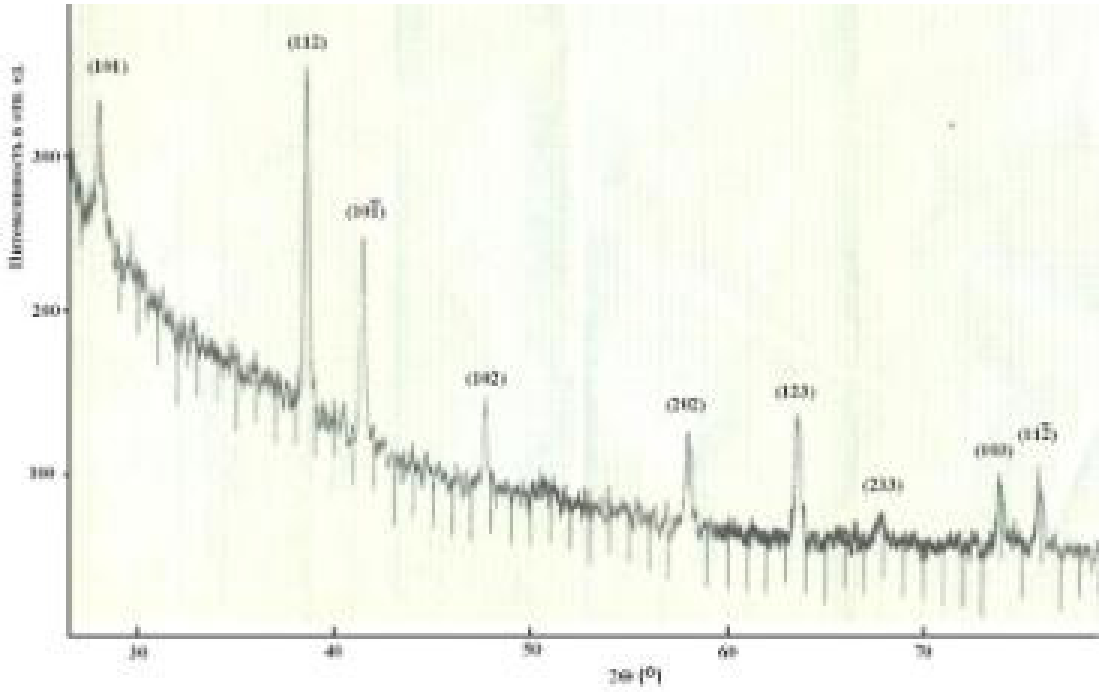

Рис. 1. Дифрактограмма кристаллитов a-Fe_2O_3.

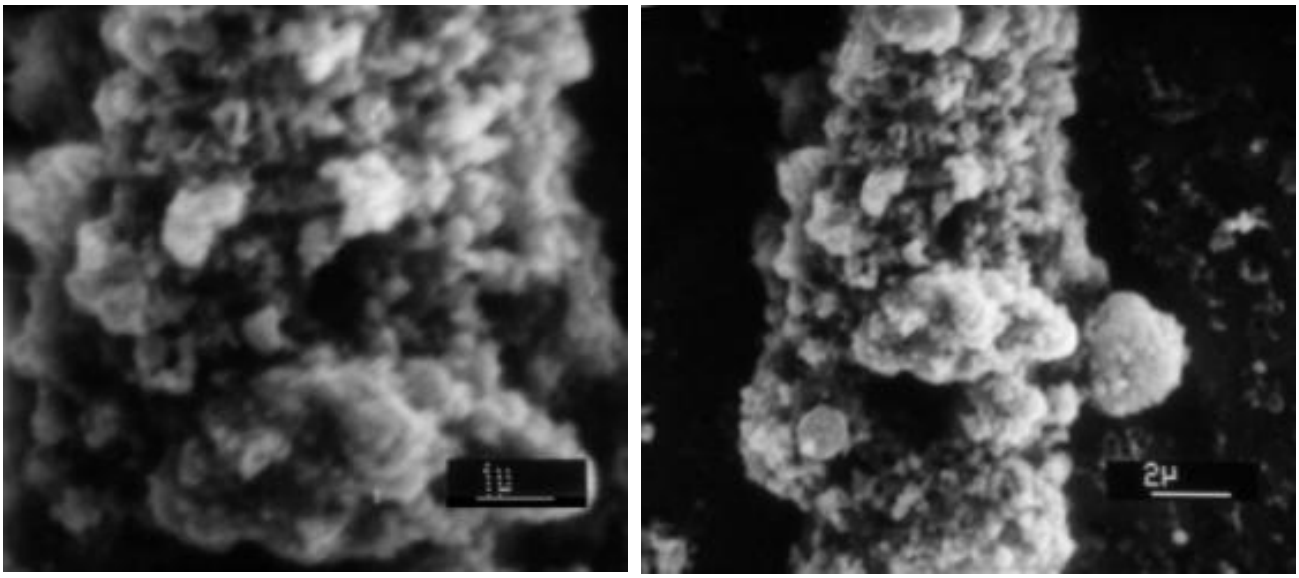

Рис. 2. Наночастицы a-Fe_2O_3, образовавшиеся при лазерной абляции (микрофотографии получены с помощью электронного растрового микроскопа Nanolab – 7).

Аналогичные исследования, проведенные с помощью трансмиссионного микроскопа (JEM 100 – Sx), подтвердили результаты, отмеченные выше: на рис. 3 видно, что размеры полученных наночастиц изменяются в широком диапазоне, наименьшие из которых ~ (10 – 20) nm. Таким образом, на наш взгляд, метод лазерной абляции может быть перспективным методом для получения наночастиц a-Fe_2O_3.

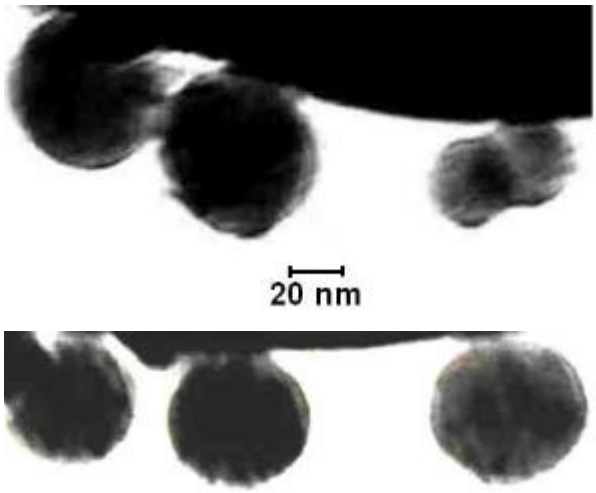

Рис. 3. Наночастицы a-Fe_2O_3, образовавшиеся при лазерной абляции (микрофотографии получены с помощью электронного трансмиссионного микроскопа JEM 100 – Sx).

Проведенные исследования показали также, что без применения поверхностно-активного вещества для стабилизации невозможно получить однородную магнитную жидкость с наночастицами a-Fe_2O_3.

3. ЗАКЛЮЧЕНИЕ

Результаты данной работы показали перспективность метода лазерной абляции для получения наночастиц a-Fe_2O_3. Целенаправленным варьированием параметров процесса лазерной абляции и выбором соответствующих поверхностно-активных веществ в дальнейшем можно значительно сократить долю агломерированных частиц и получить наночастицы с оптимальными характеристиками.

БЛАГОДАРНОСТИ

Выражаем искренную благодарность за оказанную помощь в получении микрофотографий наночастиц на растровом и трансмиссионном электронных микроскопах докторам наук Н. Джалабадзе и Г. Церцвадзе.

ССЫЛКИ

1. Б.М. Берковский, В.Ф. Медведев, М.С. Краков. Магнитные жидкости. Москва: Химия (1989).
2. Ч. Пул-мл., Ф. Оуэнс. Нанотехнологии. Москва: Техносфера (2007).
3. А.В. Симакин, В.В. Воронов, Г.А. Шафеев. Тр. Инст. общей физики им. А.М. Прохорова РАН, **60,** 83 (2004).
4. Б.Ф. Ормонт. Введение в физическую химию и кристаллохимию полупроводников. Москва: Высшая школа (1973).

SYNTHESIS OF SILVER NANOPARTICLES USING BACTERIA

N. Tsibakhashvili [1, 2], T. Kalabegishvili [1, 2], V. Gabunia [3], E. Gintury [2], N. Kuchava [2], N. Bagdavadze [2], D. Pataraya [4], M. Gurielidzse [4], D. Gvarjaladze [1], L. Lomidze [1]

[1] Ilia State University
nelly_tsibakhashvili@yahoo.com
[2] E. Andronikashvili Institute of Physics
[3] S. Durmishidze Institute of Biochemistry and Biotechnology
[4] F. Tavadze Institute of Metallurgy and Material Sciences

Accepted February 24, 2010

1. INTRODUCTION

The development of reliable experimental protocols for the synthesis of nanomaterials over a range of chemical compositions, sizes, and high monodispersity is one of the challenging issues in current nanotechnology. New methods to produce nanoparticles are constantly being studied and developed. It is important that physical and chemical methods are low-yield, energy intensive, difficult to scale up, often produce high levels of hazardous wastes, and may require the use of costly organometallic precursors. Besides, chemical synthesis may still lead to the presence of some toxic chemical species adsorbed on the surface that may have adverse effects in medical applications. Hence, there is an ever-growing need to develop inexpensive, clean, nontoxic, and environmentally benign synthesis procedures. Consequently, in last years researchers in nanoparticle synthesis have turned to biological systems for inspiration [1].

Microorganisms are recently found as possible eco-friendly nanofactories, even though they have many biotechnological applications such as remediation of toxic metals [2]. Formation of silver nanocrystallites in microorganisms including bacteria, yeasts, fungi has been reported [3,4]. However, screening of different classes of microbes as possible "nano-factories" has not been done so far. The purpose of this work was to monitor production of silver nanoparticles by cianobacteria *Spirulina platensis* and actinobacteria *Streptomyces* spp. 211A.

2. EXPERIMENTAL PROCEDURE

2.1. Model bacteria and their cultivation

All chemicals were ACS-reagent grade and purchased from Sigma (St. Louis, MO, USA).

Sp. platensis was cultivated in the Zarrouk growth media at constant shaking at (30 – 31) °C, at pH 5. The bacterial cells were harvested after (5 – 6) days and then were washed twice in distilled water. Silver nanoparticles formations were carried out by taking 1 g of wet biomass in a 250 ml Erlenmeyer flask with 10^{-3} M aqueous $AgNO_3$ for different times (2, 4, 7, 8 days) and incubated at room temperature. The pH was checked during the course of reaction and it was found to be 5.6.

The alkaliphilic (extremophilic) actinobacteria – *Streptomyces* spp. 211A have been isolated from solonetz soil of Sagarejo Region (Georgia). The strain develop at pH 7 – 11, with optimum growth temperature at (28 – 30) °C. Bacterial cells were grown aerobically in 500 ml Erlenmayer flasks. The cells were grown in a liquid medium Gauze – 1: K_2HPO_4 (0.05 %), $MgSO_4$ (0.05 %), NaCl (0.05 %), KNO_3 (0.1 %), $FeSO_4 \cdot 7H_20$ (0.001 %), starch (2 %), east extract (0.03 %), pH 7.5. The culture was grown with continuous shaking on a shaker (200 rpm) at 30 °C for 9 days. After cultivation, mycelia (cells) were separated from the culture broth by centrifugation (4500 rpm) for

20 min and then the mycelia were washed thrice with sterile distilled water under sterile conditions. The harvested mycellial mass (16 g of wet mycelia) was then resuspended in 100 ml of 10^{-3} M aqueous $AgNO_3$ solution in 500 ml Erlenmeyer flasks. The whole mixture was put into a shaker at 30 °C (200 rpm).

For X-ray analysis bacterial cells were harvested by centrifugation at 12000 rpm for 20 min.

2.2. Methods

Silver nanoparticles exhibit striking color (light yellow to brown for silver) due to excitation of surface plasmon vibrations in the particles, and thus provide a convenient means of visually determining their presence in samples [5]. The UV−Vis spectra of the solution were recorded on a spectrophotometer "Cintra 10e" (GBC Scientific Equipment Pty Ltd, Australia, with digital data acquisition system, wavelength range (190 – 1100) nm).

XRD measurements of bacterial biomass were made on a "Dron – 2.0" diffractometer instrument. X-ray tube BCV−23 with Cu anode (Cuka – $\lambda = 1.541781$ Å) was used as a source of irradiation; Ni grid with a width of 20 μm was used for filtration of irradiation; the rate of detector was 2° / min, the interval of intensity was 1000 impulse / min and the time constant was 5 s.

3. RESULTS AND DISCUSSION

Addition of *Sp. platensis* biomass to 10^{-3} M aqueous $AgNO_3$ solution led to the appearance of yellowish brown color in solutions after 2 days, indicating the formation of silver nanoparticles. Fig. 1 shows the UV−Vis spectra recorded from the aqueous silver nitrate – *Sp. platensis* reaction medium, as a function of time of reaction. The presented spectra exhibit the appearance of an absorption peak at 425 nm, which progressively increases in intensity as a function of time of reaction without any shift in the peak wavelength. The presence of the absorption peak at 425 nm is characteristic of silver nanoparticles [5].

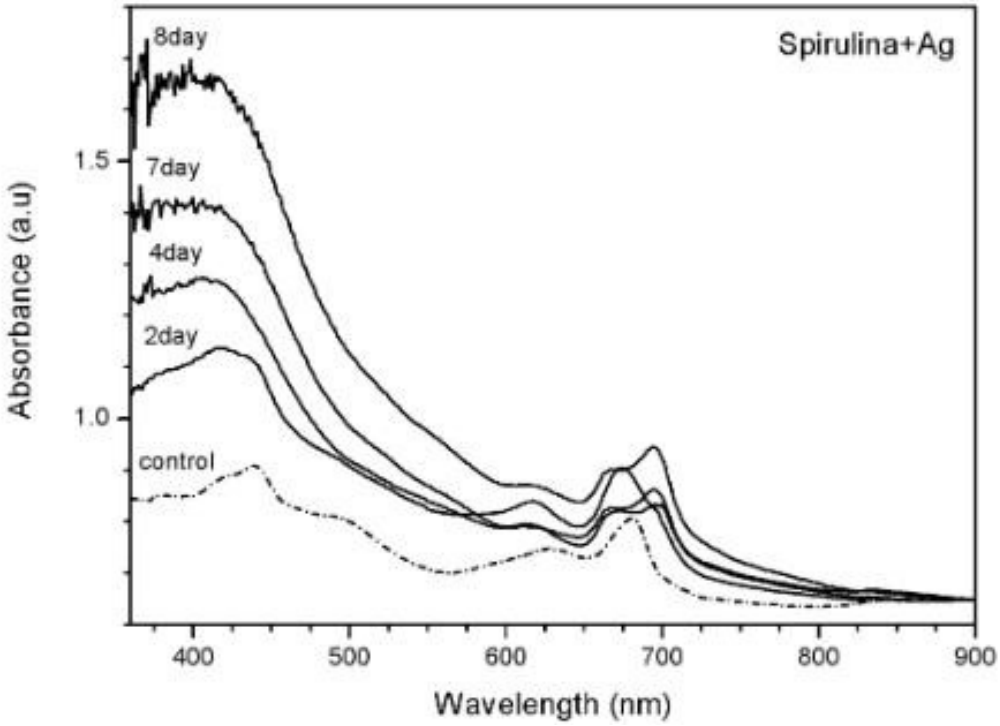

Fig. 1. UV−Vis spectra recorded as a function of time of reaction of aqueous solution of silver nitrate with *Sp. Platensis*.

In Fig. 2 UV–Vis spectrum recorded from the *Streptomyces* spp. 211A – silver nitrate aqueous solution at 9 days is presented. Fig. 2 also shows the strong absorption peak characteristic to silver nanoparticles.

The observation of peak at 425 nm in the aqueous silver nitrate – *Sp. platensis* and silver nitrate – *Streptomyces* spp. 211A reaction medium indicates the extracellular synthesis of silver nanoparticles. Our further experiments confirm this result. Really, we applied X-ray analysis to detect silver nanoparticles in bacterial biomass. We observed silver nanoparticles in biomass of *Sp. platensis* treated with silver nitrate (Fig. 3).

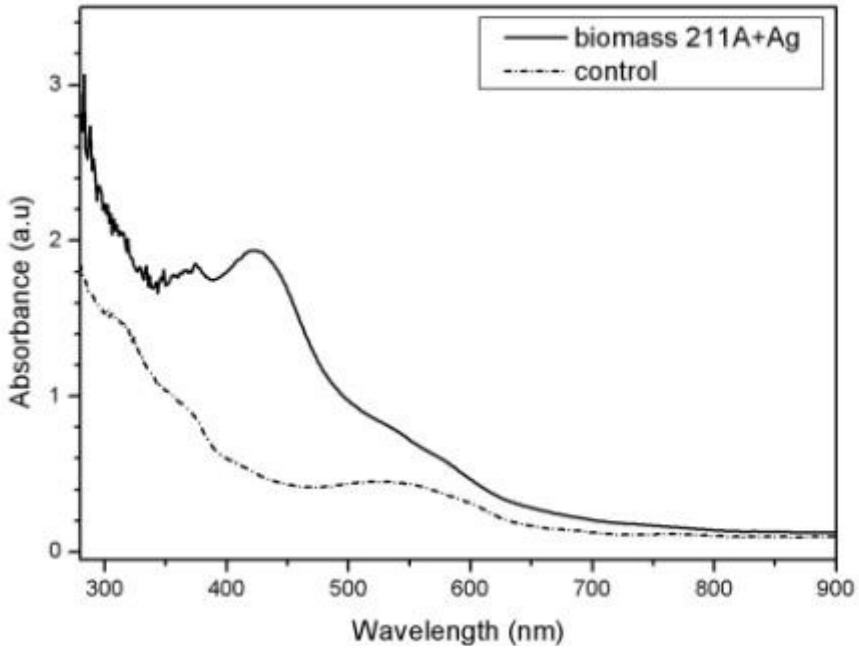

Fig. 2. UV–Vis spectra of biomass of *Streptomyces* spp. 211A treated with 10^{-3} M $AgNO_3$ aqueous solution for 9 days.

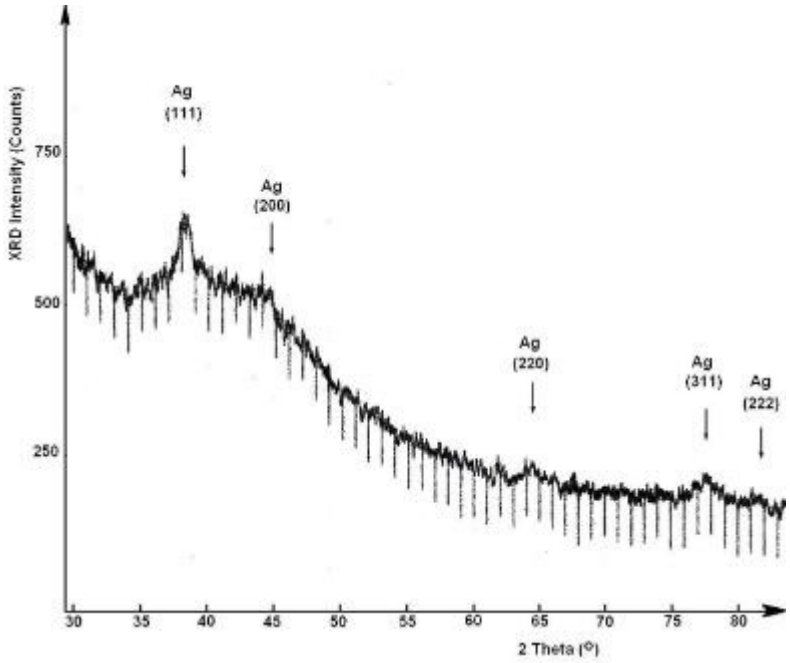

Fig. 3. Diffractogram of *Sp. platensis* biomass after exposure to 10^{-3} M $AgNO_3$ aqueous solution for 2 days.

In Fig. 3, as an example, the XRD patterns of silver nanoparticles synthesized by treating of *Sp. platensis* with silver nitrate aqueous solution for 2 days is presented. The obtained diffractogram corresponds to amorphic structure of the sample. However patterns of nanoparticles are also visualized. It should be noted that the content of crystalline silver was not high in tested samples. It was no more than 1 %, suggesting that silver nanoparticles were produced, in general, extracellularly. The grains of silver nanocrystalles had small size which caused the broadening of peaks. We estimated the size of silver grains by this broadening using the Debye–Sherrer equation:

$$\Delta(2\theta) = m\lambda / D\cos\theta \quad . \qquad (1)$$

Here $\Delta(2\theta)$ is the half-width of interference maximum (in radians); m is the factor of shape of crystal, which corresponds to 1 for centered cubic phase; λ is the wave length (Cuka – $\lambda = 0.154178$ nm); D is the size of grain (nm); θ is the Bregg's angle.

According to (1), D is in the range of $(10 - 15)$ nm. The obtained result corresponds well with the result reported recently in [6]. Specifically, interaction of single cell protein of *Sp. platensis* with aqueous $AgNO_3$ caused extracellular synthesis of Ag nanoparticles with sizes in the range of $(7 - 16)$ nm.

4. CONCLUSION

In this study, we have demonstrated that the use of cianobacteria *Spirulina platensis* and actinobacteria *Streptomyces* spp. 211A offers a means of developing "nanofactories" for production of silver nanoparticles simply and inexpensive. Silver nanoparticles have a great number of applications such as in non-linear optics, spectrally selective coating for solar energy absorption, biolabelling, intercalation materials for electrical batteries, as optical receptors, high-sensitivity biomolecular detection and diagnostics, antimicrobials and therapeutics, catalysis and micro-electronics.

ACKNOWLEDGEMENT

This work was funded by Grant # 4744 from the Science and Technology Center in Ukraine (STCU).

REFERENCES

1. Biological Nanostructures and Applications of Nanostructures in Biology: Electrical, Mechanical, and Optical Properties (Eds. M.A. Stroscio, M. Dutta). New York: Kluwer Academic Publisher (2002).
2. G.M. Evans, J.C. Furlong. Environmental Biotechnology: Theory and Applications. Weinhem: Weinheim & Sons (2003).
3. D. Mandal, M. Bolander, D. Mukhopadhyay, G. Sarkar, P. Mukherjee. Appl. Microbial Biotechnol., **69**, 485 (2006).
4. P. Mukherjee, S. Senapti, D. Mandal, A. Ahmad, M.I. Khan, R. Kumar, M. Sastry. Chem. Bio.Chem., **3**, 461 (2002).
5. P. Mulvaney. Langmuir, **12**, 788 (1996).
6. K. Govindaraju, S.K. Basha, V.G. Kumar, G. Singaravelu. J. Mater. Sci., **43**, 5115 (2008).

ON RELATIVE STABILITY OF SINGLE-WALLED BORON NITRIDE NANOTUBES

L. Chkhartishvili, I. Murusidze

Ilia State University
miv@uliauni.edu.ge

Accepted February 25, 2010

1. INTRODUCTION

Boron nitride with the chemical formula BN can be found in the form of one-dimensional diatomic molecule, two-dimensional nanotubes and fullerenes, three-dimensional crystals like the layered hexagonal h-BN and rhombohedral r-BN as well as turbostratic t-BN, cubic zinc-blende c-BN and wurtzite w-BN modifications as well as their nanostructures etc. Boron and nitrogen atoms are surrounded tetrahedrally in both denser c-BN and w-BN crystals.

Any constituent atom of an h-BN crystal, which is believed to correspond to the boron nitride ground state, may be considered as a 3-coordinated atom because the strong chemical binding (covalence with some deal of ionic) occurs only within the layers, while weak van der Waals forces seem to be responsible mostly for interlayer binding. The h-BN crystal has a "graphitic" structure with a two-layer stacking sequence (r-BN is characterized by a three-layer stacking). These layers consist of regular hexagons (i.e. 6-membered atomic rings) with vertexes alternatively occupied by B and N atoms. In the h-BN crystal, B atoms are placed directly above N atoms and vice versa. Therefore one might suppose that the ionicity contributes to interlayer bonding as well. However, actually the electrostatic component is insignificant due to the large interlayer distances. It is argued also by the existence of a layered r-BN crystal, in which each subsequent layer is turned around an angle of $\pi/3$, and also by the isolated plane defects and their bundles included in real h-BN crystals, in which any given atom can be placed above the same atom. In addition, it is possible to obtain turbostratic t-BN and amorphous structures in the form of mixes of various boron nitride crystalline phases, and multi-walled nanotubular and multi-shelled fullerene-like BN structures. Strong chemical bonding between atoms in a given layer and weak interlayer interaction in layered boron nitrides specify an opportunity of physical and chemical intercalations by various atoms and molecules.

Based upon the similarity of structures of the boron nitride layered phases with graphite, it was assumed [1] that, along with carbon C nanotubes, stable BN nanotubes – the fragments of hexagonal or mixed BN layers wrapped into cylinders – could also exist.

Indeed, by means of arc discharge BN nanotubes had been obtained both from carbon nanotubes [2] and in carbon-free plasma [3]. The arc discharge methods were used to produce $B_xC_yN_z$ nanotubular structures identified by the high-resolution transmission-electron-microscopy (TEM) together with *K*-edge electron-energy-loss-spectrometry (EELS) determining the local atomic composition, while in a carbon-free plasma discharge area between a BN-packed W-rod and a cooled Cu-electrode it was produced multi-walled pure BN tubes with inner diameters on the order of 1 to 3 nm and with lengths up to 200 nm; EELS of individual tubes yielded B / N ratio of approximately 1.

At present various methods of synthesis of the BN nanotubular structures are developed.

The arc discharge in a molecular nitrogen atmosphere between electrodes made of graphite and refractory boron compounds, e.g., hafnium diboride HfB_2, forms BN–C nanotubes with strong phase separation between BN and C layers along the radial direction [4,5]. If both electrodes are made of HfB_2 rods, single- or double-walled chemically pure BN nanotubes are formed with a

structure close to stoichiometric B / N ~ 1 [6]. Most obtained tube ends are closed by flat layers perpendicular to the tube axis. A closure by a triangular facet resulting from three 120°-disclinations was proposed to account for this specific shape. For the most part, the multi-walled BN nanotubes are formed with electrodes made of zirconium diboride ZrB_2 [7,8]. In this case most of the nanotubes have diameters from 3 to 40 nm and lengths on the order of 100 nm. Single-layer tubes with diameters of 2 to 5 nm are also formed rarely. The morphology of the tube tips suggests the presence of pentagons and heptagons which are energetically less favorable compared with squares.

A laser melting of the solid-state boron nitride (of any crystal structure, not only layered but also amorphous) at high nitrogen pressure, (5 – 15) GPa, forms nanotubes free from inclusions, containing from 3 up to 8 walls, and having a characteristic outer diameter of (3 – 15) nm [9].

BN nanotubes have been also obtained by pyrolysis of the molecular precursor with the use of Co catalysts [10].

Bundles of single-walled (or containing few layers) BN nanotubes with almost stoichiometric structure can be formed in substitution reactions – by thermal treatment of a mixture of boron trioxide or trichloride, and bundles of single-walled C-nanotubes at high temperatures, (1250 – 1350) °C, in a nitrogen flow [11,12].

BN nanotubes also grow in solid-state process that involves neither deposition from the vapor phase nor chemical reactions [13]. The nanotubes were produced by first ball-milling of the layered h-BN powder to generate highly disordered or amorphous nanostructures and followed by the product annealing at temperatures up to 1300 °C. The annealing leads to the nucleation and growth of hexagonal BN nanotubes both of cylindrical and bamboo-like morphologies.

Multi-walled BN nanotubes have been obtained by carbothermal reduction of the ultra-dispersive amorphous boron oxide B_2O_3 at simultaneous nitriding at high temperatures, (1100 – 1450) °C [14,15]. For large tubes, it is found that the ratio of length to radius is preserved.

Besides of arc-melting, pyrolysis, and chemical reactions, boron nitride nanotubular structures were created by means of ballistic nuclear displacements caused in a h-BN layered crystal structure by electron irradiation in TEM [16,17].

High growth temperatures (above 1100 °C), a low production yield, and impurities have prevented progress in applications of BN nanotubes in the past decade. Rather recently, it has been shown that these tubes can be grown on substrates at lower temperatures (of about 600 °C) [18]. High-order tubular structures were constructed, which can be used without further purification.

For synthesizing BN nanotubular material, some methods were inspired from carbon. In particular, these include techniques such as laser ablation and non-ablative laser heating [19]. Transformation of the compressed powders of the fine-grained h-BN into nanotubular form can be induced [20] by the concentrated light energy in nitrogen flow. Fiber-like clusters synthesized by evaporation of the layered BN in a nitrogen atmosphere and obtained in powders formed on substrate or chamber surfaces contained nanotubes with diameters and lengths equal to (0.05 – 200) and (100 – 3000) μm, respectively. Applying TEM, there were obtained their associations in tree- and coral-like aggregates.

BN nanotubes can be grown from a nanococoon seed as well [21].

Recently the development of a new method for producing long, small-diameter, single- and few-walled, BN nanotubes in macroscopic quantities has been reported [22]. The pressurized vapor / condenser (PVC) method produces highly crystalline, very long, small-diameter nanotubes without catalysts. Their palm-sized, cotton-like masses of raw material were grown by this technique and spun directly into centimeters-long yarn. Nanotube lengths were observed to be ~ 100 times that of those grown by the most closely related method.

Soon after synthesizing the first BN nanotubes, it was proposed a number of their possible applications in technique [3]. For example, a system of the collinear BN nanotubes forms a boron nitride fiber. At the same time, the theory [23] developed for structural and electronic properties of nanotubular heterojunctions, in which one of the layers is nanotubular boron nitride (namely, for

C / BN and BC_2N / BN systems), leads to a conclusion that on basis of it a different electronic devices can be designed. In particular, sandwich nanostructures with C-layers both in the center and at the periphery separated by a few BN-layers may allow the creation of nanotubular electronic devices [4]. Within the special semiempirical approach [24] C / BN superlattices and isolated junctions have been investigated as specific examples by the wide variety of electronic devices that can be realized using such nanotubes. The bottom of the conduction bands in pure BN nanotubes is controlled by a nearly-free-electron-state localized inside the tube suggesting interesting electronic properties under doping.

Other opportunities of application of the BN nanotubes are connected with the features of their phonon spectrum [25]. Such dielectric tubes without inversion center can be used as a phonon laser in GHz – THz range or hypersound quantum generator. Because of the presence of special nanotubular oscillatory modes, there is a strong enhancement of electron–phonon interaction in comparison with a bulk material. It is not excluded that close-packed one-dimensional BN nanotubes will serve as high-temperature superconductors. The GHz oscillatory behavior of double-walled BN nanotubes was also predicted [26,27]. The same system can also be employed for making good shock absorbers because application of low pressure leads to its significant compression.

The band gap progression with BN nanotube diameter (which is of crucial importance for device applications) was presented and analyzed in detail in [28]. In zigzag BN nanotubes, radial deformations that give rise to transverse pressures decrease the gap from 5 to 2 eV, allowing for optical applications in the visible range [29]. Importantly, both the zigzag and chiral tubes are found [30] (see also [31]) to exhibit large second-order nonlinear optical behavior with the second-harmonic generation and linear electro-optical coefficients being up to 15-times larger than that of bulk BN in both denser zinc-blende and wurtzite structures. This indicates that BN nanotubes are promising materials for nonlinear optical and optoelectronic applications.

The Electronic structure of BN nanotubes can be tuned within a wide range through covalent functionalization [32] (see also [33]). The ultraviolet (UV) and visible absorption spectra indicate that their electronic structure undergoes drastic changes under functionalization. First principle calculations revealed that the covalently functionalized BN nanotubes can be either n- or p-doped depending on the electronegativity of molecules attached. Their energy gap can be adjusted from UV to visible optical range by varying concentration of functionalizing species.

One-dimensional crystals of potassium halides, including KI, KCl, and KBr, were inserted into BN nanotubes [34]. High-resolution TEM and energy-dispersive X-ray spectrometry were used to characterize their microstructures and compositions. The fillings are usually single crystals with lengths up to several μm. The wetting properties (static contact angles of the liquids and surface tension) of individual BN nanotubes were studied [35] experimentally using a nanotube-based force to measure the interactions between nanotubes and liquids in situ.

First principles simulations on the interaction of molecular hydrogen H_2 with the native and substitutional defects in small-diameter (8,0) BN nanotubes were performed in [36]. The adsorption of H_2 in structures found to be endothermic with respect to dissociation, with the small-diameter nanotube possessing the smaller barrier. Although chemisorption along the tube axis is energetically preferred, the barrier for dissociation is lower for chemisorption across the tube axis. This implies that chemisorbed hydrogen can be kinetically trapped in a higher energy state. Dopants that maximize the localization of the higher-occupied-molecular-orbital (HOMO) and lower-unoccupied-molecular-orbital (LUMO) states maximize hydrogen binding energies. C-dopants do not enhance H_2 binding, whereas Si-dopants substituting for N provide H_2 binding energies of 0.8 eV, at the upper end of the range required for hydrogen storage. The formation energy of most defects is reduced with increasing curvature except for the C-substitutionals. Vacancies do not reduce the barriers for H_2 dissociation for strongly curved nanotubes. The surface stress induced by the nanotube curvature boosts the hydrogen storage capabilities of vacancies with the nitrogen vacancy chemisorbing 4H and allowing a H_2 molecule to enter the interior of the tube. The

hydrogen binding properties of BN systems strongly depend on existing defects and dopants. Pretreating of these systems so as to partially remove nitrogen should enhance H_2 adsorption properties. The hydrogen absorption capacity of Ti-covered single-walled BN nanotube was investigated using first principles plane-wave (PW) method [37]. The weak interaction of H_2 molecules with the outer surface of bare nanotube can be significantly enhanced upon functionalization by Ti atoms: each Ti atom adsorbed on tube can bind up to four H_2 molecules with average binding energy suitable for room temperature storage.

The morphology of BN nanotubes with a collapsed structure has been discovered by a metal-catalyzed treatment [38]. The collapse causes the dramatic enlargement of a specific surface area of BN nanotubes and remarkably enhances the hydrogen storage capacity of BN nanotubes.

It was reported [39] that proteins are immobilized on boron nitride nanotubes. There is a natural affinity of a protein to BN nanotube: it can be immobilized on tube directly, without using of an additional coupling reagent. Besides, boron nitride nanotubes may be dissolved in organic solvents by wrapping them with a polymer [40].

It was proposed [41] that BN polymers, having the structures similar to organic polymers, can serve as a cheap alternative to inorganic semiconductors in designing modern electronic devices. Some related potential innovations, including band gap tuning, were also demonstrated.

The observed giant Stark effect significantly reduces the band gap of BN nanotubes and thus greatly enhances their utility for nanoscale electronic, electromechanical, and optoelectronic applications [42]. In particular, this effect may be important for tuning the band gap of BN nanotubes for applications as a nanoscale field-effect-transistor (FET).

Boron nitride nanotubes have also manifested stable currents in field emission geometry and may be more stable than carbon nanotubes at high temperatures [43,44].

As it was mentioned, boron nitride nanotubes exhibit many similarities with the carbon ones (such as high Young modulus etc) and might have superior unique mechanical, thermal, and electronic properties [45]. In addition, BN nanotubes are characterized by chemical inertness and poor wetting [46].

The factor that distinguishes BN from C is partial heteropolarity of the chemical bonding. For this reason, one more sphere of possible applications of BN nanotubes can be new pyroelectric and piezoelectric materials promising for applications in nanometer-scale sensors and actuators. The 3-fold symmetry of a BN sheet, a III–V analog to graphite, prohibits an electric polarization in its ground state. However, this symmetry is broken when the sheet is wrapped to form a BN tube. It was shown [47] that this leads to an electric polarization along the nanotube axis which is controlled by the quantum-mechanical boundary conditions of its electronic states around the tube circumference. Thus, the macroscopic dipole moment has an intrinsically nonlocal quantum-mechanical origin from the wrapped dimension. Combining first principles, tight-binding methods and analytical theory, the piezoelectricity of heteropolar (in particular, BN) nanotubes was found [48] to depend on their chirality and radius. This effect can be understood starting from the piezoelectric response of an isolated sheet along with a structure specific mapping from the sheet onto the tube surface. It was demonstrated that a linear coupling between the uniaxial and shear deformations occurs for chiral nanotubes, and the piezoelectricity of nanotubes is fundamentally different from its counterpart in a bulk material. First principles calculations of the spontaneous polarization and piezoelectric properties of BN nanotubes have shown [49] that they are excellent piezoelectric systems with response values larger than those of piezoelectric polymers. The intrinsic chiral symmetry of the nanotubes induces an exact cancellation of the total spontaneous polarization in ideal, isolated nanotubes of arbitrary indexes. But the breaking of this symmetry by the intertube interaction or elastic deformations induces spontaneous polarization comparable to that of wurtzite bulk semiconductors [50].

Multielement nanotubes comprising multiple SiC-core, an amorphous SiO_2-intermediate layer, and outer shells made of BN and C layers separated in the radial direction with diameters of a few tens of nm and lengths up to 50 μm were synthesized by means of reactive laser ablation [51].

They resemble a coaxial nanocable with a semiconductor-insulator-semiconductor (SIS) geometry and suggest applications in nanoscale electronic devices that take advantage of this self-organization mechanism for multielement nanotube formation.

A theoretical description of electron irradiation of single-walled BN nanotubes was presented in [52]. As a first step, the anisotropy of the atomic emission energy threshold was obtained within extended molecular-dynamical (MD) simulations based on the density-functional-theory (DFT) tight-binding method. As a second step, total cross section for different emission sites as a function of the incident electron energy was numerically derived. Two regimes were then described: at low irradiation energies (below 300 keV), atoms are ejected mostly from the upper and lower parts of the tube while at high energies (above 300 keV) atoms are ejected mostly from the side walls. Typical values of the total cross section of knock-on processes are obtained to vary from a fraction of barn (at side wall for 150 keV electrons) up to around 20 barns (for 1 MeV electrons). In BN nanotubes, the emission energy threshold maps were reported to show B sputtering to be more favorable for low irradiation energies, while N sputtering is more favorable at high energies. These calculations of the total knock-on cross section for nanotubes can be used as a guideline for TEM experimentalists using high energy focused beams to shape nanotubes, and also, more generally, if electron irradiation is used to change nanotube properties such as their optical behavior or conductivity.

For purposeful design of devices based on nanotubular BN, it is important to be able to predict reliably the binding energies and sizes of the nanotubes with given indexes and their relative stability. In present work, this task is solved for the most stable – achiral (zigzag and armchair) – single-walled forms. Paper is organized as follows. In Section 1, we have introduced methods of synthesis of the boron nitride nanotubes and their technological applications. Section 2 is a brief summary of the structural and binding data available on nanotubular boron nitride. In Section 3, the theoretical approach based on the quasi-classical approximation to the binding energy calculation and geometries is presented. In Section 4, results of the performed calculations are presented in the form of curves "molar binding energy – structural parameter". Section 5 is devoted to estimation of the nanotube lattice zero-point vibration energy. And finally, Section 6 discusses relative stability of the boron nitride nanotubes of various radii and makes an attempt to generalize the obtained results.

2. STRUCTURAL AND BINDING DATA

Let us start with a brief overview of the structural and binding data available on a boron nitride diatomic molecule, isolated sheet, and nanotubular form.

2.1. Molecular boron nitride

The diatomic molecule BN can be considered as a simplest (degenerated) form for boron nitride nanotubes. In general, electronic theory of substance considers a diatomic molecule as a special problem for its intermediate structural and, consequently, electronic properties between mono- and polyatomic systems. Peculiarities are related mainly with the system axial symmetry and uniqueness of the structural parameter – interatomic distance d. Unlike the solid state or nanoscale boron nitrides, which are materials with a diversity of technical and industrial applications, BN molecule, which exists under the extreme conditions, is only of academic interest as a "building block" for two- and three-dimensional boron nitride structures. From the standard thermochemical data, the energy of B–N bond at the equilibrium length is known to be considerably higher compared with those of B–B and N–N bonds. In addition, any stable regular BN structure is a network of atomic rings with alternating atoms such that the nearest-neighbor environment of both B and N atoms consists of only B–N bonds. Therefore, the B–N bond length is a key interatomic distance in the analysis of boron-nitrogen binding.

There are known some old first principles and semiempirical investigations for boron-nitrogen interaction (see [53,54]). Applying a self-consistent-field (SCF) procedure to the BN molecule in [55], it was calculated molecular orbitals (MOs) in order to minimize total energy of the diatomic system. Then using the spectroscopic data available for the corresponding ground state, the BN molecule dissociation energy value E was found to be 4.6 eV. According to the original theoretical approach of [56], the equilibrium interatomic distance in this molecule equals to 1.307 Å. At the same time, spectroscopic parameters characterizing the calculated boron-nitrogen interaction potential curve lead to the dissociation energy estimation of 5.05 eV. Nearly the same theoretical value for the bond length of 1.320 Å was suggested in [57]. In [58], a short-ranged classical-force-field (CFF) modeling of BN modifications was performed on the basis of experimental and first principles solid-state and diatomic-molecular data. In particular, assuming that CFF can be correctly determined by a sum of only two-body interaction terms, the B–N potential energy had been expressed analytically via Morse potential, which gave $d \approx 1.32521$ Å and $E \approx 5.50007$ eV. However, it was noted [25] that standard forms of the pair interatomic potentials, such as the Morse, Mee–Grüneisen, Buckingham, and other potentials, converge slowly and, therefore, a cutoff procedure should be used. But, in such a case a non-physical jump on the potential radial function can arise. In order to eliminate this problem, based on the embedded atom method, a new B–N interatomic potential was designed which fulfills the conditions for smooth end: the potential function and its derivative (i.e. the interatomic force) vanish at the cutoff radius. The equilibrium bond length of 1.4457 Å and binding energy of 4.00 eV were found to reproduce correctly relative stabilities of the boron nitride layered structures.

We also suggested [59] a theoretical, namely, quasi-classical method of calculation of the dependence the B–N interatomic binding energy E upon the bond length d. The constructed $E = E(d)$ curve was shown to be useful for estimations of BN crystalline structures cohesion parameters as well. This function reveals standard behavior characteristic for the central pair potentials. $E(0) = -\infty$, and $E(d) \equiv 0$ if d is equal or greater than the sum of B and N quasi-classical atomic radii $r_{(B)} \approx 2.30$ and $r_{(N)} \approx 1.70$ Å, i.e. $d \geq r_{(B)} + r_{(N)} \approx 4.00$ Å (note that quasi-classical B–N interatomic potential automatically fulfills the conditions for the smooth end at $d = r_{(B)} + r_{(N)}$), while within the intermediate region $0 < d < r_{(B)} + r_{(N)}$ it is an oscillating function with several maxima. Among these maxima only one is available kinetically and, therefore, it corresponds to the equilibrium. Analysis of the piece of the quasi-classical $E = E(d)$ curve for BN diatomic molecule, in the vicinity of this maximum, yields the values of bond length of 1.55 Å and binding energy of 4.51 eV. Same dependence determined earlier [60,61] within the frames of another quasi-classical parameterization scheme (for this purpose the screening factor of the potential affecting the given electron in interacting atom was approximated by the radial polynomial, not by the constant) is relatively flat and leads to the estimations of 1.58 Å and 4.79 eV.

Thus, the spread in theoretical and semiempirical values for BN molecule binding energy is (4.0 – 5.5) eV, which overlaps with the recommended [62] experimental dissociation energy value of (4.0 ± 0.5) eV. The available first principles and semiempirical calculations and thermochemical experimental data lead to the binding energy values of about (4 – 7) eV per B–N bond for various, differently coordinated, BN modifications (for sheet and nanotubular structures see below). Such kind of estimations may be considered to be in qualitative agreement with the quasi-classically calculated B–N bond energy as the ground state energetic parameters are quite sensitive to the atomic coordination. For this reason, we focus our attention on the differences in the bond length values between BN molecular and crystalline phases. The quasi-classical values for the isolated B–N bond length and other relevant theoretical and semiempirical data, which lie over the range (1.307 – 1.58) Å, are overestimated in comparison with 1.281 Å measured in $^{11}B^{14}N$ molecule [63].

An explanation may be that molecular spectra [64] verify triplet ground state, but at the same time reveal a low-lying singlet state with longer bond.

Quasi-classically calculated interatomic vibration energy in a B–N diatomic system of 0.178 eV / mole (the corresponding vibration quantum equals to 1435 cm^{-1}) was found by fitting the quasi-classical B–N potential curve with parabola [60,65]. This value is in good agreement (accurate within 5 %) with the values experimentally obtained for a neutral BN molecule of 0.187 (1514.6) [63] and 0.188 eV / mole ((1519.0 ± 0.2) cm^{-1}, from the absorption spectra Fourier analysis for laser-induced molecular fluorescence) [64]. According to the SCF theoretical method of [56], the ground state vibration energy in molecular BN estimated as 0.179 eV / mole (1446 cm^{-1}), which is almost the quasi-classical result. In [57], it was suggested the higher theoretical value of 0.217 (1750), what is close with 0.216 eV / mole (1740 cm^{-1}) measured in ionized molecule BN^+ [66].

Studies of more complex molecular clusters of B and N are also interesting to get deeper insight into the defect formation processes in boron nitride nanotubes. High-temperature Knudsen cell mass spectrometry was used to study the equilibria involving the B_2N molecule [67]. The thermal functions necessary to evaluate the mass spectrometric equilibrium data had been calculated from available experimental and theoretical molecular parameters. In particular, in some B_2N formation reactions changes in enthalpy have been measured. Room temperature atomization and formation enthalpies were determined to be 10.84 and 5.71 eV, respectively. At the same time, first-principles calculations were performed to estimate the electronic parameters of B_2N, such as ionization energy and electron affinity. Mixed clusters of B and N atoms – B_2N, BN_2, B_3N, B_4N, B_2N_2, and B_3N_2 – can be produced by sputtering of a solid state BN [68]. Atom ordering in assumed linear species had been derived from measurements of the mass distribution of both the positive and the negative products from the fragmentation of the anionic clusters in a gas target. As for neutral configurations, they were calculated. A tendency was found that a structure with the highest number of B–N bonds is most stable both in neutral and anionic species (an exception is the BN_2 molecule). In contrast to this, the species with the highest number of adjacent same atoms (except for triatomic chains) had the largest electron affinity.

2.2. Boron nitride sheet

The facts that boron nitride layered crystals and nanotubes may be prepared suggest the necessity of analyzing the hypothetic isolated infinite hexagonal layer, i.e. the BN sheet. Corresponding two-dimensional BN crystal is represented as a planar layer composed of regular hexagons with vertexes alternately occupied by B and N atoms. Classification and discussion of the BN haeckelite sheet structures, consisting of not only hexagonal atomic rings but also other even-membered rings, one can find in [69].

For the first time, the truncated crystal approach in the form of two semiempirical (standard and extended iterative Hückel) methods was applied to a two-dimensional hexagonal boron nitride structure [70]. The bond length was found to be 1.48 or 1.50 Å. However, when semiempirical calculations were performed on a two-dimensional periodic small cluster of the h-BN layer the equilibrium B–N distance was computed as 1.441 Å [71]. In [72], the 3-coordinated $B_{12}N_{12}$ network of 6-membered atomic rings was examined theoretically. Namely, the total energy calculated using Hartree–Fock (HF) approach and DFT in local and gradient-corrected forms was minimized with respect to the B–N bond length. But, "graphitic" isomer $B_{12}N_{12}$ is only a fragment of the BN sheet and its geometry appears to be somewhat distorted because of finite sizes. As is to be expected, slight deviations of the bonds' angles from the ideal value of 120° were observed for the bonds of atoms forming the central hexagon: – (2.52 – 2.65)° for B atoms and + (2.52–2.65)° for N atoms. There were also obtained number of unequal bond lengths: (1.266 – 1.283), (1.371 – 1.378), (1.427 – 1.442), (1.434 – 1.444), (1.520 – 1.536), and (1.553 – 1.576) Å. The finiteness of the

quasi-classical atomic radii allowed us to obtain the B–N bond length for an infinite boron nitride sheet within the initial quasi-classical approximation [73]. The calculated dependence of the molar binding energy on the lattice constant exhibits a maximum of 23.0 eV at 2.64 Å, which should correspond to the equilibrium state for an isolated hexagonal layer (analytical optimization [74] of the lattice parameter using the binding energy calculated in quasi-classical approximation, which is possible only by neglecting the vibration energy, yields slightly different values: 23.2 eV and 2.66 Å, respectively). The lattice constant of 2.64 Å implies B–N bond length of 1.52 Å. Correction in energy introduced by zero-point vibrations was estimated as 0.242 eV / mole [65,73].

The quasi-classical bond length of 1.52 Å in an isolated BN sheet is in reasonable agreement (accurate within 4.6 %) with the bond length of 1.45 Å observed in layers of real h-BN crystals. At first glance, the surprising thing is that the theoretical result for the isolated layer is in better agreement (with the accuracy of (2.6 – 3.8) %) with the bond lengths in tetrahedrally coordinated modifications c-BN (1.57 Å) and w-BN (1.56 and 1.58 Å). However, it is worth noting that to a certain extent two-dimensional boron nitride looks like three-dimensional crystals c-BN and w-BN: these three structures do not contain weak interlayer bonds, which occur in the h-BN layered modification. The lengths of (1.52 – 1.54) and (1.55 – 1.58) Å obtained in [72] for the bonds of atoms forming the central (almost undistorted) hexagon in $B_{12}N_{12}$ plane-fragment are also in good agreement with the quasi-classical result found for an idealized infinite BN sheet. Another quasi-classical approach using a different scheme of parameterization, employed to calculate h-BN binding and zero-point vibration energies, slightly underestimates the intralayer bond length [75]. The plausible reason may be that the crystalline equilibrium configuration was selected to maximize its static binding energy with respect only to the layer lattice parameter, while the interlayer distance was fixed.

Summarizing other theoretical and semiempirical results concerning intralayer bond lengths in h-BN (and r-BN), one can state that all of them are in agreement with the experimental value of 1.446 Å [76]. For instance, in [77] the total energy of h-BN crystal as a function of unit cell volume V had been calculated using orthogonalized linear-combinations-of-atomic-orbitals (LCAO) method within the local-density-approximation (LDA). The equilibrium was found at $V/V_{\exp} = 0.998$, where $V_{\exp}$ is the experimental value of V. Such result corresponds to the intralayer B–N distance of 1.438 Å. The calculations of [78] were also based on DFT within LDA, but PW expansion was used both for the pseudo-potential (PP) and the wave-function. The computed total energies and, consequently, the intralayer bond lengths in h-BN and r-BN were nearly the same: 1.441 and 1.439 Å, respectively. The short-ranged CFF modeling of boron nitrides leads to exactly the same intralayer B–N bond lengths in both layered structures: 1.454 Å [58]. The results presented show satisfactory accuracy for the quasi-classically determined boron-nitrogen binding characteristics: accuracies of quasi-classical approach to determine isolated B–N bond length and length of bonds in solid state structure amount a few percents, 7.2 and 5.1 %, respectively. Thus, the quasi-classically obtained B–N binding curve and its parameters mentioned above (namely, equilibrium bond length, binding energy, and vibration frequency) would be useful for investigations of compounds containing B–N bonds and, especially, BN nanosystems.

As for the BN sheet binding and vibration energies, it is also reasonable to analyze correctness of the given predictions by comparing them with data available on the cohesion characteristics of h-BN layered crystals. As follows from standard thermochemical data, the binding energy of h-BN equals to 13.0 eV / mole [79]. The binding energies of 14.5, 16.0, and 14.4 eV / mole were determined from semiempirical calculations performed using two variants of the semiempirical LCAO method and an approach based on a periodic small-sized cluster [70,71]. Within the CFF potential model, the lower semiempirical estimate of 11.5 eV / mole was obtained [58]. In the framework of DFT, optimization of the structural parameters led to the theoretical binding energy of 12.5 eV / mole [78]. Therefore, it can be expected that the molar binding energy for h-BN layered crystal lies in the range from 11.5 to 16.0 eV. The binding energy of 23.0 eV / mole found

by the quasi-classical method for the isolated layer is considerably higher. However, when comparing these energies, one should take into account that interlayer bonds are substantially weaker than intralayer ones and that each atom in layered BN structures is involved in the formation of 5 bonds, of which only 3 are intralayer bonds. Consequently, if the interlayer energy is ignored as compared to the intralayer energy, we can assume that the binding energy per B–N bond of similar modifications is equal to 3 / 5 of the molar binding energy of the isolated layer. Making use of the result 23.0 eV / mole for layer, we find the molar binding energy of $3 / 5 \times 23.0$ eV = 13.8 eV. Indeed, this energy is close to the midpoint (13.75 eV) of the aforementioned energy range. On the other hand, the vibration energies of the isolated layer and layered crystals can be directly compared because the atoms of the low-dimensional system can execute vibrations in three independent directions in physical space. The quasi-classical result of 0.242 for two-dimensional BN agrees well with analogous calculations of 0.266 [65], with the semiempirical estimate of 0.225 for zero-point vibrations energy in h-BN [58], and coincides in order of magnitude with the estimate of 0.350 eV / mole from the theoretical phonon spectrum [78].

A few words about the defects in BN layer. Using methods of model PP and expanded unit cell, it was found that N-vacancies in BN sheet, as well as di- and trivacancional clusters including neighbor defects in BN layer, are characterized by small binding energies [80]. Calculated spectra and oscillator strengths allow to interpret local bands of the optical absorption in real (pyrolitic) layered h-BN crystals before and after irradiation by fast-neutrons, protons, and C-ions. Charge contour maps of the defects also were given. By first-principles calculations the 20 structures $B_xC_yN_z$, derived from a hexagonal layer by placing B, N, or C atoms on each site, were considered [81] to investigate their relative stabilities. First-principles simulations of the interaction of molecular hydrogen H_2 with the native and substitutional defects of a single hexagonal BN sheet were performed in [36]. The adsorption of H_2 on structures found to be endothermic with respect to dissociation. In planar sheets, vacancies reduce the barriers for H_2 dissociation.

The geometries of haeckelite BN sheets were constructed by DFT [82]. Their molar energy of cohesion is found to be higher (by ~ 0.6 eV / mole) than that of regular one.

2.3. Nanotubular boron nitride

The elementary form of a BN nanotube is a wrapped closed hexagonal surface inscribed in the cylinder. Such BN nanotubes can be found in regular – achiral, i.e. zigzag (n,0) or armchair (n,n), and also in chiral (n,m) forms, $0 \le m \le n$. Here n and m are the tube indexes. Their symmetry operators have been identified in [83]: each type belongs to different family of the non-symmorphic rod groups; armchair tubes with even n are found to be centro-symmetric. The types and structures of the non-carbon, in particular, BN nanotubes were reviewed in [84]. In addition, the deformed regular or haeckelite nanotubes can exist. Concerning the haeckelite structures of BN tubes, a variety of chiral angles, including zigzag and armchair types, were observed. Depending on the structure formation kinetics characteristic for a given technology, BN nanotubes quite often take the bamboo-like morphology, forms of a nanoarch (i.e. half-tube at the ends closed by planes) etc. Real nanotubular structures are not infinite in length: they are definitely truncated.

The three main different possible morphologies of the cylindrical tube closing with flat [8], conical, and amorphous ends, as observed in experiments, were shown [85] to be directly related to the tube chirality. There are also possible rectangular BN nanotubes with linear defects on edges and with tips in the form of triangular flags. Such kind of morphologies suggest the presence of energetically unfavorable odd-membered atomic rings (i.e. pentagons and heptagons) in addition to favorable even-membered rings (e.g. squares).

As the growth of BN nanotubes cannot be directly observed and, consequently, the underlying microscopic mechanism is a controversial subject, in [86] first-principles MD simulation of the single-walled nanotube edges was performed. The behavior of growing BN nanotubes was found to strongly depend on the nanotube network chirality. In particular, open-ended zigzag tubes close

rapidly into an amorphous tip, preventing further growth. In the case of armchair tubes, formation of squares traps the tip into a flat cap presenting a large central even-membered ring. This structure is meta-stable and is able to revert to a growing hexagonal framework by incorporating incoming atoms. These findings are directly related to frustration effects, namely that B–N bonds are energetically favored over B–B and N–N bonds.

For purposeful designing devices based on nanotubular BN, it is important to be able to predict reliably the sizes of nanotubes with given indexes. This task was solved for the most stable forms. Namely, the expressions of radii, $R_{(n,0)}$ and $R_{(n,n)}$, of the zigzag and armchair, (n,0) and (n,n), BN nanotubes in terms of the index and the structure parameter a were obtained [87]. The parameter a corresponds to the lattice constant of the boron nitride layered crystals, i.e., intralayer B–B or N–N bonds lengths. Therefore, the B–N bond length d equals to $a/\sqrt{3}$. The nanotube index $n = 1,2,3,...$ determines the number of atoms as nanotube unit cell consists of $2n$ formula units BN. The estimations of radii of the single-walled BN nanotubes, for their part, can be used for predicting their most probable combinations in multi-walled structures.

Analyzing this problem, it is necessary to take into account that actually the question involves the average radii. A detailed study using the generalized tight-binding MD method has revealed [85] that, as a result of the dynamical relaxation, the structure acquires a wave-like or "rippled" surface in which B atoms are displaced inward, while N atoms are displaced outward. This relaxation is similar to the reconstruction occurring at clean surfaces of III–V type crystalline semiconductors. However a general feature of BN nanotubular systems is that stronger surface potentials are associated with regions of higher curvature [88]. Thus, the interlayer interaction in BN nanotubes differs from bonding in three-dimensional layered crystals. However, most probably, these distinctions for nanotubular BN are weak enough to change essentially the equilibrium interlayer distances which are observed in h-BN and r-BN crystals. This conclusion is also confirmed by the results of an experimental study of the multi-walled nanotubes by high-resolution electronic microscopy [89]. In these structures, like in three-dimensional layered BN crystals, hexagonal and rhombohedral stacking sequences can freely coexist in nanotube wall-assembly. There are also possible some different cross-section flattening, as well as ordering of layers in non-spiral zigzag. According to first-principles total-energy calculations [90], the most favorable double-walled BN nanotubes are structures in which the inter-wall distances are about 3 Å, i.e., as interlayer distances in layered BN crystals. Therefore, due to the weakness of the interlayer van der Waals forces, various types of multi-walled BN nanotubes can exist. Consequently, it is more probable the formation of such multi-walled BN nanotubes in which the difference between the radii of adjacent regular nanotubes is close to the interlayer distance in a layered h-BN crystal, i.e., to half of the height of the hexagonal unit cell $c \approx 6.6612$ Å [91]. Thus, the similarity between types of the adjacent nanotubes has no crucial importance.

In view of these factors, from the calculated single-walled nanotubes [87] pairs most suitable for the formation of the stable double-walled BN nanotubes have been chosen. Remaining small divergences in sizes of the neighboring regular nanotubes can be compensated by defects and small chiral distortions. Such transformations of the zigzag and armchair nanotubes into chiral one will be accompanied, respectively, by the increase and decrease in their radii. If the difference in radius between regular nanotubes is more (less) than $c/2$, the realization of structure in which the internal wall will be zigzag (armchair) and external – armchair (zigzag) is more probable. Hence, based on estimations of sizes of the single-walled BN nanotubes, it is possible to predict successfully the most stable double-walled forms. But, how can be solved the same problem for multi-walled nanotubes? A few words on the problem. In this case, all over, it will be necessary to calculate radii of nanotubes with high indexes to choose sequences of single-walled nanotubes, whose radii are close to terms of arithmetic progression with common difference of $c/2$. However, now only geometrical considerations will be insufficient. The point is that unlike double-walled nanotubes in multi-walled ones there are also medial layers. For this reason, the choice of the most stable multi-

walled structure should be based on the comparison between the gains in energy, which are caused by the deviation from the equilibrium interlayer distance, on the one hand, and by chiral distortions, on the other hand.

We can mention some theoretical results available on binding properties and stabilities of BN nanotubes. Stabilities of the boron nitride nanotubular structures were studied by means of non-orthogonal tight-binding formalism [92]. The radii and energies of the BN nanotubes also were estimated by MD simulation [25] within the embedded atom model in which parameter d took the experimental value 1.4457 Å of the intralayer B–N bond length in real h-BN crystals. In [69], the binding energy of the regular BN nanotubes has been calculated within the DFT in generalized gradient approximation (GGA). Seeking equilibrium values of B–N bond length and radii, the geometry of the tubular 32-atom supercell was optimized. For $(8,0)$, $(10,0)$ and $(4,4)$ tubes, it has been found $d \approx 1.46\,\text{Å}$, and for $(5,5)$ tube, $d \approx 1.45\,\text{Å}$. Within the frame of semiempirical calculations of the nanotubular piezoelectric characteristics performed by the method of modified neglecting of diatomic overlapping (MNDO) [50], their radii also were determined. In this case the dependence of energies on the bond length was calculated for the molecular fragments containing 3 or 4 elementary layers (presumably, in this work for d the empirical value known for h-BN crystals was fixed as an equilibrium value).

The possible contribution of ionicity of bonds in boron nitride structures is important to explain the binding differences between BN tubes and similar C tubes [1]. In order to facilitate understanding and prediction of nanotube interactions in a multi-walled structure, the electrostatic potentials on both outer and inner surfaces of some single-walled BN nanotubes have been calculated at a HF Slater-type-orbital level [88]. Structures were optimized computationally. Fictitious hydrogen atoms were introduced at the ends of the open tubes to satisfy the unfulfilled valences. It was found that BN tubes have stronger and more variable surface potentials than graphitic ones. There are characteristic patterns of positive and negative sites on the outer lateral surfaces, while the inner ones are markedly positive.

The binding and vibrations in small-radius single-walled BN nanotubes in [93] were studied by DFT using LDA. The results show that the chirality preference observed in experiments may be explained from the relative stability of the corresponding BN strips: the zigzag strips have larger binding energies and thus may be more easily formed. The smallest stable BN nanotube is found to be the $(5,0)$ zigzag nanotube. The dependence of the tube deformation energy on its radius R was approximated by the formula $\Delta E\,[\text{eV/mole}] = 5.82 / R^{2.09}\,[\text{Å}]$. The phonon dispersions of BN nanotubes were calculated and the frequency of the radial breathing mode is found to be inversely proportional to the nanotube radius. The geometries of the BN nanotubes were also constructed in DFT [82]. Based on DFT calculations [69], it was found that the energies of haeckelite BN nanotubes exceed by ~ 0.6 eV / mole those of corresponding hexagonal nanotubes. They are less stable in comparison with corresponding haeckelite sheets as well, however, still they are stable and can be synthesized. Energy of deformation (i.e. energy needed to wrap nanotube from its sheet prototype) for large haeckelite BN tubes extrapolated by the formula $\sim C / R^{\alpha}$, where R is the tube radius, with different parameters C and $\alpha \approx 2$ for different structures.

Using the symmetry properties in [83], it was determined the numbers of Raman- and IR-active vibrations in single-walled BN nanotubes. In contrast to the regular carbon nanotubes, zigzag boron nitride tubes possess almost twice as many vibrations as armchair ones. An extensive first principles study of the phonons in BN nanotubes using perturbation DFT in the LDA was performed in [94], where, based on the non-symmorphic rod group symmetry of tubes, the Raman- and IR-active modes at the point of the one-dimensional Brillouin zone were evaluated. For zigzag and chiral nanotubes, the set of IR-active modes is a subset of the Raman-active modes. In particular, the radial breathing mode is not only Raman-, but also IR-active. However, for armchair tubes, the sets of IR- and Raman-active modes are disjoint. The frequencies of the active modes of zigzag, chiral, and armchair tubes were presented as a function of the tube diameter. They were

compared with the frequencies obtained by the zone-folding method (i.e. by rolling of a BN sheet into a tube). Except for the high-frequency tangential modes, the zone-folding results are in very good agreement with the first principles calculations. The radial breathing mode frequency can be derived by folding a sheet of finite width. Finally, the effects of bundling on the phonon frequencies are shown to be small. First principles calculations of the nonresonant Raman spectra of zigzag and armchair BN nanotubes were presented in [95]. In comparison, a generalized bond-polarizability model, where the parameters are extracted from first principles calculations of the polarizability tensor of a BN sheet, was implemented. For light polarized parallel to the tube axis, the agreement between model and first principles spectra is almost perfect, but for perpendicular polarization, depolarization effects have to be included in the model in order to reproduce Raman intensities.

The possible dislocation dipoles as defect nuclei under tension in BN nanotubes were identified by dislocation theory and MD simulations [96]. Formation energies of the dipoles evaluated by gradient-corrected DFT are high and remain positive at large strains, thus suggesting great yield resistance of BN nanotubes. The dipole appears to be more favorable in spite of its homoelemental B–B and N–N bonds. The resonant photoabsorption and vibration spectroscopy combined with scanning tunneling microscopy unambiguously identify the presence of Stone–Wales defects in BN nanotubes [97]. Based on extensive time-dependent DFT calculations, it was proposed to resonantly photoexcite such defects in the IR and UV regimes as a means of their identification. Intrinsic defects in zigzag BN nanotubes, including single vacancy, divacancy, and Stone–Wales defects, were systematically investigated using DFT calculation in [98]. It was found that the structural configurations and formation energies of the topological defects are dependent on tube diameter. The results demonstrate that such properties are originated from the strong curvature effect in BN nanotubes. The scanning tunneling microscope images of intrinsic defects in the BN nanotubes also were predicted. The defected BN tubes with C-substitutions were considered in [50].

The theoretical studies of the elastic properties of single-walled BN nanotubes, carried out using the total-energy non-orthogonal tight-binding parameterization, were reported in [99]. Tubes of different diameters, ranging from 0.5 to 2 nm, were examined. The study found that in the limit of large diameters the mechanical properties of nanotubes approach those of the graphite-like sheet. The stiffness and plasticity of BN nanotubes was investigated [100] using generalized tight-binding MD and first principles total-energy methods. Due to the B–N bond rotation effect, the compressed zigzag nanotubes were found to undergo anisotropic strain release followed by anisotropic plastic buckling. The strain is preferentially released toward N atoms in the rotated B–N bonds. The tubes buckle anisotropically toward only one end when uniaxially compressed from both ends. Based on these results, a skin-effect-model of smart nanocomposite materials is proposed, which localizes the structural damage toward the surface side of the material. B–N bond-rotation mode of plastic yield in BN nanotubes in [101] was investigated combining first principles computations with a probabilistic rate approach to predict the kinetic and thermodynamic strength. BN nanotubes yield defects have low activation, but high formation energies. In [50], elastic characteristics of BN nanotubes also were calculated applying MNDO method.

3. THEORETICAL BASIS

Our calculations are based on the quasi-classical expression for binding molar energy of a substance, on the one hand, and on the geometric characterization of nanotubular boron nitride, on the other hand.

3.1. Quasi-classical binding energy of substance

Under the term ‘substance’ we imply polyatomic structures at the ground state, i.e. molecules, various clusters, and crystals. Consequently, any substance is considered as a non-relativistic electron system affected by the static external field of nuclei, which are fixed at the sites in

structure, and the averaged self-consistent field of electrons. Because of singularities at the points, where the nuclei are located, and electron shell effects as well the inner potential of substance does not satisfy the standard Wentzel–Kramers–Brillouin (WKB) quasi-classical condition of spatial smoothness. Nevertheless, beginning from Bohr's fundamental work 'On the constitution of atoms and molecules' up to the present the semi-classical analysis of the electronic spectrum has been widely used for light atoms and their small complexes. Besides, heavy atoms, large molecules, and crystals can be treated within the LDA using the total energy functional in the form of quasi-classical expansion. Success of quasi-classical approaches can be attributed to the diffuseness of atomic potentials. The expression for bounded electron states energies obtained by Maslov yields that precise and quasi-classical spectra are close to each other independently from the potential smoothness properties if the characteristic values of potential Φ_0 and the radius of its action R_0 meet requirement $2\Phi_0 R_0^2 >> 1$ (here and below all relations are given in atomic units). For atomic potential $\Phi_0 \sim Z/R$ and $R_0 \sim R$ where $Z \geq 1$ is the atomic number and R is the radius of electron cloud. Therefore, in case of atoms it is required that $2ZR >> 1$. Even for light atoms their radii are several times larger than Bohr radius, $R >> 1$. Thus atoms and all polyatomic structures indeed are quasi-classical electron systems in the sense specified above and their structural and electronic characteristics can be calculated based on the quasi-classically parameterized electric charge density and electrical field potential distributions in constituent atoms.

The values of i-th electron classical turning point radii r_i' and r_i'', $r_i' < r_i''$, are obtained by solving the equations

$$E_i = -\Phi_i(r) + \frac{l_i(l_i+1)}{2r^2} \qquad (i = 1,2,3,...,Z) \tag{1}$$

where r denotes the distance from the center of atom, $\Phi_i(r)$ is the potential affecting the given electron, $E_i < 0$ and l_i are its energy and orbital quantum number, respectively.

In the ground state the inner classical turning point for relative motion of atomic nucleus and electron cloud coincides with the center of system. As for the corresponding outer classical turning point radius $\tilde{r}$, it is obtained by solving the equation

$$\tilde{E} = Z\tilde{\Phi}(r), \tag{2}$$

where $\tilde{E} < 0$ denotes the energy associated with relative motion and

$$\tilde{\Phi}(r) = -\frac{1}{Z-1}\left(\frac{Z^2}{r} - \sum_{i=1}^{Z}\Phi_i(r)\right) \tag{3}$$

is the electron cloud potential affecting the nucleus.

In particular, using the quasi-classical parameterization based on the Coulomb-like atomic potentials $\Phi_i(r) = Z_i/r$ we are able to get exact formulas

$$r_i' = \frac{n_i\left(n_i - \sqrt{n_i^2 - l_i(l_i+1)}\right)}{Z_i}, \tag{4}$$

$$r_i'' = \frac{n_i\left(n_i + \sqrt{n_i^2 - l_i(l_i+1)}\right)}{Z_i}, \tag{5}$$

$$\tilde{r} = \frac{2(Z-1)}{Z^2\left(Z^2 - \sum_{i=1}^{i=Z} Z_i\right)^2}, \tag{6}$$

$$\tilde{E} = -\frac{Z^3\left(Z^2 - \sum_{i=1}^{i=Z} Z_i\right)^2}{2(Z-1)^2}. \qquad (7)$$

Here $Z_i = n_i\sqrt{-2E_i}$ is the effective charge of the screened nucleus and n_i is the principal quantum number of i-th electron. The numerical values of Z_i, $\tilde{E}$, r_i', r_i'' and $\tilde{r}$ can be found by fitting the quasi-classical energy levels E_i to ab initio (for instance HF) ones.

Quasi-classical limit implies the truncation of electron states charge densities outside the classical turning points and space-averaging within the range between them. In this case i-th electron partial charge density is approximated by the piecewise-constant radial function

$$\begin{aligned} \rho_i(r) &= 0 && r < r_i' \\ &= -\frac{3}{4\pi(r_i''^3 - r_i'^3)} && r_i' < r < r_i'' \\ &= 0 && r_i'' < r. \end{aligned} \qquad (8)$$

As for the nucleus charge density, it should be averaged inside the $\tilde{r}$ -sphere:

$$\begin{aligned} \tilde{\rho}(r) &= \frac{3Z}{4\pi\tilde{r}^3} && 0 < r < \tilde{r} \\ &= 0 && \tilde{r} < r. \end{aligned} \qquad (9)$$

Consequently, the full atomic charge density is expressed by the step-like radial function

$$\rho(r) = \tilde{\rho}(r) + \sum_{i=1}^{i=Z}\rho_i(r) \equiv \rho_k \qquad r_{k-1} < r < r_k \qquad (k = 1,2,3,...,q), \qquad (10)$$

where r_k and ρ_k denote known constants which depend on parameters r_i', r_i'' and $\tilde{r}$, $0 \equiv r_0 < r_1 < r_2 < \cdots < r_q < \infty$, $q \le 2Z$ is the number of different homogenous-charge-density spherical layers in atom.

Using the Poisson equation, the radial dependence of the full atomic potential also can be approximated by the step-like function,

$$\varphi(r) = \frac{3a_k(r_k^2 - r_{k-1}^2)}{2(r_k^3 - r_{k-1}^3)} + \frac{3b_k(r_k^5 - r_{k-1}^5)}{5(r_k^3 - r_{k-1}^3)} + c_k \equiv \varphi_k \qquad r_{k-1} < r < r_k \qquad (k = 1,2,3,...,q)$$

$$a_k = \sum_{i=1}^{i=k-1}\frac{4\pi\rho_i(r_i^3 - r_{i-1}^3)}{3} - \frac{4\pi\rho_k r_{k-1}^3}{3},$$

$$b_k = -\frac{2\pi\rho_k}{3},$$

$$c_k = \sum_{i=k+1}^{i=q} 2\pi\rho_i(r_i^2 - r_{i-1}^2) + 2\pi\rho_k r_k^2, \qquad (11)$$

if it is substituted by the space-averaged values inside each of the $r_{k-1} < r < r_k$ intervals.

In the region $r > r_q$, both the charge density and potential vanish identically, $\rho(r) \equiv 0$ and $\varphi(r) \equiv 0$. Thus finite parameter r_q acquires a meaning of the quasi-classical atomic radius.

Based on the presented step-like parameterization of the charge density and potential distributions in an atom, its quasi-classical total energy can be expressed in the following form:

$$E_{(Atom)} = \frac{\pi}{3}\sum_{k=1}^{i=q}\rho_k\varphi_k(r_k^3 - r_{k-1}^3) < 0. \qquad (12)$$

Note that it includes the non-physical energy of self-action, $E_{(Atom)\,Self-Action} > 0$ which arises from substituting the charge density for the probability density. Its value can be easily calculated in the quasi-classical approximation and then excluded from the total energy.

When the molecular or crystalline charge densities and potentials are expressed by the superposition of the step-like atomic charge densities and potentials, respectively, the molar (i.e., per chemical formula unit of the substance) ground state static energy and its zero-point vibration correction are calculated as

$$E_{Static} = \frac{1}{4}\sum_{\vec{t}}\sum_{(i)=1}^{(i)=N}\sum_{(k)=1}^{(k)=N}\sum_{j=1}^{j=q_{(i)}}\sum_{l=1}^{l=q_{(k)}}\rho_{(i)j}\varphi_{(k)l}V_{(ik)jl}(r_{(ik)\vec{t}}) < 0\,, \tag{13}$$

$$E_{Vibration} = \frac{3}{2}\sum_{(i)=1}^{(i)=N}\sqrt{\sum_{\vec{t}}{}'\sum_{(k)=1}^{(k)=N}\sum_{j=1}^{j=q_{(i)}}\sum_{l=1}^{l=q_{(k)}}\frac{\rho_{(i)j}\phi_{(k)l}+\rho_{(k)l}\phi_{(i)j}}{2M_{(i)}r_{(ik)\vec{t}}}\frac{\partial V_{(ik)jl}(\vec{r}_{(ik)\vec{t}})}{\partial\vec{r}_{(ik)\vec{t}}}} > 0\,. \tag{14}$$

Here the primed summation symbol denotes the elimination of the terms with $\vec{t}=0$ and $i=k$; indexes in parentheses (i) and (k) denote the atoms in the molecule or crystal unit cell, N is the full number of atoms, $M_{(i)}$ is the mass of i-th atom, $\vec{t}$ is the crystal translational vector – in case of a molecule $\vec{t}\equiv 0$, $\vec{r}_{(ik)\vec{t}}$ is a distance between atomic sites and

$$\begin{aligned}V_{(ik)jl}(r_{(ik)\vec{t}}) = {} & V(r_{(i)j}, r_{(k)l}, r_{(ik)\vec{t}}) + V(r_{(i)j-1}, r_{(k)l-1}, r_{(ik)\vec{t}}) - \\ & - V(r_{(i)j}, r_{(k)l-1}, r_{(ik)\vec{t}}) - V(r_{(i)j-1}, r_{(k)l}, r_{(ik)\vec{t}})\,.\end{aligned} \tag{15}$$

We have introduced an universal geometric function $V(R_1, R_2, D_{12})$ which expresses the volume of the intersection of two spheres as a function of their radii R_1 and R_2, and the inter-center distance D_{12}. $V(R_1, R_2, D_{12})$ and its partial derivative $\partial V(R_1, R_2, D_{12})/\partial D_{12}$ both are continuous piecewise algebraic functions as follows:

$$\begin{aligned}V(R_1, R_2, D_{12}) &= \frac{4\pi R_1^3}{3} && D_{12} \le R_2 - R_1\,,\\ &= \frac{4\pi R_2^3}{3} && D_{12} \le R_1 - R_2\,,\\ &= \frac{\pi(R_1+R_2-D_{12})^2((R_1+R_2+D_{12})^2 - 4(R_1^2 - R_1R_2 + R_2^2))}{12D_{12}} && |R_1 - R_2| \le D_{12} \le R_1 + R_2\,,\\ &= 0 && R_1 + R_2 \le D_{12}\,;\end{aligned} \tag{16}$$

$$\begin{aligned}\frac{\partial V(R_1, R_2, D_{12})}{\partial D_{12}} &= 0 && D_{12} \le R_2 - R_1\,,\\ &= 0 && D_{12} \le R_1 - R_2\,,\\ &= -\frac{\pi((R_1+R_2)^2 - D_{12}^2)(D_{12}^2 - (R_1-R_2)^2)}{4D_{12}^2} && |R_1 - R_2| \le D_{12} \le R_1 + R_2\,,\\ &= 0 && R_1 + R_2 \le D_{12}\,.\end{aligned} \tag{17}$$

In the lowest quasi-classical approximation, the equilibrium structure of substance is obtained by maximizing the molar binding energy of expected structures with respect to their structural parameters:

$$E_{Binding} = \sum_{(i)=1}^{(i)=N}(E_{(i)} - E_{(i)Self-Action}) - (E_{Static} - E_{Self-Action}) - E_{Vibration} > 0\,. \tag{18}$$

However, neglecting the insignificant redistribution of valence electrons arisen from association of atoms into a molecular or crystalline structure, the quasi-classical self-action energy

of the substance is approximated by the sum of quasi-classical self-action energies of constituent atoms:

$$E_{Self-Action} \approx \sum_{(i)=1}^{(i)=N} E_{(i)Self-Aaction} \,. \tag{19}$$

And consequently, the binding energy approximately can be calculated without excluding of the self-action terms in advance:

$$E_{Binding} \approx \sum_{(i)=1}^{(i)=N} E_{(i)} - E_{Static} - E_{Vibration} > 0 \,. \tag{20}$$

The expected errors of the quasi-classical approach can be estimated for the model inner potential in the form of the analytical solution of the Thomas–Fermi (TF) equation for the semiclassical atomic potential: structural and energy parameters of the electronic system determined within the initial quasi-classical approximation are shown to differ from their exact values by factors of $(10/3\pi)^{1/3} \approx 1.02 \sim 1$ and $(3\pi/10)^{2/3} \approx 0.96 \sim 1$, respectively. Thus the expected errors of the quasi-classical approach amount to a few percents. Even more, within the initial quasi-classical approximation there are no uncontrollable calculation errors due the finiteness of quasi-classical atomic radii – the pair interactions without series termination are truncated at the distances exceeded the sums of atomic radii.

A complete quasi-classical theory of substance including calculation schemes for structural and binding, as well as for electronic spectrum characteristics, one can find in [102,103]. These schemes have been applied successfully for Na molecular and crystalline structures [104], various diatomic molecules [60,61], boron nanotubes [105,106], and mainly for one-, two- and three-dimensional structural modifications of boron nitride – diatomic molecule, isolated plane sheet, hexagonal h-BN, cubic c-BN, and wurtzite-like w-BN crystals [59,60,64,73–75,107,108].

3.2. Geometries of the boron nitride regular single-walled nanotubes

Summarizing previous subsection, one can conclude that equilibrium structural and binding parameters of the boron nitride nanotubes can be calculated quasi-classically based on analytical expressions describing their geometries. This task has been solved in [87,108,109] for regular (achiral), i.e., zigzag (n,0) and armchair (n,n) BN nanotubes. A model of regular nanotubes used here assumes that all atomic sites are located on cylindrical surfaces at the vertexes of regular hexagons broken along B–N or B–B and N–N diagonals, i.e., the expected small differences in bond length distinguished by their orientation toward the tube axis are neglected.

Namely, radii $R_{(n,0)}$ and $R_{(n,n)}$ of the zigzag and armchair nanotubes have been obtained [87,108] in terms of the nanotube index n = 1, 2, 3,… and the structure parameter a:

$$R_{(n,0)} = \frac{a}{4\sin\pi/2n}, \tag{21}$$

$$R_{(n,n)} = \frac{\sqrt{5+4\cos\pi/2n}\; a}{4\sqrt{3}\sin\pi/2n}. \tag{22}$$

As it was mentioned, the parameter a corresponds to a lattice constant of the boron nitride layered crystals, i.e., to an intralayer B–B or N–N bond length. Therefore, the B–N bond length d equals to $a/\sqrt{3}$. The nanotube index n determines the number of atoms, as a nanotube unit cell consists of $2n$ formula units, $B_{2n}N_{2n}$.

Detailed regular geometries of zigzag and armchair BN nanotubes have been described in [108,109] using cylindrical coordinates (ρ, φ, z), which are useful for calculating binding energy.

A unit cell of zigzag nanotubes consists of 4 atomic rings in parallel planes perpendicular to the axis. There are 2 pairs of rings, each consisting of 2 planes with n boron or n nitrogen atoms. Obviously, the cylindrical coordinate ρ for all atomic sites equals to the tube radius:

$$\rho_{\mathrm{B}} = \rho_{\mathrm{N}} = R_{(n,0)}. \tag{23}$$

As for the coordinates φ and z in the first and second pairs of atomic rings, they equal to

$$\varphi_{\mathrm{B}} = \varphi_{\mathrm{N}} = 2l\pi / n, \tag{24}$$

$$z_{\mathrm{B}} = (6m+1)a / 2\sqrt{3}, \tag{25}$$

$$z_{\mathrm{N}} = (6m-1)a / 2\sqrt{3}, \tag{26}$$

and

$$\varphi_{\mathrm{B}} = \varphi_{\mathrm{N}} = (2l+1)\pi / n, \tag{27}$$

$$z_{\mathrm{B}} = (3m-1)a / \sqrt{3}, \tag{28}$$

$$z_{\mathrm{N}} = (3m+1)a / \sqrt{3}, \tag{29}$$

respectively. Here $l = 0,1,2,...,n-1$ and $m = 0,\pm1,\pm2,...$ number atomic pairs in a given pair of the atomic rings and these rings themselves, respectively.

The unit cell of armchair nanotubes consists of 2 atomic rings in parallel planes perpendicular to the tube axis. For its part, each ring consists of n boron and n nitrogen atoms. The coordinate ρ for all atomic sites again equals to the tube radius:

$$\rho_{\mathrm{B}} = \rho_{\mathrm{N}} = R_{(n,n)}, \tag{30}$$

while the rest cylindrical coordinates in the first and second atomic rings equal to

$$\varphi_{\mathrm{B}} = \varphi_1 + 2l\pi / n, \tag{31}$$

$$\varphi_{\mathrm{N}} = -\varphi_1 + 2l\pi / n, \tag{32}$$

$$z_{\mathrm{B}} = z_{\mathrm{N}} = ma, \tag{33}$$

and

$$\varphi_{\mathrm{B}} = -\varphi_1 - 2\varphi_2 + 2l\pi / n, \tag{34}$$

$$\varphi_{\mathrm{N}} = \varphi_1 + 2\varphi_2 + 2l\pi / n, \tag{35}$$

$$z_{\mathrm{B}} = z_{\mathrm{N}} = (2m+1)a / 2, \tag{36}$$

respectively. Here

$$\sin\varphi_1 = \frac{2\sin\pi/2n}{\sqrt{5+4\cos\pi/2n}}, \tag{37}$$

$$\sin\varphi_2 = \frac{\sin\pi/2n}{\sqrt{5+4\cos\pi/2n}}, \tag{38}$$

and $l = 0,1,2,...,n-1$ and $m = 0,\pm1,\pm2,...$ number B or N atoms in atomic rings and these rings themselves.

Based on the above discussion, the distances between a given atomic site and the sites in the so-called central atomic pairs in zigzag and armchair nanotubes have been found.

For zigzag ($l = m = 0$: $\varphi_{\mathrm{B}} = \varphi_{\mathrm{N}} = 0$, $z = a/2\sqrt{3}$, and $z = -a/2\sqrt{3}$) tubes

$$\frac{(\,{}^{lm}_{(n,0)}\mathrm{B1} - {}^{00}_{(n,0)}\mathrm{B1})^2}{a^2} = \frac{\sin^2 l\pi/n}{4\sin^2\pi/2n} + 3m^2, \tag{39}$$

$$\frac{(\,{}^{lm}_{(n,0)}\mathrm{B2} - {}^{00}_{(n,0)}\mathrm{B1})^2}{a^2} = \frac{\sin^2(2l+1)\pi/2n}{4\sin^2\pi/2n} + \frac{3(2m-1)^2}{4}, \tag{40}$$

$$\frac{(\,{}^{lm}_{(n,0)}\mathrm{N1} - {}^{00}_{(n,0)}\mathrm{B1})^2}{a^2} = \frac{\sin^2 l\pi/n}{4\sin^2\pi/2n} + \frac{(3m-1)^2}{3}, \tag{41}$$

$$\frac{(\,{}^{lm}_{(n,0)}\mathrm{N2}-{}^{00}_{(n,0)}\mathrm{B1})^2}{a^2}=\frac{\sin^2(2l+1)\pi/2n}{4\sin^2\pi/2n}+\frac{(6m+1)^2}{12}, \tag{42}$$

$$\frac{(\,{}^{lm}_{(n,0)}\mathrm{B1}-{}^{00}_{(n,0)}\mathrm{N1})^2}{a^2}=\frac{\sin^2 l\pi/n}{4\sin^2\pi/2n}+\frac{(3m+1)^2}{3}, \tag{43}$$

$$\frac{(\,{}^{lm}_{(n,0)}\mathrm{B2}-{}^{00}_{(n,0)}\mathrm{N1})^2}{a^2}=\frac{\sin^2(2l+1)\pi/2n}{4\sin^2\pi/2n}+\frac{(6m-1)^2}{12}, \tag{44}$$

$$\frac{(\,{}^{lm}_{(n,0)}\mathrm{N1}-{}^{00}_{(n,0)}\mathrm{N1})^2}{a^2}=\frac{\sin^2 l\pi/n}{4\sin^2\pi/2n}+3m^2, \tag{45}$$

$$\frac{(\,{}^{lm}_{(n,0)}\mathrm{N2}-{}^{00}_{(n,0)}\mathrm{N1})^2}{a^2}=\frac{\sin^2(2l+1)\pi/2n}{4\sin^2\pi/2n}+\frac{3(2m+1)^2}{4}. \tag{46}$$

For armchair ($l=m=0:\varphi_{\mathrm{B}}=\varphi_1$, $\varphi_{\mathrm{N}}=-\varphi_1$, and $z_{\mathrm{B}}=z_{\mathrm{N}}=0$) tubes,

$$\frac{(\,{}^{lm}_{(n,n)}\mathrm{B1}-{}^{00}_{(n,n)}\mathrm{B1})^2}{a^2}=\frac{(5+4\cos\pi/2n)\sin^2 l\pi/n}{12\sin^2\pi/2n}+m^2, \tag{47}$$

$$\frac{(\,{}^{lm}_{(n,n)}\mathrm{B2}-{}^{00}_{(n,n)}\mathrm{B1})^2}{a^2}=\frac{(5+4\cos\pi/2n)\sin^2(2l-1)\pi/2n}{12\sin^2\pi/2n}+\frac{(2m+1)^2}{4}, \tag{48}$$

$$\frac{(\,{}^{lm}_{(n,n)}\mathrm{N1}-{}^{00}_{(n,n)}\mathrm{B1})^2}{a^2}=\frac{(2\sin(2l-1)\pi/2n+\sin l\pi/n)^2}{12\sin^2\pi/2n}+m^2, \tag{49}$$

$$\frac{(\,{}^{lm}_{(n,n)}\mathrm{N2}-{}^{00}_{(n,n)}\mathrm{B1})^2}{a^2}=\frac{(\sin(2l+1)\pi/2n+2\sin l\pi/n)^2}{12\sin^2\pi/2n}+\frac{(2m+1)^2}{4}, \tag{50}$$

$$\frac{(\,{}^{lm}_{(n,n)}\mathrm{B1}-{}^{00}_{(n,n)}\mathrm{N1})^2}{a^2}=\frac{(2\sin(2l+1)\pi/2n+\sin l\pi/n)^2}{12\sin^2\pi/2n}+m^2, \tag{51}$$

$$\frac{(\,{}^{lm}_{(n,n)}\mathrm{B2}-{}^{00}_{(n,n)}\mathrm{N1})^2}{a^2}=\frac{(\sin(2l-1)\pi/2n+2\sin l\pi/n)^2}{12\sin^2\pi/2n}+\frac{(2m+1)^2}{4}, \tag{52}$$

$$\frac{(\,{}^{lm}_{(n,n)}\mathrm{N1}-{}^{00}_{(n,n)}\mathrm{N1})^2}{a^2}=\frac{(5+4\cos\pi/2n)\sin^2 l\pi/n}{12\sin^2\pi/2n}+m^2, \tag{53}$$

$$\frac{(\,{}^{lm}_{(n,n)}\mathrm{N2}-{}^{00}_{(n,n)}\mathrm{N1})^2}{a^2}=\frac{(5+4\cos\pi/2n)\sin^2(2l+1)\pi/2n}{12\sin^2\pi/2n}+\frac{(2m+1)^2}{4}. \tag{54}$$

4. BINDING ENERGIES IN DEPENDENCE ON STRUCTURAL PARAMETER

At first, based on the above stated relations (4 – 11) and HF values of the atomic electron energy-levels tabulated in [110], the required quasi-classical parameters r_k, ρ_k, and φ_k for constituent atoms B and N have been calculated. They are given in Tables 1 and 2, respectively.

Table 1. Quasi-classical parameters of step-like redial distributions of electron-charge-density and electric-field-potential in boron atom (in a.u.).

k	1	2	3	4	5
r_k	2.758476 E−02	5.098016 E−01	7.441219 E−01	4.021346 E+00	4.337060 E+00
ρ_k	5.686514 E+04	−3.610951 E+00	−7.342212 E−03	−1.028341 E−02	−2.941197 E−03
φ_k	2.105468 E+02	8.882329 E+00	3.652920 E+00	2.060720 E−01	6.135348 E−04

Table 2. Quasi-classical parameters of step-like redial distributions of electron-charge-density and electric-field-potential in nitrogen atom (in a.u.).

k	1	2	3	4	5
r_k	9.446222 E−03	3.577244 E−01	5.498034 E−01	2.909074 E+00	3.204489 E+00
ρ_k	1.982589 E+06	−1.044967 E+01	−1.939444 E−02	−4.126981 E−02	−2.187537 E−02
φ_k	8.784581 E+02	2.022523 E+01	8.464698 E+00	5.096684 E−01	3.993358 E−03

Here the values are shown in atomic units with 7 significant digits in accordance with the accuracy of input data (HF energies). Such high accuracy is useful in interim calculations. As for the final results, they should be expressed in rounded figures with 3 or 4 significant digits (in Å or eV for structure or energy parameters, respectively) because it corresponds to the usual experimental errors when determining structure and energy parameters of a substance, and the relative errors of the semiclassical calculations aimed at finding theoretically these parameters for polyatomic systems amount to a few percents.

Using these parameters and expressions (12 – 17, 20, 39 – 54) for the components of the quasi-classical molar binding energy and squared inter-atomic distances in zigzag and armchair BN nanotubes (Figs. 1 and 2), their binding energies were calculated versus the structural parameter a with spacing of 0.001 a.u., i.e., within the accuracy of 4 significant digits. The vibration energy is assumed to be zero when radicand in formula (14) becomes negative.

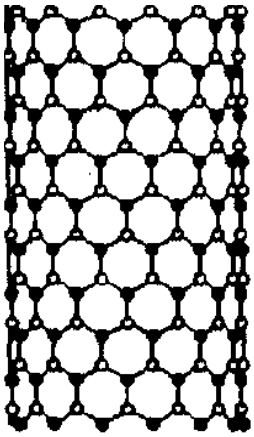

Fig. 1. Structure of a zigzag BN nanotube.

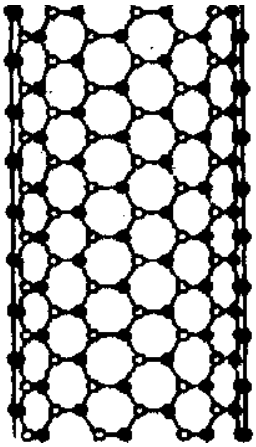

Fig. 2. Structure of an armchair BN nanotube.

In order to carry out these massive calculations, a special computer code has been designed. Calculations were carried out within the range of the structure parameter a which varied from 1 to 13 a.u. with a step $\Delta a = 0.001$ a.u. (that is quite enough to cover values having any physical sense). The nanotube indices varied from $n = 1$, covering zigzag and armchair nanotubes up to (18,0) and (10,10), respectively. The radii of the largest calculated species are approximately equal. They are sufficiently large for the tube molar binding energy to almost reach the "saturation" value, which is given by the binding energy of the planar hexagonal BN sheet. In order to make sure that such "saturation" indeed takes place, test species with very large indexes (45,0) and (26,26) (again with approximately equal radii) have also been calculated.

Figs. 3 and 4 show $E_{Binding}(a)$ curves for some zigzag and armchair BN nanotubes, respectively. One can see that at sufficiently small inter-atomic distances binding energy might take a large negative value that implies that the structure is unstable, while at sufficiently large inter-atomic distances the binding energy always equals to zero which reveals atomization of a structure. As for the intermediate distances, the molar binding energy is positive that is a signature of structural stability. In this case, general trend in binding energy value is decreasing. However, $E_{Binding}(a)$ curves are not monotonous, but with several extremes. Such kind of oscillatory behavior of the molar biding energy of any atomic structure against the inter-atomic distances reflects electron-shell-structure of the constituent atoms (note that the interaction between particles of matter with forces non-monotonously decreasing with distance was foreseen as early as in 18th

century by Boscovich [111], whose atomic theory was based only on abstract philosophical speculations).

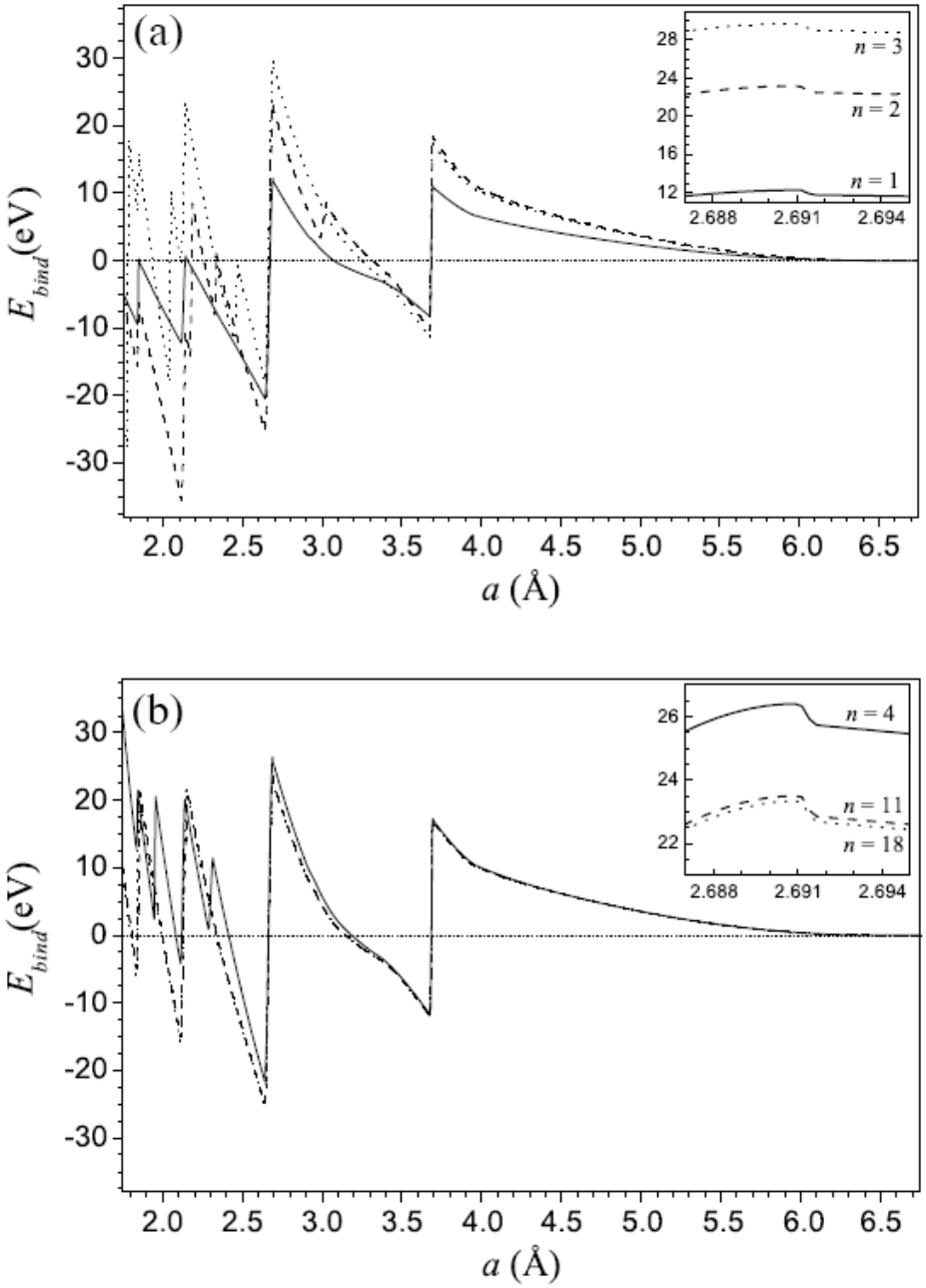

Fig. 3. Molar binding energy of zigzag BN nanotubes vs the structural parameter a.

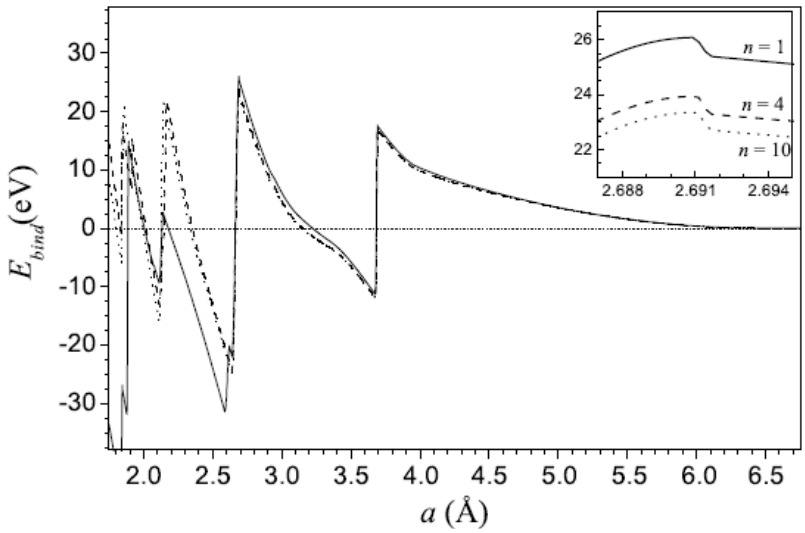

Fig. 4. Molar binding energy of armchair BN nanotubes vs the structural parameter a.

Table 3. Quasi-classically calculated radii and binding energies of BN nanotubes.

Nanotube	Radius, Å	Binding Energy, eV / mole
(1,0)	0.673	12.26
(1,1)	0.868	26.08
(2,0)	0.951	23.17
(3,0)	1.345	29.72
(2,2)	1.537	27.59
(4,0)	1.758	26.40
(5,0)	2.177	24.74
(3,3)	2.260	24.62
(6,0)	2.599	24.19
(4,4)	2.993	23.94
(7,0)	3.023	23.92
(8,0)	3.448	23.76
(5,5)	3.729	23.68
(9,0)	3.874	23.64
(10,0)	4.300	23.57
(6,6)	4.668	23.54
(11,0)	4.727	23.51
(12,0)	5.154	23.47
(7,7)	5.207	23.46
(13,0)	5.581	23.43
(8,8)	5.947	23.41
(14,0)	6.008	23.41
(15,0)	6.436	23.39
(9,9)	6.687	23.37
(16,0)	6.863	23.37
(17,0)	7.291	23.35
(10,10)	7.428	23.35
. . .	. . .	. . .
(45,0)	19.276	23.26
(26,26)	19.290	23.26

Let us discuss which of the peaks in these figures correspond to the equilibrium structure. The first peak from the left is lower than the successive one. This second peak for all tubes located at $a = 5.085$ a.u. (2.691 Å) seems to correspond to the realized stable BN nanotubular structures (the detailed behavior of $E_{Binding}(a)$ curves in its vicinity is shown in the foreground of Figs. 3 and 4). The next peak, even being higher than this, can not been reached kinetically in standard laboratory conditions because they correspond to lower interatomic distances. These two peaks are separated by very deep and sufficiently wide minima, i.e., by high and wide potential barriers which can be overcome only at ultrahigh temperatures or tunneled only at ultrahigh pressures.

The obtained equilibrium binding energies of BN nanotubes of both achiral types are summarized in Table 3 together with their radii calculated from formulas (21) and (22) for equilibrium value of the structural parameter $a = 2.691$ Å.

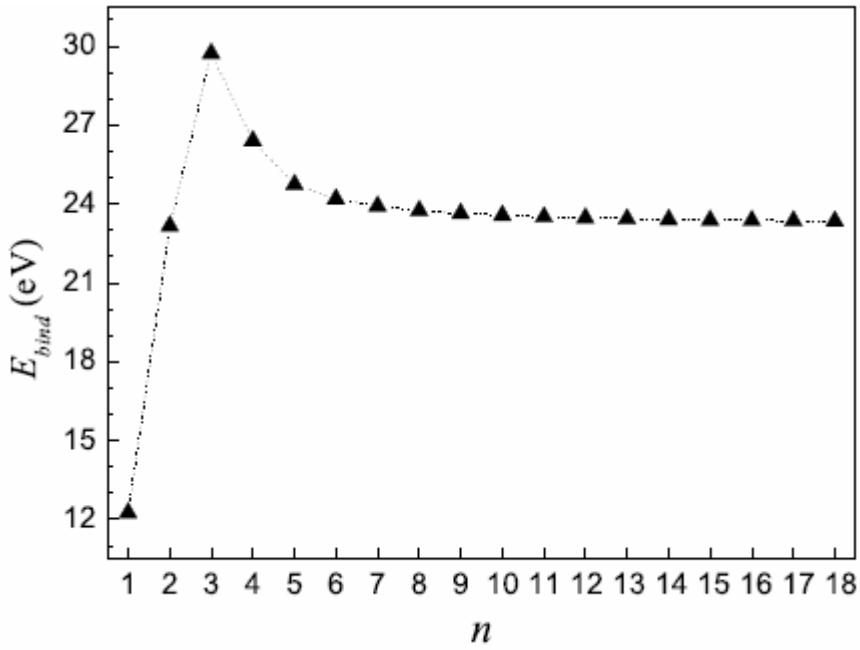

Fig. 5. Molar binding energy of zigzag BN nanotubes for different indexes n.

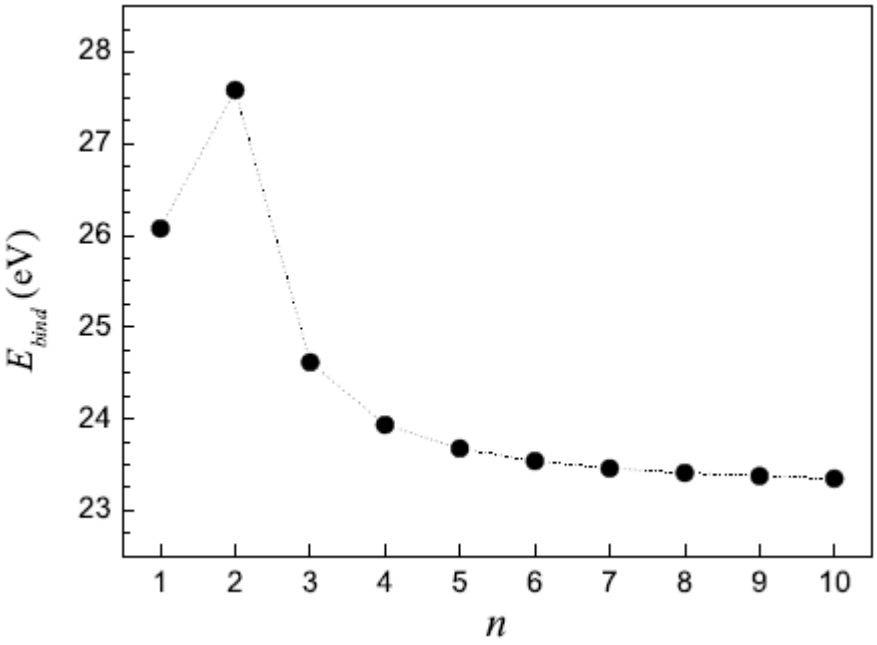

Fig. 6. Molar binding energy of armchair BN nanotubes for different indexes n.

Thus, the molar binding energies of small-sized nanotubes, both zigzag, (3,0), and armchair, (2,2), have peaks. Then for large indices the binding energies decrease toward the same constant value (see Figs. 5 and 6).

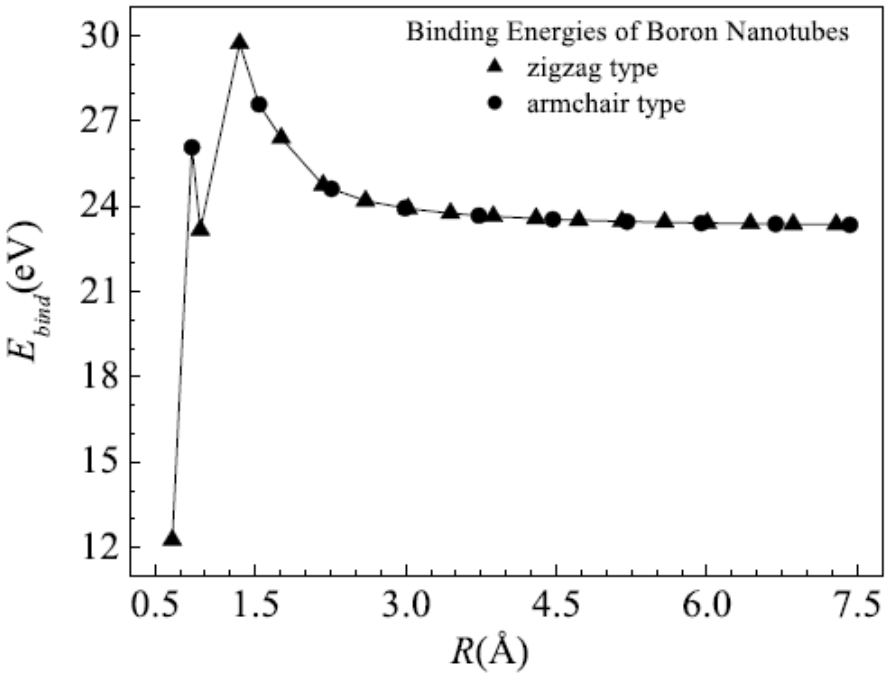

Fig. 7. Molar binding energy of achiral BN nanotubes vs the nanotube radius R.

Fig. 7 presents the dependence of the molar binding energy of achiral BN nanotubes on their radii R. It reveals pairs of minima at (1,0) and (2,0), and maxima at (1,1) and (3,0), i.e., all the extremes are located in low-radii-region. At higher radii, the molar binding energy slowly decreases to the value of 23.26 eV, which, apparently, corresponds to the value that of the plane hexagonal BN sheet.

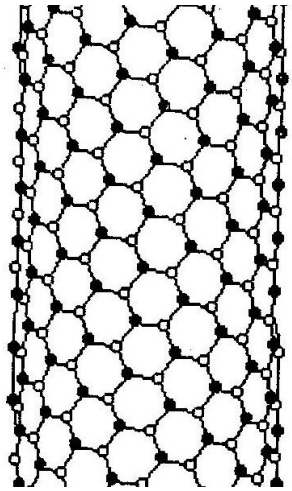

Fig. 8. Structure of a chiral BN nanotube.

The obtained dependence $E_{Binding}(a)$ in its domain of monotonicity seems to be quite smooth. It allows us to extrapolate this curve to chiral BN nanotubes (Fig. 8) too because the radius of a

chiral tube $R_{(n,m)}$, $0 < m < n$, and radii of the corresponding achiral tubes always meet the condition $R_{(n,0)} \le R_{(n,m)} \le R_{(n,n)}$.

5. ZERO-POINT VIBRATION ENERGIES

First, let us emphasize some features characteristic for the quasi-classical procedure of estimation of the zero-point vibration energies.

On the one hand, within the above formulated quasi-classical approach, all binding energy maxima are related with the onset of overlapping between certain regions of homogeneity of electric charge density and electric field potential in interacting atoms, constituents of the structure under the consideration. Namely, equilibrium point at $a \approx 5.085$ a.u. corresponds to the B–N bond length of $d \approx 2.937$ a.u. which is a sum of radii B $r_1 \approx 0.028$ a.u. and N $r_4 \approx 2.909$ a.u. (see Tables 1 and 2).

Table 4. Quasi-classically calculated vibration energies of BN nanotubes.

Nanotube	Vibration Energy, eV / mole	Corrected Binding Energy, eV / mole
(1,0)	0.25	12.01
(1,1)	0.33	25.75
(2,0)	0.32	22.85
(3,0)	0.33	29.39
(2,2)	0.32	27.27
(4,0)	0.32	26.08
(5,0)	0.32	24.42
(3,3)	0.32	24.30
(6,0)	0.32	23.87
(4,4)	0.31	23.63
(7,0)	0.31	23.61
(8,0)	0.31	23.45
(5,5)	0.31	23.37
(9,0)	0.31	23.33
(10,0)	0.31	23.26
(6,6)	0.31	23.23
(11,0)	0.31	23.20
(12,0)	0.31	23.16
(7,7)	0.31	23.15
(13,0)	0.31	23.12
(8,8)	0.31	23.10
(14,0)	0.31	23.10
(15,0)	0.31	23.08
(9,9)	0.31	23.06
(16,0)	0.31	23.06
(17,0)	0.31	23.04
(10,10)	0.31	23.04
. . .	. . .	. . .
(45,0)	0.31	22.95
(26,26)	0.31	22.95

On the other hand, quasi-classical expression of the vibration energy (14) is based on the parabolic approximation of the $E_{Binding}(a)$ curve and formula (17) for the volume of the intersection of two spheres, $V(R_1, R_2, D_{12})$, which is a continuously differentiable function of the inter-central distance D_{12}. However, one can see readily from expression (18) of its first (continuous) derivative that second derivative is not a continuous function.

That is the reason why the parabolic approximation of the $E_{Binding}(a)$ curve in the immediate vicinity of the binding energy peak is impossible. According to formula (14), $E_{Vibration}$ is identically zero at the equilibrium point and is assumed to be identically zero also on the left in the vicinity of that point, where radicand in formula (14) becomes negative. As for the right side in the vicinity of the equilibrium point, the binding energy can be estimated for nearest domain allowing parabolic approximation. Its half, i.e., arithmetic mean of the vibration energy left- and right-sided values can be considered as estimation for the vibration energy correction in the equilibrium. These values together with the correspondingly corrected binding energy are presented in Table 4.

The dependence of the molar vibration energy on the BN nanotube radius qualitatively reproduces that for the binding energy. However, this dependence is very weak and, thus, the molar vibration energy can be considered as almost independent from the tube radius, ~ 0.3 eV / mole. Of course, the vibration corrections to the binding energy are too weak to change character of the $E_{Binding}(R)$ dependence.

6. CONCLUDING REMARKS

The quasi-classically calculated structure parameter $a = 2.691$ Å of single-walled boron nitride nanotubes is in satisfactory agreement with experimental value for the h-BN layered crystals $a_{\exp} = 2.504$ Å [91], i.e., the difference is about 7 %. As is mentioned above overestimations in the structural parameter is characteristic for the quasi-classical approach. However, at least partially this overestimation seems to be related with expansion of lattice of the single hexagonal layer (plane or cylindrical) if compared with that of the three-dimensional layered crystal.

It is also expedient to analyze obtained spread of the molar zero-point vibration energy of BN nanotubes (0.25 – 0.33) eV and, in particular, its limit for ultra-large-radius tubes 0.31 eV by comparing them with the data available on the vibration characteristics of h-BN layered crystal, because the vibration energies of an isolated tubular layer and layered crystals can be directly compared as the atoms of the low-dimensional system can execute vibrations in three independent directions in physical space. Our quasi-classical estimations made for BN nanotubes agree well with analogous calculations (but in tight-binding approximation) for BN plane sheet of 0.27, the semiempirical estimate of 0.23 for zero-point vibrations energy in h-BN, and the estimate of 0.35 eV / mole from the theoretical phonon spectrum (see Subsection 2.2.).

We have found that the binding energies of BN single-walled nanotubes corrected with zero-point vibration energies lies within the interval (12.01 – 29.39) eV. In particular, the calculated corrected binding energy of the ultra-large-radius tube is predicted as 22.95 eV. Previous quasi-classical calculations (but in tight-binding approximation) performed for BN isolated plane sheet have given the binding energy 23.00 eV / mole, which coincides in order of magnitude with this interval and agrees very well with present result obtained for large tubes. As it was demonstrated in Subsection 2.2., for its part the binding energy ~ 23 eV / mole for single-layer boron nitride structures should be in good agreement with binding energy data available for BN multi-layered structures.

Summarizing the obtained results, it should be emphasized that a complex dependence of the BN nanotube molar binding energy on its radius is found out, but all binding energy values are

found to be positive, i.e., all tubes should be stable. However, they have rather different degrees of stability.

On the one hand, ultra-small-radius BN nanotubes (1,0) and (2,0) seem to be meta-stable, though their molar binding energies are positive, they are less than that for isolated hexagonal boron nitride layer. Especially the smallest (1,0) tube structure degenerated in zigzag atomic strip should be meta-stable because its binding energy is only about half of this value. Such a structure can be realized only as an inner wall in a multi-walled tube.

On the other hand, the formation probabilities for BN tubes with indexes (1,1), (3,0), and (4,0) should exceed that for isolated sheet. Among them the (3,0) tube is well pronounced, formation of which is predicted to be energetically most preferable than the layer growth.

As for other BN nanotubes, their molar binding energies only slightly exceed that of sheet and their formation probabilities should be almost same as for layered crystal growth.

Finally, it should be noted that, in addition to the energy considerations concerning the relative stability of tubular structure, it is also necessary to take into account features characteristic to BN nanosystems, in view of the general equations derived for energy fluctuations of small completely open (incompressible) systems [112]. They show that the fluctuations should be unusually large because there are no constraints on the size of a system and, in addition, the fluctuations of the total or partial number of atoms in binary systems indirectly contribute to the fluctuations in their energy.

ACKNOWLEDGEMENT

L. Chkhartishvili acknowledges the financial support from the Georgia National Science Foundation (GNSF) under the Project # GNSF / ST 08 / 4 – 411 – Geometry of the boron nitride nanostructures.

REFERENCES

1. A. Rubio, J.L. Corkill, M. L. Cohen. Phys. Rev. B, **49**, 5081 (1994).
2. Z. Weng-Sieh, K. Cherrey, N.G. Chopra, X. Blasé, Y. Miyamoto, A. Rubio, M.L. Cohen, S.G. Louie, A. Zettl, R. Gronsky. Phys. Rev. B, **51**, 11229 (1995).
3. N.G. Chopra, R.J. Luyken, K. Cherrey, V.H. Crespi, M.L. Cohen, S.G. Louie, A. Zettl. Science, **269**, 966 (1995).
4. K. Suenaga, C. Colliex, N. Demoncy, A. Loieseau, H. Pascard, F. Willaime. Science, **278**, 653 (1997).
5. K. Suenaga, F. Willaime, A. Loieseau, C. Colliex. Appl. Phys. A, **68**, 301 (1999).
6. A. Loiseau, F. Willaime, N. Demoncy, G. Hug, H. Pascard. Phys. Rev. Lett., **76**, 4737 (1996).
7. Y. Saito, M. Maida, T. Matsumoto. Jpn. J. Appl. Phys. A, **38**, 159 (1999).
8. Y. Saito, M. Maida. J. Phys. Chem. A, **103**, 1291 (1999).
9. D. Golberg, Y. Bando, M. Eremets, K. Takemura, K. Kurashima, H. Yusa. Appl. Phys. Lett., **69**, 2045 (1996).
10. R. Sen, B.C. Satishkumar, A. Govindaraj, K.R. Harikumar, G. Raina, J.-P. Zhang, A.K. Cheetham, C.N.R. Rao. Chem. Phys. Lett., **287**, 671 (1998).
11. D. Golberg, Y. Bando, W. Han, K. Kurashima, T. Sato. Chem. Phys. Lett., **308**, 337 (1999).
12. D. Golberg, W. Han, Y. Bando, L. Bourgeois, K. Kurashima, T. Sato. J. Appl. Phys., **86**, 2364 (1999).
13. Y. Chen, L.T. Chadderton, J.F. Gerald, J.S. Williams. Appl. Phys. Lett., **74**, 2960 (1999).
14. T.S. Bartnitskaya, G.S. Oleinik, V.V. Pokropivnyi, N.V. Danilenko, V.M. Vershchaka, A.V. Kotko. Superhard Mat., **6**, 71 (1998).
15. T.S. Bartnitskaya, G.S. Oleinik, A.V. Pokropivnyi, V.V. Pokropivnyi. JEPT Lett., **69**, 163 (1999).

16. C. Colazo–Davila, E. Bengu, L.D. Marks, M. Kirk. Diam. Rel. Mat., **8**, 1091 (1999).
17. T. Oku, T. Hirano, M. Kuno, T. Kusunose, K. Niihara, K. Suganuma. Mat. Sci Eng. B, **74**, 206 (2000).
18. J. Wang, V.K. Kayastha, Y.Kh. Yap, Zh. Fan, J.G. Lu, Zh. Pan, I.N. Ivanov, A.A. Puretzky, D.B. Geohegan. Nano Lett., **5**, 2528 (2005).
19. L.L. Sartinska, S. Barchikovski, N. Wagenda, B.M. Rud', I.I. Timofeeva. Appl. Surf. Sci., **253**, 4295 (2007).
20. L.L. Sartinska, A.A. Frolov, A.Yu. Koval', N.A. Danilenko, I.I. Timofeeva, B.M. Rud'. Mat. Chem. Phys., **109**, 20 (2008).
21. M.V.P. Altoe, J.P. Sprunck, J.-C.P. Gabriel, K. Bradley. J. Mat. Sci., **38**, 4805 (2003).
22. M.W. Smith, K.C. Jordan, Ch. Park, J.-W. Kim, P.T. Lillehei, R. Crooks, J.S. Harrison. Nanotechnology, **20**, 505604 (2009).
23. X. Blasé, J.-C. Charlier, A. de Vita, R. Car. Appl. Phys. Lett., **70**, 197 (1997).
24. X. Blasé, J.-C. Charlier, A. de Vita, R. Car. Appl. Phys. A, **68**, 293 (1999).
25. V.V. Pokropivnyj, V.V. Skorokhod, G.S. Oleinik, A.V. Kurdyumov, T.S. Bartnitskaya, A.V. Pokropivnyj, A.G. Sisonyuk, D.M. Sheichenko. J. Solid State Chem., **154**, 214 (2000).
26. J.H. Lee. J. Kor. Phys. Soc., **49**, 172 (2006).
27. V. Verma, K. Dharamvir. Int. J. Nanosystems, **1**, 27 (2008).
28. B. Baumeier, P. Krüger, J. Pollmann. Phys. Rev. B, **76**, 085407 (2007).
29. Y.-H. Kim, K.J. Chang, S.G. Louie. Phys. Rev. B, **63**, 205408 (2001).
30. G.Y. Guo, J.C. Lin. Phys. Rev. B, **72**, 075416 (2005).
31. G.Y. Guo, J.C. Lin. Phys. Rev. B, **77**, 049901(E) (2008).
32. Ch. Zhi, Y. Bando, Ch. Tang, D. Golberg. Phys. Rev. B, **74**, 153413 (2006).
33. Ch. Zhi, Y. Bando, Ch. Tang, D. Golberg. Phys. Rev. B, **74**, 199902(E) (2006).
34. W.-Q. Han, C.W. Chang, A. Zettl. Nano Lett., **4**, 1355 (2004).
35. K. Yum, M.-F. Yu. Nano Lett., **6**, 329 (2006).
36. S.A. Shevlin, Z.X. Guo. Phys. Rev. B, **76**, 024104 (2007).
37. E. Durgun, Y.-R. Jang, S. Ciraci. Phys. Rev. B, **76**, 073413 (2007).
38. Ch. Tang, Y. Bando, X. Ding, Sh. Qi, D. Golberg. J. Am. Chem. Soc., **124**, 14550 (2002).
39. Ch. Zhi, Y. Bando, Ch. Tang, D. Golberg. J. Am. Chem. Soc., **127**, 17144 (2005).
40. Ch. Zhi, Y. Bando, Ch. Tang, R. Xie, T. Sekiguchi, D. Golberg. J. Am. Chem. Soc., **127**, 15996 (2005).
41. M. Côté, P. D. Haynes, C. Molteni. Phys. Rev. B, **63**, 125207 (2001).
42. M. Ishigami, J. D. Sau, Sh. Aloni, M.L. Cohen, A. Zettl. Phys. Rev. Lett., **94**, 056804 (2005).
43. J. Cumings, A. Zettl. Chem. Phys. Lett., **316**, 211 (2000).
44. Y. Chen, J. Zou, S.J. Campbell, G. le Caer. Appl. Phys. Lett., **84**, 2430 (2004).
45. E. Bengu, L.D. Marks. Phys. Rev. Lett., **86**, 2385 (2001).
46. Ch. Tang, Y. Bando, Y. Huang, Sh. Yue, Ch. Gu, F.F. Xu, D. Golberg. J. Am. Chem. Soc., **127**, 6552 (2005).
47. E. J. Mele, P. Král. Phys. Rev. Lett., **88**, 056803 (2002).
48. N. Sai, E.J. Mele. Phys. Rev. B, **68**, 241405(R) (2003).
49. S.M. Nakhmanson, A. Calzolari, V. Meunier, J. Bernholc, M. Buongiorno Nardelli. Phys. Rev. B, **67**, 235406 (2003).
50. N.G. Lebedev, L.A. Chernozatonskij. Phys. Solid State, **48**, 2028 (2006).
51. Y. Zhang, K. Suenaga, C. Colliex, S. Iijima. Science, **281**, 973 (1998).
52. A. Zobelli, A. Gloter, C.P. Ewels, G. Seifert, C. Colliex. Phys. Rev. B, **75**, 245402 (2007).
53. I.V. Weiz. Supplement 2 – In: K.-P. Huber, G. Herzberg. Constants of Diatomic Molecules. Part 2: Molecules N_2 – ZrO. Moscow: Mir (1984).
54. O.I. Bukhtyarov, S.P. Kurlov, B.M. Lipenskikh. In: Abs. 8th Int. Symp. Boron, Borides, Carbides, Nitrides, Rel. Comp. Tbilisi: Metsniereba, 135 (1984).
55. J.L. Masse, M. Bärlocher. Helv. Chim. Acta, **47**, 314 (1964).

56. Yu.G. Khajt, V.I. Baranovskij. J. Str. Chem., **21**, 153 (1980).
57. H. Bredohl, J. Dubois, Y. Houbrechts, P. Nzohabonayo. J. Phys. B, **17**, 95 (1984).
58. Ch.M. Marian, M. Gastreich, J.D. Gale. Phys. Rev. B-I, **62**, 3117 (2000).
59. L. Chkhartishvili. In: Proc. 2nd Int. Boron Symp. Eskişehir: OGU, 165 (2004).
60. L. Chkhartishvili, D. Lezhava, O. Tsagareishvili, D. Gulua. Trans. AMIAG, **1**, 295 (1999).
61. L. Chkhartishvili, D. Lezhava, O. Tsagareishvili. J. Solid State Chem., **154**, 148 (2000).
62. A. Gaydon. Dissociation Energies and Spectra of Diatomic Molecules, London: Chapman & Hall (1947).
63. K.P. Huber, G. Herzberg. Molecular Spectra and Molecular Structure. IV. Constants of Diatomic Molecules. New York: van Nostrand Reinhold Co (1979).
64. M. Lorenz, J. Agreiter, A.M. Smith, V.E. Bondybey. J. Chem. Phys., **104**, 3143 (1996).
65. L. Chkhartishvili. Proc. TSU (Phys.), **40**, 130 (2006).
66. V.I. Vedeneev, L.V. Gurvich, V.N. Kondrat'ev, V.A. Medvedev, E.A. Frankevich. Chemical Bonds Breaking Energies. Ionization Potentials and Electron Affinities. Moscow: Acad. Sci. USSR (1962).
67. G. Meloni, M. Sai Baba, K.A. Gingerich. J. Chem. Phys., **113**, 8995 (2000).
68. R. Vanderbosch. Phys. Rev. A, **67**, 013203 (2003).
69. S.V. Lisenkov, G.A. Vinogradov, T.Yu. Astakhova, N.G. Lebedev. JETP Lett., **81**, 431 (2005).
70. A. Zunger. J. Phys. C, **7**, 76 (1974).
71. A. Zunger. J. Phys. C, **7**, 96 (1974).
72. D.L. Strout. J. Phys. Chem. A, **104**, 3364 (2000).
73. L.S. Chkhartishvili. Phys. Solid State, **46**, 2126 (2004).
74. L.S. Chkhartishvili. Phys. Solid State, **48**, 846 (2006).
75. L. Chkhartishvili, D. Lezhava. Trans. GTU, **439**, 87 (2001).
76. H. Werheit. Boron Nitride (BN) – In: Landolt-Börnstein, Numerical Data and Functional Relationships in Science and Technology, New Series, Group III: Crystal and Solid State Physics, Volume 17: Semiconductors, Subvolume g: Physics of Non-Tetrahedrally Bonded Binary Compounds III (Eds. K.-H. Hellwege, O. von Madelung). Berlin: Springer-Verlag (1982).
77. Y.-N. Xu, W.Y. Ching. Phys. Rev. B-I, **44**, 7784 (1991).
78. K. Albe. Phys. Rev. B-II, **55**, 6203 (1997).
79. Selected Values of Chemical Thermodynamic Properties (Eds. D.D. Wagmann, W.H. Evans, V.B. Parker, J. Halow, S.M. Bairly, R.H. Shumn). Washington: NBS (1968).
80. S.N. Grinyaev, F.V. Konusov, V.V. Lopatin. Phys. Solid State, **44**, 286 (2002).
81. M.S.C. Mazzoni, R.W. Nunes, S. Azevedo, H. Chacham. Phys. Rev. B, **73**, 073108 (2006).
82. S.V. Lisenkov, G.A. Vonogradov, T.Yu. Astakhova, N.G. Lebedev. Phys. Solid State, **48**, 192 (2006).
83. O.E. Alon. Phys. Rev. B, **64**, 153408 (2001).
84. V.V. Pokropivnyj. Powd. Metall. Met. Cer. **40**, 582 (2001).
85. M. Menon, D. Srivastava. Chem. Phys. Lett., **307**, 407 (1999).
86. J.-C. Charlier, X. Blase, A. de Vita, R. Car. Appl. Phys. A, **68**, 267 (1999).
87. L.S. Chkhartishvili. In: Thin Films in Optics in Nanoelectronics. Kharkiv: KhPTI, 367 (2006).
88. Z. Peralta-Inga, P. Lane, J.S. Murray, S. Boyd, M.E. Grice, Ch.J. O'Connor, P. Politzer. Nano Lett., **3**, 21 (2003).
89. D. Golberg, Y. Bando, L. Bourgeois, K. Kurashima, T. Sato. Appl. Phys. Lett., **77**, 1979 (2000).
90. S. Okada, S. Saito, A. Oshiyama. Phys. Rev. B, **65**, 165410 (2002).
91. Yu.B. Kuz'ma, N.F. Chaban. Boron Containing Binary and Ternary Systems. Handbook. Moscow: Metallurgiya (1990).
92. E. Hernández, C. Goze, P. Bernier, A. Rubio. Phys. Rev. Lett., **80**, 4502 (1998).
93. H.J. Xiang, J. Yang, J.G. Hou, Q. Zhu. Phys. Rev.B, **68**, 035427 (2003).

94. L. Wirtz, A. Rubio, R.A. de la Concha, A. Loiseau. Phys. Rev. B, **68**, 045425 (2003).
95. L. Wirtz, M. Lazzeri, F. Mauri, A. Rubio. Phys. Rev. B, 71, 241402(R) (2005).
96. H.F. Bettinger, T. Dumitrică, G.E. Scuseria, B.I. Yakobson. Phys. Rev. B, **65**, 041406 (2002).
97. Y. Miyamoto, A. Rubio, S. Berber, M. Yoon, D. Tománek. Phys. Rev. B, **69**, 121413(R) (2004).
98. G.Y. Gou, B.C. Pan, L. Shi. Phys. Rev. B, **76**, 155414 (2007).
99. E. Hernandez, C. Goze, P. Bernier, A. Rubio. Appl. Phys. A, **68**, 287 (1999).
100. D. Srivastava, M. Menon, K.-J. Cho. Phys. Rev. B, vol. **63**, 195413 (2001).
101. T. Dumitrica, B.I. Yakobson. Phys. Rev. B, **72**, 035418 (2005).
102. L. Chkhartishvili. Quasi-Classical Theory of Substance Ground State, Tbilisi: GTU (2004).
103. L. Chkhartishvili. Quasi-Classical Method of Calculation of Substance Structural and Electronic Energy Spectrum Parameters. Tbilisi: TSU (2006).
104. L. Chkhartishvili. Trans. GTU **427**, 13 (1999).
105. L. Chkhartishvili. J. Phys.: Conf. Ser., **176**, 012013 (2009).
106. L. Chkhartishvili. In: Proc. 4th Int. Boron Symp. Eskişehir: OGU, 153 (2009).
107. L. Chkhartishvili. In: Proc.1st Int. Boron Symp. Kütahya: DU, 139 (2002).
108. L. Chkhartishvili. J. Phys.: Conf. Ser., **176**, 012014 (2009).
109. L. S. Chkhartishvili. Mat. Sci. Nanostr., **1** 33 (2009).
110. Ch. Froese–Fischer. The Hartree–Fock Method for Atoms. A Numerical Approach. New York: Wiley (1977).
111. R.J. Boscovich. Philosophiae naturalis theoria redacta ad inicam legem vitium in natura existentiam. Milano: Collegio Romano (1758).
112. T.L Hill, R.V. Chamberlin. Nano Lett., **2**, 609 (2002).

SUMMARIES

P.J. Kervalishvili. Spin transport properties of manganese doped nanostructured magnetic semiconductors. Nano Studies, **2**, 5-14 (2010).

Technology of periodic layer GaSb / Mn nanostructure getting, the structural and magneto-transport properties of thin GaMnSb films with increased content of Mn, up to 10 at. %, grown by use the laser dispersion in vacuum was studied. The structures of GaMnSb layers, regardless to the Ga replacing by the Mn acceptors, contain ferromagnetic MnSb nanoclusters and shallow acceptor defects controlled by the growth temperature were investigated.

In obtained double phase ferromagnetic GaMnSb films, regardless to the case of previously studied single phase GaMnSb systems (Curie temperatures not exceeding 30 K), the anomalous Hall effect (AHE) and the AHE hysteresis at temperatures up to 300 K, as stronger as more the hole concentration, has been observed. The unusual properties of GaMnSb films have been interpreted as interaction of magnetic nanoclusters in a semiconductor matrix, where the matrix has huge concentration of free holes and magnetic ions, and which becomes stronger with increasing the holes concentration.

It was investigated the magnetotransport properties of GaSb / Mn discrete alloys which should be used as ferromagnetic contacts in process of formation GaMnSb / GaSb / GaMnSb and GaMnSb / GaAs / GaMnSb three layered structures for observation of spin polarized current in perpendicular geometry.

The model problem concerning the formation of a ferromagnetic cluster (magnetic polaron) consisting of the free electron bound to a non-magnetic donor impurity in an antiferromagnetic matrix was analyzed. It was shown that the magnetic polaron also produces rather long-range extended spin distortions of the antiferromagnetic background around the core. Such a magnetic polaron state can be favorable in energy in comparison to usually considered one. The studies of the structure of magnetic polarons (nanoscale ferromagnetic droplets) in magnetic semiconductors were performed with a special emphasis to frustrated lattices (square lattice with nearest-neighbor and diagonal interactions and the triangular lattice) characteristic for layered heterostructures. It was demonstrated that the magnetic polaron can produce rather extended spin distortions of the antiferromagnetic background around its ferromagnetic core. The characteristic size of this 'coat' decreases for stronger next-nearest neighbor interaction or with increase of magnetic anisotropy.

L. Chkhartishvili, T. Berberashvili. Geometries of boron nitride multi-walled nanotubes and multi-shelled fullerenes. Nano Studies, **2**, 15-21 (2010) – in Russian.

Based on models of boron nitride BN regular nanotubes and regular fullerenes, the interpolation formulas of their radii are constructed. Using them, the possible sequences of nanotubular and fullerene-like layers, respectively, in multi-walled nanotubes and multi-shelled fullerenes are predicted. Obtained results have revealed universal correlation between intra- and interlayer bond lengths in all boron nitride layered structures.

A.A. Gachechiladze, A.G. Mikeladze, D.L. Gabunia, B.G. Margiev, R.V. Chedia, T.A. Tsuladze, R.K. Zekalashvili, O.A. Tsagareishvili. Titan carbide based nano-crystalline solid solutions: Production and compacting. Nano Studies, **2**, 23-29 (2010) – in Russian.

Titan carbide based nano-crystalline solid solutions TiC + Ni (10 %) have been obtained by the chemical synthesis method in reaction between titanium hydride compounds and carbide-forming and binding components. Nickel has been chosen for the binding metal. Theoretical thermodynamic analysis performed for the ternary system (Ti – C) – Ni (10 %) has shown that TiC and TiNi compounds are able to be formed within the wide interval of concentrations, (28 – 48) wt. %. On purpose obtaining of the TiC + Ni (10 %) nano-crystalline powders titanium hydride, nickel chloride and soot were used as starting materials in charges molar-ratios as Ti : C : Ni = 1 : 1 : 0.1. Obtained product TiC + Ni was a black agglomerated nano-crystalline

powder. Then, produced powders have been compacted in two stages applying specially elaborated spark-plasma-synthesis plant. Full-stroke compacting of powders takes (3 – 4) min. Proposed method of synthesis allows to retain nano-crystalline structure even in compacted samples and goods.

A.G. Danelyan, V.A. Danelyan, R.R. Kankia, S.A. Mkrtychyan, S.V. Shotashvili, D.I. Gharibashvili, I.R. Lomidze. Some issues of precious linear measurements in nanometric region. Nano Studies, **2**, 31-44 (2010) – in Russian.

A.G. Danelyan, R.R. Kankia, C.A. Mkrtychyan, D.I. Gharibashvili, I.R. Lomidze. Nanometrology: Topicality and problems. Nano Studies, **2**, 45-52 (2010) – in Russian.

N.O. Metreveli, K.K. Jariashvili, L.O. Namicheishvili, D.V. Svintradze, E.N. Chikvaidze, A. Sionkowska, J. Skopinska. UV−Vis and FT−IR spectra of ultraviolet irradiated collagen in the presence of antioxidant ascorbic acid. Nano Studies, **2**, 53-64 (2010).

The influence of deleterious UV radiation on collagen molecules in the absence and presence of ascorbic acid using UV−Vis and FT−IR spectroscopy has been studied. Intensity of UV−Vis absorption spectrum of collagen with a maximum at 275 nm due to the aromatic residues (tyrosine and phenylalanine) increases with the increasing dose of UV radiation. This effect is significantly hindered in the presence of antioxidant ascorbic acid. Intensities of FT-IR bands (amide A, B, I and II) of collagen decrease with the increase of the UV radiation dosage. Intensities of bands are also decreased in the presence of ascorbic acid.

Results suggest that increasing the concentration of ascorbic acid increases the photo-stability of collagen, and the collagen becomes less sensitive to UV radiation. It is possible that hydrogen bonds form between the groups N – H of collagen and C = O of ascorbic acid. It is believed that under UV radiation free radicals appear in acid soluble collagen and resulting in photo-degradation of the macromolecule restore due to the ability of ascorbic acid donating one or two electrons. Increasing the dose of radiation causes more molecules of ascorbic acid to slow down, and their antioxidant effect is diminished accordingly.

N. Tsibakhashvili. Microbial synthesis of metal and semiconductor nanoparticles. Nano Studies, **2**, 65-70 (2010).

In this work a brief overview of the current research worldwide on the use of microorganisms such as bacteria and actinomycetes (both prokaryotes), as well as algae, yeast, and fungi (eukaryotes) in the biosynthesis of metal and semiconductor nanoparticles and their application is presented.

A.P. Bibilashvili. Carbon nanosystems. Nano Studies, **2**, 71-83 (2010) – in Georgian.

Z. Gogua, G. Kantidze. Heat capacity of the 3D and 2D systems according to interatomic chemical bonding. Nano Studies, **2**, 85-94 (2010).

Values of bonding energies of sp^3 and sp^2s^- hybrid bonding are calculated in the paper. These calculations are performed according to the conception of the influence of anti-bonding quasi-particles on the interatomic bonding force when the bonding particle takes an anti-bonding position. Melting process of covalent crystals is considered and the critical concentration of anti-bonding quasi-particles, at which the melting process begins, is defined. It may be caused not only by temperature, but by action of light, injection of charge carriers and in other ways. Within the Einstein's model of solid, the heat capacity is calculated for 3D crystal as well as 2D systems.

K.D. Davitadze, T.A. Minashvili, G.N. Iluridze. Doping of thulium, praseodymium and neodymium sulfides thin films. Nano Studies, **2**, 95-97 (2010) – in Georgian.

Pure rare-earth-elements sesquialteral sulfides are useless in microelectronic devices. Present work deals with doping of such films. Namely, some dopants have been chosen and appropriate doping technologies has been elaborated. Not once doping with lead or cadmium is shown formation of an additional phase.

G. Dekanozishvili, D. Driaev, T. Kalabegishvili, V. Kvatchadze. Stimulated phenomena in glass doped with CdSe quantum dots. Nano Studies, **2**, 99-102 (2010).

Thermo-stimulated luminescence (TSL) of glass samples doped with CdSe quantum dots (QDs) and irradiated with X-rays and UV light has been investigated. UV effect is negligible, whereas between TSL intensity and sample exposure time to X-rays there is linear correlation. Photoluminescence and its temperature quenching were studied by thermo-optical luminescence method.

R.I. Chikovani. Proposals for formation of a nanotechnology center in Georgia. Nano Studies, **2**, 103-118 (2010) – in Russian.

Article is devoted to perspectives of the development of nanotechnology in Georgia. Section 1 presents a brief overview of the nanotechnology development in general, its characterization, already obtained results and actual perspectives. There are shown possibilities of nanotechnological applications of in various fields of human activities. It is stated that nanotechnology should radically change whole human life in future. It is emphasized that number of nations has adopted their programs on development of nanotechnology.

In Section 2, there are considered issues of development of nanotechnology in Georgia. The perspectives are shown and the factors are analyzed those favor the further development. In addition, some proposals are expressed with regard to formation of the sharing nanotechnology center in Georgia and training of its personnel.

R.E. Kazarov, R.I. Chikovani, D.I. Garibashvili, G.I. Goderdzishvili, T.I. Khachidze. On elaboration of optoelectronic elements exploiting properties of nanosilicon formed in "silicon-on-sapphire"-structure. Nano Studies, **2**, 119-121 (2010) – in Russian.

Article is devoted to very interesting and perspective issue – formation of solid-state optoelectronic elements based on light-emitting nanostructural silicon and heteroepitaxial structure "silicon-on-sapphire". There posed main technological problems, which should be solved for making various optoelectronic elements.

A.B. Guchmazov, G.N. Iluridze, T.A. Minashvili, G.V. Rtveliashvili, M.S. Taktakishvili. Photoelectric parameters determination for AlGaAs heterostructure-based photo-cells by a conctacless method. Nano Studies, **2**, 123-125 (2010) – in Georgian.

In the work, a conctacless method of investigation of the photo-cell heterostructures is described. There is shown that in such semiconductor structures parameters, like the photogenerated charge carrieers' internal interassembly collection coefficient, can be estimated based only on observations of their luminescence radiation.

T.N. Khoperia, T.I. Zedginidze. Competitive nanotechnologies for nanoelectronics, piezoengineering, photocatalysis and composites particularly using electroless deposition. Nano Studies, **2**, 127-138 (2010).

Electroless metallization technology which allowed replacing adequately Au and Ag with Ni – P or Ni – B alloys and simplifying significantly the metallization process was developed. The proposed patentable nanomethods for the first time allow one to produce nanochips and photomasks with nano-sized adjacent elements by single optical UV photolithography. The proposed nanomethods are much more advantageous and simpler than other expensive and complicated

methods such as e-beam, X-ray lithography or fabrication of nanoelements using light-phase-shift photomasks. The proposed methods of metallization are widely used in electronics**,** piezoengineering and instrument-making. As a result Au, Ag and Pd were replaced with the alloys of non-precious metals; usage of toxic substances was eliminated.

L. Chkhartishvili. Boron nitride nanostructures: Molecules, sheets, tubes, fullerenes (An overview). Nano Studies, **2**, 139-174 (2010).

An overview of the present state of studies in synthesizing methods, atomic geometry, binding, stability, electron structure, and applications of boron nitride BN nanosystems is given. In particular, the explicit expressions in term of B–N bond length are obtained for atomic sites coordinates and intersite distances in regular boron nitride nanotubes and fullerenes.

V.G. Kvachadze, T.I. Pavliashvili, G.G. Abramishvili, T.L. Kalabegishvili, V.M. Gabunia. Preparation of iron oxide nanoparticles by laser ablation method. Nano Studies, **2**, 175-177 (2010) – in Russian.

The a-Fe_2O_3 nanoparticles are obtained in distilled water by the laser ablation method (using Laser OGM – 20). Their sizes have been determined by the X-ray diffraction, scanning and transmission electron microscopies. Alongside with large-scale agglomerates, product contains nanoparticles with sizes about (10 – 20) nm.

N. Tsibakhashvili, T. Kalabegishvili, V. Gabunia, E. Gintury, N. Kuchava, N. Bagdavadze, D. Pataraya, M. Gurielidzse, D. Gvarjaladze, L. Lomidze. Synthesis of silver nanoparticles using bacteria. Nano Studies, **2**, 179-182 (2010).

A simple route for the synthesis of silver nanoparticles by *Spirulina platensis* (cianobacteria) and *Streptomyces* spp. 211A (actinobacteria) has been demonstrated in this work. The silver nitrate solution incubated with bacteria biomass changed to a yellowish color, indicating the formation of silver nanoparticles. Spectroscopic analysis demonstrated that tested solutions yielded the maximum absorbance peak at 425 nm due to silver nanoparticles. Also, X-ray analysis of the bacterial biomass confirmed the formation of silver nanoparticles.

L. Chkhartishvili, I. Murusidze. On relative stability of single-walled boron nitride nanotubes. Nano Studies, **2**, 183-212 (2010).

Molar binding energy of the boron nitride single-walled zigzag and armchair nanotubes is calculated within the quasi-classical approach. Its oscillation depending on the tube radius is found out in the range of ultra-small-radii. Nanotubes (1,1), (3,0), and (4,0) are predicted to be more stable species among single-walled boron nitride nanotubes.

ISSN 1987 – 8826